SEISMIC RESPONSE OF CANTILEVER SHEAR WALL BUILDINGS

by

EHSAN DEZHDAR

B.Sc., Sharif University of Technology, 2004

M.Sc., Imperial College London, 2006

A THESIS SUBMITTED IN PARTIAL FULFILLMENT OF

THE REQUIREMENTS FOR THE DEGREE OF

DOCTOR OF PHILOSOPHY

in

THE FACULTY OF GRADUATE STUDIES

(Civil Engineering)

The University of British Columbia

(Vancouver)

December 2012

Abstract

Nonlinear time history analysis was carried out in order to estimate the demands on cantilever shear wall buildings due to the design level earthquakes. A hysteretic bending moment - curvature relationship was developed and implemented into computer program OpenSees. The study included 15 different shear wall buildings that ranged in height from 10 to 50 stories with a range of elastic bending moment demand at the base as a ratio of bending moment capacity from 1.3 to 3.7.

The influence of ground motion selection and scaling on different structural response quantities was studied. The input ground motions were scaled to uniform hazard spectrum (UHS) and conditional mean spectrum (CMS). It was observed that a fewer number of spectrum matched ground motions can be used to establish the mean response, while a reasonable similarity was found between the mean demand parameters from spectrum matched and the envelope of CMS ground motions.

Mean roof displacements from nonlinear time history analysis were used to determine appropriate effective stiffness values to be used in response spectrum analysis to accurately predict the maximum roof displacement. It was observed that stiffness reduction factor reduced from 1.0 to about 0.5 as the ratio of elastic bending moment demand at the base to the wall flexural capacity increased from 1.3 to 3.7. In addition, models were proposed for the complete envelopes of curvature demand and interstory drift demand over the wall height, including an accurate estimate of the maximum curvature demand at the wall base, midheight curvature demand, and maximum interstory drift at the roof. The developed models for base curvature and roof interstory drift demands were expressed in term of roof displacement demand. The midheight curvature demand was found to be less than the recommended values for yield curvature. Lastly, the results of nonlinear time history analysis were used to determine an expression for estimating base shear force demands. The shear amplification factor, defined as the ratio that the design base shear force needs to be increased, was found to be independent of the building height and to have a maximum value of 2.0.

Table of Contents

List of Tables

List of Figures

Acknowledgements

The author wishes to thank Dr. Perry Adebar for his invaluable advice and constant support during these years from the start to completion of my research. The completion of this thesis would have not been possible without his insightful comments and valuable feedback. The author also acknowledges Dr. Donald Anderson for his astute guidance throughout the course of this research work.

I would like to extend special thanks to my father Ali Dezhdar and to my mother Efat Shokri. My father has encouraged me to pursue a PhD degree since I was in grade school. My mother has been a major source of emotional support for me throughout the years. Her calming words and unwavering optimism have provided me with the strength and stamina to push ahead whenever I was feeling exhausted and frustrated. Thanks also go to my brother Omid Dezhdar, who has always believed in my potential, ever since I was a teenager.

I wish to sincerely thank my fellow graduate students at UBC, especially Majid Baradaran Shoraka for his generous friendship during the years I have lived in Vancouver.

To my mother, for whom I have nothing but forever love and respect

and to my father who taught me integrity and perseverance

Chapter 1 : Introduction

1.1 Concrete Shear Wall Buildings

Concrete shear walls are a popular seismic force resisting system for high-rise buildings in North America. Excellent performance in past earthquakes, less architectural restrictions compared to moment resisting frames, and faster construction times are some advantages of concrete shear walls compared to other seismic force resisting systems. Figure 1.1 shows one common form of high-rise concrete shear wall buildings, which has a central core consisting of concrete walls surrounding a cluster of elevator and stair shafts. The rectangular-shaped cores have large openings in the walls on at least two opposite sides to provide access into the elevators and stairways. The vertical wall segments adjacent to the openings are coupled together by the horizontal wall segments above and below the openings creating a coupled wall system in the direction parallel to the walls with openings (E-W direction in Figure 1.1). When two sides of the core do not have large openings, the core acts as a cantilever wall system perpendicular to the coupled walls (N-S direction in Figure 1.1). Such core wall systems with cantilever walls in one direction are the predominant seismic force resisting system for high-rise buildings in western Canada and have been used for a number of buildings in the US.

Another form of high-rise concrete shear wall buildings is using numerous thin shear walls distributed throughout the building. In high-rise residential buildings in Chile for example, usually the 6 or 8 in. partition walls between every room are shear walls that help control the lateral movements of the building. Figure 1.2 shows the plan view of such buildings.

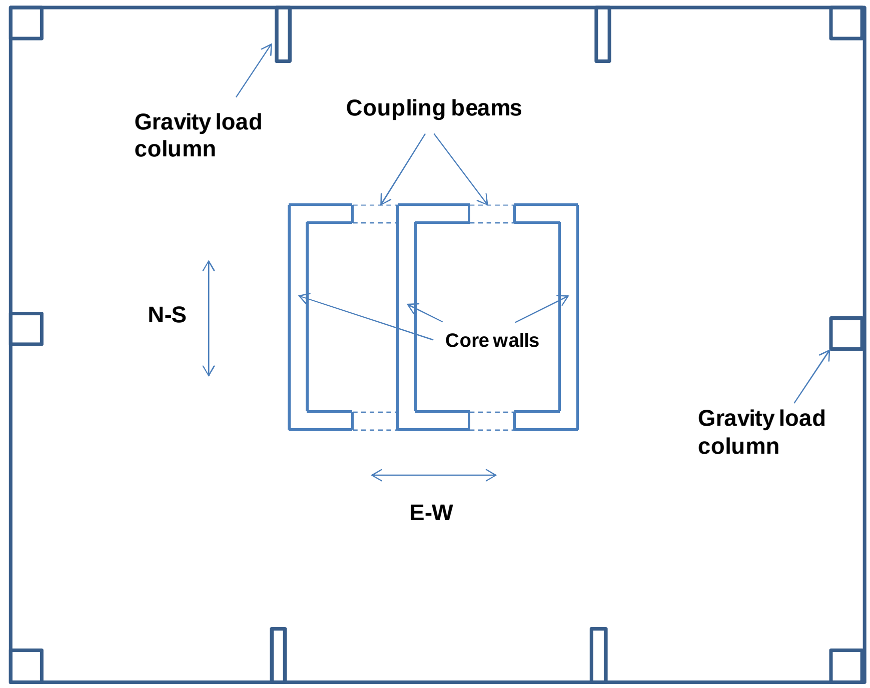

Figure 1.1 Layout of core walls in the plan of a concrete shear wall building.

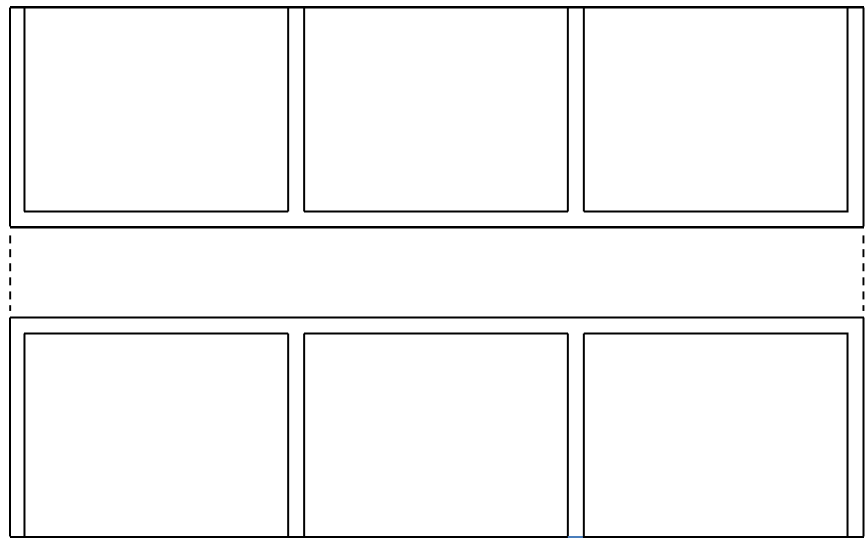

Figure 1.2 Plan view of a shear wall building showing main structural walls acting as cantilever wall system.

1.2 Seismic Design of Concrete Shear Walls

There are five important aspects of the seismic response of concrete shear walls that are investigated as a part of this thesis: (i) the maximum wall displacements at the top of buildings, (ii) the maximum flexural demands at the base of the walls, (iii) the flexural demands near the midheight of the walls due to the influence of higher modes, (iv) the profile of interstory drifts over the height of the shear walls, and (v) wall shear force demands. Each of these is discussed briefly below.

1.2.1 Roof Displacement Demands

Estimating roof displacement demand is one of the most important aspects of the seismic design of concrete shear walls. For example, the Canadian Concrete Code for the design of concrete structures (CSA A23.3-04) uses this parameter to determine the inelastic rotation demands at the base of the wall, the punching shear failure of slabs around gravity-load columns, and the shear strength of concrete shear walls in the plastic hinge region.

Linear dynamic analysis - in the form of response spectrum analysis (RSA) - is commonly used to estimate roof displacement demands by design engineers. The predicted roof displacement demand depends on the effective sectional stiffness (flexural rigidity) EI_e used for the shear walls in the RSA. Available recommendations on effective stiffness of concrete shear walls vary considerably. CSA A23.3-04 recommends an effective stiffness of $0.7EI_g$ for a wall with axial compression force of $0.1f_c'A_g$. ATC 72 (2010) recommends using an effective stiffness of $0.4EI_g$ to $0.5EI_g$ for walls with a similar axial compression force level based on limited shake table results. Some researchers have suggested using much lower effective stiffnesses - in the order of $0.2EI_g$ - to obtain a good estimate of the roof displacement demand of a 7-story shear wall building (Panagiotou 2008). One of the topics of this thesis is to investigate what is the appropriate effective stiffness that should be used in an RSA to estimate the maximum roof displacement demand.

1.2.2 Inelastic Deformation Demands at the Base of Wall

In Canada, the geometry of concrete cantilever shear walls is usually chosen so as to limit the maximum compression strain demands in the concrete such that confinement reinforcement is not needed. The maximum compression strain demands are a function of the maximum curvature demand and the compression strain depth, which depends on the geometry of the concrete wall and the axial compression load applied to the wall. Flexural deformation demands, such as curvatures, are largest at the base of a cantilever shear wall.

Both the Canadian concrete code CSA A23.3-04 and the ACI 318 building code use relatively recently developed rational models for relating the maximum curvature demands in the wall to the maximum top wall displacement. The details of these models are presented in Section 5.4.1.1.

In the Canadian code approach, the inelastic rotation demand θ_{id} is compared with the inelastic rotation capacity of the wall at the base θ_{ic} to ensure that the wall has enough ductility to undergo the induced seismic displacements. The inelastic rotational capacity is equal to the inelastic curvature capacity times the plastic hinge length, which is assumed to be equal to half the wall length ($0.5l_w$). The inelastic rotation demand at the base of a cantilever shear wall is determined from the inelastic portion of roof displacement demand Δ_{id}. Figure 1.3 summarizes the relationship between total roof displacement Δ_t and inelastic rotation at the base of the wall. The elastic portion of the roof displacement Δ_e is based on the time history results of White (2004) who used a limited number of ground motions (10 ground motions) and restricted the inelastic response of the shear walls to the base of the wall. The relationship between top wall displacement and maximum curvature at the base of cantilever shear walls is investigated in the current thesis using a larger number of different shear wall heights h_w and a larger number of ground motions in order to achieve more reliable time history results.

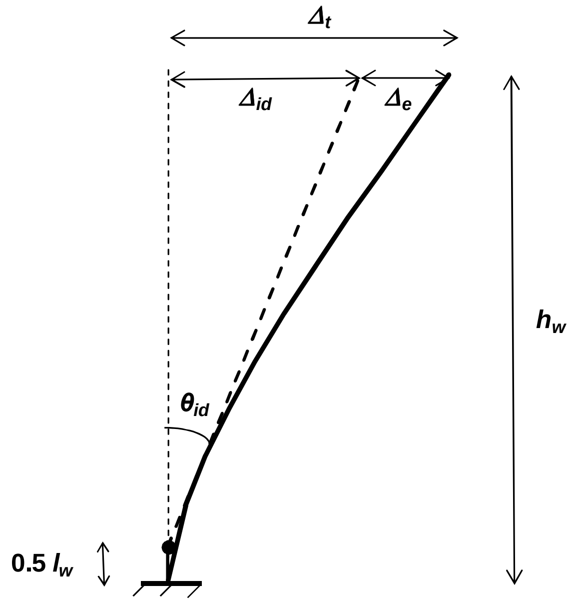

Figure 1.3 Determination of inelastic rotation demand from roof displacement demand (l_w = wall length, h_w = wall height, θ_{id} = inelastic rotation demand, Δ_{id} = inelastic portion of roof displacement demand, and Δ_e = elastic portion of roof displacement demand).

1.2.3 Flexural Demands at Wall Midheight

The current procedures for designing cantilever shear wall buildings in Canada assumes there will be a plastic hinge zone at the base of the wall, which is detailed for ductility; but the rest of the wall will remain elastic. A number of time history analyses have shown that very large bending moments may develop near the midheight of cantilever shear walls due to higher mode bending moments, and thus cantilever shear walls may experience significant flexural yielding near midheight. As the walls are not provided with ductile detailing near midheight, this yielding is of significant concern.

One solution that has been proposed is to increase the flexural capacity of shear walls to restrict flexural yielding to the base of the wall; however as the walls have much reduced axial compression near midheight, very significant increases in vertical reinforcement is needed to prevent yielding near mid-height. Some researchers have proposed design envelopes, which correlate the design bending moment at the midheight to displacement ductility and fundamental period of the structure. Using such envelopes is equivalent to providing higher percentages of longitudinal reinforcement than using the conventional bending moment envelope determined using response spectrum analysis.

In the current thesis the maximum curvature demands at midheight are investigated to determine whether special ductile detailing should be provided near the midheight of cantilever shear walls.

1.2.4 Interstory Drift Demands

Interstory drift demands strongly influence the deformation demands on the gravity-load system including the columns and the slab-column connections. For example, larger interstory drifts cause larger rotational demands on slab-column connections, and this increases the likelihood of a punching shear failure of the slabs. In practice, interstory drift demands are usually determined from a linear analysis such as response spectrum analysis. Due to the concentration of inelastic rotation at the base of a cantilever wall, the interstory drift profile may be significantly different than determined from a linear analysis. The typical profiles of maximum interstory drifts is another topic that will be investigated in the current thesis.

1.2.5 Shear Force Demands

Accurately estimating the shear force demands is of particular importance in the seismic design of cantilever shear walls in order to ensure these structures will have a ductile response. In practice, the shear force demand is normally estimated from response spectrum analysis using the same reduction factor as is used to determine the bending moment demand accounting for flexural ductility. As flexural yielding at the base of a cantilever wall has much less influence on the higher mode shears compared to the first mode shear, the shear force demands determined from nonlinear time history analysis are usually considerably larger than those determined from a linear analysis. The difference between the shear force demands from the two approaches is often called the dynamic shear amplification. Available recommendations on the shear amplification factor are generally based on nonlinear time history results using limited number of ground motions and simple hysteretic models.

In the current thesis, a state-of-the-art hysteretic model and a large number of ground motions are used to determine a better estimate of shear force demands on high-rise shear walls. As the flexural rotations at the base of a wall significantly influence the shear resistance, the relationship between base rotation and base shear force demands are investigated.

1.3 Nonlinear Time History Analysis of Concrete Shear Walls

Nonlinear time history analysis has been used extensively by researchers to investigate the seismic response of structures and it is increasingly used by design engineers undertaking performance-based earthquake engineering design. A state-of-the-art nonlinear time history analysis requires a detailed analytical model as well as a comprehensive study on the selection and scaling of ground motions.

1.3.1 Analytical Models for Concrete Shear Walls

Available modeling tools for concrete shear walls include a finite element approach, fiber models, and bending moment - curvature models. The finite element approach is suitable for studying the behavior of shear-critical structures, where the influence of shear force and shear deformation play a significant role in the structural response. The accuracy of this approach has been validated with experimental results on large-scale slender and squat reinforced concrete shear walls (Palermo and Vecchio 2004), and it was proved that the finite element approach is a reliable tool for predicting the hysteretic behavior of concrete shear walls under reverse cyclic loads.

The problem associated with the finite element approach is the amount of output data produced and extracting useful data from the analysis. The output data can be overwhelming if this approach is used to perform nonlinear time history analysis. Fiber models and bending moment - curvature models are used more often than the finite element method due to less computational cost and more manageable outputs. In the fiber model, the cross section of a reinforced concrete element is discretized into a series of fibers with a prescribed constitutive relationship for concrete and reinforcing steel. The strains in the concrete and reinforcement are obtained using the assumption that plane sections remain plane, a valid approximation for flexural dominated structures but not for shear-critical structures. Implementing fiber model with detailed material models in commercial softwares makes the use of this analytical tool more appealing since the user has the option of modeling the concrete softening in compression, the concrete tension stiffening, and the softening of reinforcing steel under cyclic loads. Comparison of the fiber model prediction of the cyclic response of large-scale slender concrete shear wall specimens with experimental data showed good agreement (Orakcal and Wallace 2006).

The main concern associated with the fiber model is that it does not explicitly reflect the influence of wall characteristics - such as axial compression force, cross sectional geometry, and the percentage of longitudinal reinforcement - on the cyclic response of these structural elements. The hysteretic bending moment - curvature models are more transparent than the fiber model since the user can compute the parameters of the hysteretic model from the properties of the shear wall. Also, the user can easily control the shape of the hysteretic loops by changing the key parameters of the hysteretic model. Developing a hysteretic bending moment - curvature relationship results in better insights into the factors that influence the hysteretic characteristics of concrete shear walls.

Hysteretic models usually feature bilinear backbone curves. Although these models have been used extensively for modeling the hysteretic behavior of concrete shear walls (Priestley 2003; Rutenberg and Nsieri 2006; Panagiotou 2008), they are not suitable for modeling the backbone curve for high-rise concrete shear walls. Core walls in high-rise buildings have large flanges and are subjected to high axial compression force. For these elements, a large portion of the backbone segment is similar to the uncracked portion of the flexural response, and a bilinear backbone cannot approximate both the stiffness and yield curvature of the shear wall simultaneously. Figure 1.4 compares the bending moment - curvature relationship for a 30 story building core with an axial stress ratio $P/f_c'A_g$ of 10.1% and 0.5% longitudinal reinforcement in the flanges determined from fiber analysis with trilinear and bilinear approximations. If the slope of the bilinear curve is adjusted to approximate the initial stiffness of the predicted nonlinear curve, the yield curvature is significantly underestimated, while if the initial stiffness of the bilinear curve is adjusted to match the yield curvature, the bilinear approximation underestimates the stiffness characteristics of the shear wall. Figure 1.4 shows that the trilinear backbone curve gives a better approximation of the nonlinear response in terms of capturing both the initial stiffness and the yield curvature.

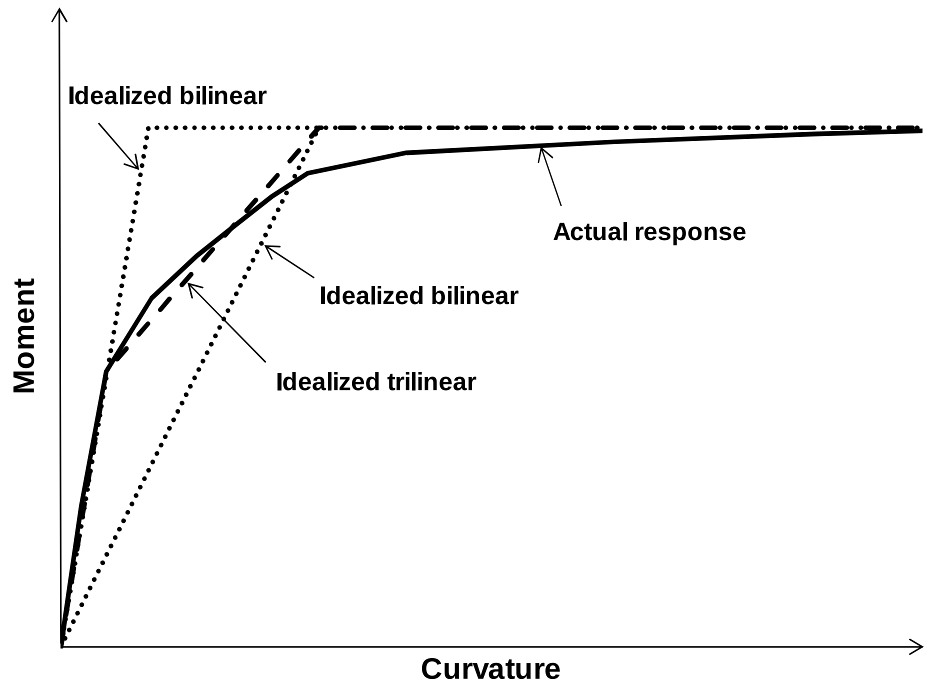

Figure 1.4 Comparison of actual bending moment - curvature relationship determined from fiber analysis with trilinear and bilinear approximations.

Nonlinear structural models include detailed 3-dimensional models, 2-dimensional models, and equivalent single-degree-of-freedom (SDOF) oscillators. The 3-dimensional and 2-dimensional models are performed by assigning bending moment - curvature relationship or fibre models to each component. Plasticity can be assumed to be spread over the length of the element or concentrated at both ends. Higher mode effects can also be detected by both models. Performing time history analysis using a 3-dimensional model gives insight into the additional demands on gravity-load columns associated with torsion. Using 2-dimensional models can still be used to estimate seismic demands on the shear wall itself since out of plane deformations are negligible in shear walls with doubly symmetric dross sections for which shear wall response is generally attributed to in-plane deformations. Also, the computational cost associated with nonlinear time history analysis on 3-dimensional models is relatively high, and it hinders the use of large number of ground motions in time history analysis. The 2-dimensional modeling of concrete shear is referred to as multi-degree-of-freedom (MDOF) models in this thesis. It consists of beam-column elements that represent the individual segments of the shear wall within floors (see Figure 1.3) and lumped seismic masses in every floors.

The nonlinear modelling of structures can be further simplified by developing an equivalent SDOF system. The properties of the SDOF model are determined from pushover analysis, which usually defines the relationship between base shear force and roof displacement demands. The most common load pattern used to perform pushover analysis would be proportional to the first mode displacement shape of the structure. It is, in fact, demonstrated in section 3.2 of this thesis that the SDOF oscillators can provide a reasonable estimate of the mean roof displacement determined from the MDOF method. It should be mentioned that the computational cost associated with SDOF models is much less than that for 3-dimensional and MDOF models. The limitation of SDOF models is that it does not explicitly detect the influence of higher modes on response quantities.

1.3.2 Ground Motion Selection and Scaling

Nonlinear time history analysis is the most rigorous method to estimate demands on high-rise structures due to earthquakes. The tall Building Initiative (PEER 2010) recommends this method of analysis to detect higher mode effects on the structural response of tall walls rather than using nonlinear static (pushover) analysis. In addition to the details of the nonlinear model, ground motion selection and scaling can impact the results of the time history analysis. A significant amount of research has been carried out in recent years to provide guidelines on appropriate ground motion selection and scaling schemes (PEER GMSM, Haselton et al. 2009; ATC 82 2011). Traditionally, the input ground motions are selected based on the magnitude and distance of a potential earthquake happening at the site as well as the source mechanism and site soil condition. The selected ground motions are then scaled to a target spectrum, which is generally in the form of uniform hazard spectrum (UHS). The common methods of scaling are spectrum matching, scaling at the fundamental period, and scaling over a range of periods. Recently, Baker and Cornell (2006) introduced conditional mean spectrum (CMS) as an alternative target spectrum to the UHS. The CMS accounts for the correlation between spectral accelerations at other periods given a target spectral acceleration at the period of interest (also called conditioning period T^*); thus it is a more realistic scenario than the UHS, which is essentially the envelope of spectral accelerations at all periods. It means that scaling the ground motions to the

UHS gives response quantities that are larger than those determined using the ground motions scaled to the CMS.

Most of the research carried out thus far deals with the sensitivity of the seismic response of concrete moment resisting frames to different ground motion selection and scaling approaches. Further research is needed to quantify the influence of scaling methods on the seismic response of concrete shear walls. It is also important to include demand parameters that are of particular importance for the seismic design of shear walls, e.g. roof displacement, curvature, interstory drift, and shear force demands. Lastly, it is necessary to include adequate number of conditioning periods for computing the target CMS, and compare the envelope of the responses from different conditioning periods with the demand parameters corresponding to the ground motions scaled to the UHS.

1.4 Research Approach

Nonlinear time history analysis is used in this thesis to study the seismic behavior of cantilever shear wall buildings. The approach taken in this research is to preserve the transparency of the analysis as much as possible by using the simplest model that is appropriate for the phenomenon being investigated. As the torsional response of shear wall buildings is not a part of the current investigation, a 2-dimensional model of the cantilever shear walls is used. One part of the current study involved examining how the shape of the force - displacement relationship influences the displacement demands. For this part of the study, a simple nonlinear single-degree-of-freedom model was used. Simple hysteretic models such as a trilinear bending moment - curvature relationship was used to model the cantilever shear walls rather than a more general fiber model, which is less transparent.

Fifteen different shear wall buildings are included in this study. The differences between the buildings are the heights (number of stories) and the flexural capacity of the shear walls in the buildings. The amount of longitudinal reinforcement in each shear wall is determined for different values of flexural strength reduction factor *R*, which is defined as the ratio of elastic bending moment demand to nominal flexural strength of the cantilever walls, both calculated at the base of the buildings. The flexural strength reduction factor is similar to the force reduction factor R_d in CSA A23.3-04, and is termed "force reduction factor" throughout this thesis to specify the ratio of elastic bending moment demand at the base to the wall flexural capacity.

The results from nonlinear time history analysis depend greatly on what ground motions are used and how these motions are scaled. Thus an extensive study was undertaken on the influence of ground motion selection and scaling on the response of cantilever shear walls. The uniform hazard spectrum (UHS) and conditional mean spectrum (CMS) computed at different conditioning periods were considered as the target spectrum for scaling the ground motions. Fifteen cantilever shear walls with various height and percentage of longitudinal reinforcement are designed and modelled in OpenSees. The study includes 10 to 50 story walls with fundamental period varying from 1.0 to 5.0 seconds. The results from time history analysis were used to develop models for an accurate prediction of response quantities that are of particular importance in the seismic design of concrete shear walls.

1.5 Thesis Objectives

The objectives of this thesis are:

- Develop a hysteretic trilinear bending moment - curvature relationship that can be used to perform nonlinear time history analysis of concrete shear walls.
- Investigate the influence of ground motion selection and scaling on the seismic response of cantilever shear walls.
- Develop a recommendation for effective stiffness EI_e to be used in response spectrum analysis of cantilever shear walls in order to obtain a good estimate of roof displacement demand.
- Investigate the relationship between roof displacement and base curvature demands for cantilever shear walls of different heights.
- Evaluate available models for estimating base curvature demand and propose a new model to accurately estimate the mean and mean plus one standard deviation base curvature demand.

- Investigate the relationship between flexural strength and curvature demand at the midheight of cantilever shear walls and develop a simple estimate of midheight curvature demands.
- Develop a simplified model to estimate interstory drift demand profiles over the height of cantilever shear walls.
- Develop a simplified shear force envelope accounting for the so called dynamic shear amplification due to the influence of higher modes after a cantilever wall develops a plastic hinge at the base.
- Investigate the relationship between shear force demand and inelastic rotation at the base of the wall, which directly influences the shear resistance of the wall.
- Validate the developed models for effective stiffness, base curvature, and interstory drift demands using the results of a shake table test of a full-scale 7-story cantilever shear wall.

1.6 Thesis Organization

This thesis consists of eight chapters and five appendices. Chapter 2 deals with the development of a hysteretic bending moment - curvature relationship for modeling the flexural response of slender shear walls. Fiber analysis is extensively used in this chapter to understand the bending moment - curvature relationship of slender walls subjected to reverse cyclic loads. The model is verified with the experimental results of two concrete shear wall specimens with different geometry and axial compression stress ratio. The hysteretic bending moment - curvature relationship is used to model 15 different high-rise concrete shear walls with different heights and flexural capacities designed according to the requirements of the Canadian Building Code CSA A23.3-04.

Chapter 3 focuses on the influence of the characteristics of force - displacement response of concrete shear walls on the effective stiffness. A summary of current recommendations on effective stiffness is presented at the beginning, followed by the analogy used in this thesis for estimating effective stiffness. The equivalent SDOF approach is used in this chapter for predicting roof displacement demands. The influence of hysteretic model and tension stiffening on the effective stiffness is also discussed in this chapter.

Chapter 4 presents the influence of ground motion selection and scaling on the structural response of cantilever shear walls. This chapter starts with a detailed summary of the previous research. It also contains time history results using different ground motion scaling method including spectrum matching, scaling at the fundamental period, and over a range of periods. Both UHS and CMS computed at different conditioning periods are considered as the target spectrum. Dispersion of time history results and the adequacy of seven ground motions for calculation of mean response are also discussed in this chapter.

Chapter 5 presents simplified models for predicting flexural demands on cantilever shear walls. Mean roof displacements are used to obtain appropriate effective stiffness values for performing response spectrum analysis. The CSA and ACI approaches for predicting base curvature demand is discussed and a refined model is developed for estimating mean and mean plus one standard deviation results. A design curvature profile is introduced that addresses midheight curvature demands on cantilever shear walls. A simple interstory profile is proposed for predicting interstory drift demands over the height. Influence of shear deformation and base flexibility on flexural demands is also studied in this chapter. Lastly, a modified RSA using varying effective stiffness over the height is introduced in this chapter for accurate estimate of curvature demands.

Chapter 6 presents seismic shear force demands of cantilever shear walls. This chapter begins with a summary of existing recommendations on shear amplification factor. An investigation is then carried out to obtain a simple base shear force - base rotation interaction diagram for three highly nonlinear walls. The influence of period lengthening on midheight shear force demands is also investigated. This chapter ends with a simple design envelope for predicting shear force demands over the height of cantilever shear walls.

Chapter 7 presents a comparison between the simplified flexural models developed in Chapter 5 with the shake table results of a full scale 7-story shear wall building. Roof displacement demand from the test is used to validate the effective stiffness values, while base curvature and interstory drift envelope are compared with the experimental results.

Contributions and recommendations for future work are presented in Chapter 8. Appendix A presents the layout of the core walls in example shear wall buildings. The percentage of longitudinal reinforcement and the parameters of the hysteretic trilinear bending moment - curvature relationship over the height of example shear wall buildings are presented in Appendix B. The details of the hysteretic force - displacement model used in the SDOF study conducted in Chapter 3 are shown in Appendix C, while the response spectra corresponding to ground motions used in this chapter are presented in Appendix D. The analytical results for the full range of walls studied in Chapter 3 are also included in Appendix E.

Chapter 2 : Hysteretic Bending Moment - Curvature Relationship for Nonlinear Analysis of Cantilever Shear Walls

2.1 Overview

In this chapter, a hysteretic bending moment - curvature relationship is developed as a tool to perform nonlinear time history analysis of cantilever shear walls. The model is verified by making comparisons with the experimental data from two large-scale tests of slender flanged and rectangular cantilever shear walls.

2.2 Nonlinear Modelling of Concrete Shear Walls

2.2.1 Fiber Analysis

Fiber analysis has been used extensively to predict the response of reinforced concrete members subjected to both static and dynamic loads (Orakcal and Wallace 2006; Taucer et al. 1991; Khaled et al. 2011). In this model, the cross section of an element is discretized into a series of uniaxial elements and an appropriate constitutive relationship is assigned to each fiber. The cross section response is obtained from integration of the response of fibres using the assumption that plane sections remain plane. Element forces are then calculated from integrating section forces at several integration points along the element.

Fiber analysis presented in this work was conducted in OpenSees (OpenSees 2008). There are several constitutive models for concrete and reinforcing steel in OpenSees which allow the user to model the response of concrete in compression and tension as well as the response of reinforcing steel. The so called *Concrete03* and *Steel02* models were used as the constitutive relationship for concrete and reinforcing steel, respectively. The general shape of the two models is shown in Figure 2.1.

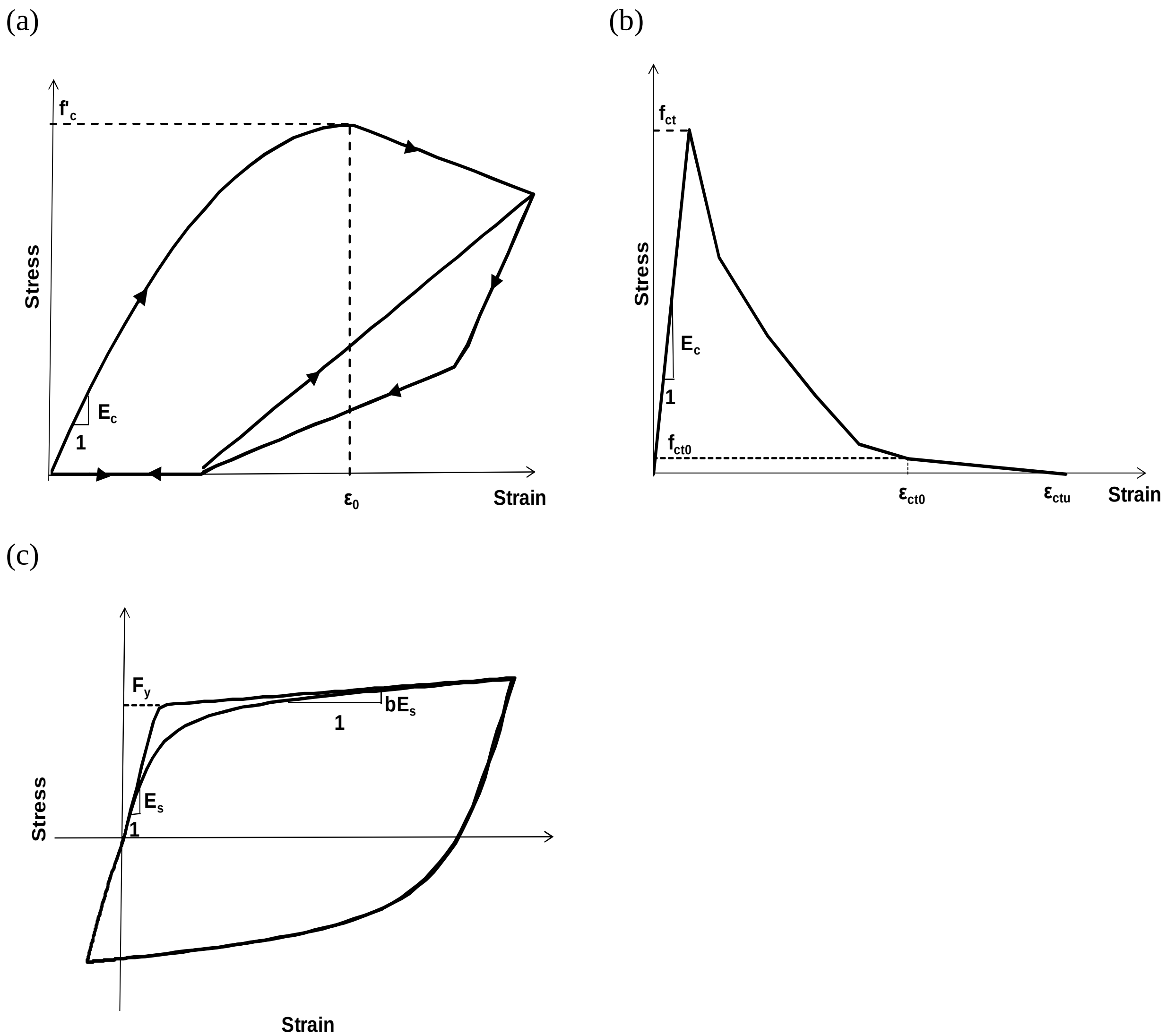

Figure 2.1 Constitutive relationships for: (a) concrete in compression, (b) concrete in tension, and (c) reinforcing steel.

The behaviour of concrete in compression (Figure 1(a)) consists of an ascending parabola branch until the stress reaches concrete compression strength f_c' at compressive strain of ε_0, followed by a descending linear branch. The behaviour of concrete in tension (Figure 1(b)) consists of a linear segment until tensile stress reaches the concrete tensile strength f_{ct}, followed by a nonlinear curve and linear branch until the stress gets to zero at tensile strain of ε_{ctu}. Note that f_{ct0} and ε_{ct0} are the stress and strain corresponding to the transition from the nonlinear to linear segment, respectively. The *Steel02* constitutive model can be described by defining the yield stress F_y, elastic modulus E_s, post yield slope bE_s as well as three parameters that control the transition from elastic to plastic branches. The *Steel02* constitutive relationship is based on the Menegotto and Pinto (1973) material model and is a well established model that can reasonably represent the response of reinforcing bars subjected to cyclic loading.

2.2.2 Hysteretic Bending Moment - Curvature Models

Hysteretic bending moment - curvature models have been used as an alternative to the fiber model for simulating the inelastic behaviour of reinforced concrete members in flexure. These models incorporate stiffness degradation and pinching under reversal and have been implemented in different computer programs. For example, the Takeda and Clough hysteretic rules have been implemented in computer program Ruaumoko (Carr 2002). These hysteretic models feature bilinear backbone relationship, which is not essentially a suitable approximation of the backbone curve for concrete shear walls with high axial compression force. In fact, White (2004) compared the force - displacement response predicted from the Clough model with experimental results of a slender shear wall specimen (Adebar et al. 2007), and he concluded that using the Clough model resulted in hysteretic loops that were much larger than those observed from the experiment, i.e. the Clough model did not capture the pinching characteristics of the flanged cross section subjected to high axial compression force.

Although the Takeda and Clough hysteretic models have been used extensively in research, the hysteretic response of concrete walls is better understood if a hysteretic bending moment - curvature model is developed based on the cross sectional analysis of the walls. Ibrahim (2000) studied the flexural response of walls with high axial compression force and light amount of longitudinal reinforcement and concluded that the uncracked segment of the bending moment - curvature relationship for such walls is significant. Based on the fiber analysis of different cross sections with a wide variety of axial compression force and longitudinal reinforcement ratio, Ibrahim proposed the concept of upper-bound and lower-bound response (see Figure 2.2). The upper-bound response corresponds to a previously uncracked wall loaded monotonically to failure, while the lower-bound response represents response of a wall reloaded after being severely damaged. The initial and secondary slope of both responses is uncracked flexural stiffness EI_g and cracked flexural stiffness EI_{cr}, respectively. The flexural capacity of the section M_n can be calculated from sectional analysis, and the parameters M_L' and M_L'' can be determined from the following equations:

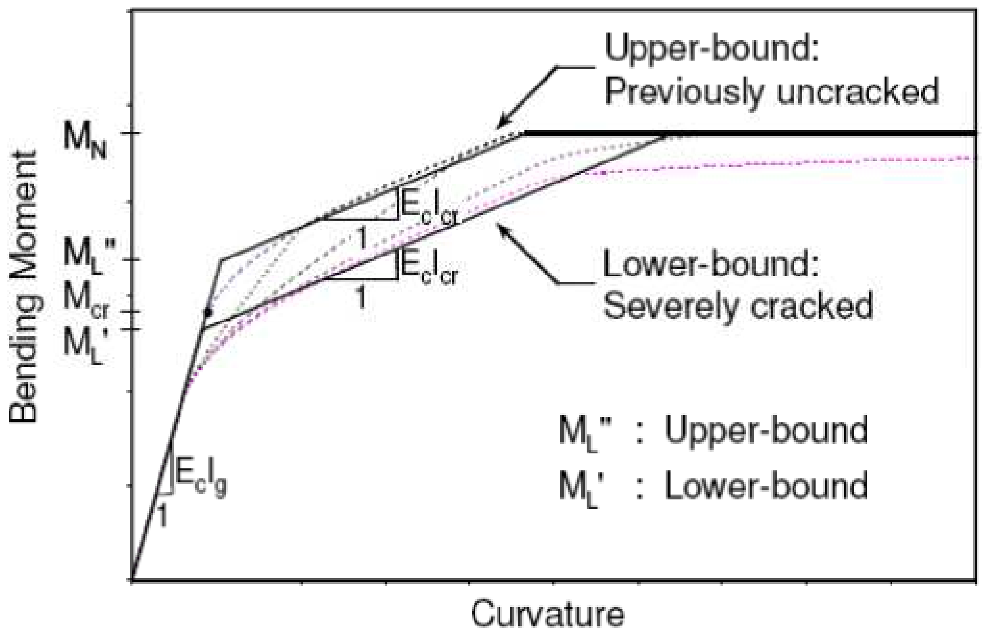

Figure 2.2 The upper-bound and lower-bound trilinear bending moment – curvature relationship (from Ibrahim 2000).

$$M_L'' = \left(1.5f_{cr} + \frac{P}{A_g}\right)S_g + 0.08Pl_w \qquad Eq\ 2.1$$

$$M_L' = \frac{P}{A_g}S_g + 0.08Pl_w \qquad Eq\ 2.2$$

where f_{cr} is the cracking strength of concrete, P is the axial compression force, A_g is the gross cross sectional area, S_g is the gross section modulus, and l_w is the wall length. In developing the upper-bound and lower-bound responses, Ibrahim (2000) assumed that i) concrete in compression unloads and reloads to the envelope of the monotonic stress - strain relationship with a slope equal to the elastic modulus of concrete E_c, and ii) the stress - strain relationship for reinforcing steel is bilinear. Consequently, the difference between the upper bound and lower bound response is contributed to the loss of tension stiffening in the concrete as the wall is loaded from an uncracked stage to a severely cracked stage.

The upper-bound and lower-bound trilinear models depicted in Figure 2.2 are suitable for predicting the response of walls subjected to monotonic loading. A full hysteretic bending moment - curvature relationship needs to be developed for performing time history analysis. The hysteretic model must have appropriate stiffness degradation and unloading rules that represent the behaviour of high-rise wall cross sections subjected to cyclic loads. For this purpose, the experimental data from two large-scale specimens are used to validate the fiber model and the assumptions used to develop the trilinear models shown in Figure 2.2. The fiber model is then used to develop appropriate stiffness degrading rules to be used in the hysteretic bending moment - curvature model. A simple unloading rule is also developed based on test data from a large-scale reinforced concrete section subjected to cyclic axial load. Lastly, the hysteretic bending moment - curvature model is validated with experimental results.

2.3 Experimental Program

2.3.1 UBC Shear Wall Specimen

Figure 2.3 shows the details of the test specimen. The specimen was 11.76 m high and was 1.625 m long with a flanged cross section. The flanges were 380 mm thick and 203 mm long, while the web was 1219 mm long and 127 mm thick. The flanges consisted of 5-10M vertical bars (ρ = 0.65%) enclosed by No.3 hoops spaced at 64 mm in the lower 3 m of the wall and spaced at 150 mm over the rest of the wall. Vertical reinforcement in the web consisted of 4-10M bars spaced at 305 mm over the length of the wall (ρ = 0.26%). The web was also reinforced with 10M horizontal bars spaced at 305 mm vertically. The clear cover to the reinforcement was 6 mm.

Average concrete compressive strength at the time of testing was 49 MPa, while the yield strength and ultimate strength of reinforcing bars were 455 MPa and 650 MPa, respectively. Testing of the specimen consisted of loading the specimen to a specific displacement in one direction and then unloading and reloading it to the same displacement in the opposite direction. A constant axial compression load of $0.1f_c'A_g$was applied to the wall throughout the test in addition to the lateral load applied at the top of the specimen. The experimental data was gathered for the four loading/unloading cycles for each specific displacement. During the test, it was observed that first concrete cracking and vertical reinforcement yielding occurred at global drift ratios of 0.18% and 0.39%, respectively. Cover of concrete at the compression face started to fall off at the global drift ratio of 1.5%, and the flange vertical reinforcement buckled and pushed off the concrete cover at the fourth cycle at the global drift ratio of 2.4%.

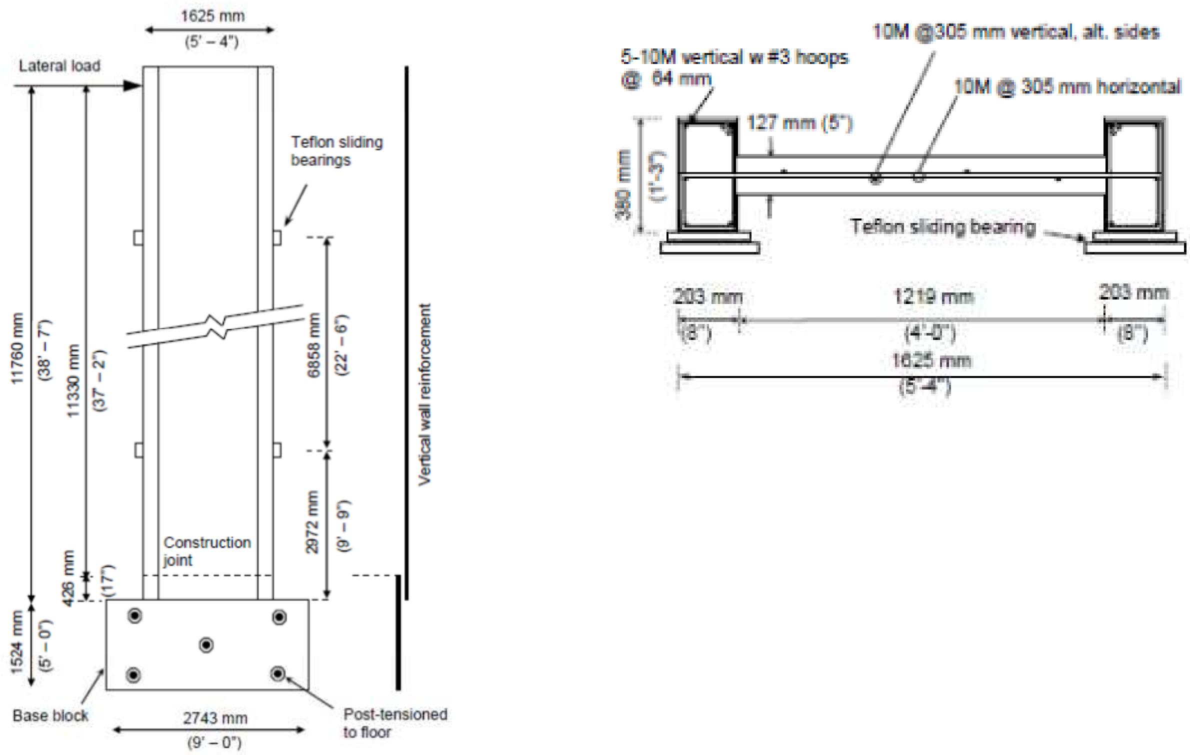

Figure 2.3 Details of the UBC specimen: (a) elevation, and (b) cross section. From Adebar et al. (2007), © ACI Structural Journal, by permission.

2.3.2 Clarkson Shear Wall Specimen

Figure 2.4 presents the details of the test specimen. The specimen was 3660 mm high and 1219 mm long with a rectangular cross section. The cross section was 102 mm thick, and the cover to the reinforcement was 19 mm. Longitudinal reinforcement at the boundaries included 8#3 bars (ρ = 3.6%) enclosed by 4.76 mm diameter wires spaced at 76 mm. Vertical reinforcement in the web consisted of 8#2 bars spaced at 191 mm over the length of the wall (ρ = 0.21%). Horizontal reinforcement at the web consisted of two curtains of #2 bars spaced at 191 mm over the height of the specimen.

Average concrete compressive strength at the time of testing was 42.8 MPa, while the yield strength for #3 and #2 web bars was 414 MPa and 448 MPa, respectively. The specimen was subjected to a cyclic lateral load applied at the top as well as a constant axial compression force of $0.07 f'_c A_g$. Similar to the UBC specimen, the Clarkson specimen was loaded to a specific displacement in one direction to the same displacement in the opposite direction. At least two complete cycles was performed for each specific displacement. During the test, it was observed that the longitudinal reinforcement at the boundaries yielded at the global drift ratio of 0.75%, while the concrete crushed at the edge of the specimen at 1% global drift ratio. The longitudinal reinforcement buckled at the global drift ratio of 2.5%.

(a)

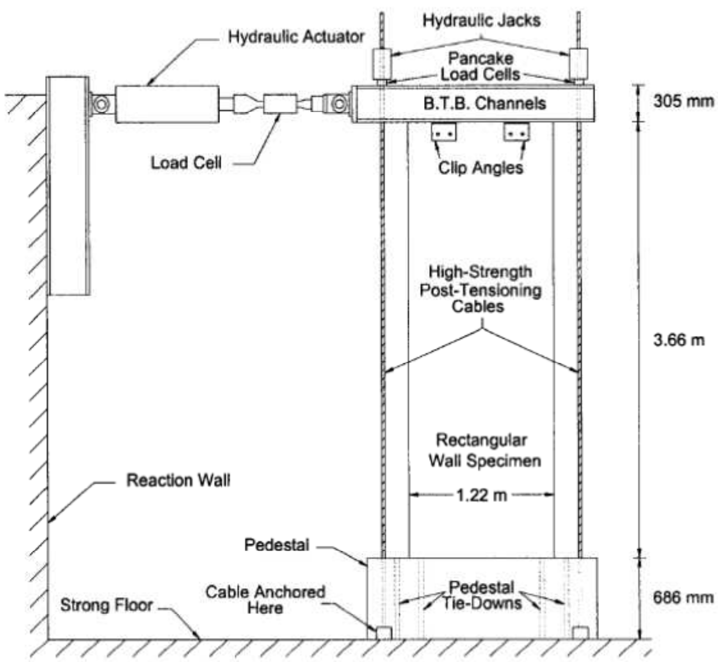

(b)

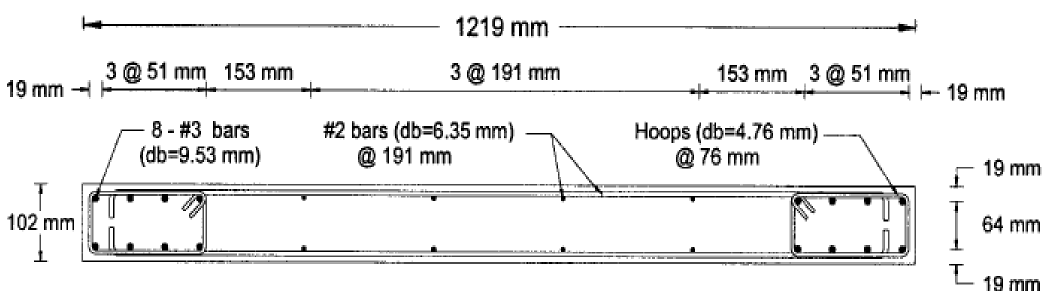

Figure 2.4 Details of the Clarkson specimen: (a) elevation (from Thomson and Wallace 2004, © Journal of Structural Engineering, by permission), and (b) cross section (from Orackal and Wallace 2006, © ACI Structural Journal, by permission).

2.4 Fiber Modelling Prediction of UBC and Clarkson Shear Wall Specimens

Fiber analysis of UBC and Clarkson specimens was performed in OpenSees using *Concrete03* and *Steel02* constitutive models depicted in Figure 2.1. Elastic modulus of concrete E_c and concrete tensile strength f_{ct} was assumed to be $4500\sqrt{f_c'}$ and $0.33\sqrt{f_c'}$, respectively. The strain corresponding to peak stress at compression, ε_0, was assumed to be 0.002 and the Kent and Park (1973) model was used to determine the slope of the descending branch of *Concrete03* backbone. The tensile strength f_{ct0} was assumed to be 10% of the concrete tensile strength f_{ct}, while ε_{ct0} and ε_{ctu} were considered to be 0.002 and 0.003, respectively (Adebar and Ibrahim 2002). Elastic modulus of steel E_s was set to 200,000 MPa and steel strain hardening was assumed to be 0.02. Both UBC and Clarkson specimens were modelled in OpenSees using five beam-column elements with displacement formulation. A fixed base support was assumed for both specimens. It should be noted that no shear deformation was considered in the fiber modelling of the two specimens. Recorded shear deformations were negligible for the UBC specimen. For Clarkson specimen, however, relatively large shear deformations were recorded in the lower 0.9 m of the specimen. As a result, it is necessary to separate the experimental results for top displacement into flexural and shear deformation components. Figure 2.5 and Figure 2.6 compare the lateral load - top displacement prediction from the fiber model with experimental results. The fiber model predictions are shown with a thick line. Note that the drift values indicated in Figure 2.6 correspond to the total top displacement recorded during each cycle. The horizontal axis in Figure 2.6, on the other hand, shows the flexural component of the measured top displacement for the Clarkson specimen.

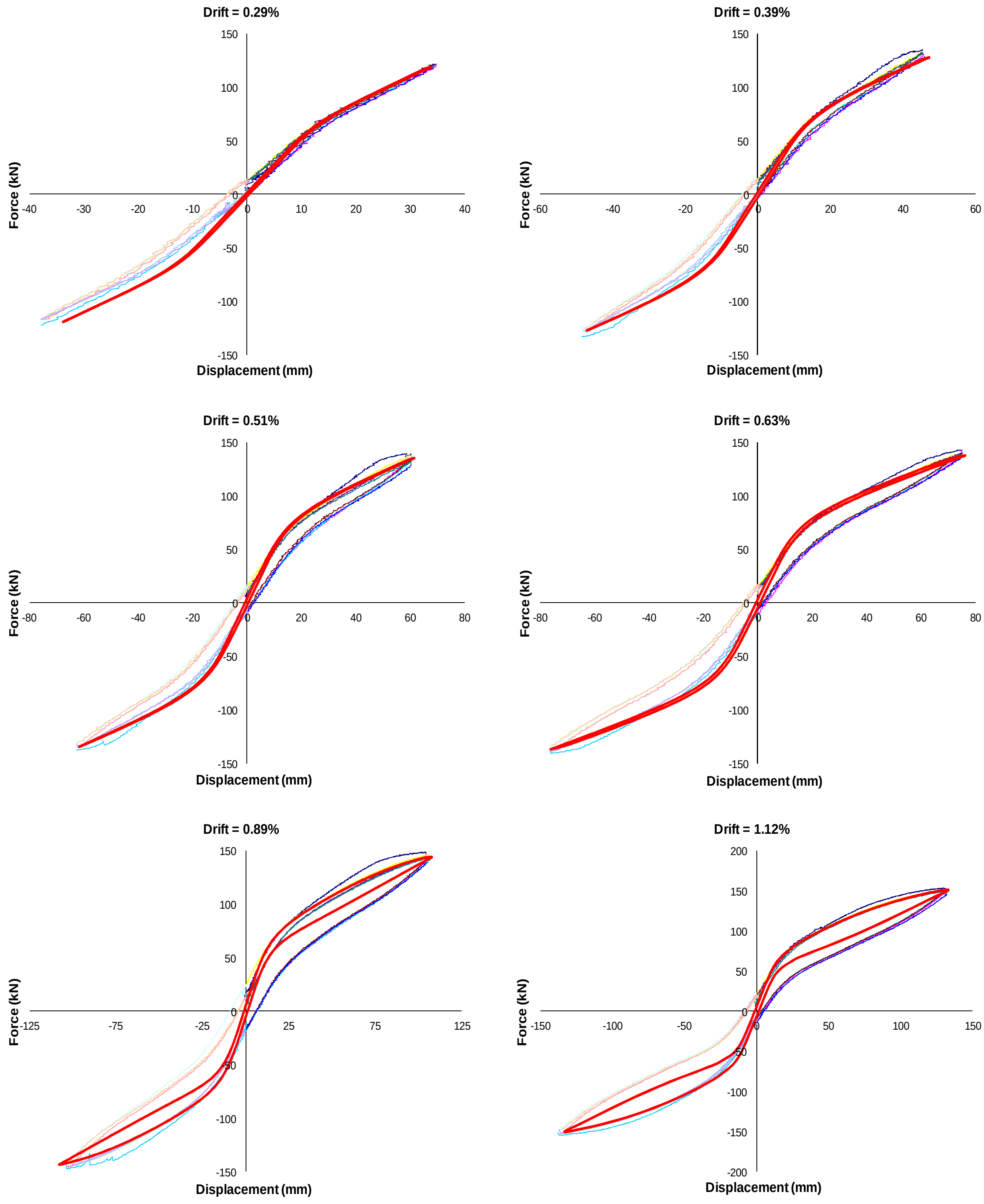

Figure 2.5 Lateral force - top displacement relationship for the UBC specimen from fiber model (shown with thick line) and its comparison with experimental results for different drift ratios.

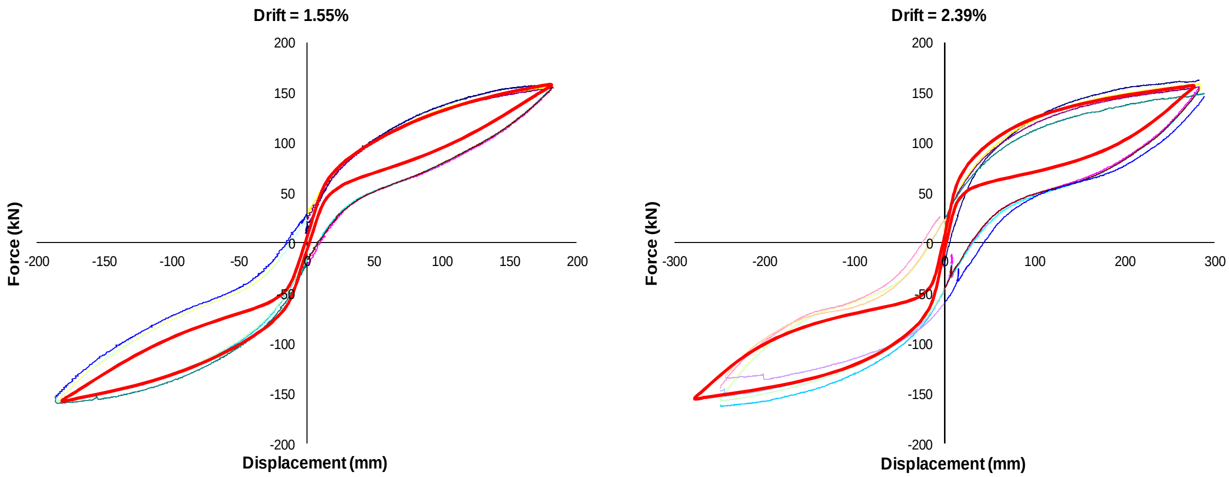

Figure 2.5 Cont'd.

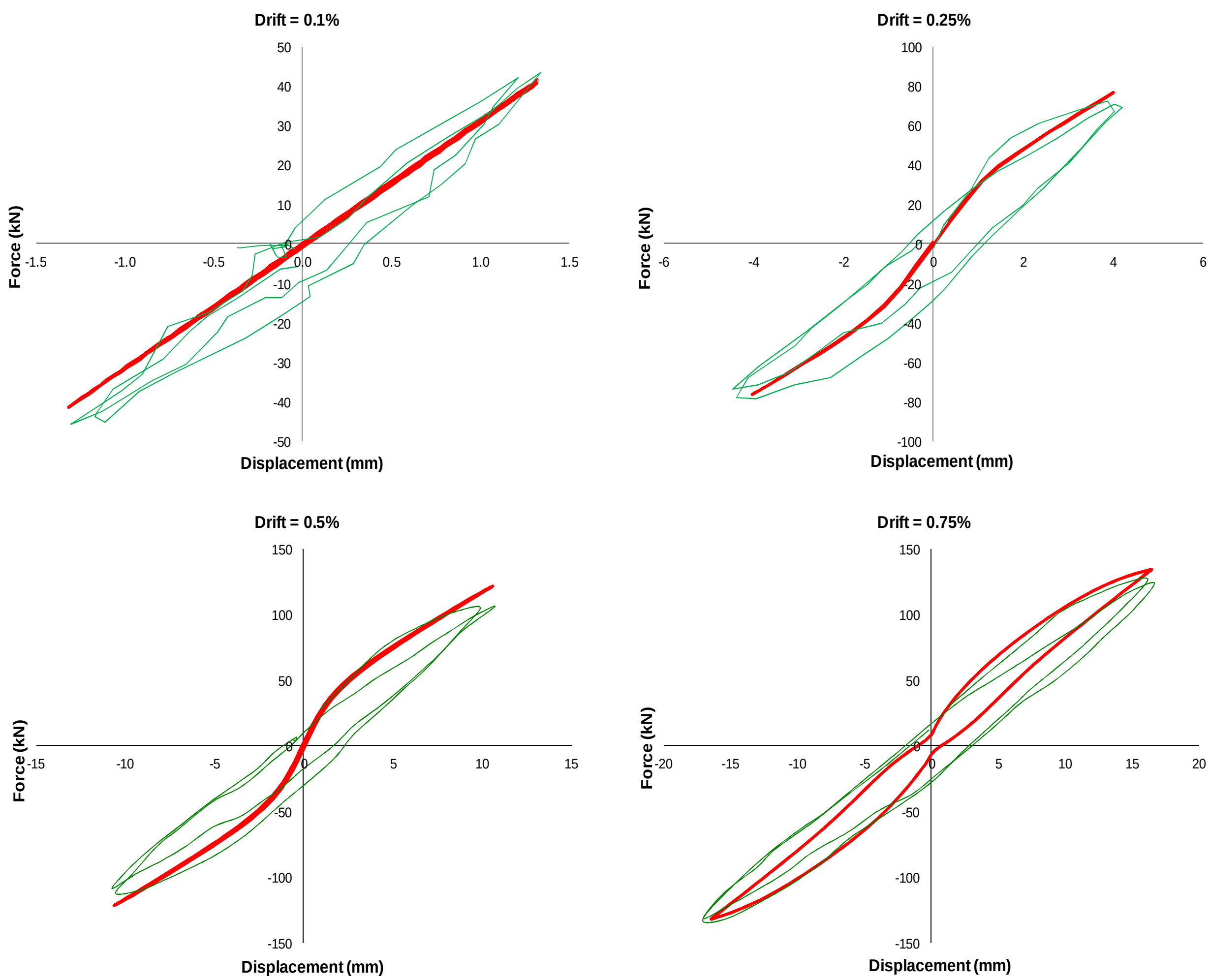

Figure 2.6 Lateral force - top displacement relationship for the Clarkson specimen from fiber model and its comparison with experimental results for different drift ratios.

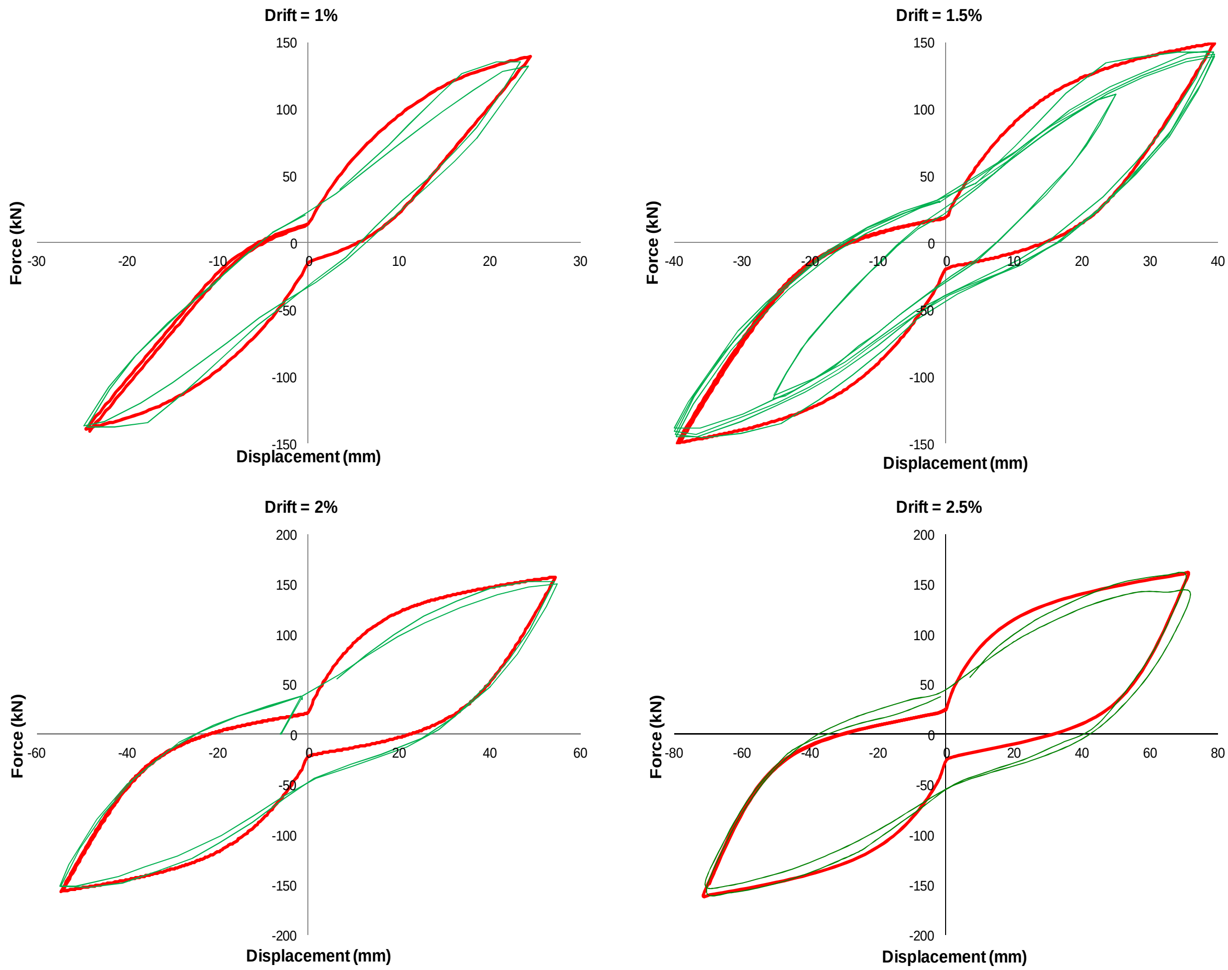

Figure 2.6 Cont'd.

Figure 2.5 and Figure 2.6 indicate that the fiber model captures the measured response reasonably well for both specimens. Particularly, the stiffness degradation in subsequent cycles is well represented by the fiber model. The fiber model also provides a good prediction of the measured lateral load capacity. It should be noted that the lateral strength of both specimens dropped during the last cycle due to the buckling of the longitudinal bar. Since the fibre model cannot capture such response, it overestimates the lateral load capacity at global drift ratios of 2.39% and 2.5% for UBC and Clarkson specimens, respectively. The fiber model prediction of the residual displacements for the Clarkson specimen agrees well with the recorded residual displacements at higher global drift levels. For the UBC specimen, on the other hand, the fibre model prediction of residual displacements is lower than the measured values. Residual displacements for the UBC specimen were considerably small due to high axial compression force and low percentage of longitudinal steel, two properties that are common characteristics of high-rise shear walls in Canada.

Figure 2.7 and Figure 2.8 show the predicted compressive stress-strain response in the extreme fibre of confined concrete and the stress-strain response in the outermost layer of the longitudinal steel for the UBC and Clarkson specimens, respectively. It can be seen from Figure 2.7 that concrete compressive strains are less than 0.003 for all drift values, while maximum tensile strain in the reinforcing steel is approximately 2.5%. For the Clarkson specimen, however, concrete compressive strains are greater than 0.003 for drift values of 1.5%, 2%, and 2.5% (see Figure 2.8). Also, the maximum tensile strain in the reinforcing steel is nearly twice as much as that for the UBC specimen at the drift ratio of 2.5%. Note that 0.003 is generally considered as the compressive strain capacity of unconfined concrete.

(a) (b)

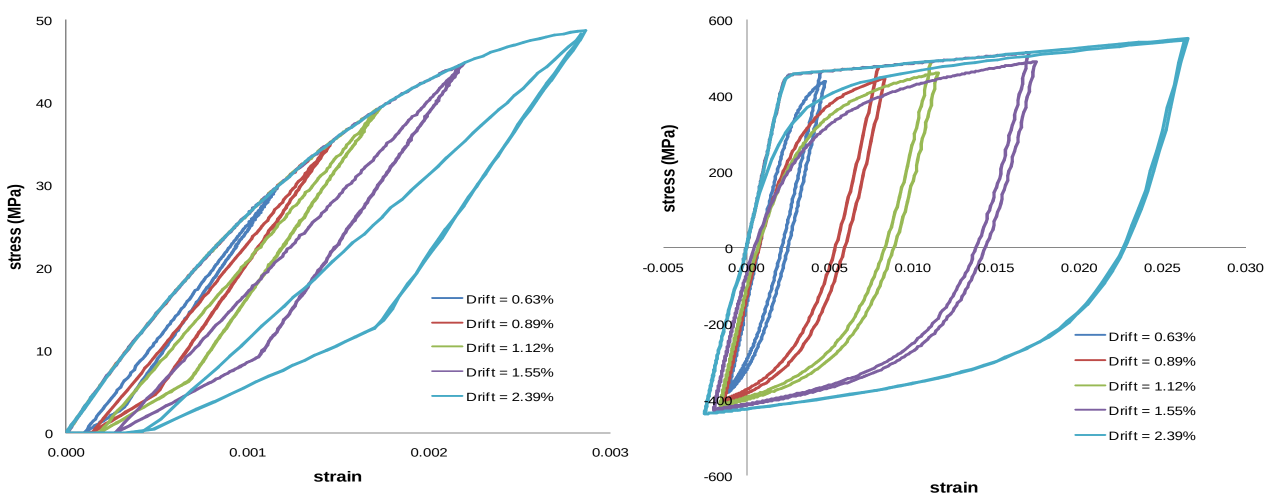

Figure 2.7 Fiber model prediction of the stress-strain response of: (a) the extreme fibre of the concrete core, and (b) the outermost layer of longitudinal steel for the UBC specimen.

(a) (b)

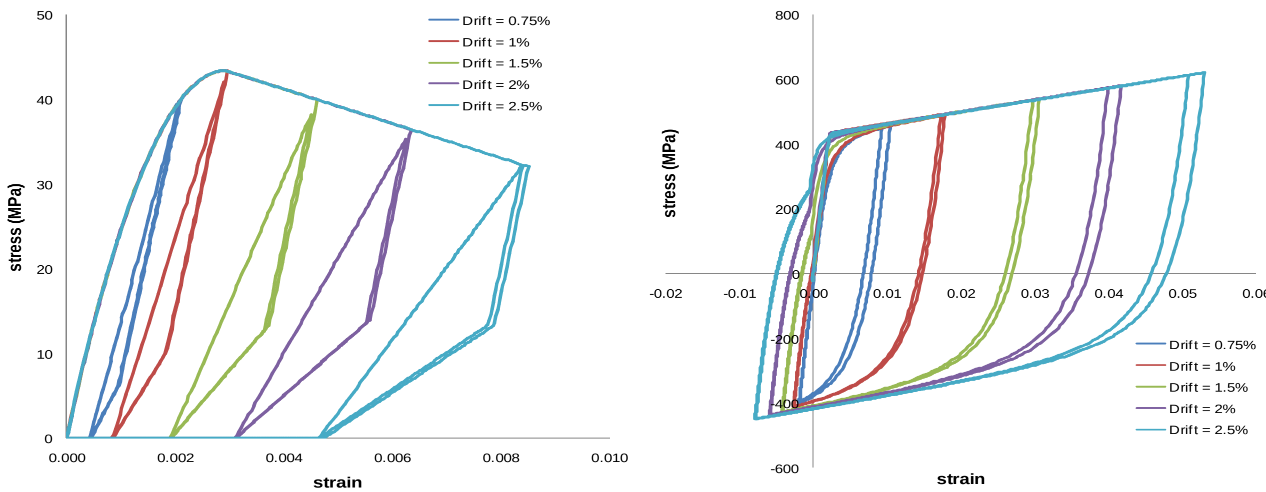

Figure 2.8 Fiber model prediction of the stress-strain response of: (a) the extreme fibre of the concrete core, and (b) the outermost layer of longitudinal steel for the Clarkson specimen.

The following observations can be made:

1. Concrete compressive strains for the UBC specimen are lower than those associated with the Clarkson specimen. The reason is due to the fact that neutral axis depth is smaller for the UBC specimen since it has a flanged cross section and low percentage of longitudinal reinforcement.

2. The concept of upper-bound and lower-bound response proposed by Ibrahim (2000) were based on the assumption of fixed elastic modulus for concrete and reinforcing steel. This assumption is valid for reinforced concrete cross sections subjected to monotonic loading or cyclic loads in which concrete and reinforcing steel strains remain small. The *Concrete03* and *Steel02* constitutive models used in this work for modelling the hysteretic behaviour of concrete and steel fibers are more realistic since they capture the softening of concrete and reinforcing steel under cyclic loading. This softening in the material behaviour needs to be considered in the Ibrahim's lower-bound bending moment - curvature model. The details of the analytical procedure for this modification will be presented hereafter.

2.5 Refinement of Lower-bound Bending Moment - Curvature Relationship

As discussed in the previous section, reinforced concrete sections can have a softer response than the lower-bound bending moment – curvature relationship due to the stiffness degradation of concrete and reinforcing steel fibers under cyclic loading. It is known that the flexural response of well detailed reinforced concrete sections is ductile, but the stiffness of the section degrades as the curvature demand increases. Therefore, it is necessary to replace the constant lower-bound response with a trilinear bending moment – curvature relationship with a yield curvature that is correlated to the maximum curvature demand in the previous cycle. The fiber model can be used for this purpose since as it was seen in section 2.4, it captured the measured response of UBC and Clarkson specimens reasonably well.

The first step in refining the lower-bound response is to establish a range of cross sections with varying geometry and the percentage of longitudinal reinforcement. The considered cross sections are then subjected to a reverse cyclic loading protocol, and a simplified method is adopted to determine the yield curvature from the results of the fiber analysis. The influence of reinforcing steel constitutive model and the wall length is also examined.

2.5.1 Example Cross Sections Used in Fiber Analysis

A series of shear walls were considered in this study that are commonly used as the seismic force resisting system for a typical 30 story residential building in Vancouver BC. Both rectangular and flanged cross sections were included although walls in high-rise buildings typically have flanged cross sections. The ratio of height to the length of the walls (h_w/l_w) was chosen to be 10, which gives a wall length of approximately 10 m. Figure 2.9 presents the general cross section of the considered walls. The considered cross sections are rectangular (denoted as *R*), flanged with small flange width (denoted as *SF*), and flanged with big flange width (denoted as *BF*). A flange thickness of 0.75 m was considered for the three geometries, while the web thickness was assumed to be 1.0 m for the *BF* and 0.5 m for other cross sections. The percentage of longitudinal reinforcement in the web, ρ_w, was assumed to be 0.25% for all cross sections, while three values 0.5%, 1%, and 2% were considered as the percentage of longitudinal reinforcement in the flange (ρ_f). Table 2.1 summarizes the properties of the cross sections. For each cross section with a given geometry and the percentage of longitudinal reinforcement, axial compression force varied from $0.05f_c'A_g$ to approximately $0.15f_c'A_g$. The former is considered as the lower bound for axial compression stress ratio for high-rise walls, while the latter is selected such that neutral axis depth is limited to the flange thickness for the flanged cross sections or 0.2 times the wall length for rectangular cross sections. This was done to ensure that the considered cross sections have adequate curvature capacity associated with the unconfined concrete in compression. A total of 17 various cases were considered by varying cross sectional geometry, longitudinal reinforcement percentage, and axial compression stress ratio.

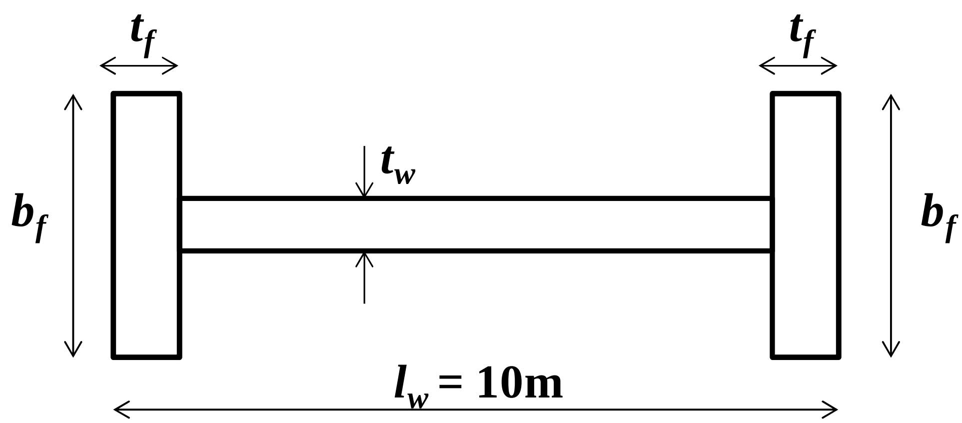

Figure 2.9 General schematic of the cross sections included in the study.

Table 2.1 Properties of the cross sections used in fiber analysis.

Cross section	b_f [1](m)	t_f [2](m)	t_w [3](m)	ρ_f [4](%)	ρ_w [5](%)
R	0.5	0.75	0.5	0.5, 1.0, 2.0	0.25
BF	5.0		1.0		
SF	3.0		0.5		

[1] flange width, [2] flange thickness, [3] web thickness, [4] percentage of longitudinal reinforcement in the flange, [5] percentage of longitudinal reinforcement in the web.

Fibre analysis of the 17 cross sections was performed in OpenSees using *Concrete03* and *Steel02* constitutive models for concrete and reinforcing steel, respectively. Concrete compressive strength f_c' was considered to be 50 MPa, and Kent and Park (1973) model was used to determine the slope of the descending linear branch of stress-strain relationship for concrete in compression. It was assumed that the ratio of the volume of the confinement reinforcement to the confined concrete is 0.1%, which gives an ultimate compressive strain capacity of 0.005 for concrete. Note that such amount of confinement steel results in only 0.8%

increase in concrete compressive strength. Figure 2.10 shows the details of the constitutive relationship for concrete in compression. Concrete tension stiffening details are identical to those specified in section 2.4 for UBC and Clarkson specimens. The yield strength and strain hardening for *Steel02* model was assume to be 400 MPa and 0.02, respectively.

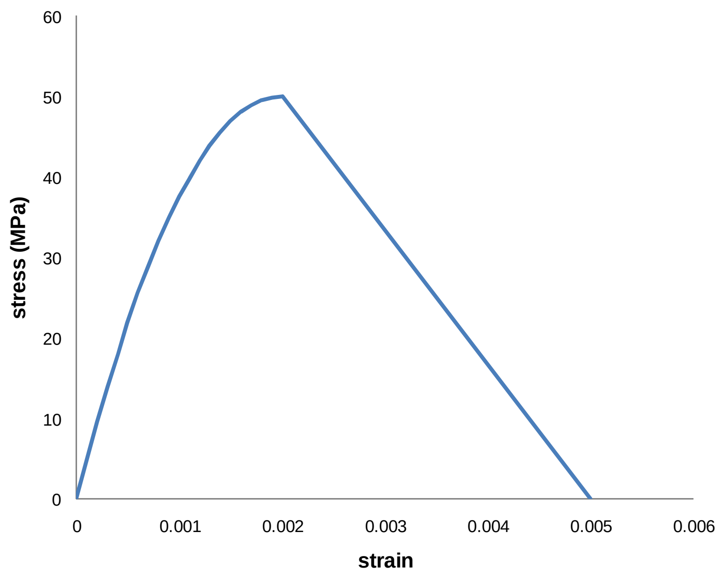

Figure 2.10 Stress-strain relationship for concrete in compression.

2.5.2 Modified Lower-bound Bending Moment - Curvature Relationship

The 17 cross sections introduced in Section 2.5.1 were subjected to reverse cyclic curvature histories. For each cross section, the curvature demand was increased incrementally until it reached section curvature capacity defined as 0.0035/c. Note that 0.0035 is the maximum compressive strain capacity of unconfined concrete and c is the neutral axis depth determined from sectional analysis. The reason for limiting maximum curvature demand to 0.0035/c is that there is zero or little confinement for concrete in most high-rise walls constructed in Vancouver, BC. As a result, the cross section curvature capacity is almost reached as the concrete strain at the extreme compression fiber reaches 0.0035.

Figure 2.11 shows the hysteretic bending moment - curvature relationship determined from fiber analysis for a given cross section. A trilinear bending moment - curvature model was developed to fit the results from fiber analysis. The trilinear model consists of the following segments: an initial segment which represents the uncracked response of reinforced concrete section (with a slope equal to the uncracked flexural stiffness EI_g), and a second segment that represents the section stiffness accounting for concrete and reinforcing steel softening under cyclic loading. The bending moment that defines the transition from the first segment to the second segment is the bending moment at crack opening M_{co}, and was defined as $P/A_g.S_g$. Note that M_{co} is similar to parameter M_L' defined in Equation 2.2, except that the latter has an additional empirical term $0.08Pl_w$.

Determining the slope of the second segment of the trilinear bending moment - curvature relationship requires defining an additional point since the yield curvature ϕ_y^* is not known. For this purpose, it was assumed that the second segment of the trilinear model passes through a point on the fiber model prediction with a bending moment equal to 60% of the cross section flexural capacity M_n. Note that the selection of 60% was made after reviewing a number of curves determined from fiber analysis, and it was observed that choosing $0.6M_n$ results in a reasonable fit to the nonlinear prediction. Figure 2.12 shows the variation of the yield curvature as a function of curvature demand times the wall length for different cross sections.

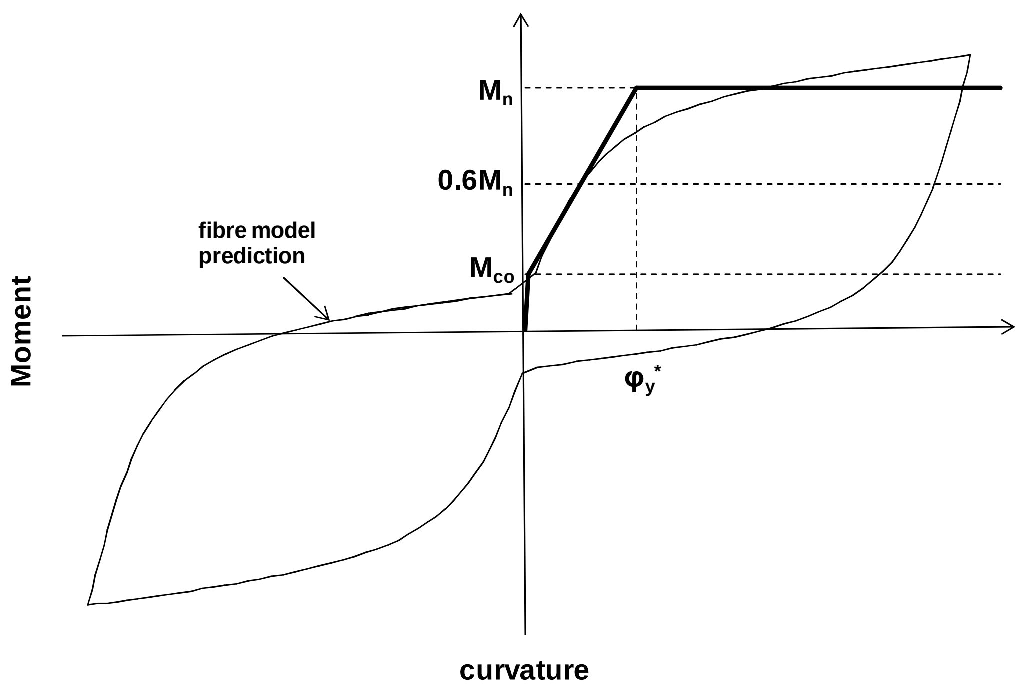

Figure 2.11 Development of trilinear bending moment – curvature relationship from fibre model prediction.

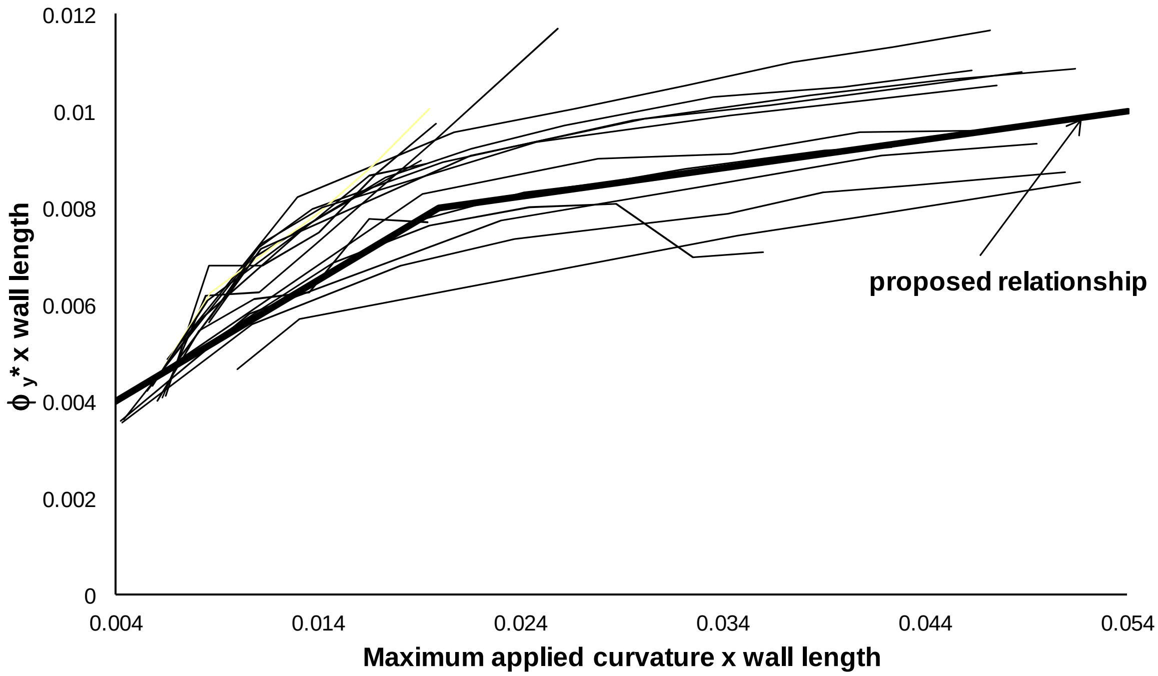

Figure 2.12 Variation of yield curvature as a function of maximum applied curvature for considered cross sections.

Figure 2.12 indicates that the yield curvature is equal to $0.004/l_w$ for low curvature demands and it increases to $0.012/l_w$ as the curvature demand exceeds $0.05/l_w$. Choosing the value of $0.004/l_w$ for yield curvature is consistent with Adebar et al. (2005) recommendation for this parameter. Also shown in Figure 2.12 is the proposed line that relates the yield curvature to the applied curvature demand. The proposed line consists of two segments: the first line with a steeper slope which represents mostly rectangular cross sections, and the second line with a shallower slope which represents flanged cross sections. It should be noted that walls with rectangular cross sections have less curvature capacity compared to flanged walls; therefore lines corresponding to rectangular sections tend to stop at lower curvature demands. The proposed line shown in Figure 2.12 will be used to define the stiffness degradation rules of the trilinear hysteretic bending moment - curvature relationship. The details of this model will be presented in section 2.7.

The results shown in Figure 2.12 were developed using the *Steel02* constitutive model for reinforcing steel and fixing the length of cross sections to 10 m. A sensitivity analysis needs to be carried out to investigate the influence of these parameters on the yield curvature ϕ_y^*. The results are presented in the following sections.

2.5.3 Influence of Reinforcing Steel Constitutive Model on Yield Curvature

As it was shown in Figure 2.1, the *Steel02* constitutive relationship addresses the softening of reinforcing steel under cyclic loading. Ibrahim (2000), on the other hand, used a bilinear stress-strain model for reinforcing steel to develop the trilinear models shown in Figure 2.2. In order to observe the effect of steel constitutive model on the yield curvature, a *BF* cross section with 1% longitudinal reinforcement in the flanges and axial compression force of $0.12f_c'A_g$ was selected. Fibre analysis was performed using the so called *Steel01* model in OpenSees, which has a bilinear backbone and is identical to what Ibrahim used to model the reinforcing steel response under cyclic loading. Figure 2.13 shows the variation of the yield curvature corresponding to the two constitutive models.

Figure 2.13 indicates that details of steel constitutive model barely affects the yield curvature for lower curvature demands, but the difference between the yield curvatures associated with the two steel models tend to increase as the curvature demand increases. Also, it can be seen from Figure 2.13 that the yield curvature would be constant if bilinear steel model (*Steel01*) was used in the fiber analysis. This observation is consistent with the idea of constant lower-bound bending moment - curvature relationship. Determination of the yield curvatures using the *Steel02* stress-strain model seem to be more realistic than using the *Steel01* relationship since the latter cannot capture the softening of reinforcing bars subjected to cyclic loading.

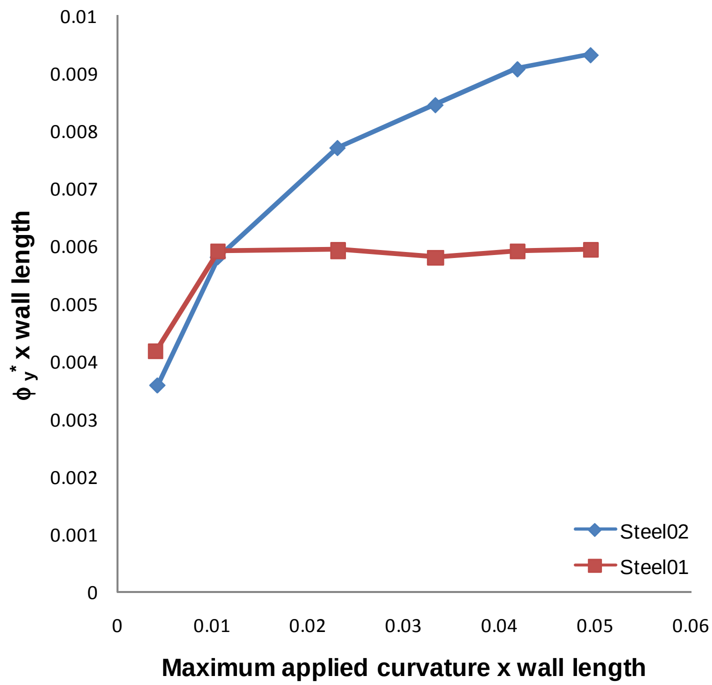

Figure 2.13 Influence of reinforcing steel constitutive model on the yield curvature.

2.5.4 Influence of Cross Section Length on Yield Curvature

As it was shown in Figure 2.9, the cross sections used to obtain yield curvature ϕ_y^* were 10 m long. Both axes in Figure 2.12 were multiplied by the wall length so the proposed line for computing the yield curvature can be used for any cross section. However, it is necessary to consider cross sections with different length to ensure that the proposed line for computing the yield curvature is still valid. For this purpose, two additional flanged cross sections were added. The first one is 7.5 m long, and the flanges are 3.75 m long and 0.6 m thick. The web is 6.3 m long and 0.75 m thick. The second one is 14 m long, and the flanges are 7 m long and 1 m thick. The web is 12 m long and 1.4 m thick. Longitudinal reinforcement ratio in the flanges and in the web is 2% and 0.25%, respectively, for both cross sections. Axial compression force for both walls is assumed to be $0.12 f_c' A_g$. Figure 2.14 shows the variation of the yield curvature for both walls. Note that the two additional walls are identified in Figure 2.14 according to the wall length.

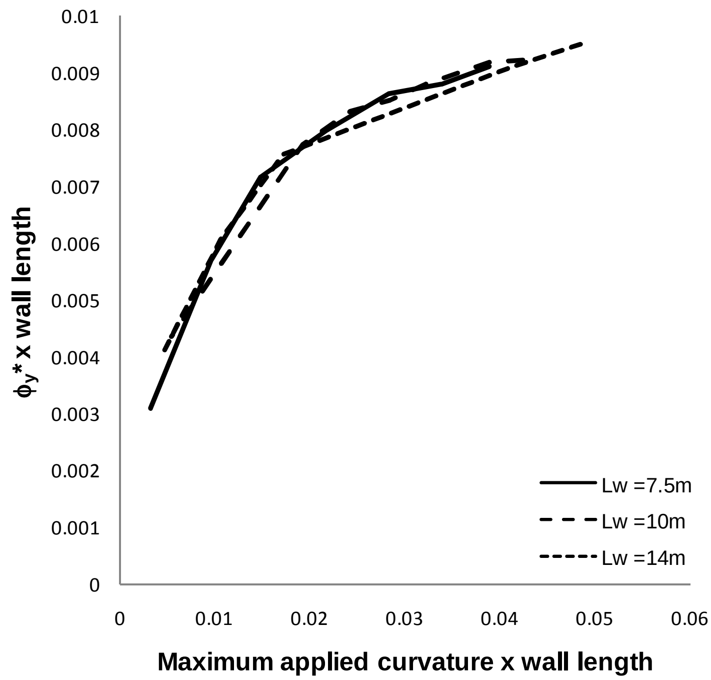

Figure 2.14 Variation of the yield curvature for walls with different length.

Also shown in Figure 2.14 is the yield curvature variation for the *BF* cross section with an axial compression force, flange and web longitudinal reinforcement ratios equal to those for the two additional cross sections (labelled as L_w = 10 m). Figure 2.14 indicates that walls with different length have similar yield curvature values provided that they have similar axial compression force and longitudinal reinforcement ratios. As a result, the proposed line presented in Figure 2.12 can be applied to any cross section with a length other than the length of 10 m considered for the cross sections shown in Figure 2.9.

2.6 Unloading Point and Modelling Residual Curvatures

In this section a simple model will be developed to define the unloading point, which accounts for the amount of axial compression force and longitudinal reinforcement. Also, the results from testing a large-scale reinforced concrete element under reverse cyclic axial load will be combined with plane section analysis to model residual curvature in the hysteretic bending moment - curvature relationship. The details are presented in the following sections.

2.6.1 Unloading Point

A simple model for computing the bending moment at crack closing, M_{cc}, is presented in Figure 2.15. According to this model, some portion of the axial compression force is required to yield the longitudinal reinforcing steel in compression before closing the cracks in concrete when the cross section is loaded from a given displacement in one direction to a specific displacement in the opposite direction. The M_{cc} parameter can be determined from the following equation:

$$M_{cc} = \frac{(P - P_s)S_g}{A_g} - M_s \qquad Eq\ 2.3$$

where

$$P_s = P_{sf} + P_{sw} = A_{sf} f_y + A_{sw} f_y \qquad Eq\ 2.4$$

and

$$M_s = \frac{1}{2} P_{sf} \left(l_w - t_f\right) \qquad Eq\ 2.5$$

Note that A_{sf} ,A_{sw}, f_y, t_f, and l_w are longitudinal steel area in the flange and in the web, yield strength of reinforcing steel, flange thickness, and wall length, respectively. Also, M_s in Equation 2.5 is the bending moment from the yielding of flange longitudinal reinforcement in tension.

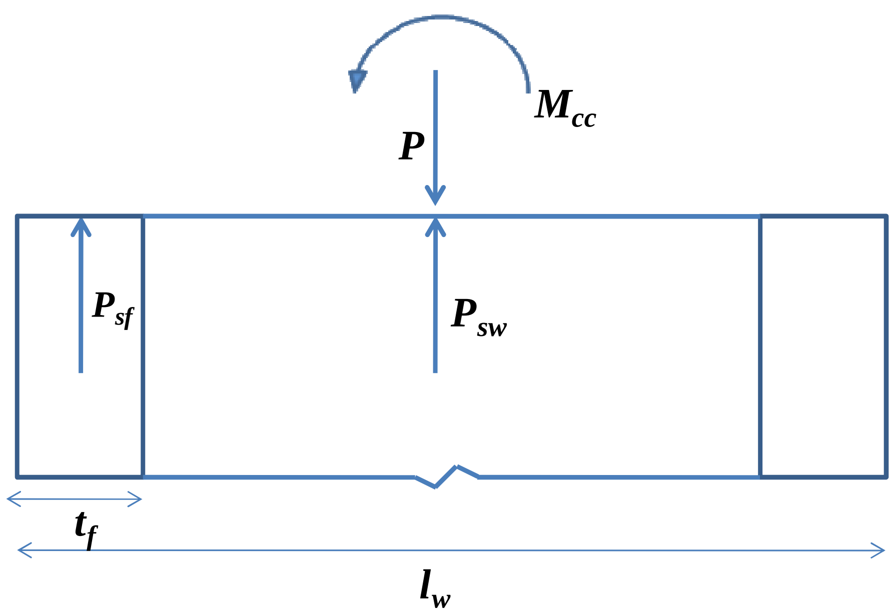

Figure 2.15 Model for computing bending moment at crack closing.

2.6.2 Residual Curvatures

In order to estimate residual curvatures, experimental results were first used to establish the relationship between residual strains and maximum applied strains for a reinforced concrete section under cyclic axial load. Residual strains were then converted to residual curvatures using the assumption that plane sections remain plane. The details are presented in the following sections.

2.6.2.1 Experimental Program

Fronteddu (1992) tested five large-scale reinforced concrete members to study the effect of cyclic loading on concrete tension stiffening. The specimens had various cross sections and longitudinal reinforcement percentages; however, they were all 1500 mm long and were subjected to cyclic axial loading. The experimental results for so called UC4 specimen are presented here because this was the only specimen that was subjected to both axial tension and compression loads.

Figure 2.16 shows the cross sectional details and loading history for specimen UC4. The cross section was 700 mm wide and 350 mm deep and longitudinal reinforcement consisted of eight 20M bars (reinforcement ratio of 1%). There was no transverse reinforcement, and clear cover to longitudinal reinforcement was 87.5 mm in both directions. Concrete compression strength was 33.5 MPa, and the average yield strength and ultimate strength of steel was 435 MPa and 626 MPa, respectively. The load history consisted of both forced controlled and displacement controlled strategies. It should be noted that the force controlled strategy was consistently used for loading the specimen in compression.

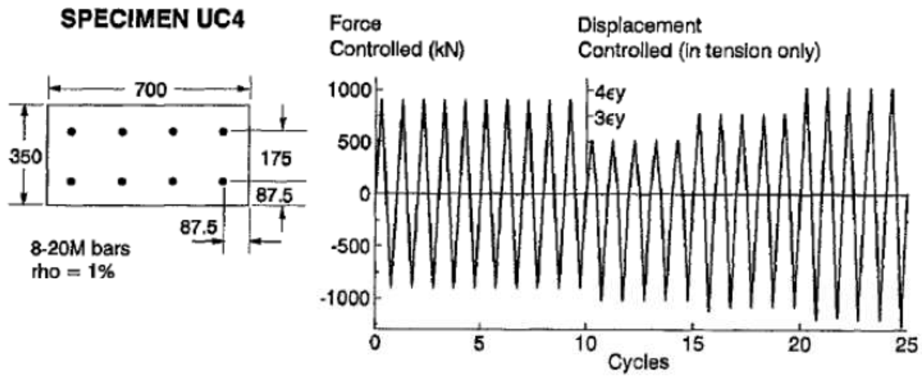

Figure 2.16 Cross sectional details and loading history for specimen UC4 (from Fronteddu 1992, © MA.Sc thesis, by permission).

The measured load - deformation response of the specimen is presented in Figure 2.17. It can be seen from Figure 2.17 that residual strain is equal to zero for strain demands less than 0.002, while it tends to increase as the applied strain demand increases. Figure 2.18 plots the measured residual strain as a function of maximum applied strain. A straight line was fitted to experimental results in order to define a simple model for estimating residual strains from maximum applied strains.

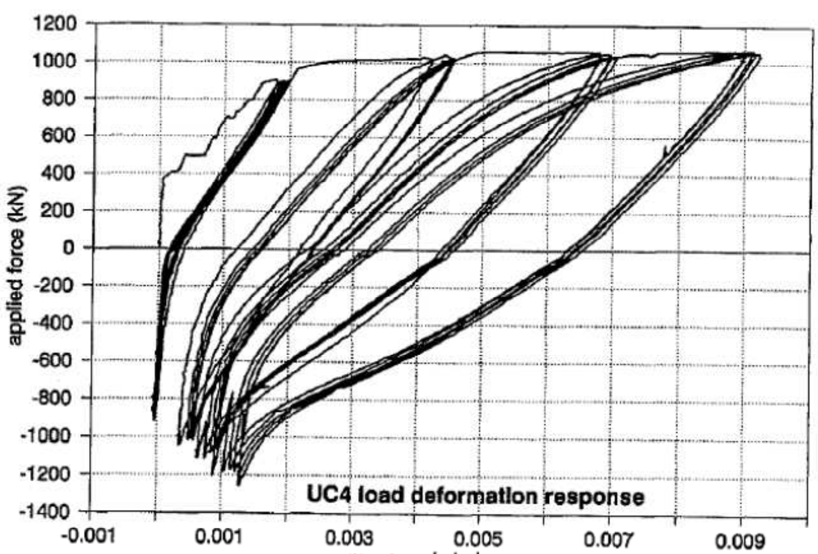

Figure 2.17 Measured load - deformation response for specimen UC4 (from Fronteddu 1992, © MA.Sc thesis, by permission).

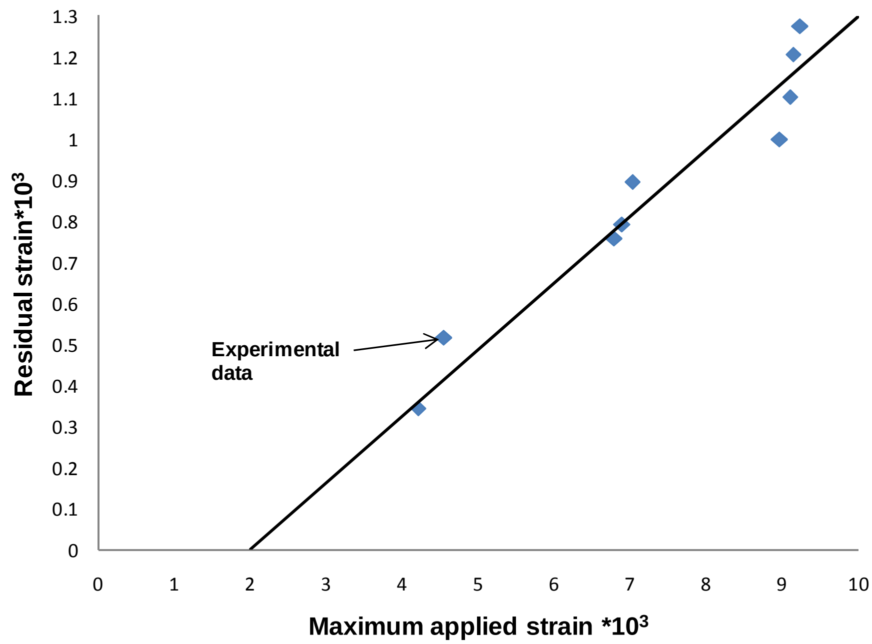

Figure 2.18 Residual strain as a function of maximum applied strain.

2.6.2.2 Relationship between Residual Curvature and Residual Strain

The relationship between residual strains and maximum applied strains for a reinforced concrete cross section was presented in Figure 2.18. The common assumption of plane sections remain plane is used to convert residual strains to residual curvatures. As a result, curvature at a given section is the ratio of tensile strain in the longitudinal reinforcing steel to a portion of the wall length. This portion of wall length is essentially the distance between the reinforcing steel and the neutral axis (denoted as d_s). As the curvature demand increases, d_s tend to increase since the neutral axis depth reduces. Pushover analysis of the cross sections depicted in Figure 2.9 showed that d_s varies between 0.6 and 0.7 times the wall length when the tensile strain in the outermost longitudinal reinforcing steel reaches 0.002. The d_s values for the UBC and Clarkson specimens are 0.68 and 0.60, respectively. It should be noted that d_s is bigger for flanged sections than rectangular sections with equal length since the neutral axis depth is smaller for flanged sections.

Figure 2.19 shows the variation of residual curvature for the UBC and Clarkson specimens as the d_s parameter changes from 50% to 70% of the wall length. Maximum applied curvature shown in Figure 2.19 corresponds to 1% tensile strain in the outermost reinforcing steel in the Clarkson specimen and a d_s value of 0.5 times the wall length. It can be seen from Figure 2.19 that the difference between residual curvatures associated with different d_s values is small at higher curvature demands, while the difference becomes more evident at lower curvature demands.

In this work, $0.6l_w$ was chosen as the appropriate value for the d_s since changing this parameter from $0.5l_w$ to $0.6l_w$ did not have a big impact on the residual curvature for flanged sections. It also gives lower residual curvatures than assuming d_s = $0.5l_w$ for a given curvature demand. It should be noted that low residual curvatures is a characteristic of high-rise shear walls with high axial compression force and low amount of longitudinal steel, as it was seen from experimental results of the UBC specimen.

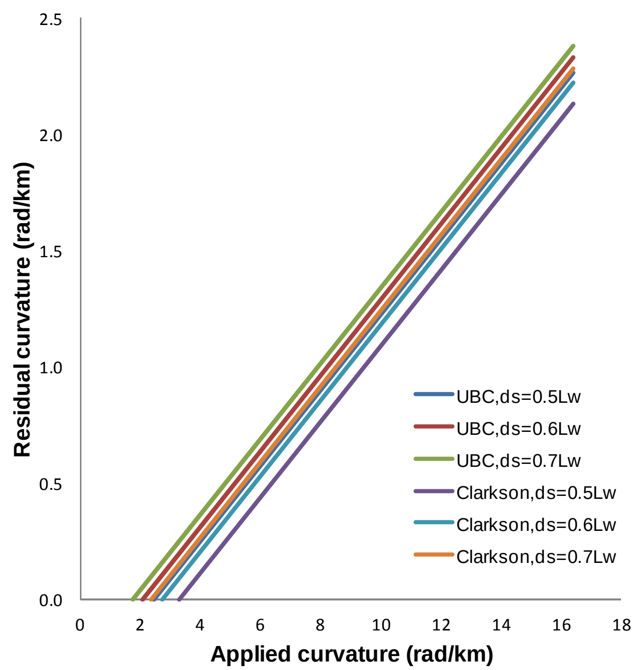

Figure 2.19 Variation of residual curvature as a function of the d_s parameter.

2.7 Trilinear Hysteretic Bending Moment - Curvature Relationship

The findings from Sections 2.5 and 2.6 are used to develop a hysteretic bending moment - curvature model. Figure 2.20 shows a schematic of this model. According to this model, the backbone of the hysteretic model (denoted as path A) consists of a linear elastic segment until the bending moment reaches the bending moment at crack opening M_{co}. This parameter can be determined from the following expression:

$$M_{co} = \left(f_{cr} + \frac{P}{A_g}\right) S_g \qquad Eq\ 2.6$$

where all parameters in Equation 2.6 were defined in Section 2.2.2. Note that the slope of the linear elastic segment is the uncracked flexural stiffness, EI_g. For bending moments greater than M_{co}, the loading path would be linear from M_{co} to the bending moment at flexural capacity, M_n. The slope of this segment is cracked flexural stiffness, EI_{cr}. Having known M_{co}, M_n, EI_g, and EI_{cr}, the upper bound yield curvature, $\phi_{y,UB}$, can be computed from the geometry. The third segment of path A has a slope equal to βEI_g, which represents the post yield stiffness due to steel strain hardening. A β value of 0.5% was specified to represent the slope of path A for curvature values greater than the upper-bound yield curvature. This value was selected based on the experimental results for the UBC and Clarkson specimens. It should be noted that path A is similar to the upper-bound bending moment - curvature relationship presented in Figure 2.2, except that the parameter M_L'' is replaced by M_{co}.

For subsequent reloading, the hysteretic path consists of a series of lines originating from M_{co} to a point on the envelope (denoted as path E). The slope of the loading path tends to decrease as the maximum curvature demand in the previous cycle increases. Note that the yield curvature, ϕ_y^*, is a function of maximum curvature in the previous cycle and can be determined from Figure 2.12.

The unloading paths prior to yielding (denoted as path B) return linearly from maximum curvature to the bending moment at crack closing M_{cc}. It is assumed that the unloading point corresponding to path B is located at the linear elastic segment of the backbone; therefore, curvature at crack closing is equal to M_{cc}/EI_g. The unloading paths after yielding consist of two linear segments: the first line originates from maximum curvature and continues until bending moment is equal to M_{cc} (denoted as path D), and the second line that passes through the residual curvature,ϕ_{res}, and it ends to M_{co} in the reverse direction (denoted as path F). It should be noted that residual curvatures are the ratio of residual strains shown in Figure 2.18 to a d_s value equal to 0.6 times the wall length.

For mid-cycle reloading, the reloading path (denoted as path C) follows the uncracked flexural stiffness $EI_g$from the point it leaves the unloading path. The reloading path intersects and follows a linear path from M_{co} to maximum previous curvature.

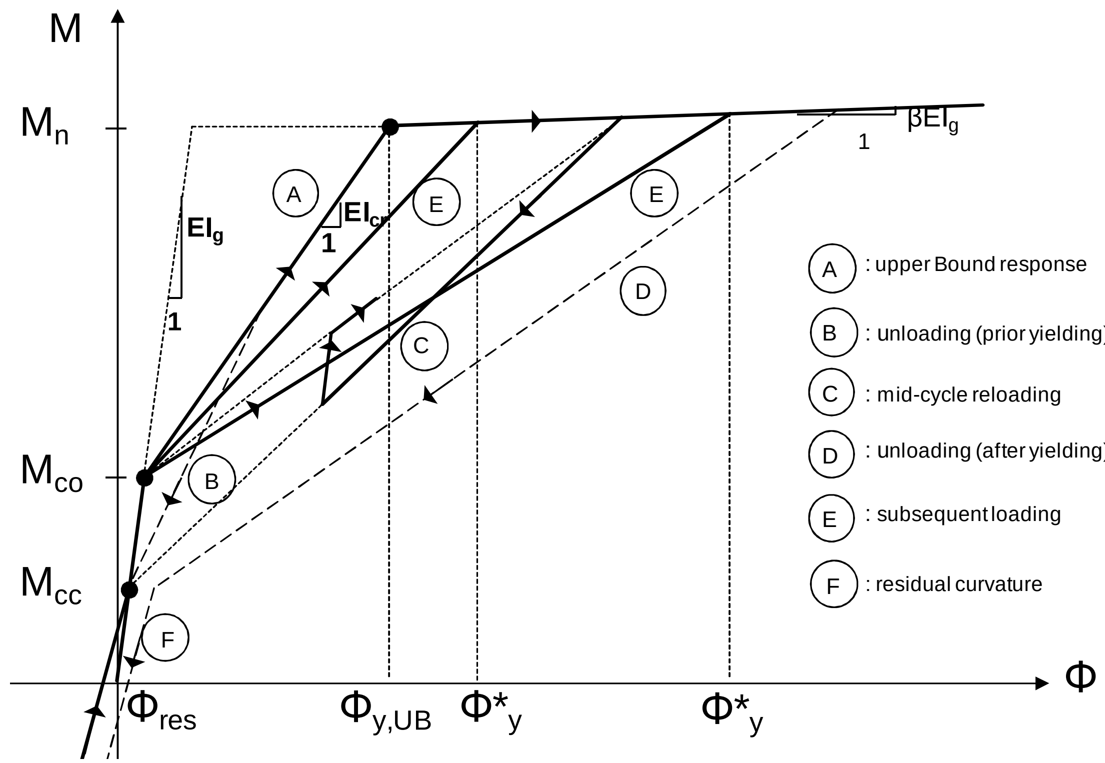

Figure 2.20 Trilinear hysteretic bending moment - curvature relationship for reinforced concrete cross sections.

2.8 Validation of Trilinear Hysteretic Bending Moment - Curvature Relationship with Experimental Results

Figure 2.21 and Figure 2.22 compare the lateral load - top displacement prediction from the hysteretic bending moment - curvature model shown in Figure 2.20 (denoted as trilinear model) with experimental results for UBC and Clarkson specimens. The analytical model predictions are shown with a thick line. Figure 2.21 indicates that the trilinear model can capture the observed stiffness degradation and residual displacements of the UBC specimen very well. The predicted residual displacements are generally lower than the measured ones for most drift ratios. It should be noted that the bending moment at crack closing, M_{cc}, is positive for the UBC specimen because according to Equations 2.3 to 2.5, high axial compression force and low amount of longitudinal reinforcing steel ratio results in positive values for M_{cc}.

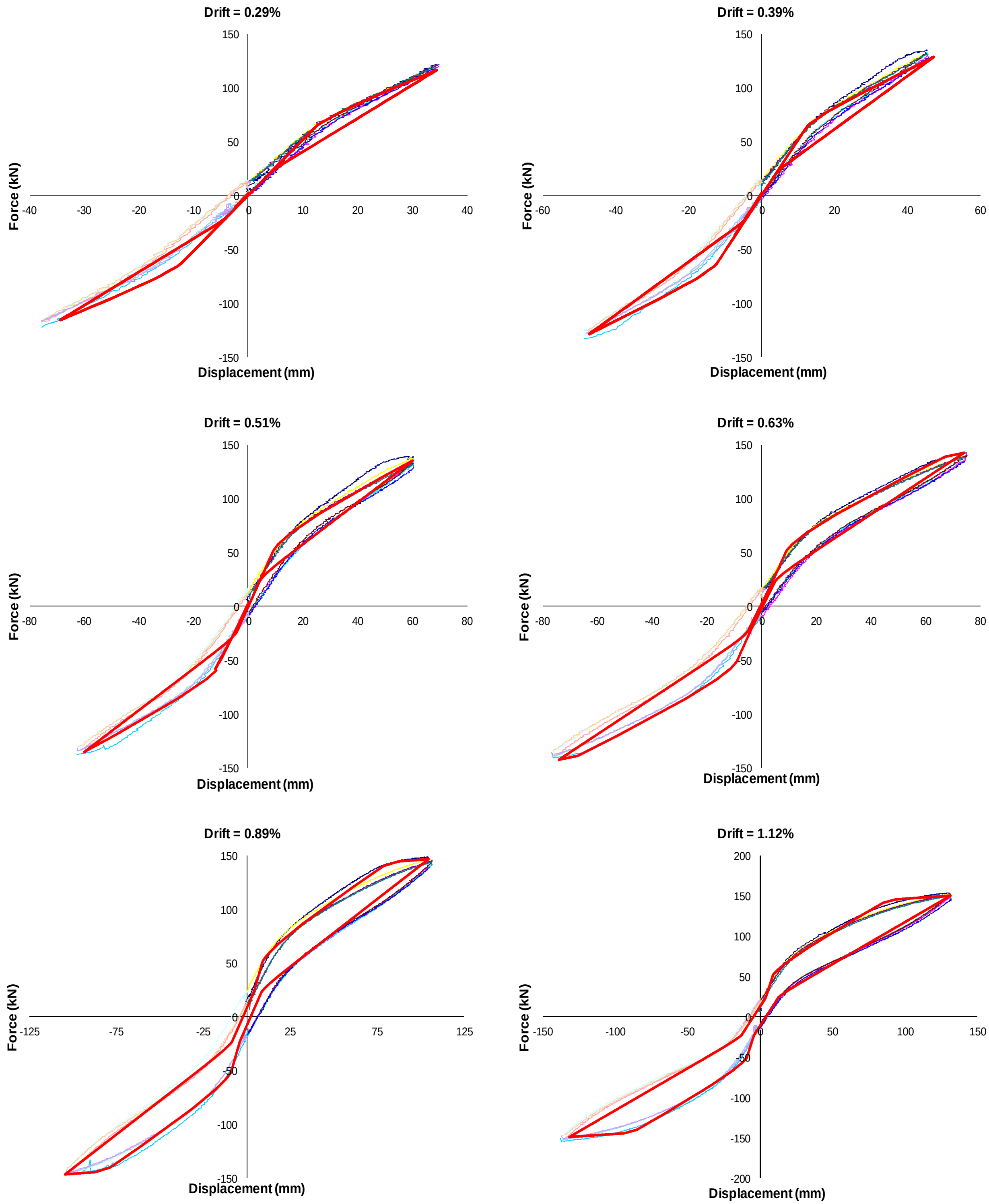

Figure 2.21 Lateral force - top displacement relationship for the UBC specimen from the trilinear model (shown with thick line) and its comparison with experimental results for different drift ratios.

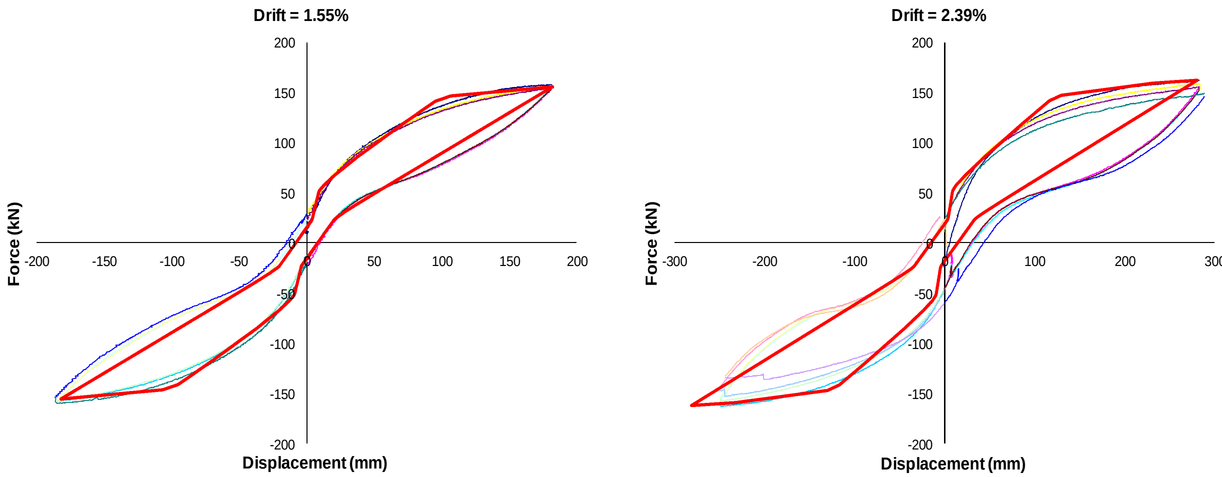

Figure 2.21 Cont'd.

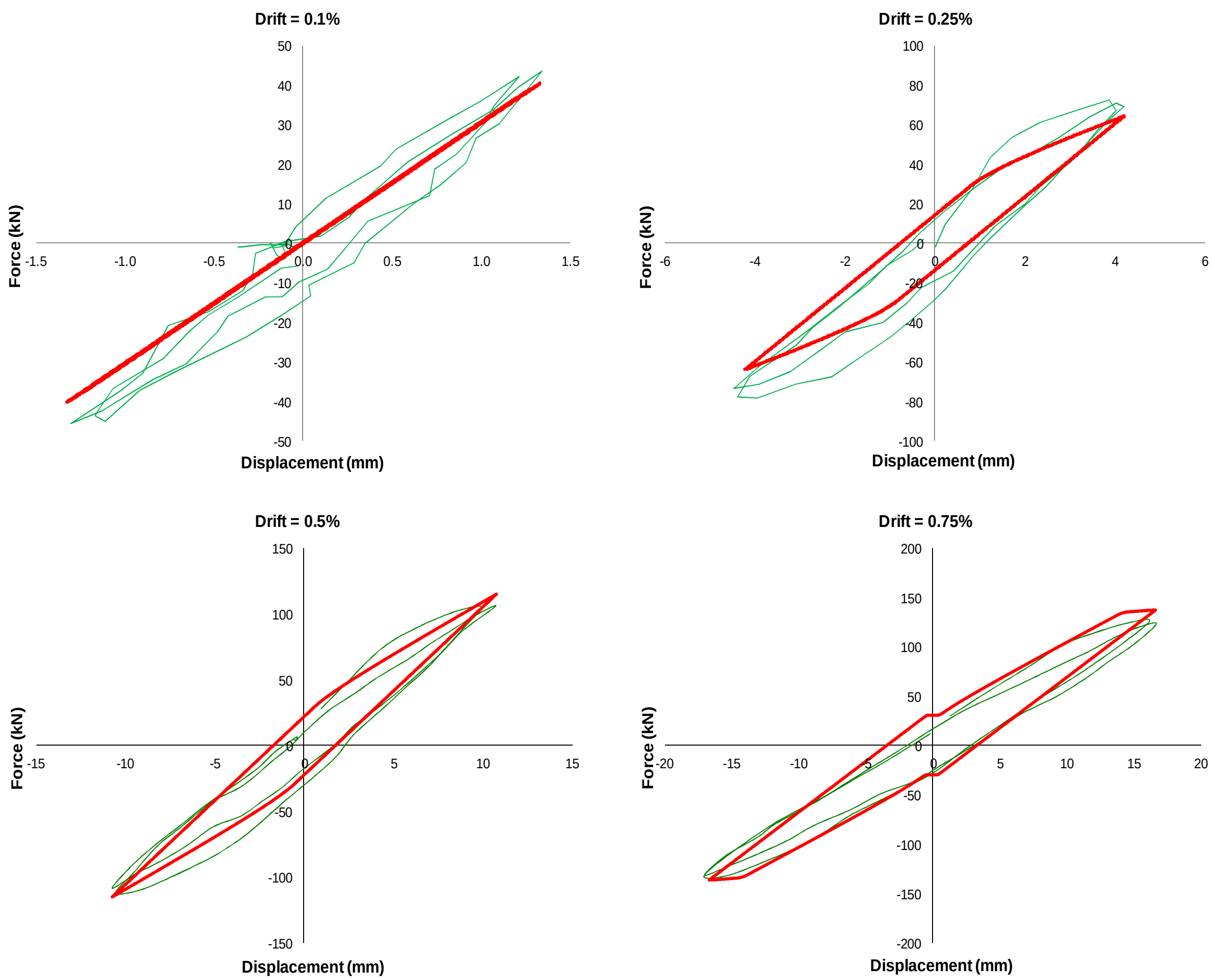

Figure 2.22 Lateral force - top displacement relationship for the Clarkson specimen from the trilinear model (shown with thick line) and its comparison with experimental results for different drift ratios.

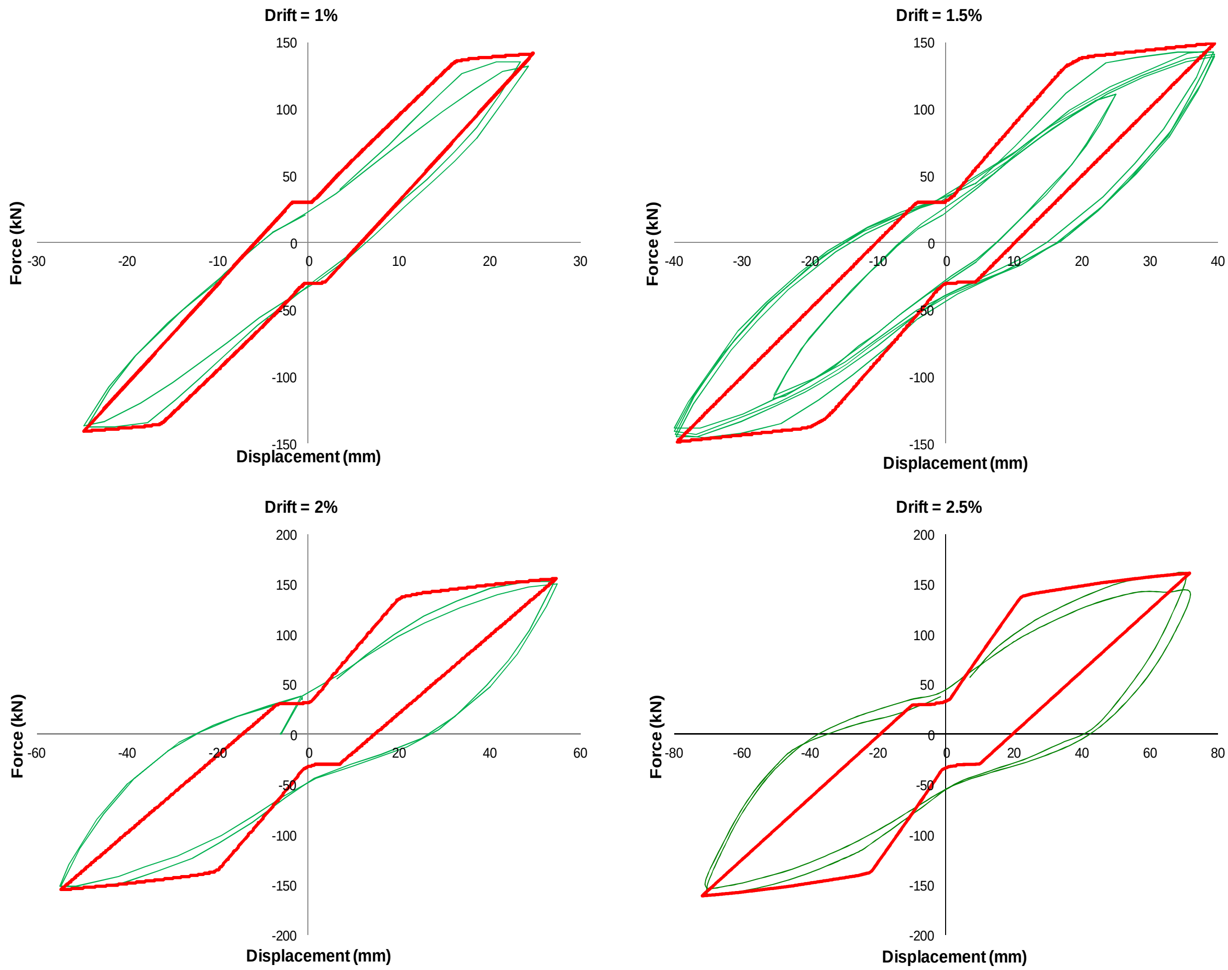

Figure 2.22 Cont'd.

Figure 2.22 indicates that the predicted lateral force - top displacement relationship agrees reasonably well with the measured response for drift ratios up to 1.5%. For drift ratios of 2% and 2.5%, however, the predicted response is stiffer than the measured response due to the fact that the trilinear hysteretic bending moment - curvature relationship was mainly developed to predict the response of cross sections subjected to curvature demands up to the curvature capacity corresponding to unconfined concrete. As it can be seen from Figure 2.8, concrete compressive strains in the extreme fibre associated with drift ratios of 2% and 2.5% are considerably greater than the value of 0.0035 considered as the compressive strain capacity for unconfined concrete. It implies that base curvature demand corresponding to these drift ratios are considerably higher than the curvature capacity for unconfined concrete. Concrete compressive strains in the UBC specimen and generally in high-rise cantilever shear walls are less than 0.0035 because of the large width of the flanged cross sections. Also note that M_{cc} is negative for the Clarkson specimen due to the combination of low axial compression force and high longitudinal reinforcing steel ratio at the boundaries.

2.9 Example Shear Wall Buildings

Fifteen different high-rise concrete shear wall buildings were included in this study. The differences between the buildings are the heights (number of stories) and the flexural capacities of the shear walls in the buildings. Five different building heights were included: 10, 20, 30, 40, and 50 stories. The corresponding heights of the cantilever shear walls in these buildings measured from the seismic base (grade level) are 29.7, 57.7, 85.7, 113.7, and 141.7 m. For these buildings, the first floor has a height of 4.5 m, while other floors have a typical height of 2.8 m. Additional shear walls provided below grade causes the critical section for bending of the tower shear walls to be at grade level. The base of the wall was assumed to be fixed. All buildings with the same number of stories have the same concrete shear wall geometry dictated by the number and size of required stairway and elevator shafts.

Figure 2.23 shows the arrangement of concrete core walls in the 30 story buildings. The layout of the core walls for other buildings are presented in Appendix A. The core walls shown in Figure 2.23 act as three C-shaped cantilever walls in one direction and three U-shaped coupled walls in the transverse direction. In the current study, the results are presented only for the analysis in the cantilever direction. The overall dimensions of the core are 9.00 x 11.44 m, where 9.00 m is the overall length of the cantilever walls and 11.44 m is the overall length of the coupled walls. The 30 story coupled walls have two openings that are 1.22 m each. Thus the sum of the lengths of the coupled wall segments are 9.0 m, and this is called sum of flange widths in Table 2.2, i.e., flanges of the three C-shaped cantilever walls. The 10 story buildings have a 5.50 x 7.22 m core with one opening in each coupled wall resulting in a 6.0 m sum of flange widths, while the 50 story buildings have a 13.75 x 17.16 m core with three openings in each coupled wall resulting in a 13.50 m sum of flange widths. It should be noted that the cantilever walls in the five different height buildings have height-to-length ratios of 5.4, 7.7, 9.5, 10.6, and 10.3, respectively.

The 30 story core has three C-shaped cantilever walls - two have a web thickness of 0.45 m and one has a thickness of 0.30 m. The sum of these wall thicknesses, called sum of web widths in Table 2.2, is 1.20 m. The 10 story core has two 0.30 m thick C-shaped walls (0.60 m), while the 50 story core has two 0.50 m thick C-shaped walls and two 0.30 m thick C-shaped walls (sum of 1.60 m).

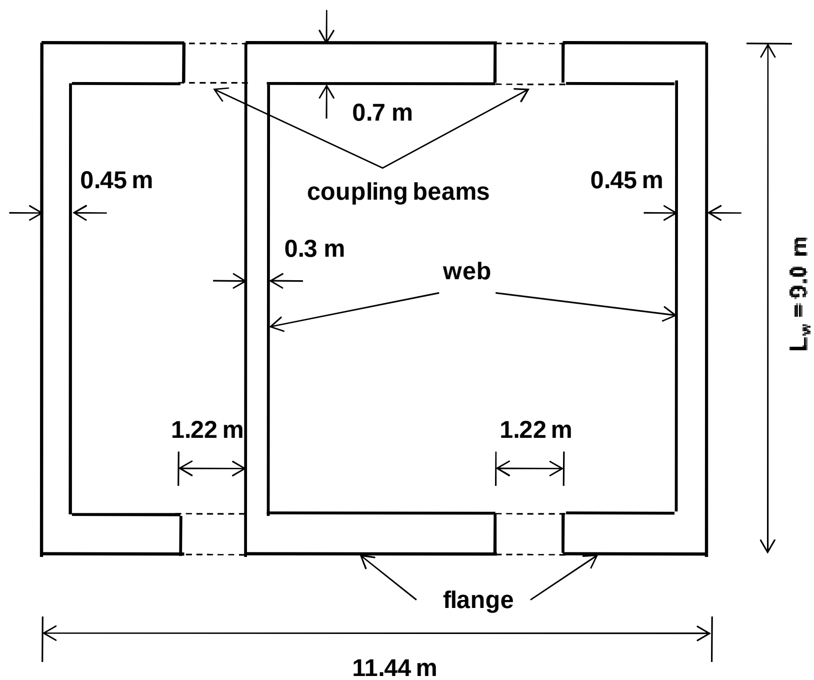

Figure 2.23 Outline of core walls in 30 story buildings.

Table 2.2 Properties of fifteen shear wall buildings used in current study.

No. Stories	**10**				**20**	**30**				**40**		**50**			
l_w (m)[1]	5.50				7.50	9.00				10.75		13.75			
b_f (m)[2]	6.00				8.00	9.00				11.50		13.50			
t_w (m)[3]	0.60				0.90	1.20				1.40		1.60			
t_f (m)[4]	0.45				0.55	0.70				0.80		0.85			
A_g (m^2)[5]	8.2				14.6	21.7				31.2		42.2			
I_g (m^4)[6]	39.4				126.2	261.4				545.8		1189.5			
f_c' (MPa)	30				35	40				45		55			
E_cI_g (kNm^2)	9.71×10^8				3.36×10^9	7.44×10^9				1.65×10^{10}		3.78×10^{10}			
m (kg)[7]	825,700				927,625	998,980				1,284,400		1.946,993			
T_1 (s)[8]	1.0				2.0	3.0				4.0		5.0			
$P/f_c'A_g$ (%)[9]	5.9				8.7	10.1			6.1	11.4	6.2	12.7			6.2
ρ_f @ base(%)[10]	4.0	2.5	1.2	0.8	0.60	3.5	1.2	0.5	0.5	0.52		3.5	1.0	0.5	0.5
ρ_f @ mid-ht (%)[11]	1.9	1.3	0.8	0.8	0.60	1.9	0.7	0.5	0.5	0.52		1.8	0.5	0.5	0.5
ρ_w (%)[12]	1.2	0.25			0.25	0.25				0.25		0.25			
R_g[13]	1.7	2.6	4.2	5.2	4.0	1.4	2.4	3.1	4.3	2.6	4.4	1.4	2.1	2.4	4.1

[1] cantilever wall length, [2] sum of flange width, equal to length of coupled walls minus total door openings, [3] sum of cantilever wall thicknesses, [4] thickness of coupled walls, [5] wall cross sectional area, [6] gross moment of inertia, [7] mass per floor, [8] fundamental period of the building corresponding to EI_g, [9] axial compression stress ratio at the base, [10] average percentage of vertical reinforcement in coupled walls ("flange" of core) at the base of structure, [11] average percentage of vertical reinforcement in coupled walls at mid-height, [12] average percentage of vertical reinforcement in cantilever walls ("web" of core), [13] Force reduction factor R_g = ratio of elastic bending moment demand at base of structure (calculated using EI_g) to nominal flexural strength M_n.

The reinforcement in the walls was designed to meet the requirements of the Canadian building code CSA A23.3-04. Three different reinforcement designs were completed for 10, 30, and 50 story walls. The amount of vertical reinforcement in the walls was kept constant from the base to a height equal to 1.5 times the wall length and then decreased approximately linearly over the building height. A brief summary of the reinforcement percentages at the base and midheight of the walls are given in Table 2.2. The average reinforcement percentages are reported for the flanges of the C-shaped cantilever walls (i.e., the coupled walls) and the webs of the cantilever walls. Note that minimum reinforcement requirements controlled the amount of vertical reinforcement in the upper levels of the building. According to CSA A23.3-04 requirements, minimum vertical reinforcement ratio is equal to $0.0015b_wl_w$ in regions of plastic hinging and $0.001b_wl_w$ outside the regions of plastic hinging for concentrated vertical reinforcement, and $0.0025b_wl_w$ for distributed reinforcement, where b_w and l_w are the width and the length of the shear wall, respectively. One reinforcement design was completed for each of the 20 and 40 story buildings. The percentage of vertical reinforcement is equal to the minimum vertical reinforcement ratio over the entire height of these two buildings. The variation of the percentage of longitudinal reinforcement over the height of the walls are presented in Appendix B.

The flexural strength of the cantilever walls depends on the amount of vertical reinforcement and the level of axial compression applied to the walls. The level of axial compression in turn depends on the tributary area of floor slabs supported by the walls. In the first nine building designs, the gravity columns were located around the periphery of the floor slabs resulting in large axial compression applied to the shear walls. As shown in Table 2.2, the axial stress ratios $P/f_c'A_g$ for these buildings were 5.9%, 8.7%, 10.1%, 11.4% and 12.7% for the 10, 20, 30, 40, and 50 story buildings, respectively. For the 30 story and 50 story buildings, a fourth design was done with additional gravity-load columns added to the building to reduce the axial compression applied to the shear walls. The reduction in axial stress ratio $P/f_c'A_g$ for the 30 story and 50 story buildings to 6.1% and 6.2% resulted in a significant reduction in flexural capacity of the cantilever shear walls. For the 40 story wall, a second design was done by reducing the axial compression force applied to the shear wall from 11.4 to 6.2%. This reduction in axial compression force resulted in 70% reduction in flexural strength of the shear wall at the base. Also, for 10 story walls, a fourth case was considered with a vertical reinforcement ratio equal to the minimum vertical reinforcement ratio, which is equal to 0.8%. Figure 2.24 shows the variation of flexural strength capacity over the height for the fifteen shear walls.

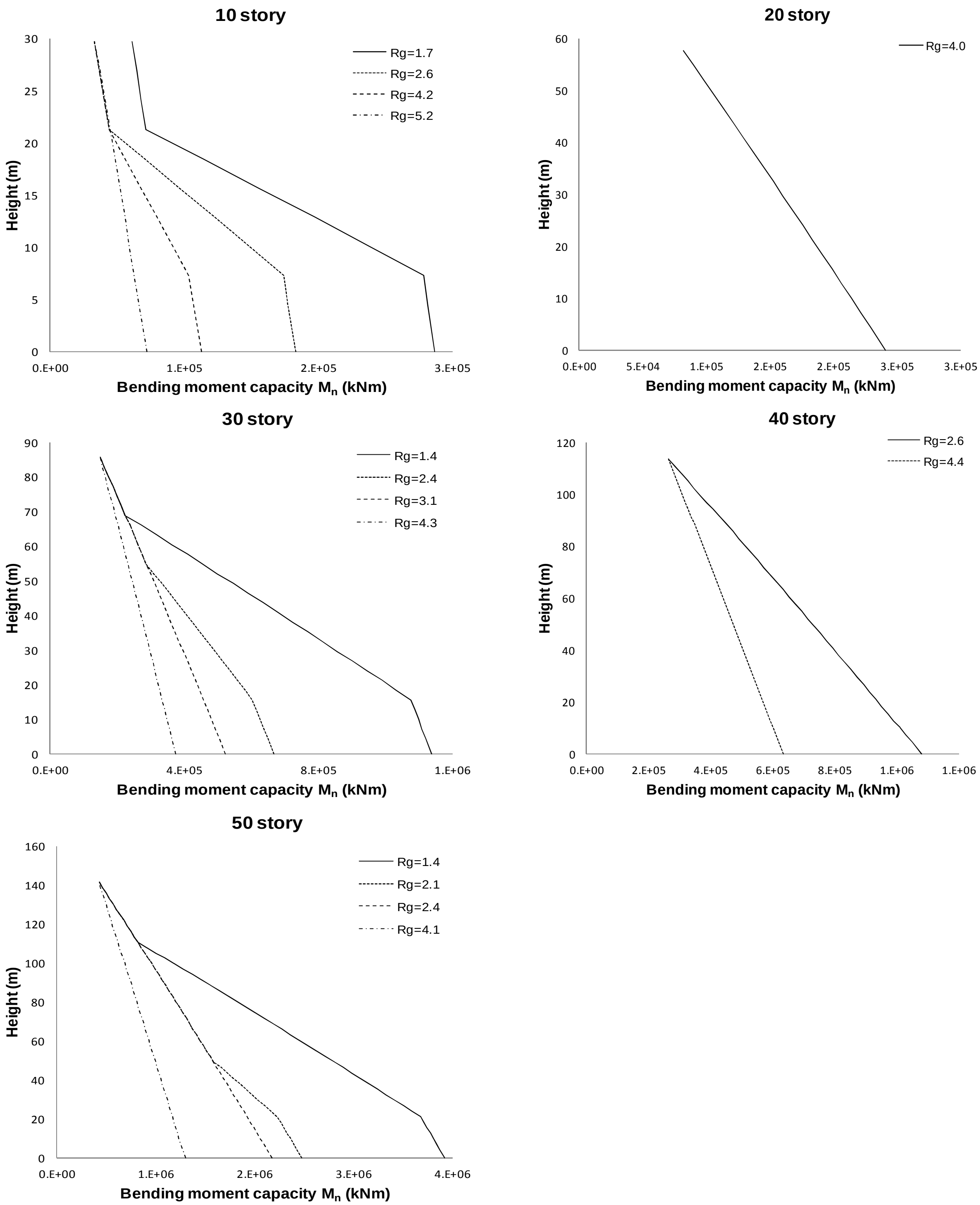

Figure 2.24 Variation of flexural bending moment capacity over the height for different shear walls.

The ratios of elastic bending moment demand to flexural bending moment capacity of the cantilever walls, both calculated at the base of the building, are called the force reduction factor

R_g for the building, and are given for all eleven buildings in the last row of Table 2.2. The elastic bending moment demands on the cantilever shear walls correspond to uncracked flexural capacity EI_g and were determined from response spectrum analysis using the target uniform hazard spectrum (UHS) shown in Figure 2.24. The target UHS is similar to the design spectrum for Vancouver, BC for site class C as specified in National Building Code of Canada (NBCC 2005) and the ASCE7-05 design spectrum (ASCE 2005) for Seattle WA for site class B. The NBCC design spectrum is in fact a uniform hazard spectrum corresponding to 2% probability of exccedance in 50 years, and it varies linearly between periods of 2 and 4 seconds and it remains constant for periods greater than 4 seconds. The target UHS decreases proportional to $1/T$ for periods between 2 and 6 seconds, and then the decrease was set proportional to $1/T^2$ for periods greater than 6 seconds. The target UHS is more consistent with ASCE7-05 design spectrum at longer periods. The target UHS is referred to as UHS throughout this thesis.

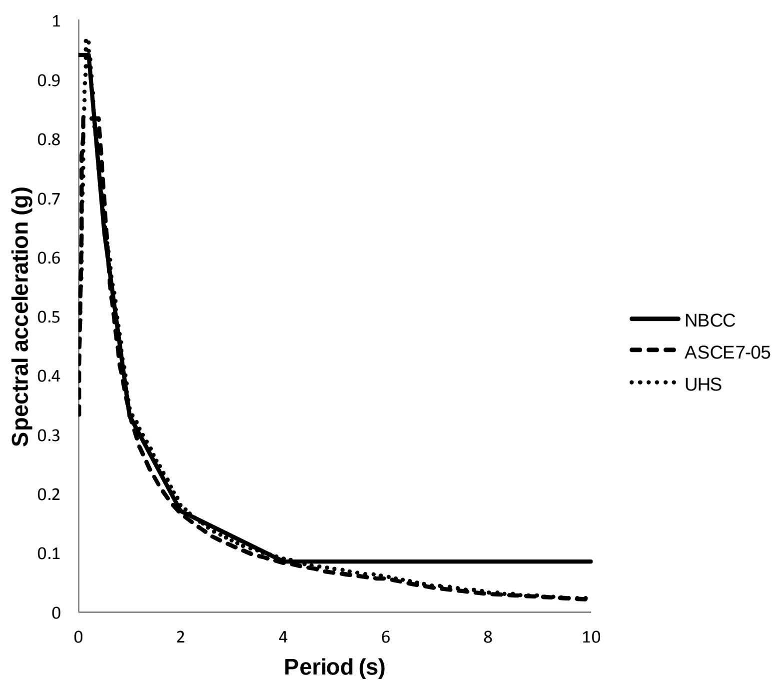

Figure 2.25 Comparison of NBCC design spectrum with ASCE7-05 design spectrum and the target UHS used in response spectrum analysis.

2.10 Summary

The aim of this work was to develop an analytical tool to simulate the flexural response of concrete shear walls. Fiber analysis and hysteretic bending moment - curvature relationship were considered as possible analytical options. The fiber analysis was proved to be a reliable analytical tool to predict the lateral force - top displacement relationship of two large-scale test specimens. A hysteretic bending moment - curvature relationship was developed with a trilinear backbone curve. Stiffness degradation rules were established based on the fiber analysis of a series of reinforced concrete cross sections with a wide range of axial compression force and longitudinal reinforcement ratios. The influence of reinforcing steel constitutive relationship and the cross section length on the bending moment - curvature relationship of concrete shear walls were examined. Hysteretic loops of the trilinear bending moment - curvature model were fully defined by developing unloading rules based on a mechanical analogy to compute the bending moment at crack closing, experimental results of a large scale reinforced concrete cross section subjected to reverse cyclic axial load, and the assumption that plane sections remain plane. The proposed hysteretic bending moment - curvature relationship was verified by making comparisons with the experimental results from two large-scale tests of cantilever shear walls.

Fifteen cantilever shear wall buildings that were 10 to 50 stories high were considered as the practical range of shear wall buildings. Longitudinal reinforcement in the walls was designed to meet the requirements of CSA A23.3-04. These walls were modelled in OpenSees using the trilinear hysteretic bending moment - curvature relationship. The parameters to define the hysteretic model were calculated at each floor considering the amount of axial compression force and the percentage of longitudinal reinforcement.

Chapter 3 : Influence of Nonlinear Force - Displacement Response of Concrete Walls on Effective Stiffness

3.1 Introduction to Effective Stiffness

In Canada and west coast of the U.S., response spectrum analysis (RSA) is widely used to estimate the maximum drift demands of concrete shear wall buildings. To reliably estimate the displacement demands, the linear model must account for stiffness loss corresponding to concrete cracking and reinforcement yielding. This is usually done by applying a single stiffness reduction factor $\alpha = I_e/I_g$ over the entire height of the shear wall. The effective stiffness of the equivalent linear system, EI_e, should be determined such that it accurately represents the nonlinear response of concrete shear walls.

Figure 3.1 shows a summary of the proposed stiffness reduction factors. FEMA 356 (2000) recommends factors of 0.8 and 0.5 for uncracked and cracked walls, respectively. CSA A23.3-04 specifies that the effective moment of inertia, I_e, is a function of axial compression force and is equal to 0.6 for a wall with no axial compression force and equal to 0.7 for a wall with an axial compression force of $0.1f_c'A_g$, where f_c' is the concrete compressive strength and A_g is the gross cross sectional area of the shear wall. Paulay and Priestley (1992) also related the effective stiffness to axial compression force. They recommended a reduction factor of 0.25 for a concrete wall with no axial compression force and a factor of 0.35 for a wall with an axial compression force equal to $0.1f_c'A_g$. Figure 3.2 shows a schematic of the CSA and Paulay and Priestley approaches to estimate effective stiffness. The CSA method defines the effective stiffness as the slope of the line that gives area under the curve equal to the actual nonlinear bending moment - curvature relationship. Paulay and Priestley define effective stiffness as the slope of the line that connects the origin to the yield point.

Some researches recommended effective stiffness based on shake table test results. Lestuzzi (2002) tested a series of 1/3-scale rectangular walls with axial compression force equal to $0.03f_c'A_g$ subjected to synthetic earthquakes. Lestuzzi concluded that effective stiffness dropped to approximately 10% of the gross stiffness. Schotanus and Maffei (2007) suggested an effective stiffness of $0.2EI_g$ from the results of a full scale rectangular wall (Panagiotou 2008) with an axial compression force of $0.05f_c'A_g$. Doepker (2008) used the shake table results of a series of reinforced concrete wall specimens and defined effective stiffness as a function of drift demand. According to Doepker model, effective stiffness is equal to 30% of the uncracked stiffness for drift ratios less than 0.3% and it decays exponentially to an effective stiffness equal to 5% of the gross flexural stiffness as the drift ratio increases to 4%.

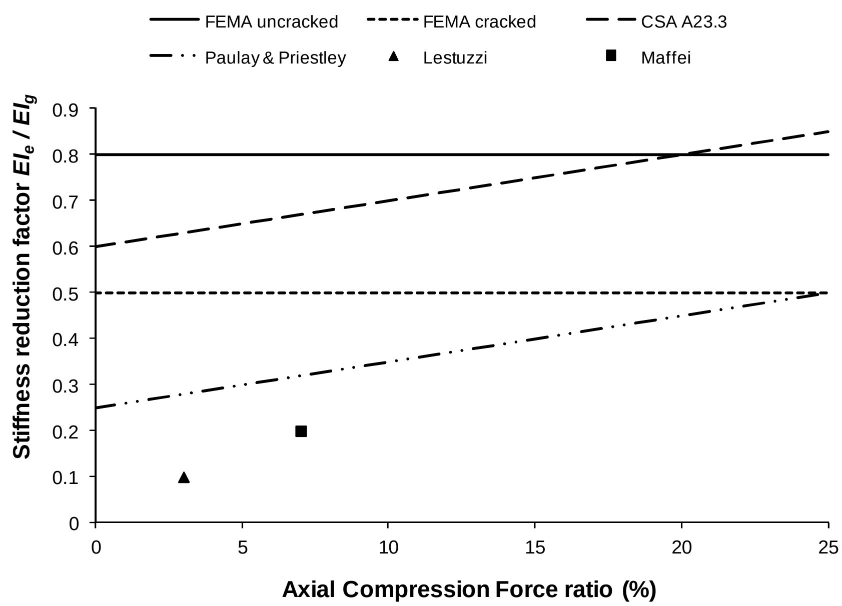

Figure 3.1 Recommended stiffness reduction factor.

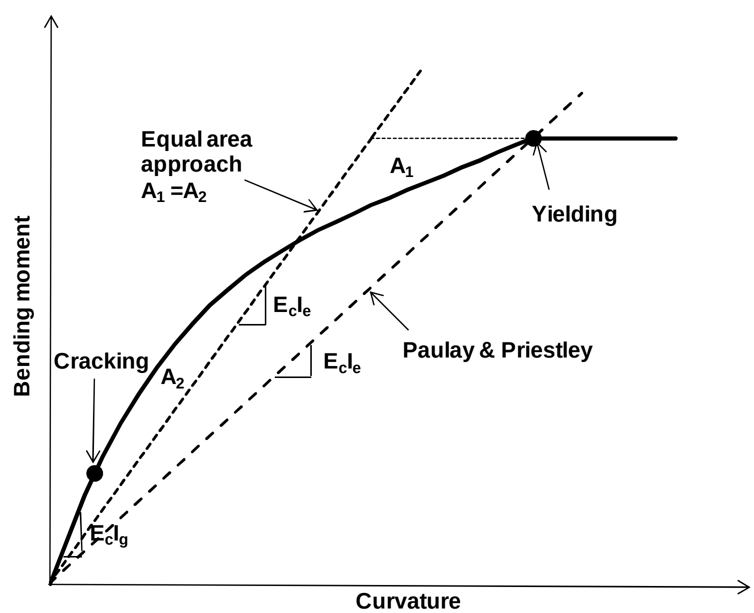

Figure 3.2 Equal area and Paulay & Priestley approaches for computing effective stiffness.

The proposed stiffness reduction factors discussed above were determined from sectional analysis or from shake table results of walls with low fundamental periods (0.2 to 0.59 second). In order to obtain a good estimate of displacement demands of shear wall buildings during earthquakes, it is necessary to compare displacement demands from nonlinear time history analysis with the displacements determined from linear analysis. Single-degree-of-freedom (SDOF) oscillators are used in this chapter to model the base shear - roof displacement relationship of cantilever shear walls. In the first step, roof displacement demands determined using SDOF oscillators are compared with the roof displacement demands from multi-degree-of-freedom (MDOF) approach for three shear walls to validate the accuracy of the SDOF approach to predict roof displacement demands. Lastly, in order to observe the influence of the force - displacement response of walls on the roof displacement demand, 13 shear walls with a wide range of axial compression force and vertical reinforcement percentage are selected. The fundamental period of these walls range from 0.5 second to 4 seconds. Both spectrum matched and real records are used in time history analysis. For each force - displacement relationship and fundamental period, the ratio of elastic force demand to strength R varies from 1.0 to 5.0.

3.2 SDOF versus MDOF Modelling for Predicting Roof Displacement Demands

In this section roof displacement demands from SDOF oscillators are compared with roof displacement demands from MDOF models for three example shear walls. This was done to validate the predicted roof displacements from the SDOF approach. Three 10, 20, and 40 story walls are selected for this purpose. That is, a 10 story wall with R_g = 5.2; a 20 story wall with R_g = 4.0; and a 40 story wall with R_g = 2.6. The three walls feature minimum longitudinal reinforcement according to CSA A23.3-04. The structural properties of the three walls are presented in Table 2.1. These walls were modelled using both SDOF and MDOF approaches. The details of the analytical models are presented hereafter.

3.2.1 SDOF Modelling of Example Shear Walls

Figure 3.3 shows a general schematic of the hysteretic force - displacement relationship used for the SDOF modelling of the three walls. The hysteretic model can be fully defined by knowing key parameters k_i, V_{co}, V_n, Δ_{yUB}, Δ_{yLB}, V_{cc}. Compared to the trilinear hysteretic bending moment - curvature model developed in Chapter 2, the hysteretic force - displacement relationship has simpler rules for stiffness degradation and unloading. This includes using a constant lower bound yield displacement Δ_{yLB}, which can be calculated by integrating curvatures from lower - bound trilinear bending moment - curvature relationship (see Figure 2.2). Also, the hysteretic force - displacement model assumes no residual displacement for positive V_{cc} values. The hysteretic model was implemented into OpenSees by Korchinski (2007), and was modified as part of the current study in order to model walls with negative V_{cc} values. Korchinski (2007) also compared the predicted force - displacement relationship from Figure 3.3 with experimental results from Adebar et al. (2007) and he concluded that the predicted hysteretic loops from the analytical model are slightly smaller than those observed in the experiment. The full description of the hysteretic force - displacement model is presented in Appendix C.

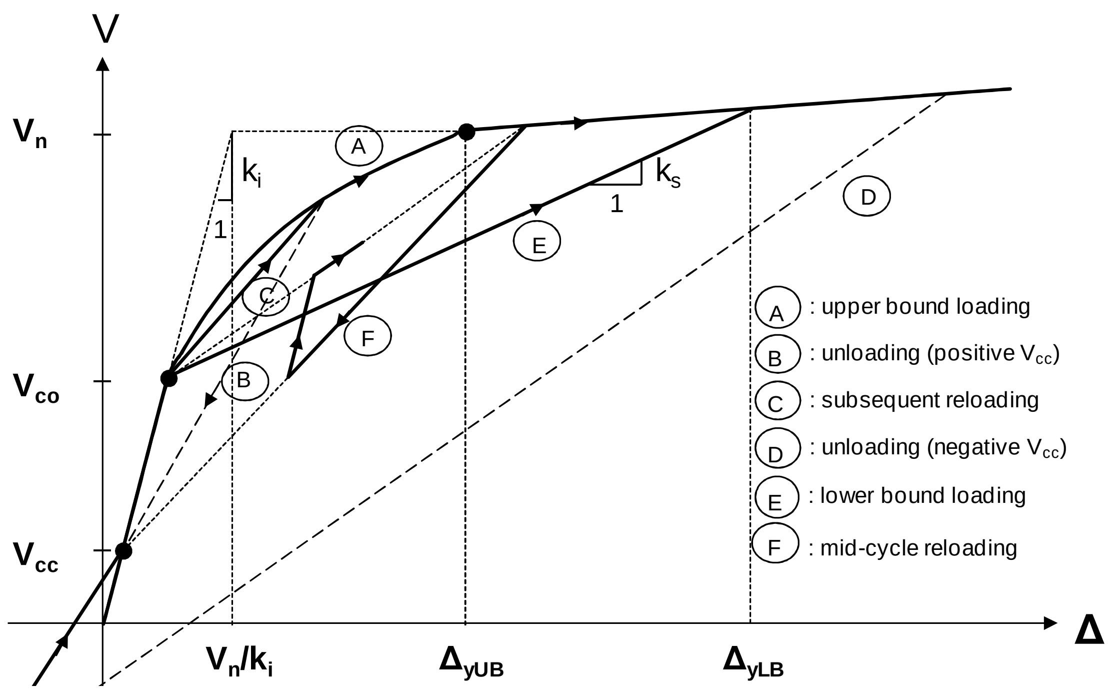

Figure 3.3 Hysteretic force - displacement relationship used for SDOF oscillators.

Figure 3.4 presents the base shear - top displacement relationship for the three walls. Each graph includes the upper bound, lower bound, and unloading points for the three walls subjected to reverse cyclic loading with a lateral load pattern proportional to the first mode shape. The values of the key points shown in Figure 3.4 is used to perform time history analysis.

A mass-spring-dashpot system was modelled in OpenSees for this purpose. The spring has a force - displacement relationship shown in Figure 3.3 with the key properties depicted in Figure 3.4. A 3% viscous damping was considered for the dashpot The mass *m* of the SDOF system was adjusted in order to achieve fundamental periods of 1.0, 2.0, and 4.0 seconds, which are the fundamental periods of the 10, 20, and 40 story walls, respectively. All time history analyses adopted the Newmark integration method with coefficients β = 0.5 and γ = 0.25. The time step was set equal to 0.005 s, and the Newton-Raphson iteration method was used to satisfy equilibrium at each time step.

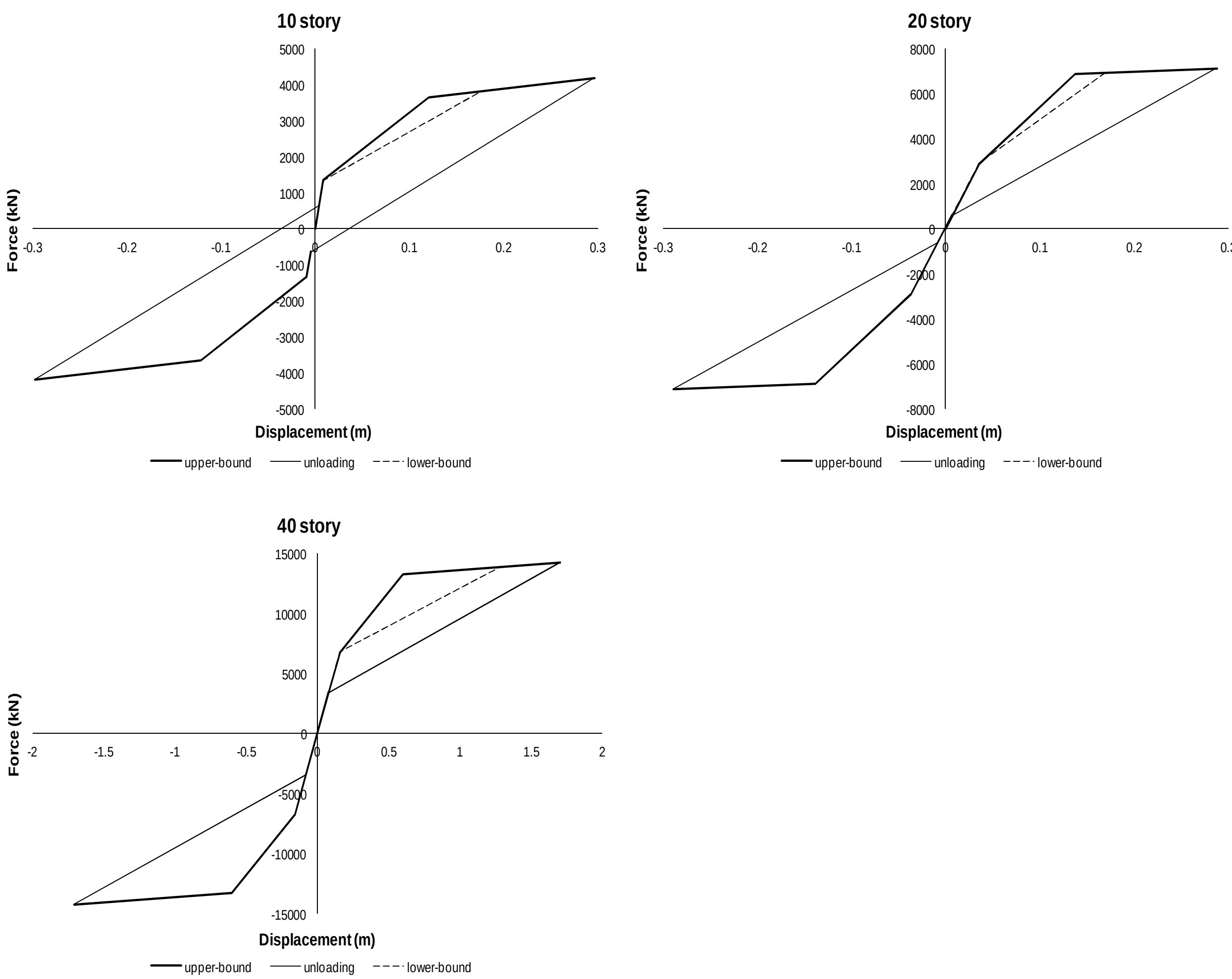

Figure 3.4 Base force - roof displacement relationship for 10, 20, and 40 story walls.

3.2.2 MDOF Modelling of Example Shear Walls

Time history analysis of the three shear walls was done using the trilinear hysteretic bending moment - curvature relationship presented in Figure 2.20. The parameters that define the trilinear model were calculated at each floor considering the variation of axial compression. A force element was defined at each floor level to model the vertical spread of plasticity in the walls. The base was assumed to be fixed, and shear deformations were not considered in the analytical model. Rayleigh damping was assumed with mass proportional and initial stiffness matrixes. A damping ratio of 3% was assigned for the first and third modes. The time step was set equal to 0.0025, and the Newton-Raphson iteration method was used to satisfy equilibrium at each time step. Lastly, the Newmark integration method with coefficients $\beta = 0.5$ and $\gamma = 0.25$ was used in time history analysis.

3.2.3 Ground Motions Used for Time History Analysis

Nonlinear time history analyses were performed using a set of forty ground motions taken from the suite of ground motions used in ATC 55 project (ATC 2005). Of these forty ground motions, twenty motions were recorded on site class B, and twenty motions were recorded on site class C. The ground motions correspond to eight different earthquakes with magnitude M_s ranging from 6.1 to 7.1 and peak ground acceleration ranging from 48.9 to 504.2 cm/s^2**.**

The target spectrum for scaling ground motions is the uniform hazard spectrum (UHS) shown in Figure 2.25. The 40 ground motions were scaled in two different ways: scaling to the UHS at the fundamental period T_1 and scaling to match the UHS over the periods between $0.2T_1$ and $1.5T_1$ as recommended by ASCE standard 7-05 (ASCE 2005). It was decided to scale the ground motions so that the mean spectrum follows the UHS between $0.2T_1$ and $1.5T_1$, rather than conservatively scaling the ground motions to be above the UHS over this period range. It means that the ground motions were scaled such that the mean spectrum has the same area under the curve as the UHS over this period range. This scaling method was applied to perform time history analysis for both SDOF and MDOF systems. Comparison between the mean spectrum of the ground motions and the UHS for different fundamental periods and the two scaling methods is presented in Appendix D.

3.2.4 Results

The SDOF oscillator has an initial period and damping ratio equal to the first mode response of the MDOF structure. If the structure remains elastic, the roof displacement corresponding to the first mode is equal to $\Gamma_1 \phi_{r1} D_1$, where ϕ_{r1} is the value of first mode vector at the roof (equal to 1.0), D_1 is the elastic spectral displacement corresponding to the first mode period, and Γ_1 is first mode participation factor, which is equal to $\phi_1 M 1 / \phi_1 M \phi_1$. Note that M and ϕ_{r1} are mass matrix and first mode vector, respectively. In the case of nonlinear response, roof displacement predicted from the SDOF oscillator is an approximation to the actual roof displacement demand since this method assumes that elastic first mode shape is still valid even when the structure response is nonlinear (Chopra et al 2003). The value of Γ_1 is 1.47, 1.51, and 1.54 for the 10, 20, and 40 story walls, respectively. Note that D_1 is the peak displacement determined from nonlinear time history analysis of the equivalent SDOF oscillators.

Figure 3.5 compares the roof displacement demand determined using the SDOF oscillators with the roof displacement demand corresponding to the MDOF system for the three shear walls. Note that both axes in these plots are expressed in terms of global drift ratio for individual ground motions, which is the ratio of maximum roof displacement demand to the wall height.

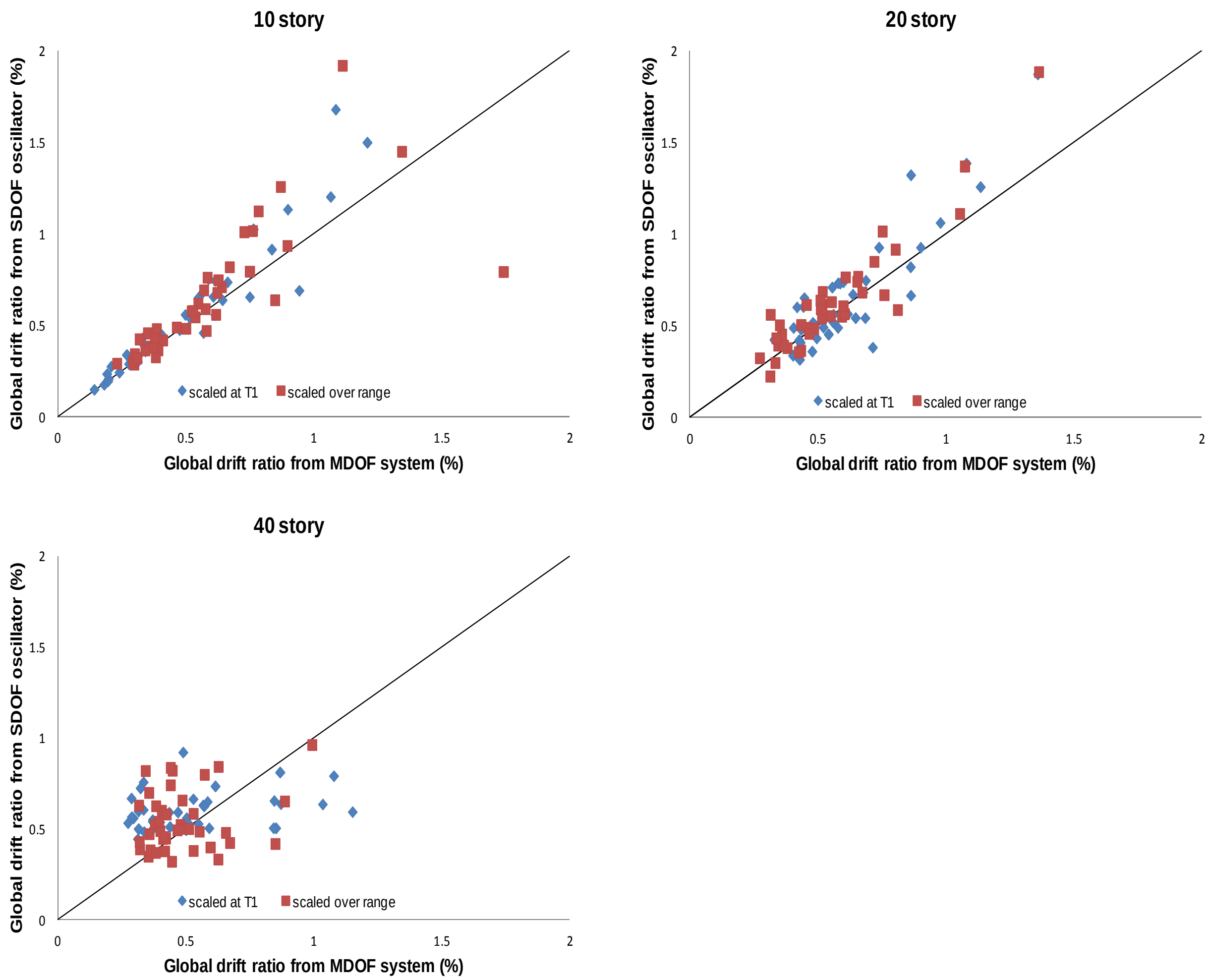

Figure 3.5 Comparison of global drift ratios from MDOF with global drift ratios from SDOF oscillator for 10, 20, and 40 story walls.

Figure 3.5 indicates that regardless of how ground motions are scaled, the MDOF and SDOF models give similar roof displacement demands for the 10 and 20 story walls although the SDOF oscillator tends to give higher roof displacement demand for the majority of ground motions. For the 40 story wall, the difference between the roof displacement demand predicted from the two models increases for individual ground motions. For some ground motions, using SDOF model results in roof displacement demands that are significantly lower than those determined using the MDOF approach.

It is also interesting to compare the mean roof displacement demands from the two analytical models. Figure 3.6 shows the ratio of roof displacement from the SDOF oscillator to the roof displacement demand from the MDOF system as a function of the fundamental period for the three walls.

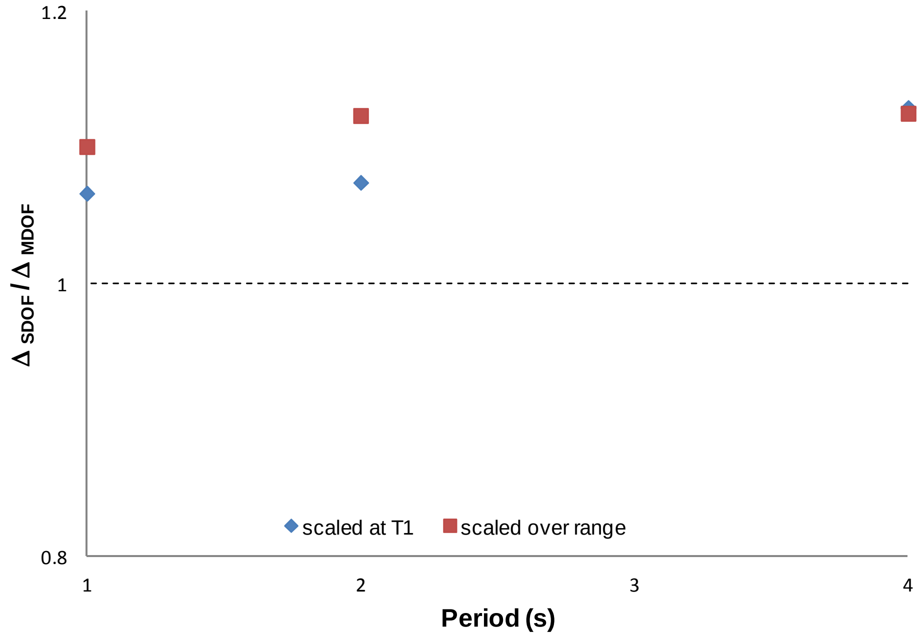

Figure 3.6 Ratio of mean roof displacement demand from MDOF model to the mean roof displacement from SDOF oscillator for different ground motion scaling methods.

The mean displacement ratios presented in Figure 3.6 are 1.06 and 1.10 for the 10 story, 1.07 and 1.12 for the 20 story, and 1.13 and 1.12 for the 40 story wall corresponding to ground motions scaled to the UHS at the fundamental period and over the range, respectively. It can be seen that the ratio increases as the fundamental period of the structure increases; however, the increase is more pronounced for the scaled over the range ground motions.

Another important issue that needs to be addressed is whether the mean displacement ratio increases as the global drift ratio increases. For this purpose, the forty ground motions were scaled at two additional scale factors of 1.0 and 5.0. These scale factors are considered as lower-bound and upper-bound scale factors since the mean scale factor for the forty records that were scaled to match the UHS either at the fundamental period or over the range lies between these bounds. Figure 3.7 shows the results for the three walls. Also included in this figure are the results for ground motions scaled to the UHS at the fundamental period and over the range of periods.

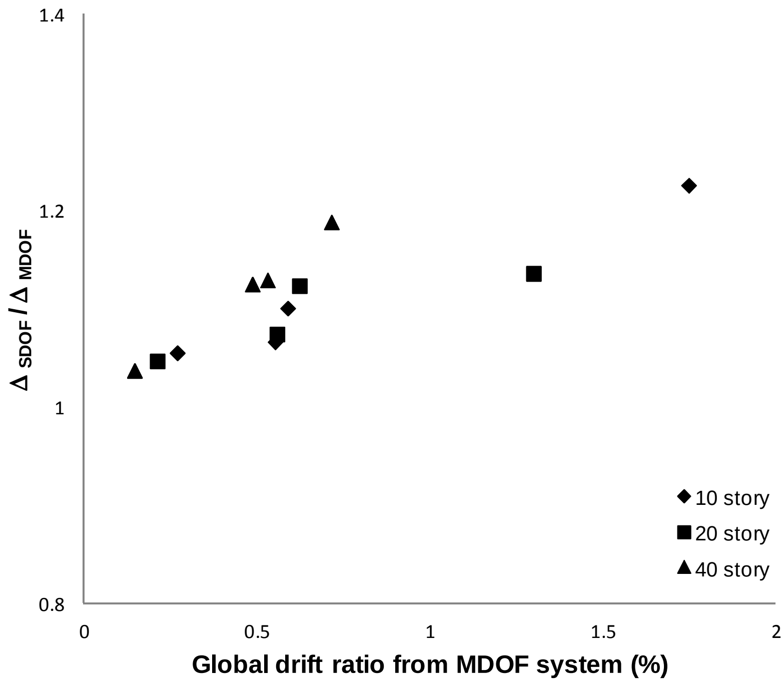

Figure 3.7 Ratio of mean roof displacement demand from MDOF model to the mean roof displacement from SDOF oscillator as a function of global drift ratio from MDOF model for the three walls.

Figure 3.7 indicates that the mean displacement ratio tend to increase as the global drift ratio increases. The maximum ratio is 1.22, 1.13, and 1.18 for 10, 20, and 40 story walls, respectively, which correspond to the scale factor of 5.0.

Comparison of roof displacement demands from two SDOF and MDOF approaches showed that the SDOF oscillator provides a reasonable estimate of mean peak roof displacement although the results for individual ground motions can be much higher or lower than those predicted from the MDOF system. It was found that the ratio of the mean displacement from SDOF oscillators to the mean roof displacement from the MDOF model varies from 1.06 to 1.13 depending on the scaling method. It was also observed that the mean displacement ratios are higher for larger scale factors (i.e. scale factor of 5.0), which indicates that the SDOF oscillator tend to overestimate the roof displacement demand as the global drift ratio increases.

3.3 Effective Stiffness of Cantilever Shear Walls using SDOF Approach

As it was observed in Section 3.2, the SDOF approach provides a good estimate of the mean roof displacement demand. This method of analysis will be used in this section to estimate roof displacement and consequently effective stiffness of cantilever shear walls. The details are presented hereafter.

The hysteretic force - displacement model presented in Figure 3.3 is fully determined by knowing key parameters k_i, V_{co}, V_n, Δ_{yUB}, Δ_{yLB}, and V_{cc}. It is necessary to generate a realistic range of the key parameters of the hysteretic model so that the considered force - displacement models can be regarded as a reasonable representation of the base shear - roof displacement relationship of high-rise walls. The parameters of the hysteretic model are a function of bending moment and lateral load distribution over the height of walls. Wall geometry, axial load level, and amount of vertical reinforcement influence the shape of the force - displacement relationship. In order to develop a realistic range for the key parameters of the hysteretic model, Korchinski (2007) studied a series of rectangular and flanged walls with different height to length ratios. Web reinforcement ratio was assumed to be 0.25% for all walls. Flanged reinforcement ratio was varied from 0.5% to 2% for flanged walls and from 1% to 4% for rectangular walls. Axial load was also varied from 0 to $0.3f_c'A_g$. From this database, 13 walls were selected to represent the practical range of key parameters of the hysteretic force - displacement model. The properties of the 13 walls are shown in Table 3.1. Each wall is labelled by a combination of "L" and "R" characters. "L" stands for Linear and represents the linear segment of the backbone curve. The number after this character is proportional to the ratio of V_{co}/V_n. "R" stands for Reinforcement and is followed by a number which is proportional to the ratio of the secondary slope k_s to the initial slope k_i.

Table 3.1 Parameters that define the hysteretic response of the 13 walls considered in the study.

Walls	V_{co}/V_n	V_{cc}/V_n	k_s/k_i	$\Delta_{yUB}k_i/V_n$	$\Delta_{yLB}k_i/V_n$
W-L2-R3	0.20	-0.20	0.286	2.00	3.00
W-L2-R2	0.20	-0.20	0.167	2.70	5.00
W-L2-R1	0.20	-0.20	0.103	3.50	8.00
10 story	0.37	-0.17	0.2	4.37	6.39
W-L4-R4	0.40	0.0	0.375	1.60	2.00
W-L4-R2	0.40	0.0	0.167	2.60	4.00
W-L4-R1	0.40	0.0	0.107	3.20	6.00
20 story	0.42	0.09	0.3	1.61	2.0
W-L5-R3	0.50	0.15	0.333	1.70	2.00
W-L5-R2	0.50	0.15	0.167	2.40	3.50
W-L5-R1	0.50	0.15	0.111	2.80	5.00
40 story	0.51	0.26	0.2	1.92	4.14
W-L6-R3	0.60	0.30	0.286	1.65	2.00
W-L6-R2	0.60	0.30	0.167	2.10	3.00
W-L6-R1	0.60	0.30	0.118	2.40	4.00
W-L8-R2	0.80	0.60	0.167	1.40	2.00

Also shown in Table 3.1 are the characteristics of the 10, 20, and 40 story walls described in section 3.2. Table 3.1 indicates that the properties of the three walls fit within the characteristics of the 13 walls. The upper-bound and lower-bound curves for the 13 walls are shown in Figure 3.8 and Figure 3.9, respectively. The horizontal axis in both figures is normalized by the displacement at which the initial slope k_i intercepts the shear force at the flexural capacity V_n, i.e. V_n/k_i. The vertical axes are also normalized by the shear force at the flexural capacity V_n.

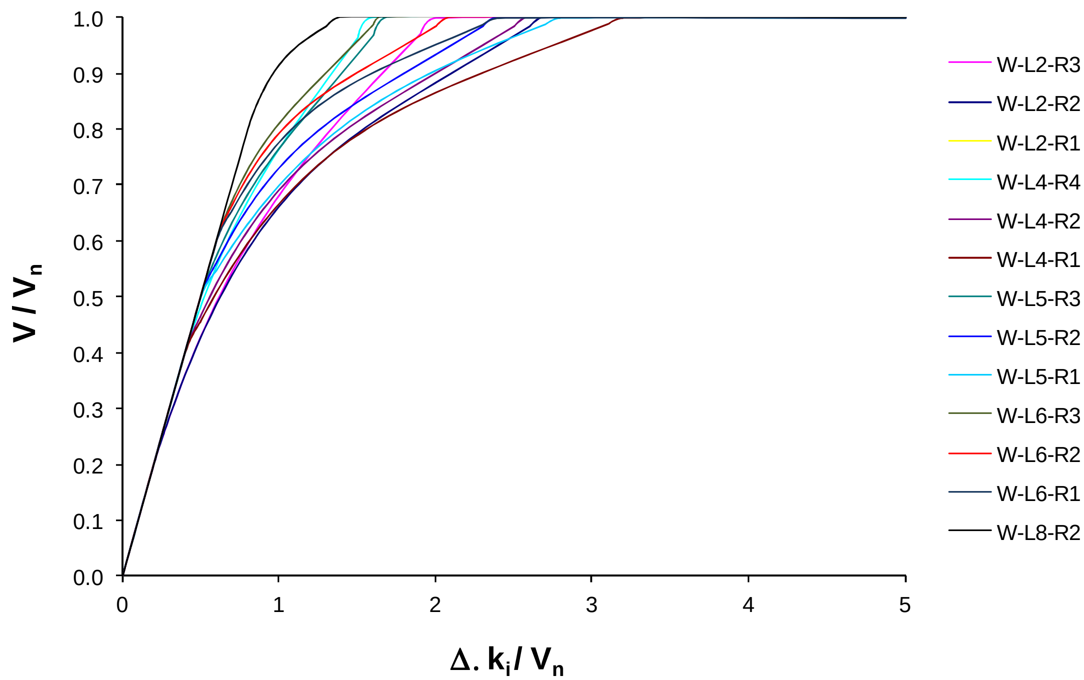

Figure 3.8 Upper-bound force - displacement relationship for the 13 shear walls.

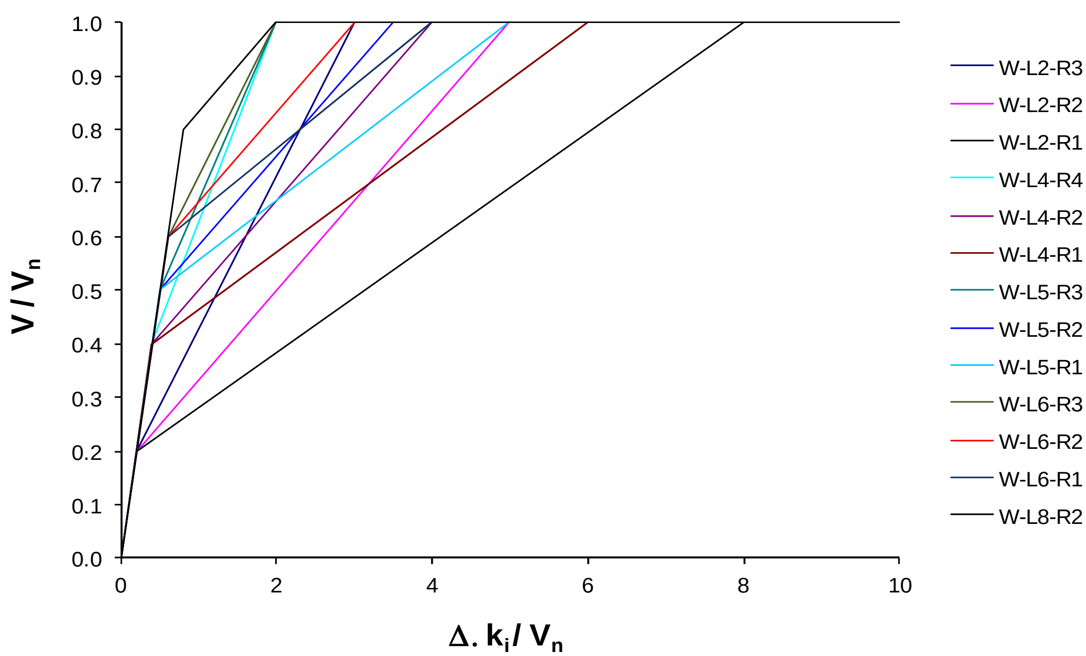

Figure 3.9 Lower-bound force - displacement relationship for the 13 shear walls.

To perform time history analysis, the forty ground motions described in section 3.2.3 were scaled to the UHS in three different ways: 1) spectrum matching using computer program SYNTH (Naumoski 2001); 2) scaling to the UHS at the fundamental period T_1, and 3) scaling to match the UHS over the period range between T_1 and $1.5T_1$. Note that the period range of $0.2T_1$ to $1.5T_1$ prescribed by ASCE7-05 is replaced by the period range of T_1 to $1.5T_1$. The lower bound $0.2T_1$ is considered to capture higher mode effects, and need not be considered in this study since the shear walls are considered as SDOF oscillators. Similar to section 3.2.3, equal area under the curve approach was used to match the ground motions to the UHS over the periods between T_1 and $1.5T_1$. Comparison of the mean spectrum corresponding to different scaling methods with the UHS is presented in Appendix D.

For each shear wall, the mass m of the SDOF oscillator was adjusted in order to achieve different periods. A period range from 0.5 to 4.0 seconds at 0.5 second intervals was considered for each wall. The force reduction factor R varied from 1.0 to 5.0 at 0.25 intervals. Note that the R factor is defined as the ratio of elastic force demand (equal to the product of mass times the spectral acceleration at the fundamental period $S_a(T_1)$) to the wall strength V_n. For each period and R value, maximum displacement from time history analysis was recorded for the three scaling methods. The mean displacement of the ground motions was then used to define the effective period and consequently effective stiffness. Effective period was defined as the period of an equivalent linear system with the same spectral ordinate as the mean displacement from time history analysis. Effective periods were obtained using the UHS. The effective stiffness is determined from the effective period and the stiffness reduction factor α is determined from the ratio of stiffnesses, i.e. $\alpha = k_e/k_i$. The stiffness reduction factor is assumed to be the ratio of effective flexural rigidity EI_e to gross flexural rigidity EI_g.

Figure 3.10 through 3.12 shows the results for the thirteen walls using spectrum matched ground motions and periods of 1.0, 2.0, and 4.0 seconds, respectively. The results for other periods and ground motion scaling methods are presented in Appendix E.

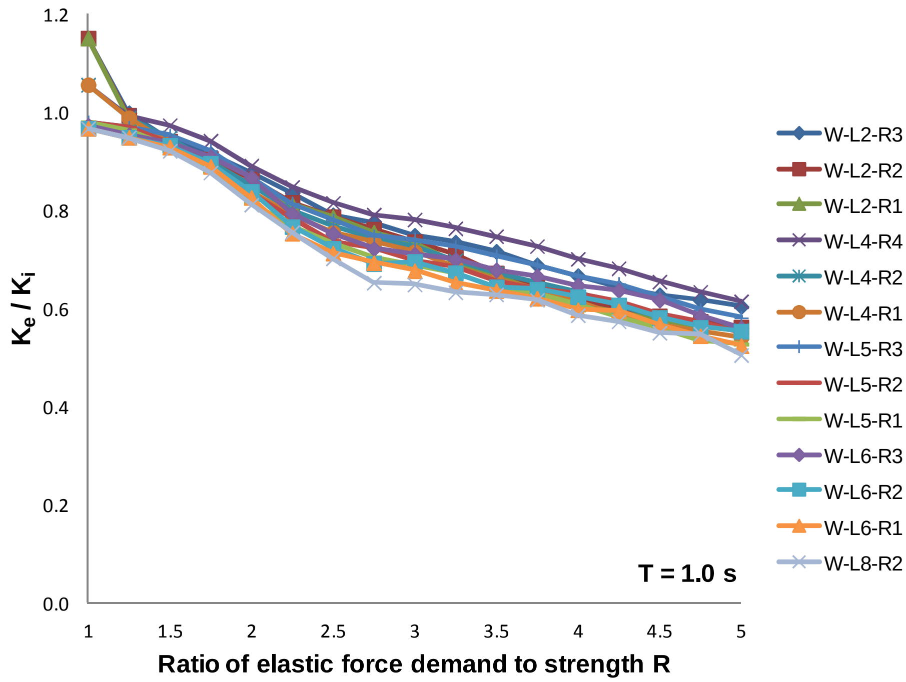

Figure 3.10 Stiffness reduction factor as a function of force reduction factor for 13 shear walls with the period of 1.0 second.

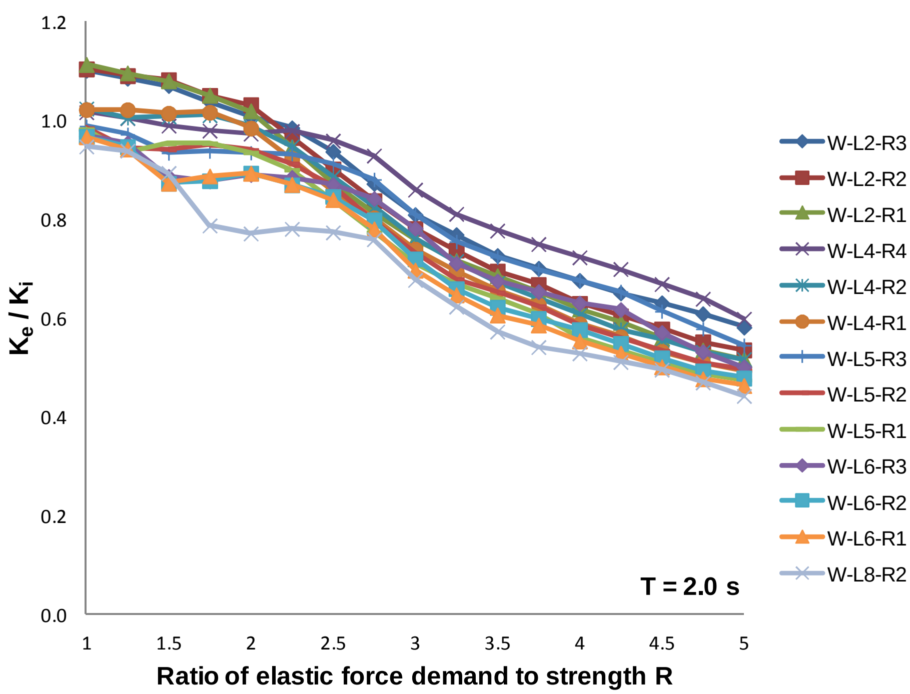

Figure 3.11 Stiffness reduction factor as a function of force reduction factor for 13 shear walls with the period of 2.0 seconds.

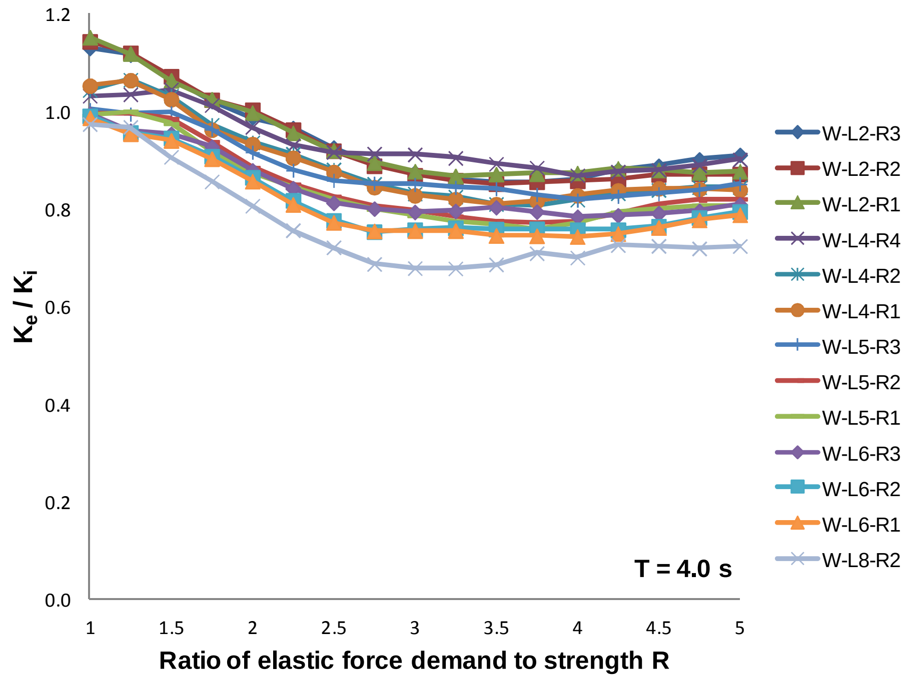

Figure 3.12 Stiffness reduction factor as a function of force reduction factor for 13 shear walls with the period of 4.0 seconds.

The following observations can be made: (a) stiffness reduction factor is close to 1.0 for low *R* values for the three periods. It means that effective period of the equivalent linear system is approximately equal to the fundamental period of the nonlinear model. It happens since most of the walls have barely yielded at low *R* values, and therefore most of the wall section is in the linear phase. As a result, nonlinear displacements are approximately equal to linear displacements, resulting in stiffness reduction factors close to 1.0. (b) W-L8-R2 has consistently the lowest stiffness reduction values. This wall has the smallest difference between loading and unloading paths meaning that the amount of energy dissipated by this wall is the least amongst the thirteen walls. This observation contradicts the initial prediction since W-L8-R2 has the highest axial compression force and consequently highest area under the backbone curve. It means that using area-under-the-curve method results in highest effective stiffness for this wall. However, maximum displacement demand of a shear wall is influenced by both loading and unloading characteristics of the force - displacement relationship. The influence of the hysteretic characteristics of the force - displacement relationship on displacement demands will be investigated in sections 3.4.1 and 3.4.2. (c) For periods of 1.0 and 2.0 seconds, stiffness reduction factor drops from 1.0 to about 0.5 as the *R* factor increases from 1.0 to 5.0. For the period of 4.0 seconds, on the other hand, stiffness reduction factor drops to about 0.8 and then it remains constant as the R value increases. This is consistent with the equal displacement rule, which states that the maximum displacement of a nonlinear system is approximately equal to the displacement of the linear system for structures with longer periods. The accuracy of this assumption is shown in Figure 3.13. Figure 3.13 illustrates the mean values of the ratio of the maximum nonlinear displacement to linear displacement for forty ground motions scaled at the initial period T_1. For a given period and R value, each point on the plot corresponds to the mean of the 520 maximum nonlinear displacements (13 walls times 40 ground motions).

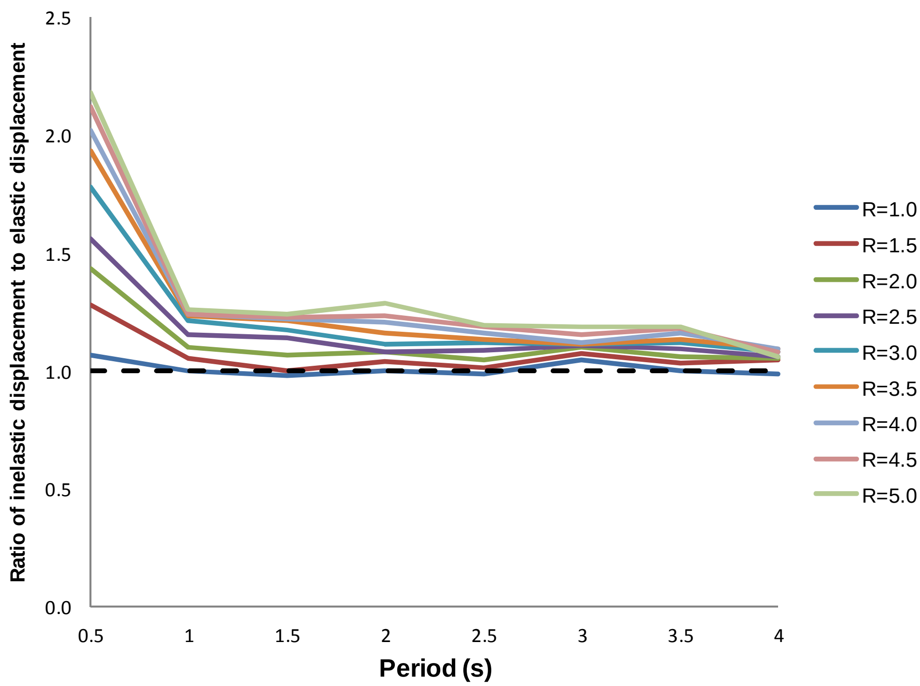

Figure 3.13 Ratio of inelastic to elastic displacement for different periods and force reduction factors.

Figure 3.13 indicates that for periods greater than 0.5 second, the ratio of inelastic to elastic displacement is relatively independent of period for a given R factor. Furthermore, for longer periods, i.e. greater than 3 seconds, the ratio is insensitive to the variation of the force reduction factor. For example, the ratio varies between 1.05 and 1.19 as R increases from 1.0 to 5.0. This observation validates the accuracy of equal displacement rule for taller shear walls. On the other hand, the ratio is very dependent on R for short period structures: as R increases from 1.0 to 5.0, the ratio of inelastic to elastic displacement increases from 1.07 to 2.18. This means that equal displacement rule significantly underestimates nonlinear displacements of short period structures.

Figure 3.14 shows the variation of stiffness reduction factor as a function of force reduction factor and period for the three ground motion scaling methods. Each line in Figure 3.14 represents the mean value of the stiffness reduction factors for the thirteen walls with a given period and *R* value. Figure 3.14 indicates that stiffness reduction factors for spectrum matched ground motions are lower than those for other scaling methods for all periods except for *T* = 0.5 s. For spectrum matched ground motions, stiffness reduction factor is relatively independent of the period for *R* factors less than 3.0; however, for higher *R* values, stiffness reduction factor increases from 0.5 to 0.8 as the period increases from 0.5 to 4.0 seconds. For scaled over range ground motions and *R* = 5.0, stiffness reduction factor varies from 0.55 to 0.7 as the period increases from 1.0 to 4.0 seconds.

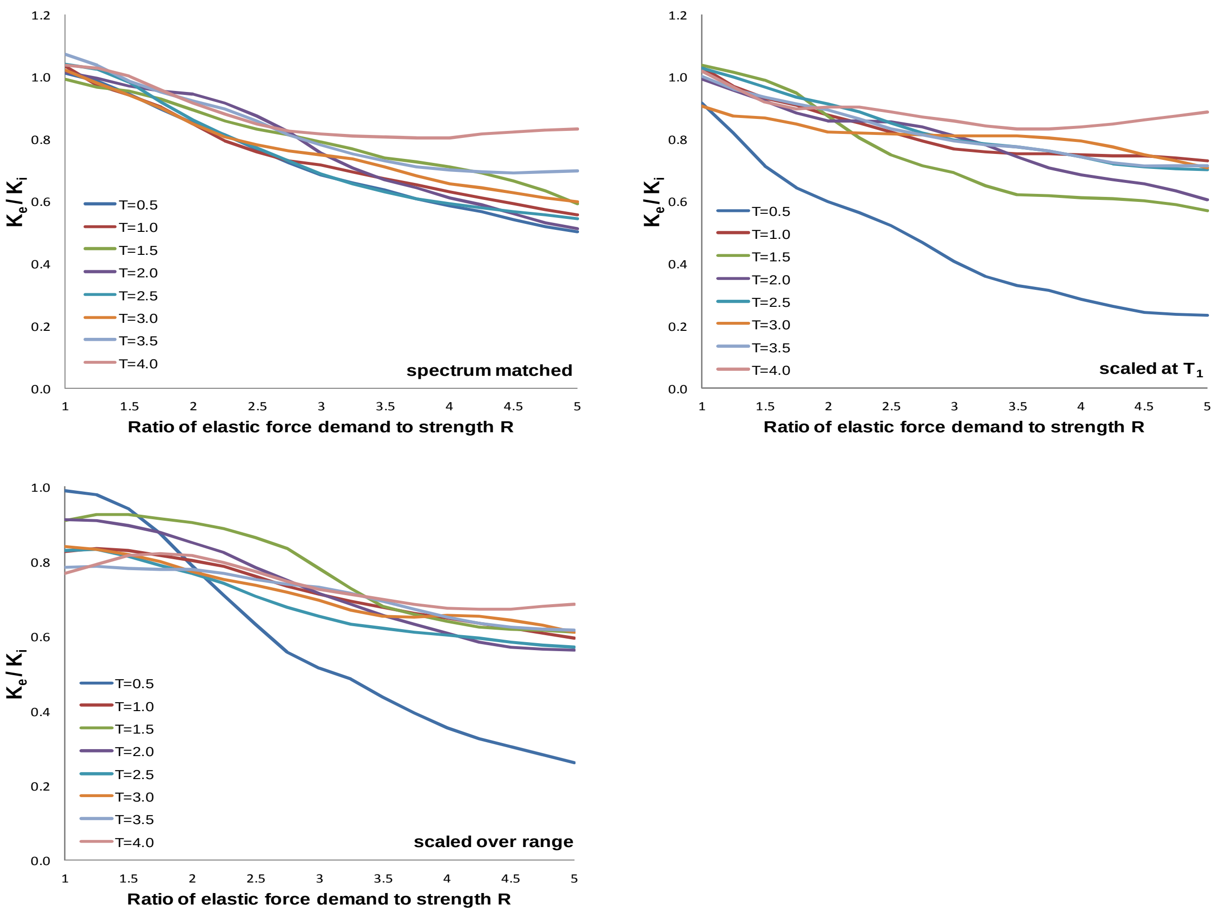

Figure 3.14 Variation of mean stiffness reduction factor as a function of period and force reduction factor for three ground motion scaling methods.

As it was shown in Figure 3.14, stiffness reduction factors corresponding to the period of 0.5 second for ground motions scaled to the UHS at T_1 and over the range are significantly lower than those for spectrum matched ground motions. This can be explained by comparing the mean spectrum of the ground motions for these scaling methods with the UHS. Figure 3.15 shows the mean spectrum for the two scaling methods.

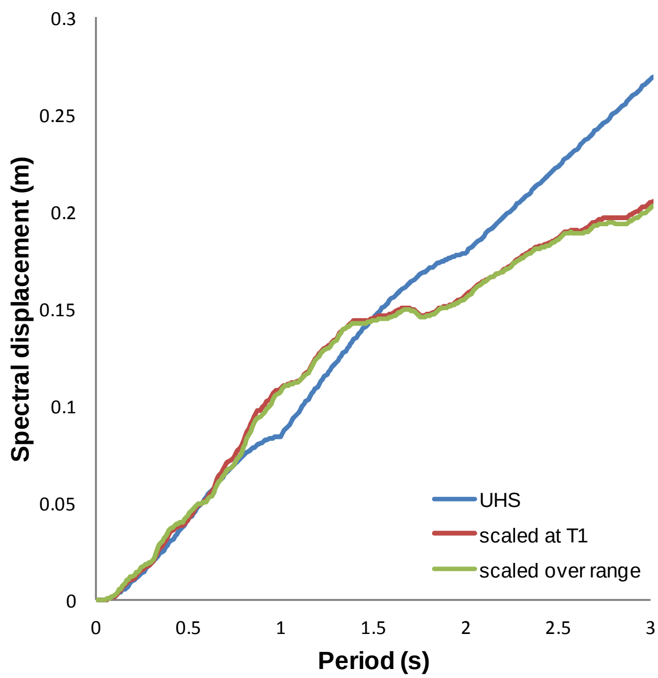

Figure 3.15 Comparison of the mean spectrum of ground motions scaled to the UHS at fundamental period and over the range of periods with the UHS.

Figure 3.15 indicates that the mean spectrum for the two sets of ground motions scaled to the UHS at T_1 and over the range of periods matches the UHS for periods up to 0.75 s and then the mean lies above the UHS as the period increases from 0.75 to 1.5 s. Since the mean spectrum increases rapidly for periods greater than 0.75 s, the shear walls attract higher accelerations and nonlinear displacements increase rapidly because the walls soften and the periods elongate beyond 0.5 s. Furthermore, effective periods were read off from the UHS, and therefore using ground motions scaled to the UHS at T_1 and over the range results in higher effective periods for T = 0.5 s compared to the case where spectrum matched ground motions were used in time history analysis.

It is also useful to investigate the influence of the shape of the force - displacement relationship on effective stiffness. Although Figure 3.10 to 3.12 showed that the resulting stiffness reduction factors are fairly well banded considering the wide range of walls studied, a closer examination is needed to observe the variation of stiffness reduction factor within the 13 shear walls. Figure 3.16 presents stiffness reduction factor using spectrum matched ground motions for R = 5.0 for two periods of 2.0 and 3.0 seconds. Horizontal axis in this figure represents the ratio of shear force at crack opening V_{co} to shear force at flexural capacity V_n (see Figure 3.3), while vertical axis shows stiffness reduction factor for different walls if equal-area-under-the-curve approach is used to determine effective stiffness from the upper-bound and lower-bound force - displacement curves shown in Figure 3.8 and Figure 3.9, respectively. Also shown in Figure 3.16 is the stiffness reduction factors determined from time history analysis.

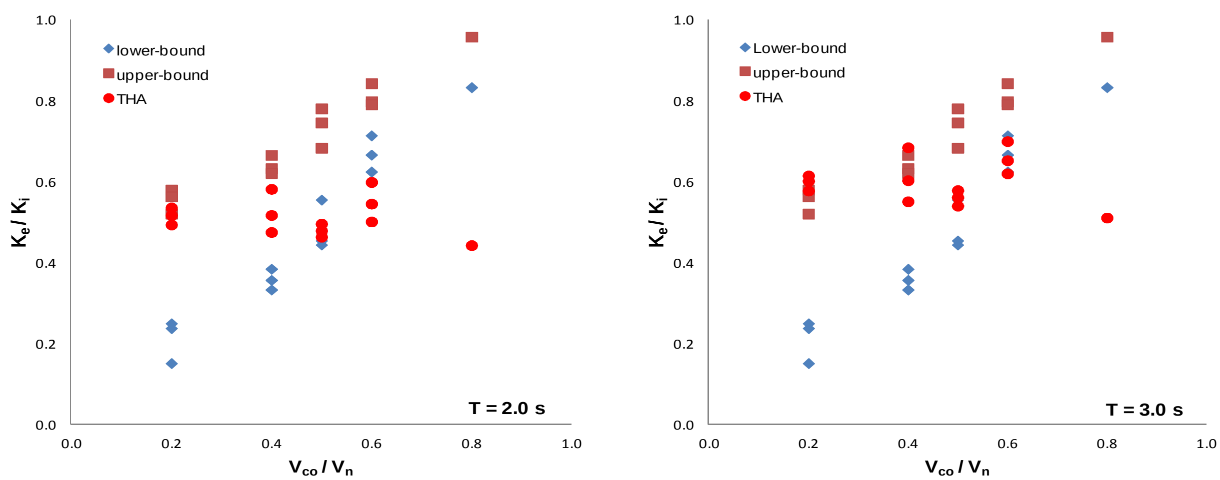

Figure 3.16 Comparison of stiffness reduction factors determined using equal-area-under-the-curve approach for upper-bound and lower-bound curves with stiffness reduction factors from time history analysis (denoted as THA) for 13 walls with R = 5.0 using spectrum matched ground motions.

It should be noted that stiffness reduction factors determined using upper-bound and lower- bound curves are proportional to the axial compression force level, i.e., the corresponding effective stiffness for the two curves increases as axial compression force increases. Stiffness reduction factors from time history analysis, on the other hand, are relatively constant as the axial compression force applied to the walls increases. This implies that the effective stiffness determined from time history results is not correlated to the wall axial compression force. Note that equal-area-under-the-curve approach gives the highest stiffness reduction factor for W-L8-

R2, while the lowest effective stiffness within thirteen walls belongs to this wall if effective stiffness is obtained from peak displacement demands from time history analysis.

It can be concluded that the ratio of elastic force demand to strength *R* has the highest influence on effective stiffness. As *R* increases from 1.0 to 5.0, stiffness reduction factor reduces from 1.0 to a value which is not generally less than 0.5 for spectrum matched ground motions. It was shown that for walls with longer periods, stiffness reduction factor is relatively independent of *R*. It was also observed that stiffness reduction factor does not depend on the period for *R* values less than 3.0. Ground motion scaling method can influence the results, but the resulting stiffness reduction factors from spectrum matched ground motions and ground motions scaled to the UHS over the range of periods were similar. Axial compression stress ratio was found to have much less influence on the effective stiffness than previously thought. Opposite to what was expected, the wall with the highest axial compression stress ratio $P/f_c'A_g$ was found to have the lowest effective stiffness because the wall had smaller hysteretic loops. Smaller hysteretic loops results in lower hysteretic energy dissipation and thus higher displacement demands.

3.4 Additional Considerations

The following analysis results are presented in this section: influence of the unloading point on the wall displacement, effective stiffness using simplified force - displacement models, and the influence of tension stiffening on effective stiffness.

3.4.1 Influence of Unloading Point on Displacement Demands

This section studies how much the variation of the unloading point influences displacement demands and hence effective stiffness of a shear wall. This was done by comparing mean displacement demands of the two walls having the same force - displacement characteristics except different crack closing (V_{cc}) points. Since the 13 shear walls listed in Table 3.1 have very different characteristics, an additional walls was created for this purpose. The additional wall, labeled W-L5-R3A, has the same characteristics as the wall W-L5-R3 except that the crack closing point for this wall was changed from $0.15V_n$ to $0.3V_n$. The period for both walls was assumed to be 2 seconds, and stiffness reduction factors were determined from mean displacements using spectrum matched ground motions. Figure 3.17 shows the results for the two walls.

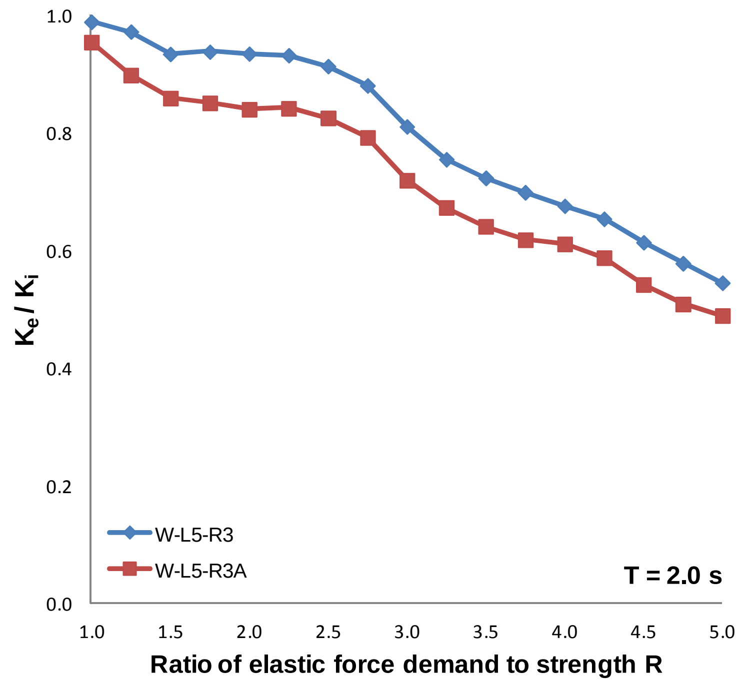

Figure 3.17 Comparison of stiffness reduction factor for two walls with different unloading characteristics.

Figure 3.17 indicates that stiffness reduction factors for wall W-L5-R3A are consistently lower than those for wall W-L5-R3. At R = 5.0, stiffness reduction factor dropped from 0.54 for W-L5-R3 to 0.49 for W-L5-R3A. Different unloading characteristic is the reason for this decrease in effective stiffness since both walls possess same loading characteristics. Wall W-L5-R3 has larger hysteretic loops between loading and unloading curves, which increases the amount of hysteretic energy dissipated by this wall compared to wall W-L5-R3A. The wall with lower hysteretic energy dissipation will experience higher displacements, which in turn results in lower stiffness reduction factors.

3.4.2 Effective Stiffness Using Simplified Force - Displacement Models

In this part, two simplified force - displacement models were used: elastic-perfectly-plastic (EPP) and nonlinear-elastic (NE) models. The first one is a basic model with large hysteretic loops and can be used to model the hysteretic behaviour of well detailed reinforced concrete beams, while the second one exhibits no hysteretic energy dissipation and can be used to model the rocking behaviour. Figure 3.18 shows a schematic of these models.

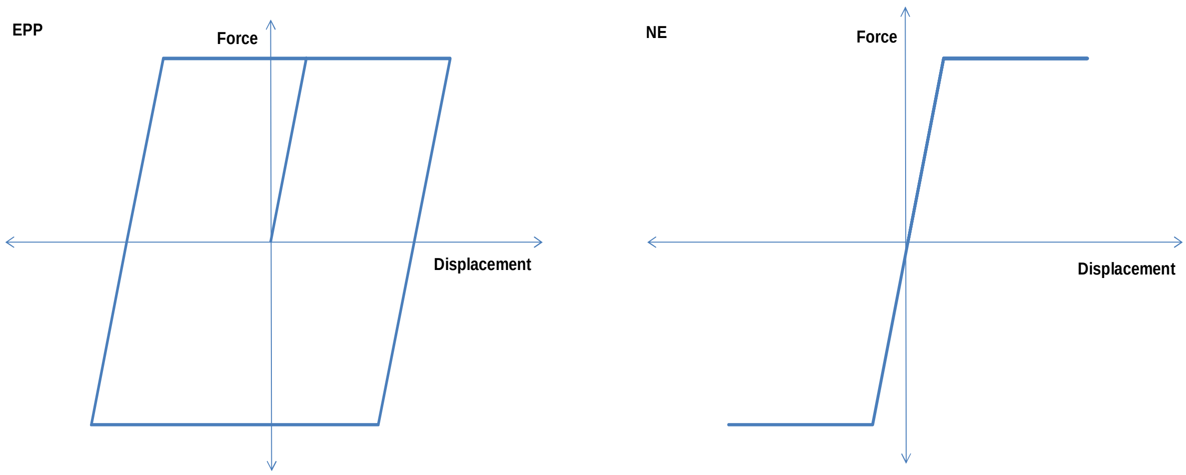

Figure 3.18 Elastic-perfectly-plastic (EPP) and nonlinear-elastic (NE) force - displacement models.

Figure 3.19 shows the variation of stiffness reduction factor for five periods ranging from 2.0 to 4.0 seconds using EPP and NE models and spectrum matched ground motions. For both models, stiffness reduction factor is equal to 1.0 for R = 1.0. For higher R values, stiffness reduction values corresponding to the EPP model are greater than 1.0 indicating that the mean nonlinear displacements are less than the corresponding elastic displacements. Low displacements could be attributed to high hysteretic energy dissipation for the EPP relationship. Stiffness reduction factors corresponding to the NE model, on the other hand, drops from 1.0 to 0.34 for T = 2.0 seconds and from 1.0 to 0.61 for T = 4.0 seconds. In fact, these stiffness reduction factors are lower than those for the 13 walls presented in Figure 3.10 and Figure 3.12 for periods of 2.0 and 4.0 seconds, respectively. High nonlinear displacements are due to zero hysteretic energy dissipation for the NE model.

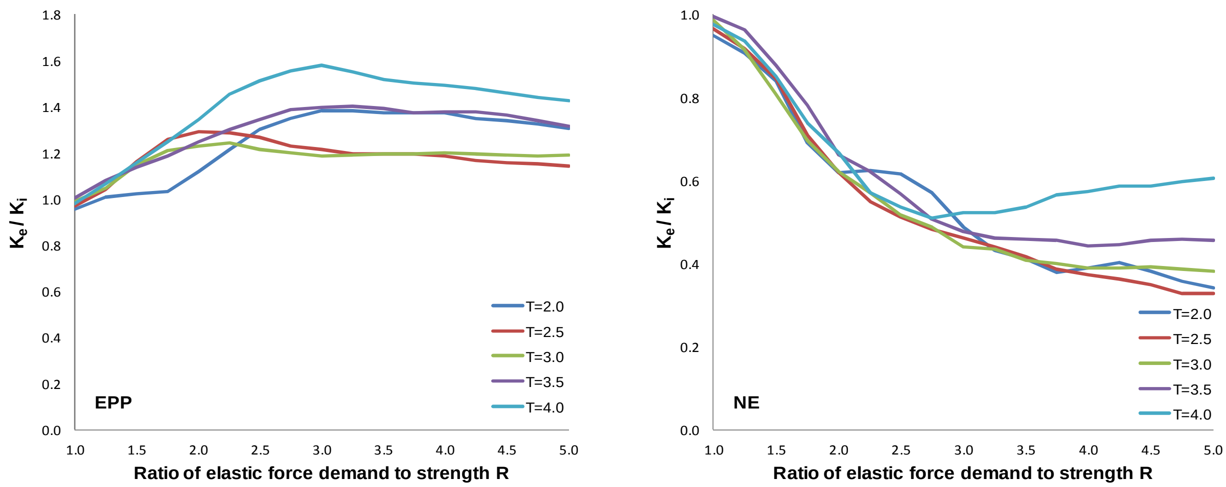

Figure 3.19 Stiffness reduction factor for walls with different periods and force reduction factors using EPP and NE force - displacement models.

3.4.3 Influence of Tension Stiffening on Effective Stiffness

It is well known that once the reinforced concrete cracks, some tension stresses are still carried by the concrete between two adjacent cracks because of the bond between concrete and reinforcing steel. This increases the average stiffness of the reinforced concrete element and is known as tension stiffening. It is interesting to investigate the influence of tension stiffening on the effective stiffness of concrete walls. The details of the tension stiffening model mainly changes the characteristics of the backbone segment of the force - displacement relationship since tension stiffening in concrete tends to diminish as the concrete becomes severely damaged and the reinforcement yields. As a result, a convenient way to study the influence of tension stiffening on the effective stiffness would be to change the characteristics of the backbone curve (upper-bound segment as shown in Figure 3.3) without changing other key points. For this purpose, the wall W-L4-R1 was selected and two additional walls - labelled W-L4-R1A and W-L4-R1B - were created with the key points of the force - displacement relationship that are identical to those for wall W-L4-R1, except that the upper-bound yield displacement Δ_{yUB} for W-L4-R1A and W-L4-R1B is 0.5 times and 1.5 times the upper-bound yield displacement for W-L4-R1, respectively. Figure 3.20 shows the upper-bound curve for the three walls.

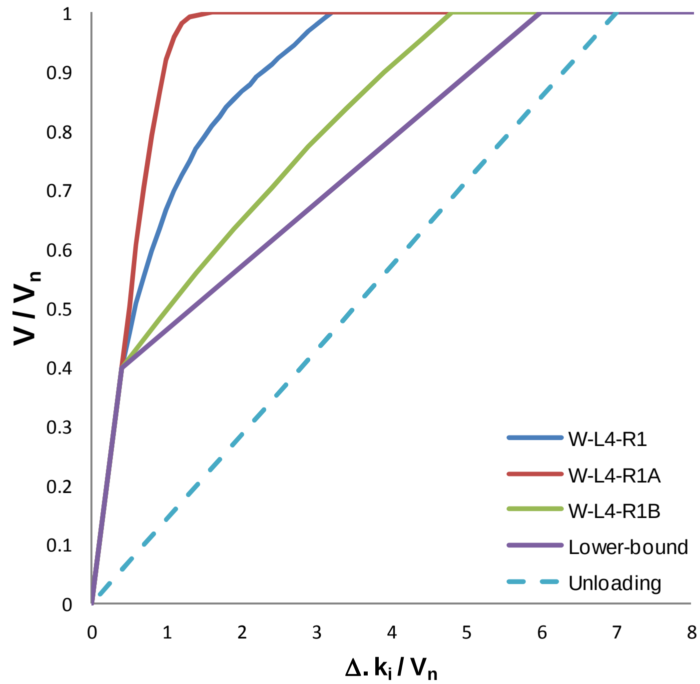

Figure 3.20 Comparison of upper-bound force - displacement relationship for the three walls.

The three walls were subjected to the suite of spectrum matched ground motions. A period of 2 seconds was assumed for the three walls, and the *R* factor varied from 1.0 to 5.0. Figure 3.21 presents the variation of stiffness reduction factor for the three walls. Figure 3.21 shows that tension stiffness has minor impact on the effective stiffness for *R* values less than 1.5. This is because maximum displacement for the three walls was less than the upper-bound yield displacement for wall W-L4-R1. The three walls have similar force - displacement characteristics in this range of displacement demands as they possess identical unloading points. As a result, variation of upper-bound response had minor influence on displacement demand and effective stiffness. For *R* = 5.0, stiffness reduction factor varied from 0.46 for W-L4-R1 to 0.52 for W-L4-R1A and 0.43 for W-L4-R1B, which is relatively small given the big difference between the upper-bound curves for the three walls. This is due to the fact that the three walls already reached the lower-bound response and therefore details of upper-bound response had slight influence on deformation demands and effective stiffness. This situation can be analogous to a severely damaged shear wall where there is no tensile stresses in the concrete. For *R* values between 2.0 and 3.5, tension stiffening has the biggest impact on the effective stiffness because the response of the three walls oscillated between the upper-bound and the lower-bound responses. The wall with lowest hysteretic energy dissipation (W-L4-R1B) had the highest displacement and lowest effective stiffness, while the wall with highest hysteretic energy dissipation (W-L4-R1A) had the lowest displacement and highest effective stiffness.

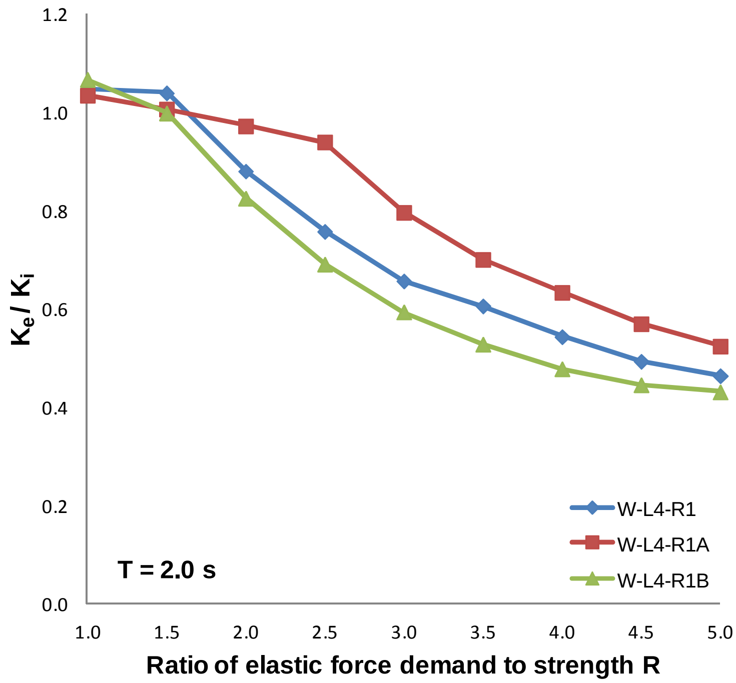

Figure 3.21 Stiffness reduction factor versus force reduction factor R for the three walls using spectrum matched ground motions.

3.5 Summary and Conclusions

Roof displacement demands from nonlinear time history analysis were used to develop appropriate effective stiffness values to be used in a linear dynamic - response spectrum - analysis. The effective flexural stiffness of a concrete shear wall is normally thought to increase with the level of axial compression applied to the wall because compression increases the bending moment to cause flexural cracking. The results of this study indicate that axial compression stress had much less influence on the effective stiffness. In fact, the wall with the highest axial compression stress ratio actually had the lowest effective stiffness because the wall had proportionally less hysteretic energy dissipation (See Figures 3.10 through 3.12).

It was found that an important parameter that influences effective stiffness is the ratio of elastic force demand to strength *R*. It was observed as *R* increases from 1.0 to 5.0, stiffness reduction factor reduces from 1.0 to a value which is not generally less than 0.5 for spectrum matched ground motions. Ground motion scaling method can influence the results, but the resulting stiffness reduction factors from spectrum matched ground motions and ground motions scaled to the UHS over the range of periods were similar.

Chapter 4 : Influence of Ground Motion Selection and Scaling on Seismic Response of Cantilever Shear Walls

4.1 Introduction

Nonlinear time history analysis is the most rigorous method to estimate demands on structures due to earthquakes. It is used by researchers to investigate the seismic response of structures and it is increasingly used by design engineers undertaking performance-based earthquake engineering design. It is well known that selection and scaling of ground motions can greatly influence the results of nonlinear time history analysis. Of particular interest with high-rise cantilever wall buildings are: (i) maximum wall displacements at the top of buildings, which strongly correlate to many other demand parameters; (ii) maximum interstory drifts over the height, which strongly influence demands on the gravity-frame systems, e.g., punching shear failure of slabs around gravity-load columns; (iii) maximum wall curvatures at the base and near midheight, which directly influence maximum compression strains in concrete and maximum tension strains in vertical wall reinforcing steel, and; (iv) wall base shear force, which must be known in order to design a wall with a ductile response. Inappropriate selection and scaling of ground motions for high-rise concrete cantilever walls can result, for example, in a large overestimation of the influence of higher modes on the base shear and on the midheight curvatures of the wall.

In the current chapter, the influence of different methods to select and scale ground motions is investigated for 11 different high-rise cantilever shear walls that are 10, 30 or 50 stories high, and are designed for different force reduction factors. This includes: 1) amplitude scaling the ground motions to match a uniform hazard spectrum (UHS) at the fundamental period and over a prescribed range of periods; 2) spectrum matching the motions to the UHS; 3) matching the ground motions to conditional mean spectrum (CMS). The influence of conditioning period for computing CMS on different demand parameters is investigated. The adequacy of choosing a set of seven ground motions to establish the mean response for design purposes is also examined.

4.2 Literature Review

Input ground motions to perform time history analysis are usually selected based on the magnitude and distance of a potential earthquake happening at the site - which can be determined from probabilistic seismic hazard analysis (PSHA) - as well as the fault mechanism. The selected records are then scaled to match a prescribed target spectrum. In Canada, the 2005 National Building Code of Canada (NBCC 2005) provides a UHS with 2% probability of exceedance in 50 years. This UHS is also used as the input spectrum for performing response spectrum analysis (RSA) in practice. Input motions are mainly matched to the UHS in three ways: 1) scale the records to the target spectral acceleration at the fundamental period of the structure T_1; 2) scale the records to match the UHS over a range of periods; 3) spectrum matching. Individual records are characterized by 5% damped elastic spectrum. Seismic code provisions such as ASCE standard 7-05 (ASCE 2005) recommends a period range of $0.2T_1$ to $1.5T_1$ for the second method. That is, for 2-dimensional analysis, the records must be scaled such that the mean spectrum of the scaled records does not fall below the target spectrum at any point within this period range. The limit $0.2T_1$ is to ensure that important higher modes are adequately excited, while the limit $1.5T_1$ is for considering the period lengthening due to nonlinearity. Katsanos et al. (2010) recommended using T_L instead of $0.2T_1$ as the lower bound, which is the period of the highest mode of vibration for which the activated mass is about 90% of total, and $2T_1$ as the upper bound for the structures that are located in the regions with high seismic intensities. The idea of scaling the records over the range of periods seems to be more rational than scaling at the fundamental period since it considers a wider range for spectral accelerations that can possibly influence different response parameters.

Spectrum matching is a process in which the frequency content of the input motions is altered to artificially match the response spectrum of individual records to the target spectrum. There are different algorithms and softwares available to generate spectrum match records (RSPMatch, Abrahamson 1992; SYNTH, Naumoski 2001; Atkinson 2009). The advantage of using spectrum matched records is that the variability of the demand parameters is substantially reduced, i.e. fewer records can be used to estimate the mean response (Watson-Lamprey and Abrahamson 2006). Similar to the second method of scaling described above, spectrum matched records can be generated to match the target spectrum over a prescribed range of periods. ATC

82 (2011) observed that scatter of demand parameters can be further reduced by matching the ground motions over a larger period range from $0.02T_1$ to $3T_1$. Huang et al. (2011) concluded that compared to the real records, spectrum matched records underestimate the mean displacement of highly inelastic single-degree-of-freedom (SDOF) oscillators. Furthermore, they cannot be used to establish the distribution of structural response if the input motions are matched to the mean target spectrum. In order to estimate the distribution of demand parameters using spectrum matched records, Hancock et al. (2008) used 84^{th}-percentile spectrum as the target spectrum instead of the mean spectrum.

Both SDOF oscillators and multi-degree-of-freedom (MDOF) buildings were used as the structural model in assessing the influence of record selection and scaling method on demand parameters. Luco and Bazzurro (2007) compared inelastic displacement demands for SDOF oscillators (with elastic periods between 0.1 second and 4.0 seconds and force reduction factors of 2, 4, 6, 8, and 10) and maximum interstory drift as well as global drift ratio for a 9 story steel moment resisting frame with a fundamental period of 2.3 seconds using scaled records with those corresponding to unscaled motions. The input motions had a moment magnitude M_w between 6.4 and 7.6 and closest source to site distance between 0 and 50 km. Bias was defined as the ratio of the median response parameter from the scaled records to that associated with unscaled records possessing a target spectral acceleration without scaling. Luco and Bazzurro demonstrated that scaling introduced bias in maximum interstory drift ratio and the bias tend to increase as the scale factor increased. It was also concluded that the amount of bias depends on the period of the structure, force reduction factor, and the response parameter under investigation.

Kurama and Farrow (2003) studied the effectiveness of different scaling methods in reducing the scatter in maximum displacement demand. Peak ground acceleration (PGA), Arias intensity-based parameter, effective peak velocity, spectral acceleration at the fundamental period, and spectral acceleration over a range of periods were considered as target intensity measures. Both SDOF oscillators (with different hysteretic models and force reduction factors of 1, 2, 4, 6, and 8) and MDOF buildings (4 and 8 story concrete moment resisting frames with fundamental periods of 0.49 and 0.87 second, respectively) were included in the study. A subset of records compiled for SAC steel project (Somerville 1997) was used as the input motion. Kurama and Farrow concluded that for soil site class C and D, scaling over a range of periods is more effective than scaling at the fundamental period, and substantially more effective than scaling to the target PGA in reducing the scatter particularly for larger force reduction factors. It was also observed that the hysteretic type did not affect the maximum displacement demand significantly, while soil type can influence the amount of dispersion for a given scaling method.

Heo et al. (2011) investigated the influence of two scaling methods on the seismic response of 4 story and 12 story concrete frame buildings with fundamental periods of 0.88 and 2.1 seconds, respectively: scaling the records to the ASCE7-05 design spectrum at the fundamental period of the buildings, and spectrum matching. A benchmark was developed by carrying out regression analysis through a complete set of 200 time history analysis to relate maximum interstory drift ratio to the spectral acceleration at different modal periods. It was demonstrated that interstory drifts using spectrum matched records were closer to the predictions from the regression model than those from the records scaled at the fundamental period. The authors stated that further study is required to refine the regression model by including more intensity measures in addition to spectral accelerations at the elastic modal periods. Also, more demand parameters in addition to maximum interstory drift ratio need to be considered.

Wood and Hutchinson (2010) investigated the influence of three ground motion scaling methods: (a) scaling between zero and four seconds, (b) scaling between the first and second modal periods, and (c) scaling at the fundamental period on the seismic response of 8, 12, and 20 story concrete frames with fundamental periods of 0.89, 1.33, and 2.07 seconds, respectively. Note that the first scaling method is similar to the recommended period range of $0.2T_1$ to $1.5T_1$ specified by the ASCE7-05 standard. A set of 21 ground motions with moment magnitude M_w between 5.5 and 7.35 and closest source to site distance between 2 and 25 km was scaled to the ASCE7-05 design spectrum using the mentioned scaling methods. Maximum floor acceleration, maximum interstory drift ratio, and maximum plastic rotation were considered as the response parameters of interest. The results of the study indicated that using the third scaling method resulted in more pronounced higher mode effects especially for the tallest frame, while the response parameters from the first and second scaling methods were reasonably close.

Naeim and Lew (1995) questioned validity of using UHS as the target spectrum for scaling ground motions since it is the envelope to spectral accelerations at different periods that will not necessarily occur within a single motion. Baker and Cornell (2006) proposed Conditional Mean Spectrum (CMS), which accounts for the correlation between spectral accelerations at other periods given a target spectral acceleration at the period of interest. Baker (2011) summarized a step by step procedure for computing the CMS. The procedure involves de-aggregation of the UHS to estimate the mean magnitude and mean distance for a specific conditioning period and return period, computing the mean and standard deviation of spectral accelerations using an attenuation model, and calculating the correlation between spectral accelerations at other periods and the conditioning period. The computed CMS will then be used as the target spectrum to select motions for use in time history analysis. Baker (2011) indicated that response parameters corresponding to the ground motions scaled and matched to the CMS are closer to the response parameters from unscaled records that have spectral accelerations equal to the target spectral acceleration at the conditioning period. Jayaram et al. (2011) extended the idea of Conditional Mean Spectrum to Conditional Spectrum (CS) in order to capture the variability in the input motions having a target mean spectrum. Selecting and matching the records to the CS results in a more accurate prediction of the variability in the demand parameters. Jayaram et al. (2011) studied the displacement demands for SDOF oscillators (with an elastic period of 0.5 second and force reduction factors of 1, 4, and 8) and maximum interstory drift ratio for MDOF structures (4 and 20 story concrete moment resisting frames with fundamental periods of 0.94 and 2.63 seconds, respectively). They concluded that time history results using ground motions selected and matched to the CS had slightly higher mean but considerably larger scatter compared to the time history results from a set of records for which only the mean spectrum matched the prescribed CMS.

The Ground Motion Selection and Modification (GMSM) program at the Pacific Earthquake Engineering Research centre (PEER) published a comprehensive report (PEER GMSM, Haselton et al. 2009) with the aim of evaluating different ground motion selection schemes and comparing the structural response using various sets of records with a benchmark model. Median maximum interstory drift ratio was considered as the response parameter of interest, and several ground motion scaling methods were considered including scaling to the target spectral acceleration at fundamental period, scaling to the UHS over a period range of $0.2T_1$ to $1.5T_1$, and scaling to the CMS computed at the fundamental period T_1. Several bins of records were used for each scaling scheme in order to better observe the variation of the interstory drift within different sets of records selected for each scaling method. The structural systems considered in the study included three reinforced concrete frames and one reinforced concrete shear wall. The concrete frames were 4, 12, and 20 story structures with fundamental periods of 0.97, 2.01, and 2.63 seconds, while the concrete shear wall had 12 stories with a fundamental period of 1.2 second. The findings for the 12 story shear wall indicated that all groups of records, except records scaled to the CMS, tend to overestimate the median interstory drift ratio compared to the prediction from the benchmark model. It was observed that scaling to the spectral acceleration at fundamental period leads to an overestimation of median response by 29%, while scaling to the CMS underestimates the median response by only 5%.

The ATC 82 (2011) project covers guidelines for selecting, scaling, and spectrum matching the ground motions for time history analysis. The UHS, CMS, and CS were considered as possible target spectrums, while scaling techniques included scaling at a target period, scaling over a range of periods, and spectrum matching. For scaling over the range, it was suggested to increase the ASCE7-05 upper bound limit of $1.5T_1$ to $2.5T_1$ for frame structures in order to better represent the period lengthening due to nonlinearity. The CMS and CS were considered as more realistic target spectrums to scale the input motions. The former can be used to provide unbiased predictions of the mean demand parameters, while the latter provides a tool to predict the mean and variability in the response parameters. ATC 82 stated that the UHS can be used as the target spectrum if it is not known which conditioning period gives highest demand parameters, although using the UHS as the target spectrum results in conservative estimates of the demand parameters. Furthermore, a parametric study was carried out to investigate the influence of conditioning period on maximum interstory drift ratio and maximum peak floor acceleration (*PFA*) for 1 to 20 story concrete moment resisting frames. Four conditioning periods of the first mode period T_1, $2T_1$, and higher mode periods of T_2 and T_3 were considered for each building. The results for the 20 story frame indicated that the drift hazard curves – annual probability of exceedance versus maximum interstory drift - corresponding to different conditioning periods are similar. On the other hand, the median interstory drift and *PFA* varied as the conditioning period changed: T_1 and $2T_1$ produced the highest median interstory drift values at smaller and larger return periods, while the third elastic mode period, T_3, resulted in the largest *PFA* response. Finally, the ATC 82 project compared demand parameters from spectrum matched ground motions with those from the records matched to the CMS and the benchmark model predictions. It was observed that the records matched to the UHS produced slightly higher median interstory drifts than the other two sets of records for a 12 story concrete moment frame with a fundamental period of 2.01 seconds. Furthermore, spectrum matching over a wider range of periods reduced the variability in the response parameters. Based on a limited amount of data, it was suggested to perform spectrum matching over a period range from $0.02T_1$ to $3T_1$. The upper bound limit of $3T_1$ and the lower bound limit of $0.02T_1$ are considered to reduce the variability in first-mode and higher-mode dominated demand parameters, respectively.

Most of the studies carried out thus far on the ground motion selection and scaling methods considered medium-rise concrete moment resisting frames as the structural model and maximum interstory drift ratio as the response parameter of interest. The GMSM program was the only study which investigated the sensitivity of the maximum interstory drift ratio of a 12 story concrete shear wall corresponding to the records scaled to the UHS and the CMS computed at the fundamental period. The influence of ground motion scaling on the seismic response of high-rise shear walls and the sensitivity of other demand parameters to the scaling method still need to be examined. Particularly, the sensitivity of first-mode dominated and higher-mode dominated response parameters to various scaling schemes and conditioning periods is investigated in this work. The variability in the structural response using different sets of records is also studied. Finally, the adequacy of ASCE7-05 rules for choosing seven ground motions to estimate the mean design quantities are discussed.

4.3 Selection and Scaling of Ground Motions to UHS

The input ground motions in this section are scaled to the uniform hazard spectrum (UHS) shown in Figure 2.25. The UHS is similar to the design spectrum for Vancouver, BC and ASCE7-05 design spectrum for Seattle, WA. Summary of ground motions and scaling methods are presented hereafter.

4.3.1 Summary of Ground Motions

Ground motions used in this work were selected from the PEER Next Generation Attenuation (NGA) strong motion database (PEER 2010). Eighty records were selected from 23 different earthquakes with the following criteria:

1- Moment magnitude (M_w) between 6.5 and 8.0.
2- Closest source to site distance (R) between 0.5 km and 50 km.
3- Motions were recorded on site class B, C, and D according to NBCC 2005 guidelines (average shear wave velocity V_s between 180 and 1500 m/s).

4- Longest usable period greater than 8.0 seconds.

The first and second criteria were established based on the mean magnitude and source to site distance determined from de-aggregation of the UHS using computer program EZ-FRISK (Risk Engineering Inc. 2010). To extract the mean magnitude and mean distance values, *R* model sources within 200 km from Vancouver were considered as seismic source zones. Table 4.1 shows the de-aggregation results.

Table 4.1 Mean magnitude and mean source to site distance from de-aggregation of the UHS.

Period (s)	**S_a (g)[1]**	**M_{mean}[2]**	**R_{mean} (km)[3]**
0.15	0.97	6.50	52.0
0.28	0.86	6.50	49.1
0.50	0.64	6.67	54.3
0.80	0.47	6.81	52.7
1.0	0.33	6.91	51.6
1.5	0.26	6.98	46.4
2.0	0.17	6.98	49.4
3.0	0.12	6.99	47.9
5.0	0.07	6.99	47.9

[1] spectral acceleration at a given period, [2] M_{mean} = mean magnitude, and [3] R_{mean} = mean source to site distance.

Shome and Cornell (1998) and Baker and Cornell (2005) studied the dependence of structural response to moment magnitude M_w and source to site distance R of the input motions, and they concluded that there is not a strong correlation between structural response parameters and the source to site distance. Therefore, in order to increase the number of strong motion records to be used in this study, the range of the source to site distance values was broadened (Atkinson, personal communication 2010). As a result, the chosen source to site distance range (0.5 km < R < 50 km) is different from the mean distance values determined from the de-aggregation. The fourth criterion was established to make sure that the ground motions have a minimum longest usable period of 8.0 seconds, which is slightly more than 1.5 times the fundamental period of the tallest building in the study (5.0 seconds for 50 story walls). Of the selected 80 records, 40 have R between 0.5 and 20 km, while the remaining 40 have R between 20 and 50 km. Among these 80 records, 51 of the ground motions were recorded in the U.S and Canada, 9 were recorded in Taiwan, 8 in Turkey, 5 in Japan, 3 in each of Iran and Italy, and 1 in

Jordan. Peak ground accelerations varied from 0.075g to 1.66g. Table 4.2 summarizes the ground motion details.

Table 4.2 Ground motion details.

Event	Station	M_w[1]	R^2 (km)	PGA (g)	V_s (m/s)	Max T[3]
Imperial Valley, 1979	Agrarias	6.53	0.65	0.2903	274.5	15.9
Imperial Valley, 1979	Bonds Corner	6.53	2.68	0.6861	223.0	8.0
Imperial Valley, 1979	El Centro Array #4	6.53	7.05	0.3745	208.9	8.0
Superstition Hills,	Parachute Test Site	6.54	0.95	0.4509	348.7	13.3
Superstition Hills,	Brawley Airport	6.54	17.03	0.1349	208.7	8.0
Superstition Hills,	Poe Road (temp)	6.54	11.16	0.3629	207.5	11.4
Kobe, Japan, 1995	Nishi-Akashi	6.90	7.08	0.4862	609.0	8.0
Kobe, Japan, 1995	KJMA	6.90	0.96	0.7105	312.0	15.9
Kobe, Japan, 1995	Shin-Osaka	6.90	19.15	0.2293	256.0	10.0
Erzican, Turkey 1992	Erzincan	6.69	4.38	0.4886	274.5	8.0
Irpinia, Italy, 1980	Sturno	6.90	10.84	0.2898	1000.0	10.0
Nahanni, Canada,	Site 3	6.76	5.32	0.1512	659.6	15.9
Nahanni, Canada,	Site 2	6.76	4.93	0.3849	659.6	15.9
Nahanni, Canada,	Site 1	6.76	9.60	1.0556	659.6	15.9
Northridge, 1994	Canoga Park - Topanga Can	6.69	14.70	0.3764	267.5	15.9
Northridge, 1994	Tarzana - Cedar Hill A	6.69	15.60	1.6615	257.2	10.0
Northridge, 1994	Newhall - W Pico Canyon	6.69	5.48	0.3848	285.9	15.9
Loma Prieta, 1989	UCSC 14 WAHO	6.93	17.47	0.5174	376.1	8.0
Loma Prieta, 1989	UCSC 16 LGPC	6.93	3.88	0.7835	477.7	8.0
Loma Prieta, 1989	Gilroy Array #3	6.93	12.82	0.4621	349.9	8.0
Imperial Valley, 1979	Delta	6.53	22.03	0.2849	274.5	15.9
Imperial Valley, 1979	Victoria	6.53	31.92	0.1353	274.5	15.9
Imperial Valley, 1979	El Centro Array #1	6.53	21.68	0.1418	237.3	8.0
Imperial Valley, 1979	Superstition Mtn Camera	6.53	24.61	0.1598	362.4	8.0
Superstition Hills,	Wildlife Liquef. Array	6.54	23.85	0.1914	207.5	8.0
Kobe, Japan, 1995	Kakogawa	6.90	22.50	0.2668	312.0	8.0
Kobe, Japan, 1995	OSAJ	6.90	21.35	0.0762	256.0	15.9
Irpinia, Italy, 1980	Bisaccia	6.90	21.26	0.0888	1000.0	13.3
San Fernando 1971	Gormon - Oso Pump Plant	6.61	46.78	0.0874	308.4	8.0
San Fernando 1971	Santa Felita Dam (Outlet)	6.61	24.87	0.1562	389.9	8.0
San Fernando 1971	Whittier Narrows Dam	6.61	39.45	0.1155	298.7	8.0
Friuli, Italy, 1976	Codroipo	6.50	33.40	0.0753	274.5	8.0
Northridge, 1994	Pacific Palisades – Sunset	6.69	24.08	0.3316	446.0	15.9
Northridge, 1994	Glendale - Las Palmas	6.69	22.21	0.2558	446.0	8.0
Northridge, 1994	Hollywood - Willoughby	6.69	23.07	0.1976	234.9	8.0
Northridge, 1994	Mt Wilson - CIT Seis Sta	6.69	35.88	0.1678	821.7	10.0
Northridge, 1994	LA - Griffith Park	6.69	23.77	0.2458	1015.9	8.6
Loma Prieta, 1989	Calaveras Reservoir	6.93	35.49	0.0908	513.7	8.3
Loma Prieta, 1989	Sunol - Forest Fire Station	6.93	47.57	0.0773	400.6	8.3
Loma Prieta, 1989	APEEL 10 – Skyline	6.93	41.88	0.0950	391.9	8.0
Landers, 1992	Joshua Tree	7.28	11.03	0.2489	379.3	14.3
Landers, 1992	Lucerne	7.28	2.19	0.7214	684.9	10.0
Landers, 1992	Coolwater	7.28	19.74	0.3733	271.4	8.0
Hector Mine, 1999	Hector	7.13	11.66	0.3062	684.9	40.0
Denali, Alaska, 2002	TAPS Pump Station #10	7.90	2.74	0.3243	329.4	40.0
Manjil, Iran, 1990	Abbar	7.37	12.56	0.5051	724.0	7.7
Kocaeli, Turkey,	Izmit	7.51	7.21	0.2037	811.0	8.0
Kocaeli, Turkey,	Yarimca	7.51	4.83	0.3055	297.0	11.4
Kocaeli, Turkey,	Duzce	7.51	15.37	0.3255	276.0	10.0

Event	Station	M_w[1]	R^2 (km)	PGA (g)	V_s (m/s)	Max T[3]
Duzce, Turkey, 1999	Duzce	7.14	6.58	0.4273	276.0	13.3
Duzce, Turkey, 1999	Bolu	7.14	12.04	0.7662	326.0	15.9
Cape Mendocino,	Petrolia	7.01	8.18	0.6236	712.8	14.3
Cape Mendocino,	Cape Mendocino	7.01	6.96	1.3455	513.7	14.3
Cape Mendocino,	Rio Dell Overpass – FF	7.01	14.33	0.4244	311.8	14.3
Tabas, Iran, 1978	Dayhook	7.35	13.94	0.3505	659.6	8.0
Tabas, Iran, 1978	Tabas	7.35	2.05	0.8128	766.8	15.9
Chi-Chi, Taiwan,	TCU078	7.62	8.20	0.3927	443.0	20.0
Chi-Chi, Taiwan,	TCU079	7.62	10.97	0.5290	364.0	11.4
Landers, 1992	Twentynine Palms	7.28	41.43	0.0701	684.9	8.3
Landers, 1992	Palm Springs Airport	7.28	36.15	0.0929	207.5	14.3
Landers, 1992	Desert Hot Springs	7.28	21.78	0.1407	345.4	14.3
Chi-Chi, Taiwan,	TCU071	7.62	5.31	0.6229	624.9	20.0
Chi-Chi, Taiwan,	TCU088	7.62	18.16	0.5230	553.4	20.0
Hector Mine, 1999	Joshua Tree	7.13	31.06	0.1498	379.3	10.98
Hector Mine, 1999	Amboy	7.13	43.05	0.1935	271.4	12.5
Sitka, Alaska, 1972	Sitka Observatory	7.68	34.61	0.0941	659.6	12.5
Denali, Alaska, 2002	ANSS/UA R109 R109	7.90	43.0	0.083	963.9	15.38
Gulf of Aqaba, 1995	Eilat	7.20	44.10	0.0954	354.9	8.0
Landers, 1992	Yermo Fire Station	7.28	23.62	0.2234	353.6	14.28
Landers, 1992	Barstow	7.28	34.86	0.1193	370.8	14.28
Landers, 1992	Mission Creek Fault	7.28	26.96	0.1286	345.4	15.87
Chi-Chi, Taiwan,	HWA056	7.62	41.10	0.1045	511.3	40.0
Chi-Chi, Taiwan,	TCU034	7.62	35.69	0.1991	393.8	40.0
Chi-Chi, Taiwan,	TCU042	7.62	26.32	0.2125	272.6	40.0
Kocaeli, Turkey,	Goynuk	7.51	31.74	0.1387	424.8	8.0
Duzce, Turkey, 1999	Mudurnu	7.14	34.30	0.0896	659.6	10.0
Kern County, 1952	Taft Lincoln School	7.36	38.89	0.1728	385.4	15.87
St Elias, Alaska, 1979	Icy Bay	7.54	26.46	0.1293	274.5	25.0
Chi-Chi, Taiwan,	TCU045	7.62	26.00	0.473	704.6	40.0
Chi-Chi, Taiwan,	HWA058	7.62	45.77	0.109	553.4	40.0

[1]Moment magnitude, [2]closest distance to source, [3]longest usable period.

4.3.2 Scaling of Ground Motions to the UHS

The 80 ground motions were scaled to the UHS at the fundamental period T_1 of the 10, 30, and 50 story walls, which is 1.0, 3.0, and 5.0 seconds, respectively. Figure 4.1 shows the mean spectrum of the records scaled at T_1 to the target UHS (denoted as ST1 for "scaled at T_1") as well as the target UHS. Figure 4.1 indicates that the mean spectrum of the records matches the UHS over a very wide range of periods, while scaling the ground motions to the UHS at fundamental periods of 3.0 and 5.0 seconds results in mean spectral accelerations that are as large as twice the spectral accelerations from the UHS at shorter periods. To address this issue, some of the ground motions with high spectral accelerations at short periods were eliminated. This results to a subgroup of 53 ground motions for T_1 = 3.0 seconds and 35 ground motions for T_1 = 5.0 seconds. These ground motions are referred to in this study as SOR for "scaled over range". Figure 4.2

shows the mean spectrum of the two suites of the records. It can be seen from this figure that the mean spectrum matches the UHS over a period range wider than $0.2T_1$ to $1.5T_1$ as recommended by ASCE7-05.

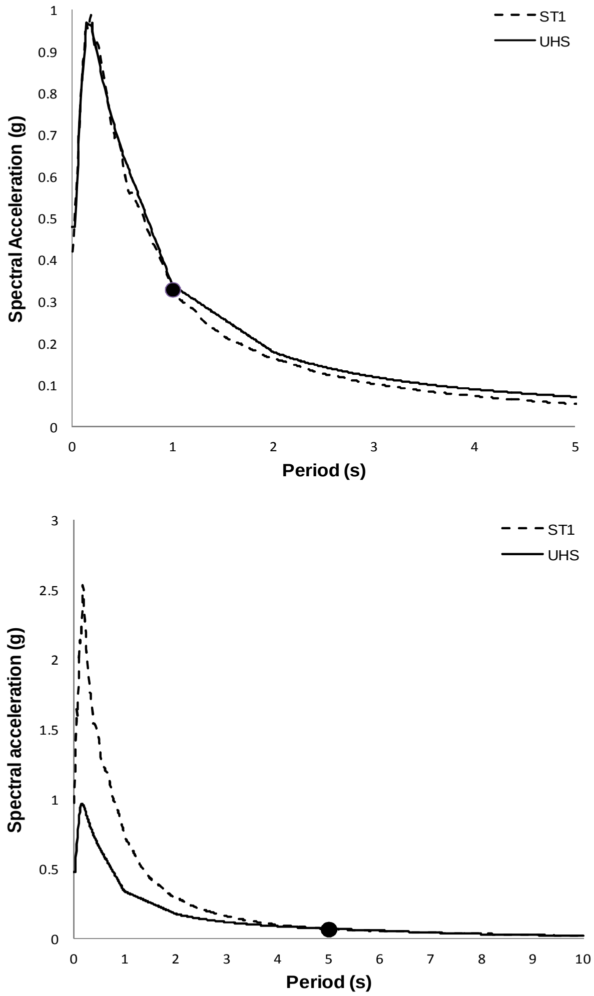

Figure 4.1 Comparison of mean spectrum of the ground motions scaled to the UHS at the fundamental period of 1.0, 3.0, and 5.0 s with the UHS.

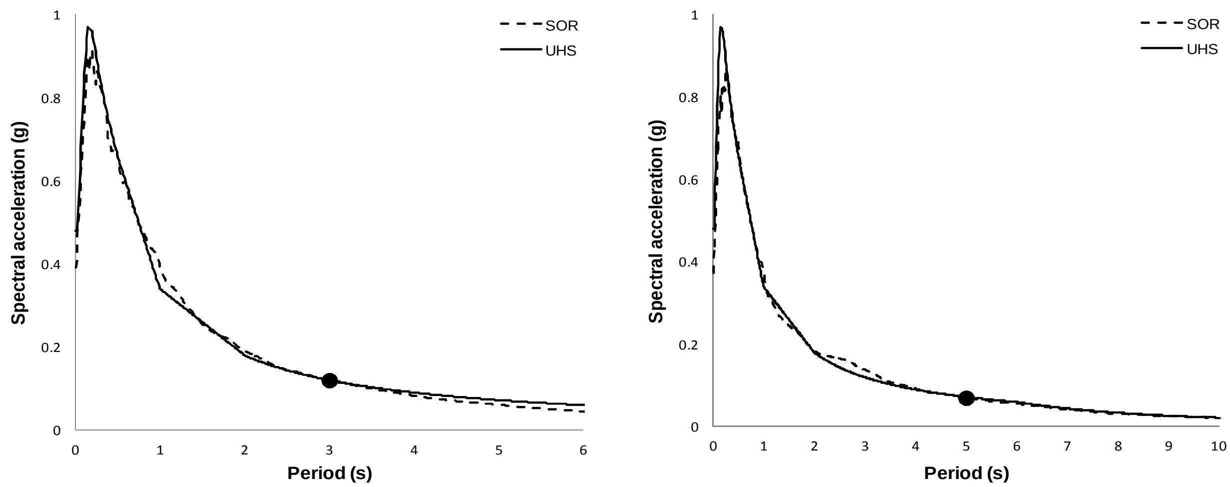

Figure 4.2 Comparison of mean spectrum of the ground motions scaled to the UHS over the range of periods for shear walls with fundamental periods of 3.0 and 5.0 s with the UHS.

Spectrum matched records were also used as input motions to perform time history analysis in this study. Forty records were randomly selected from the 80 ground motions described in section 4.3.1 and were altered to a suite of synthetic motions such that the spectrum of the individual records matched the UHS. The spectrum matched ground motions were created using computer program SYNTH (Naumoski 2001). Figure 4.3 compares the response spectra of the spectrum matched (SM) ground motions with the target UHS. There is very little deviation from the target spectrum.

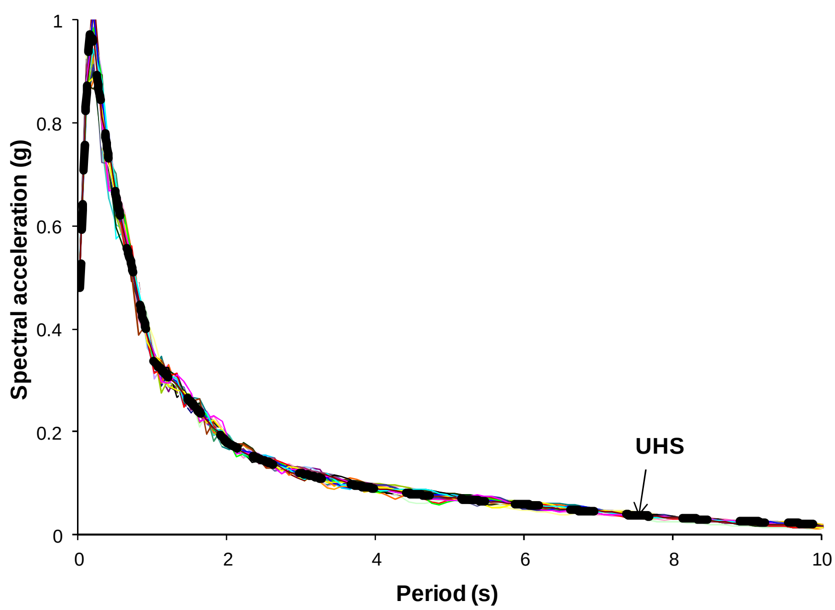

Figure 4.3 Comparison of UHS with acceleration spectra for spectrum matched ground motions.

4.4 Selection and Scaling of Ground Motions to Conditional Mean Spectrum (CMS)

Ground motions in this part were selected and scaled to match conditional mean spectrum (CMS) rather than UHS as the target spectrum. The CMS (Baker and Cornell 2006) accounts for the correlation between spectral acceleration at other periods, given a target spectral acceleration at a particular period. The equation for computing CMS is a function of the conditioning period (denoted as T^*, Baker 2011), mean and standard deviation of spectral accelerations from an attenuation model using mean magnitude and mean distance determined from de-aggregation of the UHS, and the correlation between the spectral acceleration at other periods and the conditioning period. The first step to compute CMS is to identify the conditioning period T^*. Although it is often assumed to be the fundamental period of the structure, it can be other periods depending on the structural characteristics and the response parameters to be investigated. For example, roof displacement and maximum interstory drift are deemed to be influenced mainly by first mode response, whereas higher modes contribute significantly to the base shear force. Also, it is believed that the taller the wall is, the greater higher modes would influence particular response parameters such as midheight curvature and base shear force demands. Consequently, multiple periods may need to be considered depending on the structural response to be studied. For this purpose, it was decided to include modal periods with a total modal mass equal to 90% of the total mass. Consequently, T_2 for the 10 story and T_2 and T_3 for the 30 and 50 story walls were included. Note that the second mode period for 10, 30, and 50 story walls is 0.15, 0.5, and 0.8 second, while the third mode period for 30 and 50 story walls is 0.15 and 0.28 second, respectively. In addition, two conditioning periods of $1.5T_1$ and $2T_1$ were considered for 10 story walls, which essentially represent the period elongation due to nonlinear behaviour. A period of 5.0 s was also considered for the 30 story walls for the same purpose. This conditioning period is approximately equal to 1.5 times the fundamental period of 30 story walls. Note that the maximum value for T^* is limited to 5.0 seconds since the simplified correlation model (Baker and Cornell 2006) was employed to computed the CMS. The Open source PSHA online package OpenSHA (OpenSHA 2009) was used to compute the predicted mean and standard deviation values for the Boore and Atkinson attenuation model (Boore and Atkinson 2008). Having computed the CMS, nine sets of records, each containing 40 ground motions were selected and scaled using the source code available at (http://www.stanford.edu/~bakerjw/gm_selection.html). The algorithm for this source code is developed by Jayaram et al. (2011). Figures 4.4 to 4.6 compare the UHS with the CMS computed at the fundamental periods of 1.0, 3.0, and 5.0 s as well as the CMS corresponding to other conditioning periods. Also each figure compares the mean spectrum of the ground motions selected and scaled to the CMS at various conditioning periods with the target CMS. It can be seen that the mean spectrum matches the target CMS over the period range of $0.2T_1$ to $1.5T_1$.

4.5 Example Shear Walls and Characteristics of the Analytical Model

Eleven shear walls were included in this study. That is, three 10 story walls with R_g = 1.7, 2.6, and 4.2; four 30 story walls with R_g = 1.4, 2.4, 3.1, and 4.3; and four 50 story walls with R_g = 1.4, 2.1, 2.4, and 4.1. The characteristics of these eleven shear walls are presented in Table 2.2.

Nonlinear time history analysis of the 11 shear walls was conducted in OpenSees (OpenSees 2008) using the trilinear hysteretic bending moment - curvature relationship depicted in Figure 2.20. The parameters that define the hysteretic model were calculated at each floor level considering the level of axial compression force and amount of vertical reinforcement at that level. A force element was defined at each floor level to model the vertical spread of plasticity in the walls. The base was assumed to be fixed and shear deformations were not considered in the analytical model. Rayleigh damping was assumed with mass proportional and initial stiffness matrixes. A damping ratio of 3% was assigned for the first and third modes. This is consistent with the recommendations of ATC 72 (2010) for modelling viscous damping in high-rise buildings. The time step was set equal to 0.0025, and the Newton-Raphson iteration method was used to satisfy equilibrium at each time step. Lastly, the Newmark integration method with coefficients β = 0.5 and γ = 0.25 was used in time history analysis.

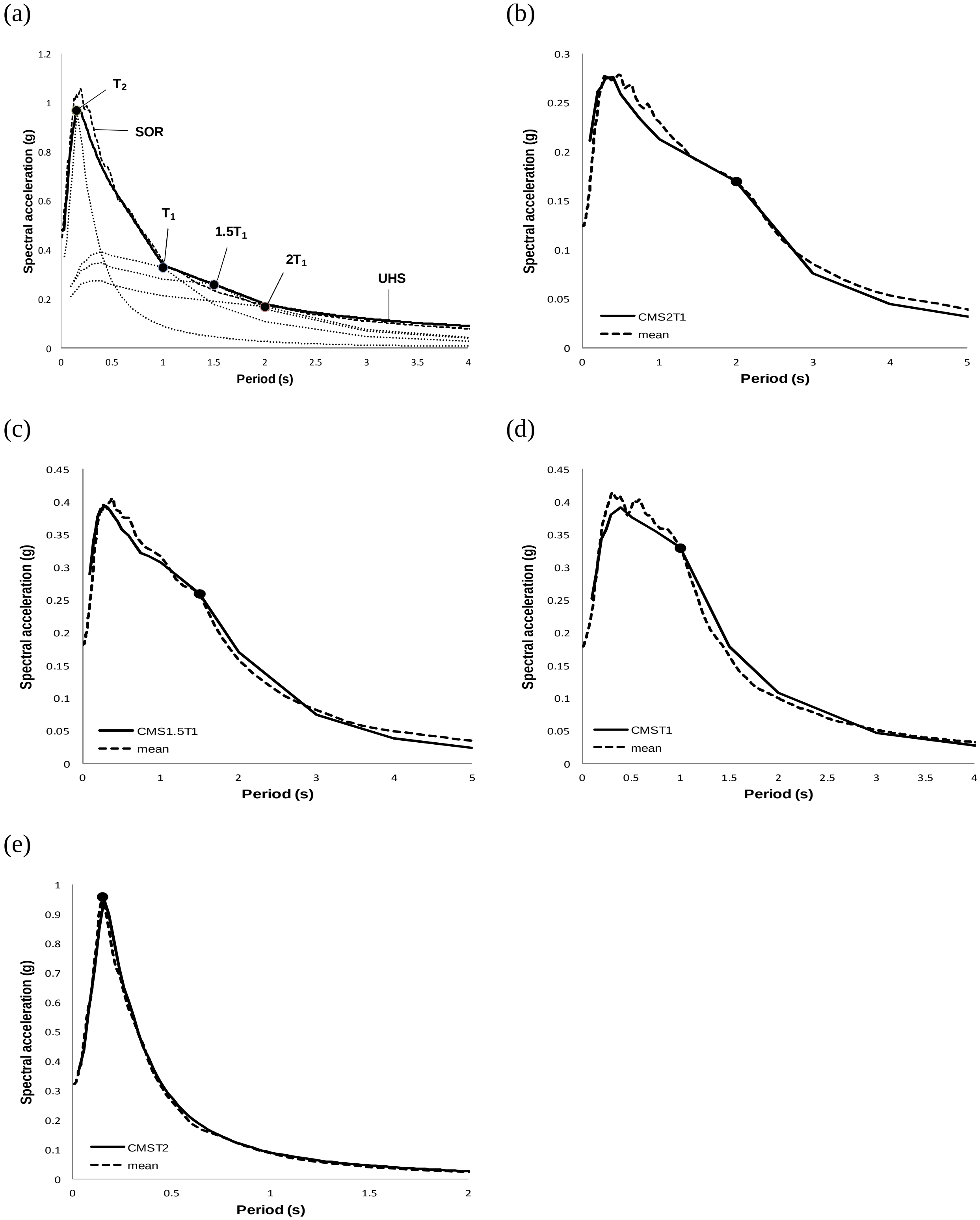

Figure 4.4 Comparison of: (a) UHS with CMS computed at different conditioning periods, (b) to (e) CMS with mean spectrum of records selected and scaled to the target CMS (T_1 = 1.0 s).

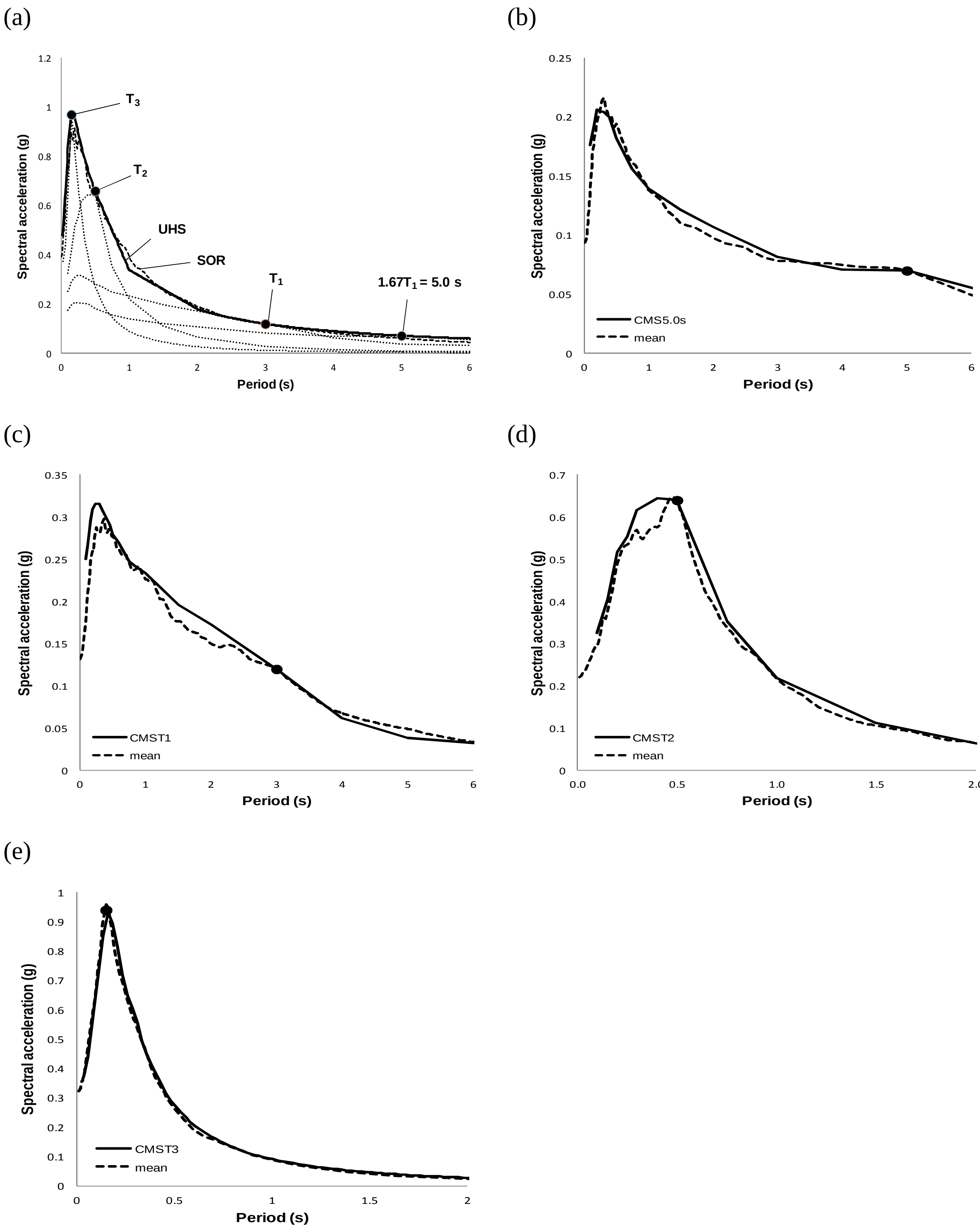

Figure 4.5 Comparison of: (a) UHS with CMS computed at different conditioning periods, (b) to (e) CMS with mean spectrum of records selected and scaled to the target CMS (T_1 = 3.0 s).

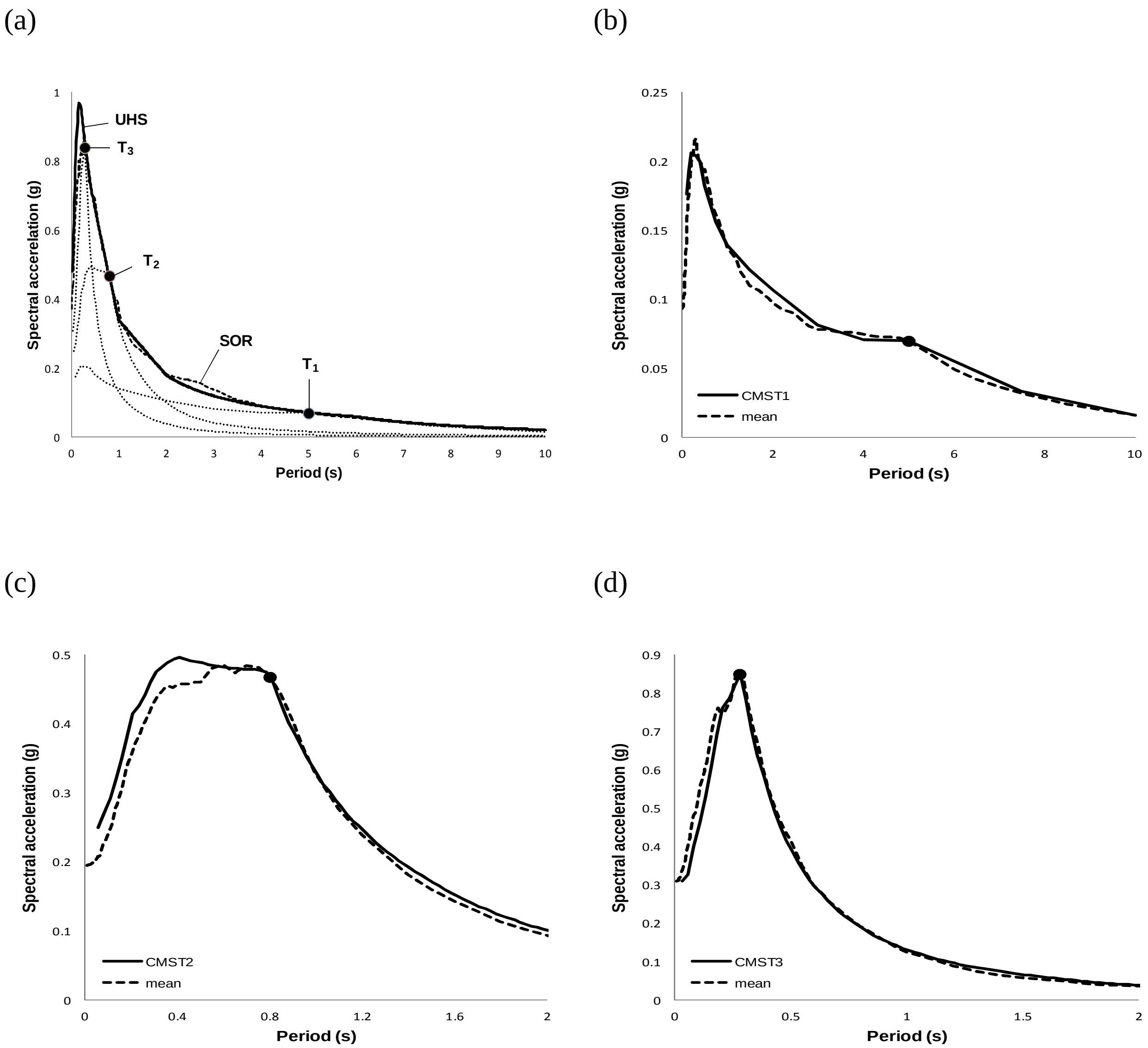

Figure 4.6 Comparison of: (a) UHS with CMS computed at different conditioning periods, (b) to (e) CMS with mean spectrum of records selected and scaled to the target CMS (T_1 = 5.0 s).

4.6 Results

The analysis results in this section are organized in two distinct parts. In Section 4.6.1, the sensitivity of various demand parameters - mean displacement, mean interstory drift, mean curvature, mean bending moment, and mean shear force envelopes - to the conditioning period T^* are examined. In Section 4.6.2, the CMS envelope associated with the largest responses (denoted as CMS-E) are compared with the results from the other three methods for scaling ground motions: ST1 = scaled to the UHS at T_1, SM = spectrum matched to the UHS, SOR = scaled to the UHS over a range of periods. The mean responses from all methods for selecting and scaling ground motions and all eleven walls are also presented in Tables 4.3 to 4.6. Note that for 10 story walls, two sets of ST1 and SOR ground motions are identical.

The following assumptions were made for interstory drift and shear force envelopes:

1. Interstory drift at elevation h_i is equal to the maximum interstory drift between elevations h_i and h_{i-1}.

2. Shear force at elevation h_i is equal to the maximum shear force demand between elevations h_i and h_{i+1}. Maximum shear force demand is constant between two adjacent floors (see Figure 4.7), while the shear force envelopes shown in Sections 4.6.1 and 4.6.2 were determined by connecting shear force demands at each elevation with a straight line.

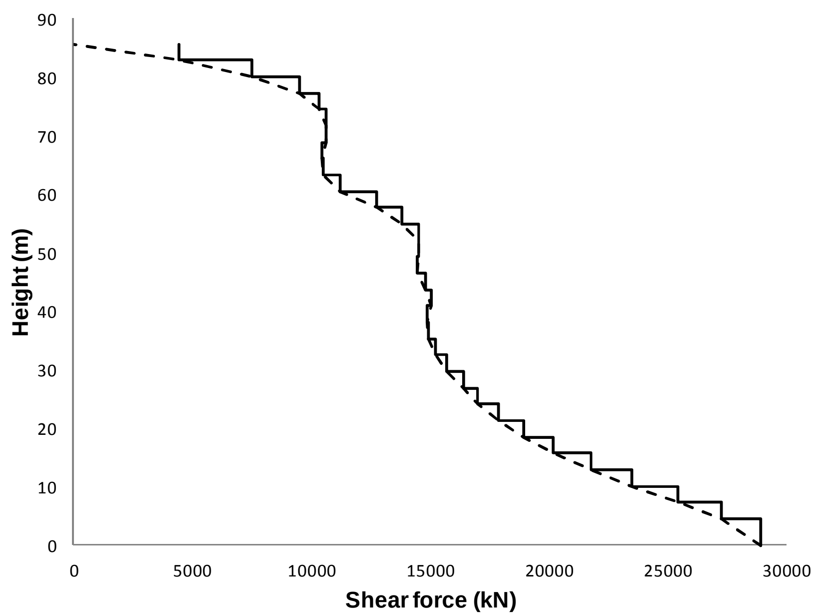

Figure 4.7 Comparison of actual mean shear force envelope (shown with a thick line) with the linear piece-wise approximation (shown with a dashed line) for the 30 story wall with R_g = 2.4 using SOR ground motions (R_g is the ratio of elastic bending moment demand at the base corresponding to EI_g to nominal flexural strength M_n).

4.6.1 Sensitivity of Response Parameters to Conditioning Period T^*

Figures 4.8 to 4.18 show the mean envelopes of various demand parameters for the eleven shear walls associated with the ground motions selected and scaled to the CMS at different conditioning periods. Note that the term "CMSTi" refers to the CMS corresponding to the conditioning period of T_i.

The following observations can be made:

1. The CMS1.5T1 set gives highest roof displacement demand for 10 story walls with force reduction factors of 2.6 and 4.2 (Figures 4.9 and 4.10). Selecting $1.5T_1$ as the conditioning period increases roof displacement demand 22% compared to the roof displacement demand from CMST1 or CMS2T1 sets for the 10 story wall with R_g = 4.2. For the 30 story walls, on the other hand, using CMST1 set gives higher roof displacement demand than the CMS1.5T1 set (Figures 4.11 through 4.14). For 50 story walls, it was not possible to develop the CMS at large enough periods to account for elongation of the fundamental period because the simplified correlation model was used to compute the target CMS.

2. In terms of mean interstory drift demand at top of walls, the CMS1.5T1 set gives highest values for 10 story walls with R_g factors of 2.6 and 4.3 (Table 4.4), while the mean interstory drift ratio corresponding to the CMST1 set is slightly higher than that for the CMS1.5T1 records for R_g = 1.7. Similar to roof displacement demand, using T_1 as the conditioning period results in higher interstory drifts than using $1.5T_1$ for 30 story walls (Figures 4.11 through 4.14).

3. The CMS1.5T1 set gives highest base curvature demand in 10 story walls with force reduction factors of 2.6 and 4.2. For the 10 story wall with R_g = 4.2, using the CMS1.5T1 set results in mean base curvature demands that are 40% and 31% higher than those corresponding to the CMST1 and CMS2T1 sets, respectively (see Table 4.5). Similar to roof displacement and interstory drift demands, the CMST1 set gives highest base curvature demand for 30 story walls (Figures 4.11 through 4.14). Also, it was observed that although the CMST2 and CMST3 sets result in low base curvature demands, they give higher midheight curvature demands compared to the CMST1 or CMS1.5T1 records (Figures 4.11, 4.12, and Figures 4.15 through 4.18).

4. The CMST1 set consistently controls the base bending moment demand in all walls except for the 10 story wall with R_g = 4.2, for which the results from the CMS1.5T1 are the largest. Similar to base curvature demands, the ground motions selected and scaled to the CMS

corresponding to T_2 and T_3 give higher midheight bending moment demands than those associated with T_1 or $1.5T_1$. For example, for the 50 story wall with R_g = 4.1 (Figure 4.18), the CMST3 gives larger moments from the height of 110 m to the top, while moment demands using the CMST2 set is the largest from the height of 80 m to 110 m. Finally, demands from the CMST1 set are the largest for heights below 70 m.

5. The lowest base shear force demands belong to the conditioning periods of $2T_1$, $1.5T_1$, and T_1 for 10, 30, and 50 story walls, respectively (Table 4.6). The CMST2 set gives highest base shear forces for 10 and 30 story walls, while using the CMST3 set results in highest demands for 50 story walls. Using higher mode periods as the conditioning period rather than the fundamental period T_1 increases the base shear force demand up to 23%, 26%, and 73% for 10, 30, and 50 story walls, respectively. For 10 story walls, CMST2 set gives higher shear forces at the top of the wall, while largest shear forces near midheight belong to CMST1 for R_g = 1.7 and R_g = 2.6 and to CMS1.5T1 for R_g = 3.2 (Figures 4.8 to 4.10). For 30 story walls, CMST2 gives largest shear forces except that CMST1 and CMST3 gives larger shear forces near the midheight for R_g = 1.4 and R_g = 4.3, respectively (Figures 4.11 to 4.14). Lastly, for 50 story walls, CMST2 and CMST3 alternatively give highest midheight shear demands (Figures 4.15 through 4.18).

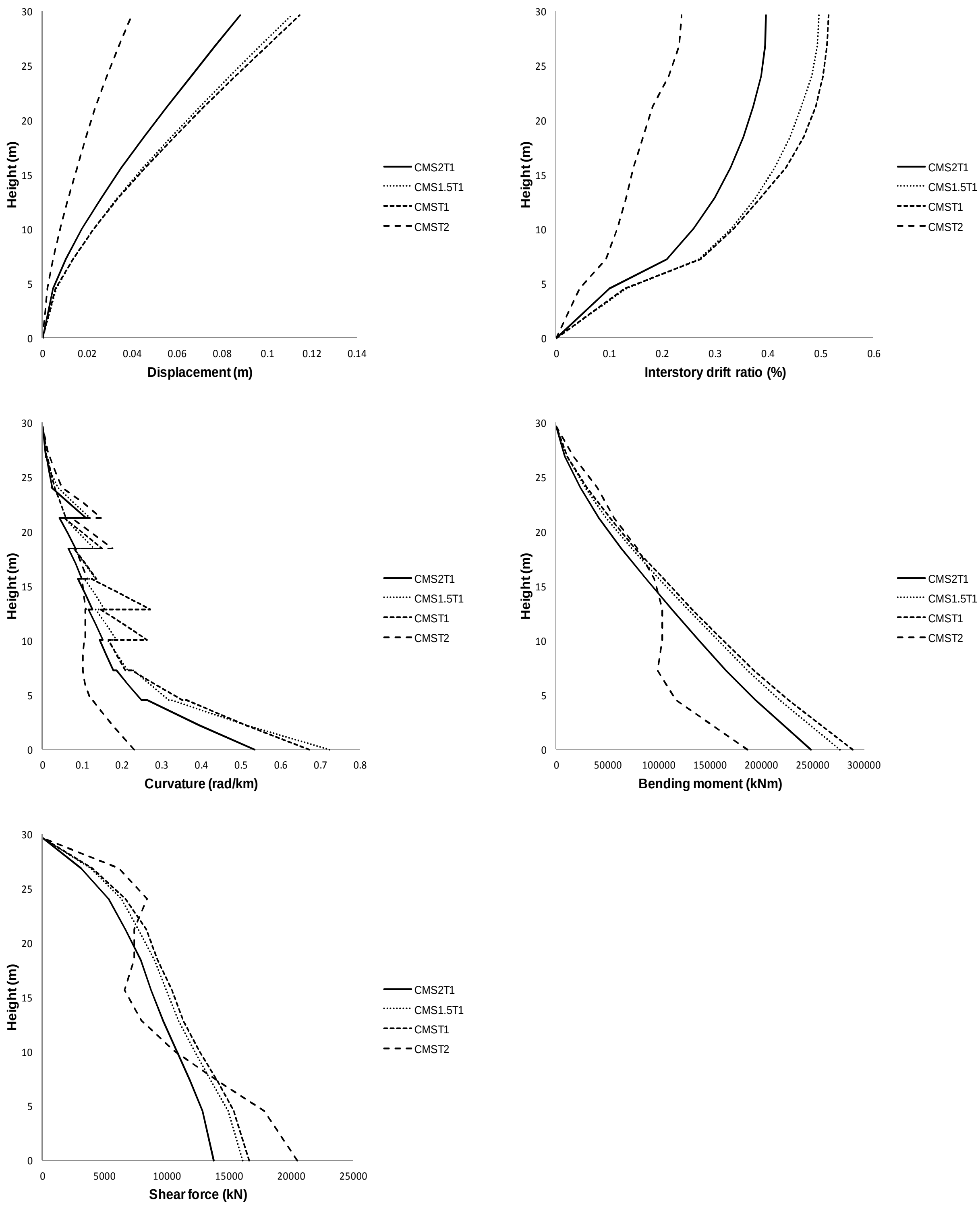

Figure 4.8 Sensitivity of demand parameters to conditioning period for 10 story wall with R_g = 1.7.

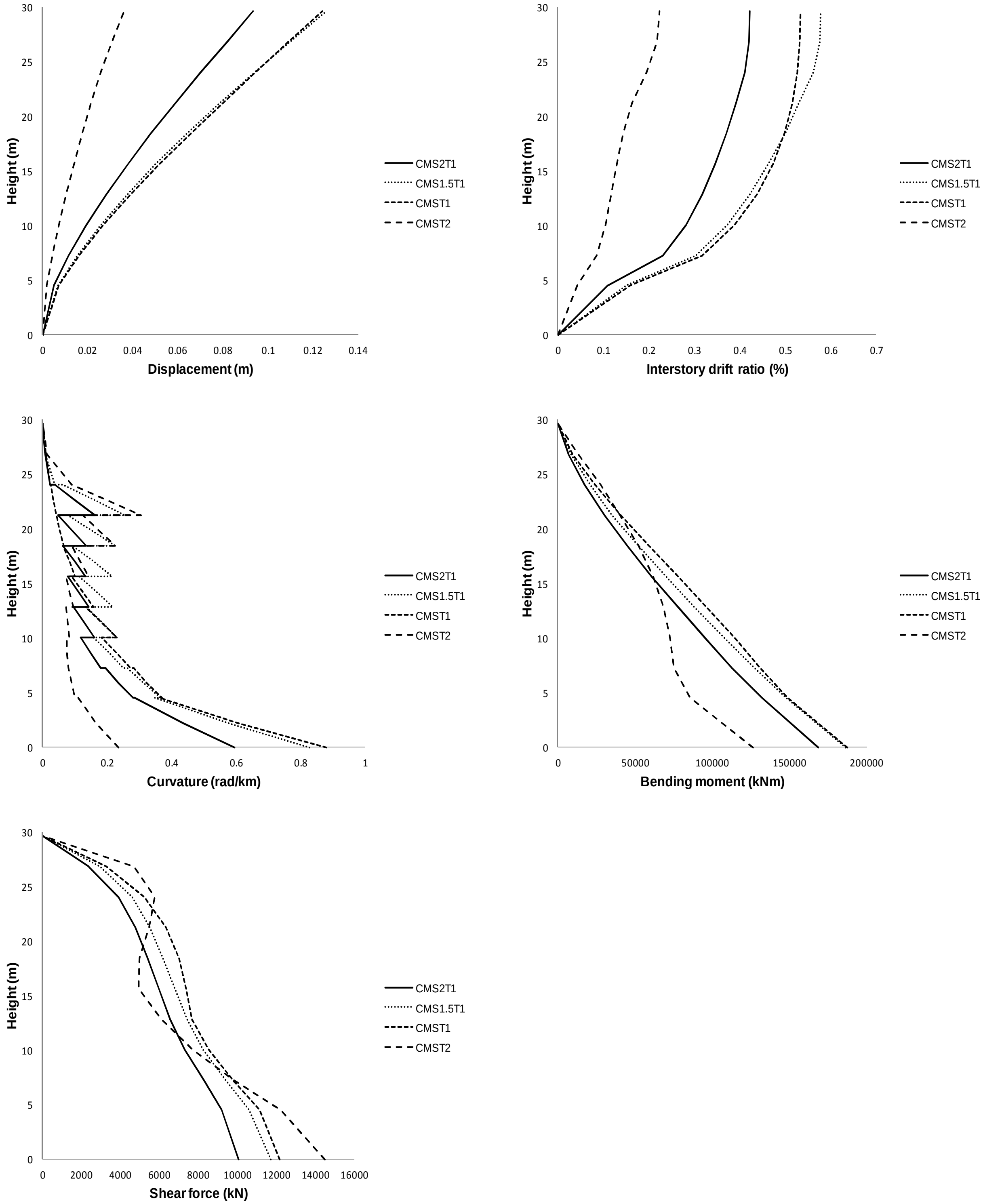

Figure 4.9 Sensitivity of demand parameters to conditioning period for 10 story wall with R_g = 2.6.

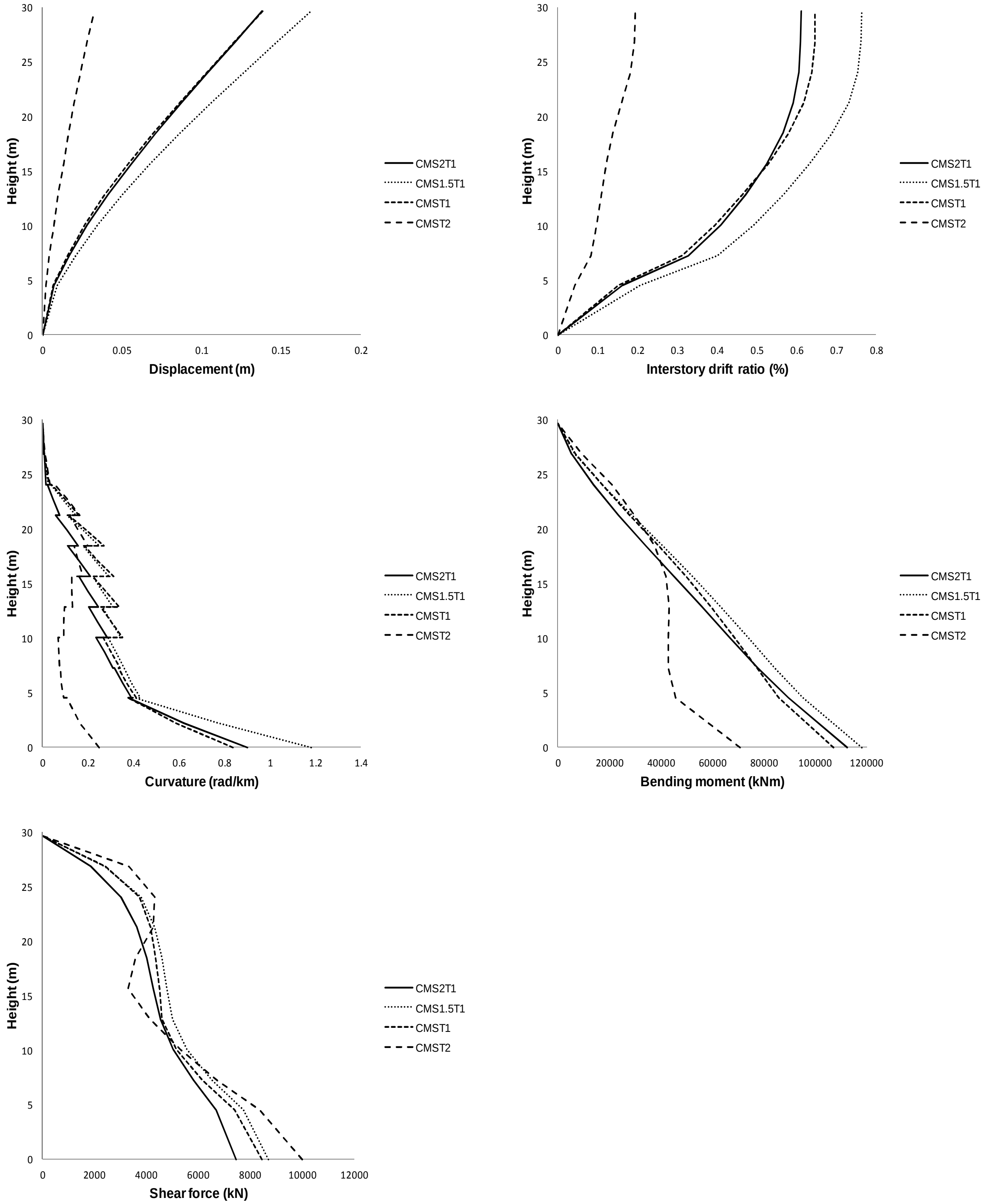

Figure 4.10 Sensitivity of demand parameters to conditioning period for 10 story wall with R_g = 4.2.

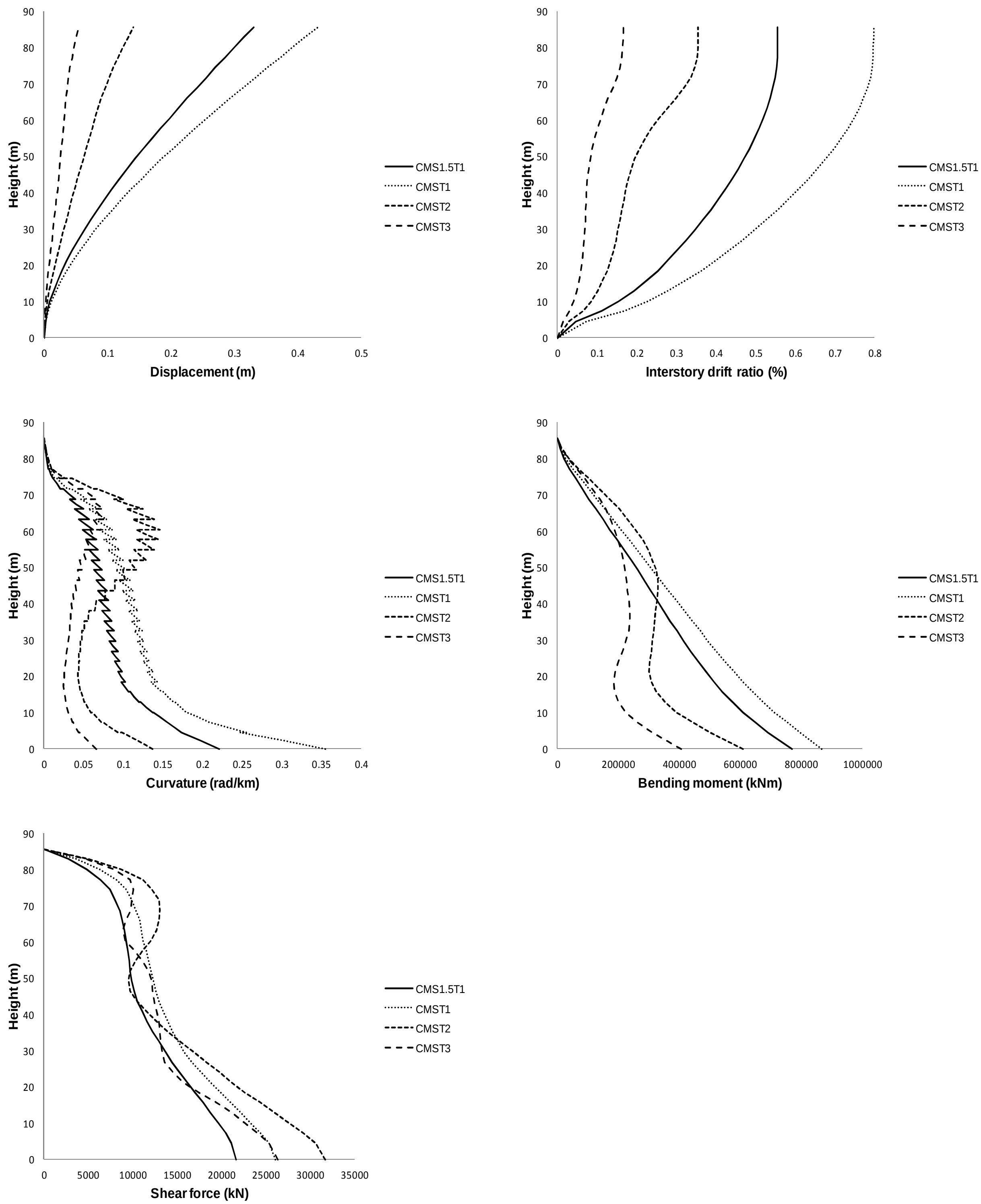

Figure 4.11 Sensitivity of demand parameters to conditioning period for 30 story wall with R_g = 1.4.

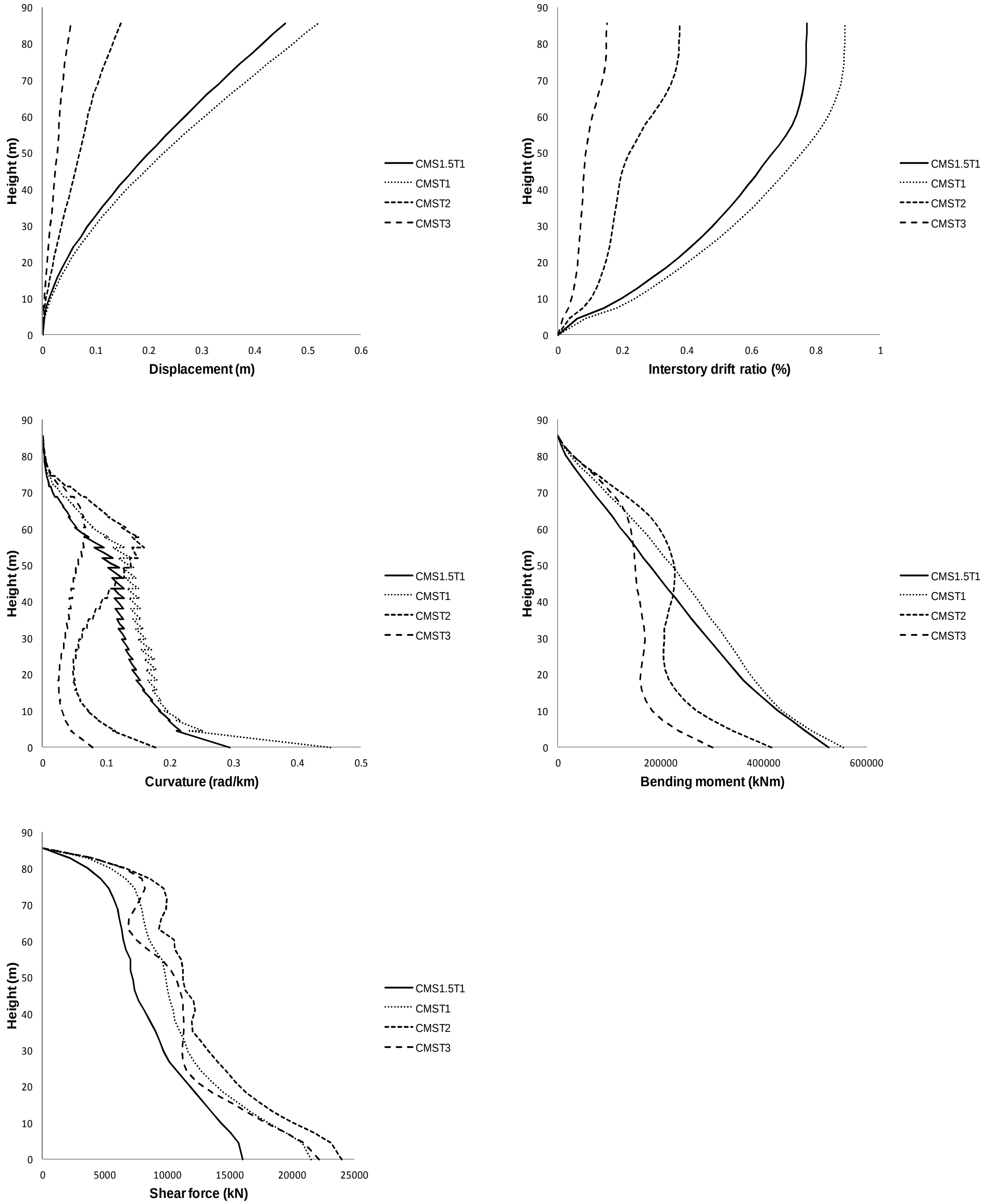

Figure 4.12 Sensitivity of demand parameters to conditioning period for 30 story wall with R_g = 2.4.

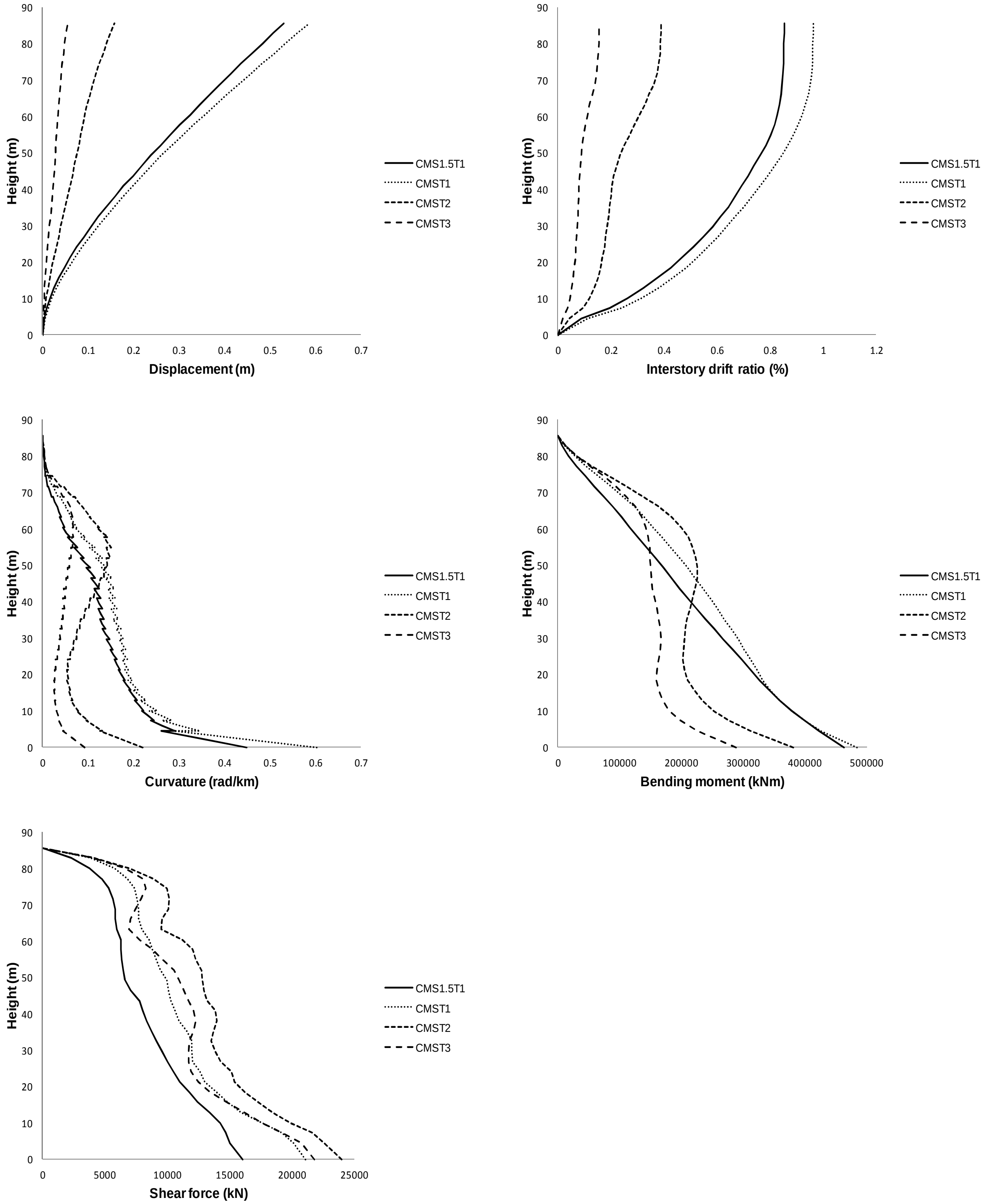

Figure 4.13 Sensitivity of demand parameters to conditioning period for 30 story wall with R_g = 3.1.

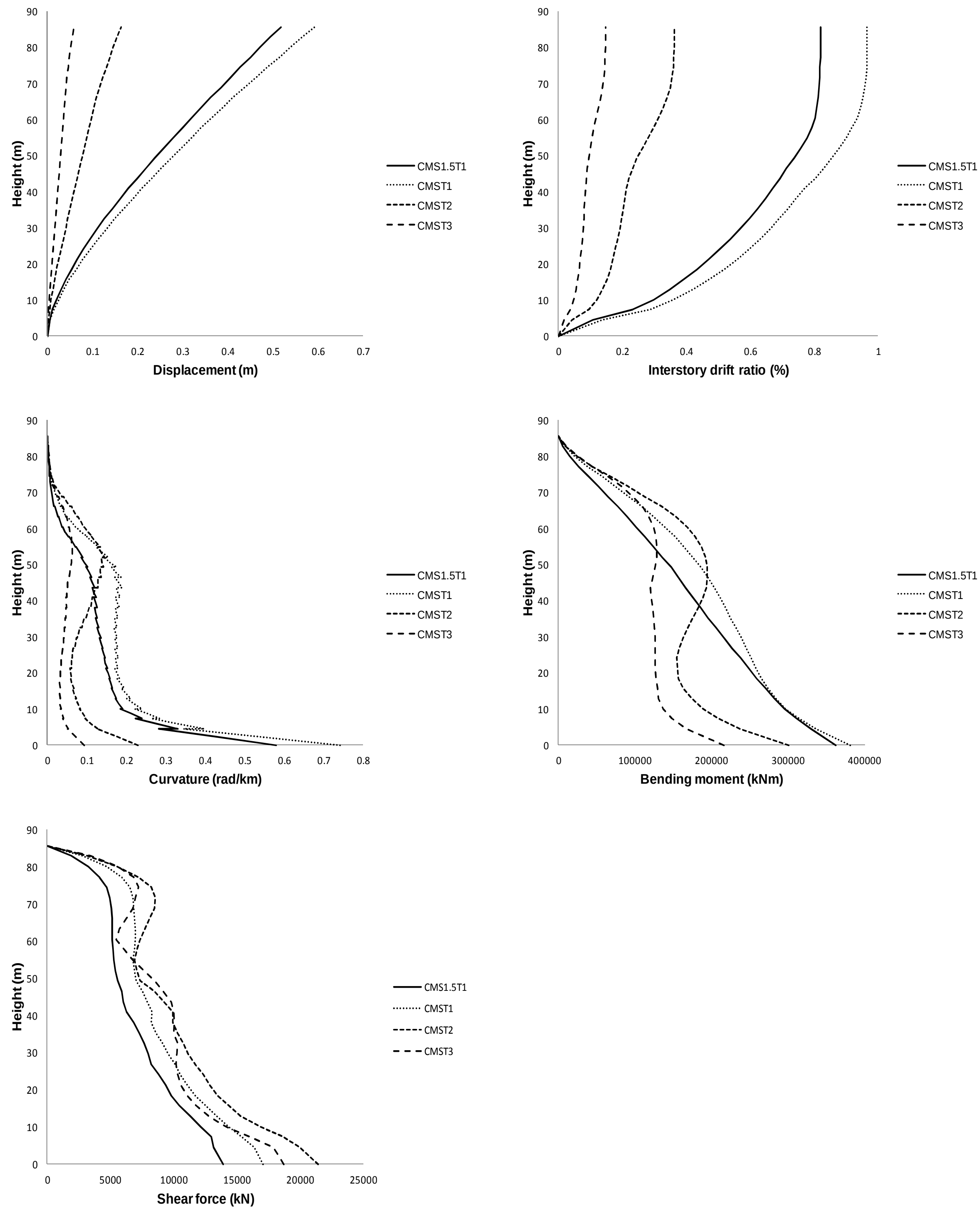

Figure 4.14 Sensitivity of demand parameters to conditioning period for 30 story wall with R_g = 4.3.

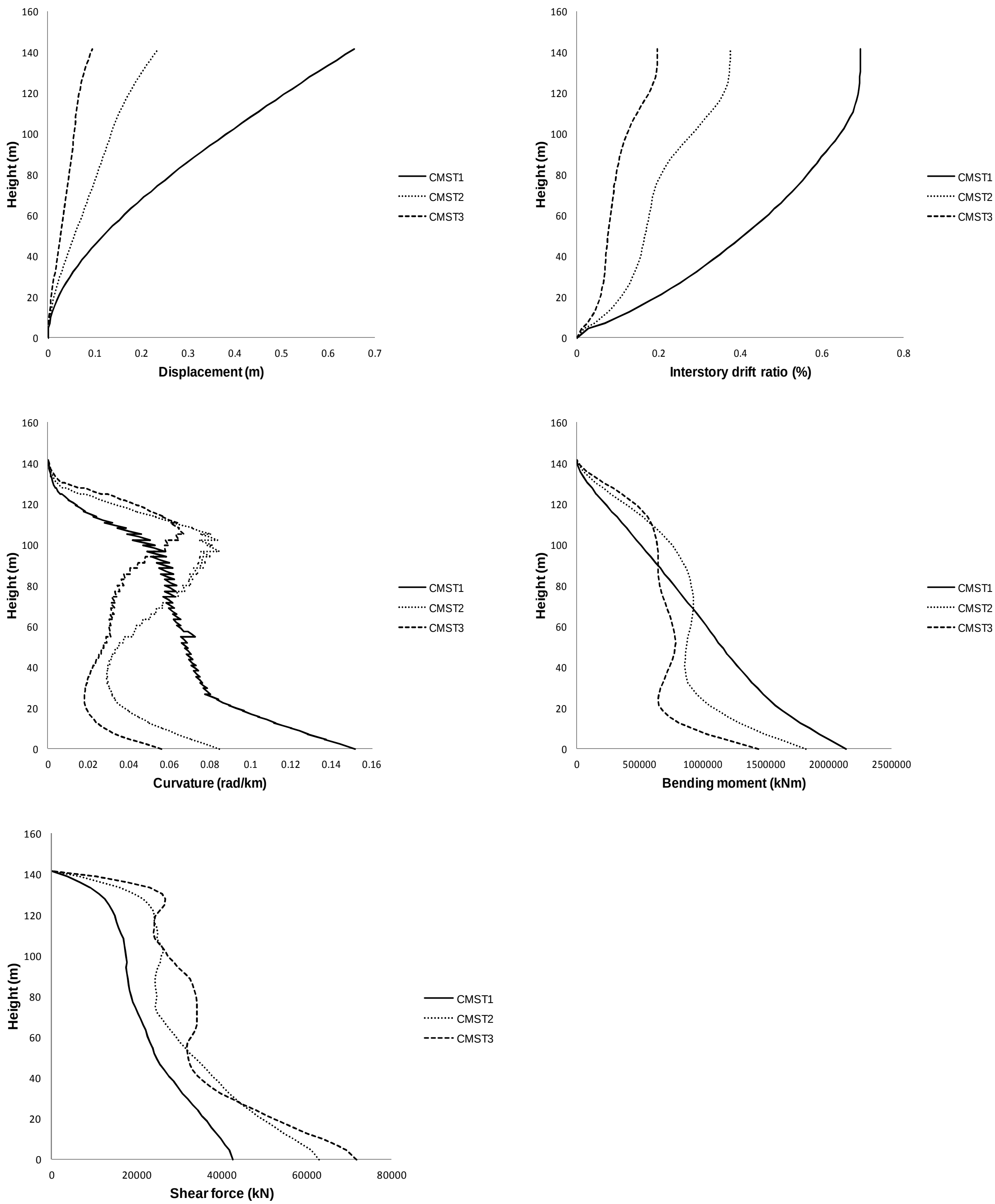

Figure 4.15 Sensitivity of demand parameters to conditioning period for 50 story wall with R_g = 1.4.

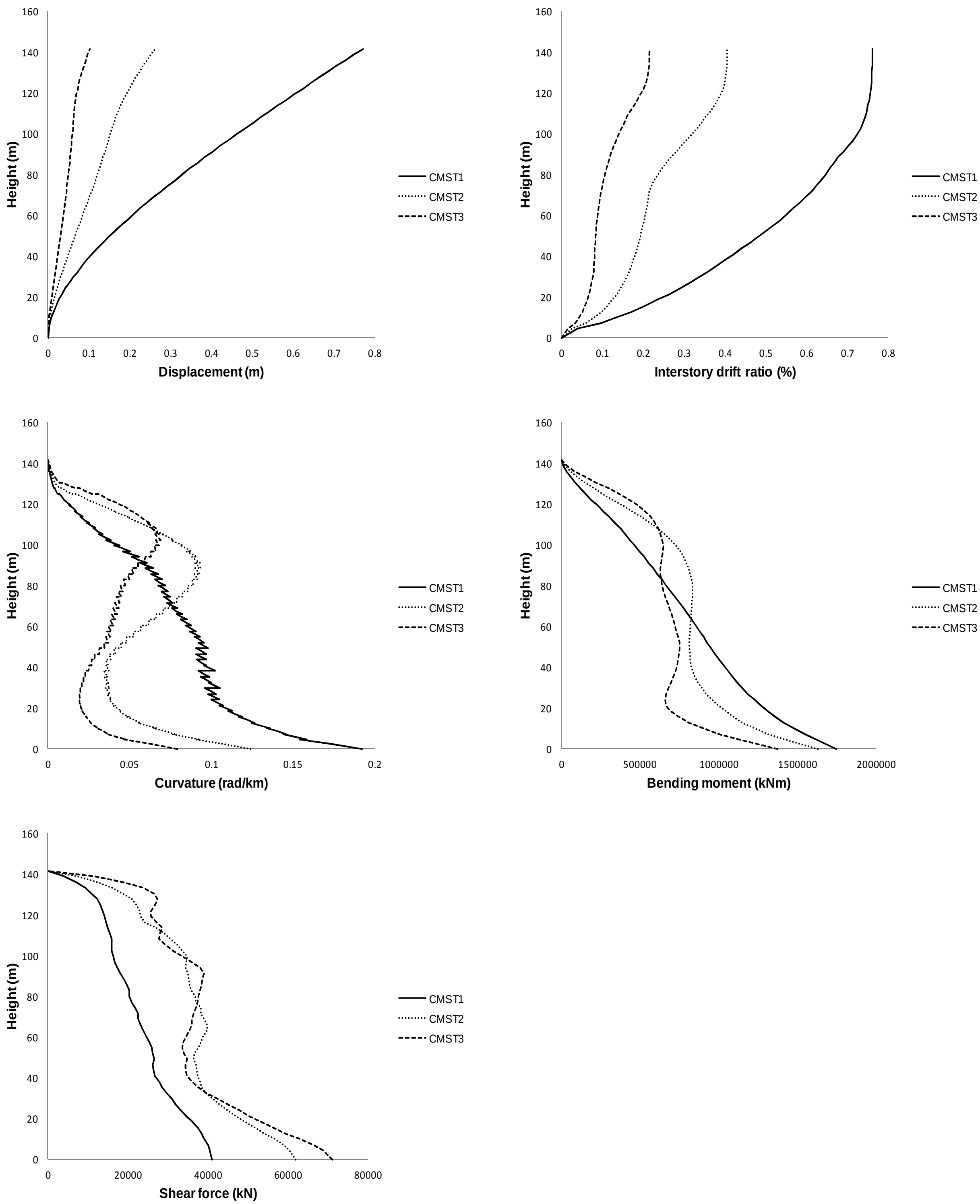

Figure 4.16 Sensitivity of demand parameters to conditioning period for 50 story wall with R_g = 2.1.

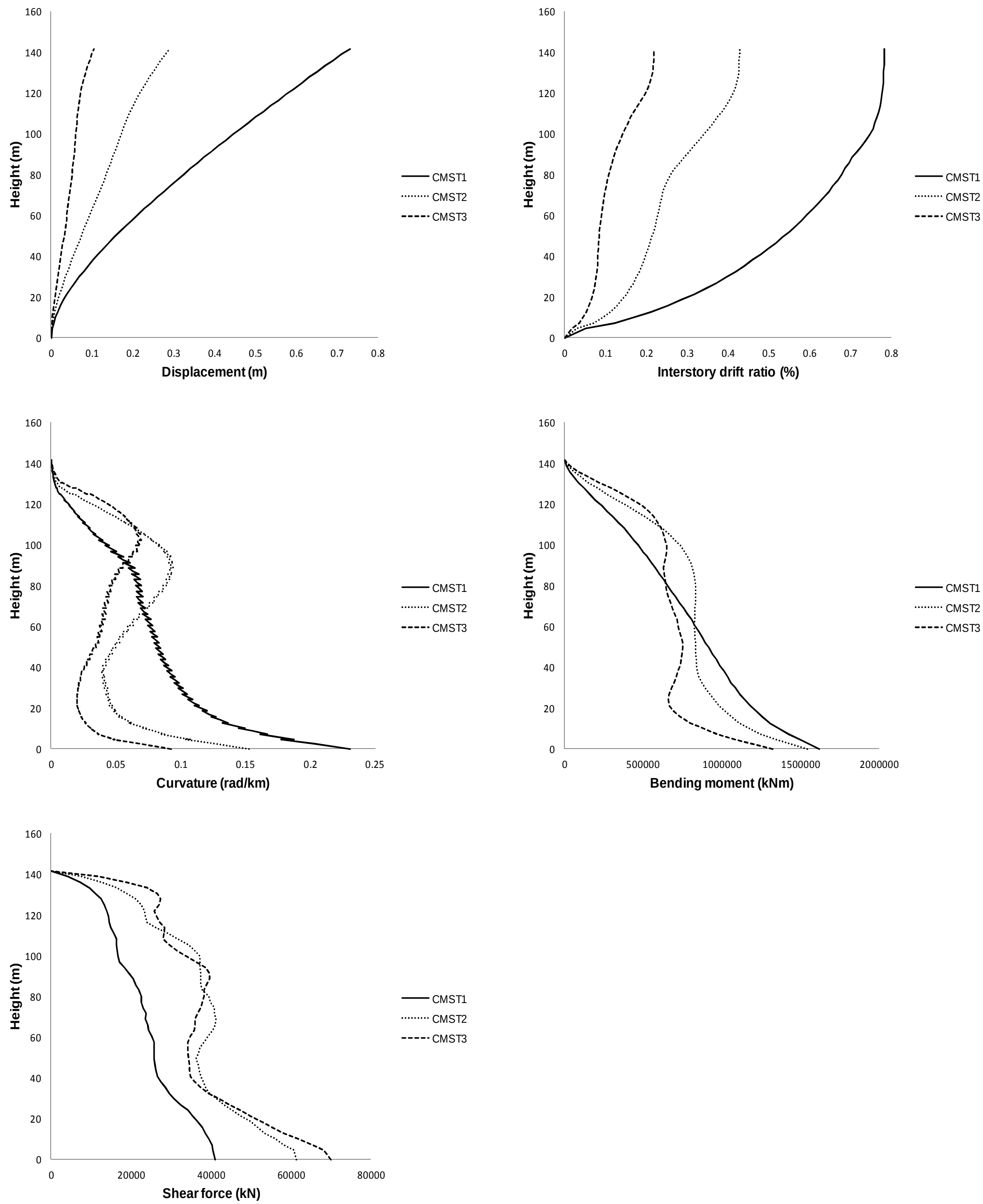

Figure 4.17 Sensitivity of demand parameters to conditioning period for 50 story wall with R_g = 2.4.

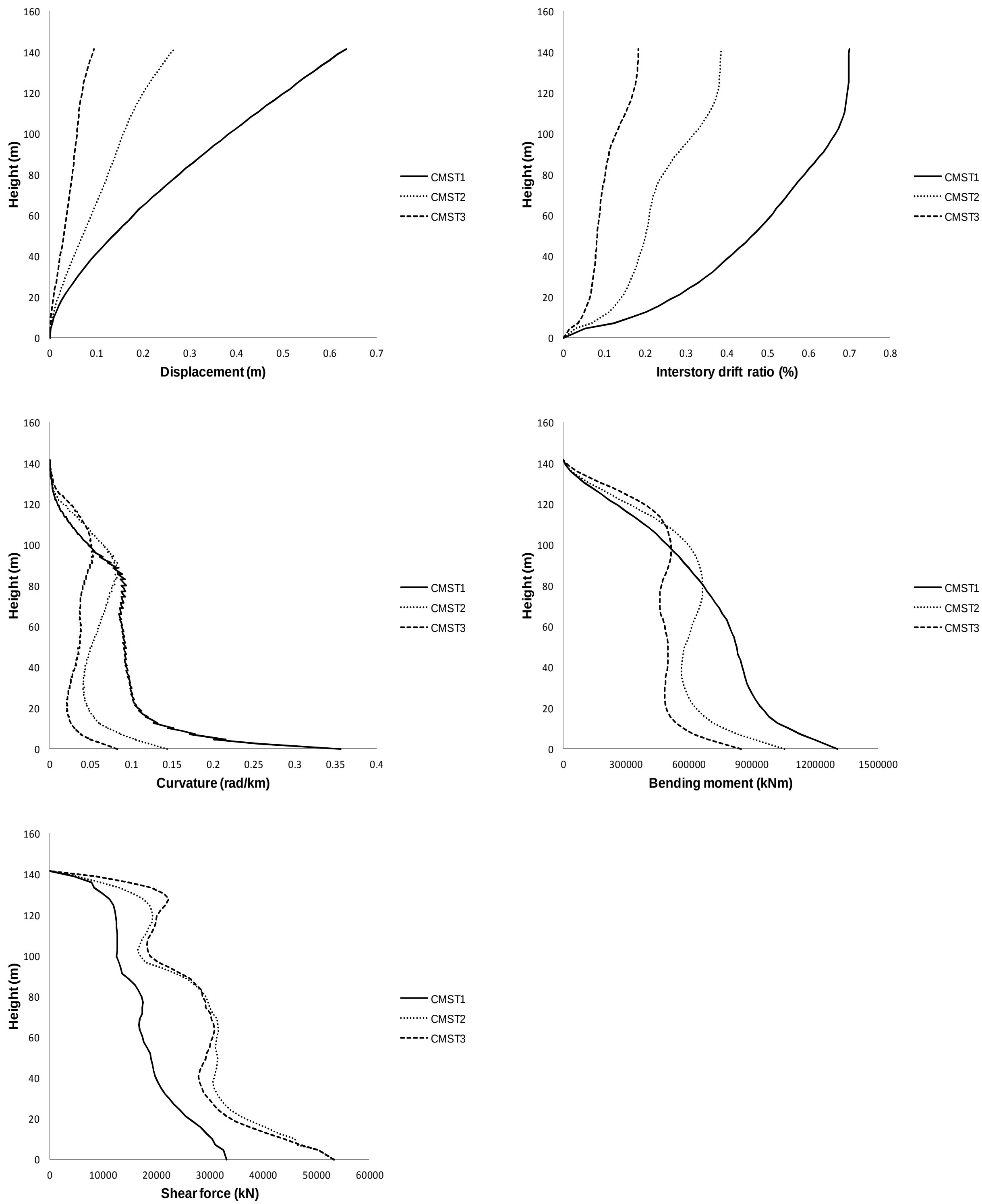

Figure 4.18 Sensitivity of demand parameters to conditioning period for 50 story wall with R_g = 4.1.

4.6.2 Comparison of Demand Parameters from Different Scaling Schemes

Figures 4.19 through 4.29 compare the mean envelope from different scaling methods - namely SM, ST1, and SOR ground motions - with the CMS envelope associated with the largest responses (denoted as CMS-E). The following observations can be made:

1. The shapes of displacement envelopes shown in Figures 4.19 to 4.29 are similar to a first mode dominated displacement profile. An influence of higher modes is evident in the displacement envelopes of the 50 story walls using ST1 ground motions. The mean roof displacements associated with the CMS-E were found to be between 90 and 100% of the mean roof displacement determined using the SM ground motions (Table 4.3). For the 10 and 30 story walls, the mean roof displacements from ST1 and SOR are within 90 to 105% of the mean roof wall displacements from the SM records. For the 50 story walls, the mean roof displacements from the SOR and ST1 ground motions are from 100 to 110% and 110 to 120% of the mean roof displacements from SM ground motions, respectively.

2. Using the SM and SOR ground motions results in very similar interstory drift envelopes over the height of shear walls. These interstory drift envelopes are dominated by the first mode displacement profile except for those corresponding to the ST1 records. The mean interstory drift at the top of walls from CMS-E is 88%, 95%, and 86% of the value from the SM ground motions for the 10, 30, and 50 story walls with the highest force reduction factors, respectively (Table 4.4). For 30 and 50 story walls, the mean interstory drifts at the top from the ST1 records is 15% and 50% higher than those using the SM ground motions, respectively.

3. The base curvature demand from the SOR ground motions are generally between 90 and 100% of the mean base curvature from the SM records. The mean base curvature demands from the CMS-E are generally lower than those from the SM ground motions (minimum of 80%) except for three 30 story walls (Table 4.5). For 50 story walls, the ST1 set gives higher base curvature demands that are at least double the results from the SM ground motions. In terms of midheight curvature demands, using SOR set results in larger curvatures above midheight than the SM records due to the increased response in higher modes. Mean curvature envelopes from the CMS-E are a lower bound to the mean curvature envelopes determined using the SM ground motions. For 30 and 50 shear walls, ST1 gives much higher curvature values above midheight due to higher modes: the ratio of curvatures around midheight from ST1 to SM are 2.8, 2.5, 2.4, 2.4 for 30 story walls and 4.6, 3.3, 3.2, and 4.2 for 50 story walls (Figures 4.22 to 4.29).

4. It was observed that scaling method has little impact on base bending moment demands. This is because for most walls, bending moment demands at the base are controlled by the flexural strength of the walls. The ST1 ground motions gives higher midheight moment demands for 30 and 50 story walls, while the lowest moment demands belong to the CMS-E (Figures 4.22 to 4.29).

5. Mean base shear force demands from the SOR records are between 93 and 102% of the mean base shear force demands using the SM ground motions (Table 4.6). The CMS-E typically gives mean base shear force demands that are 80 to 95% of the mean base shear force demands from SM and SOR sets. Mean shear force envelopes from the CMS-E are a lower bound to those from the SM ground motions, while the SOR ground motions gives higher shear forces near midheight than the SM records for 50 story walls with force reduction factors of 1.4, 2.1, and 2.4 (Figures 4.26, 4.27, and 4.28). Mean base shear force demands from ST1 set are about 35% and 200% higher than those from the SM ground motions for the 30 and 50 story walls, respectively.

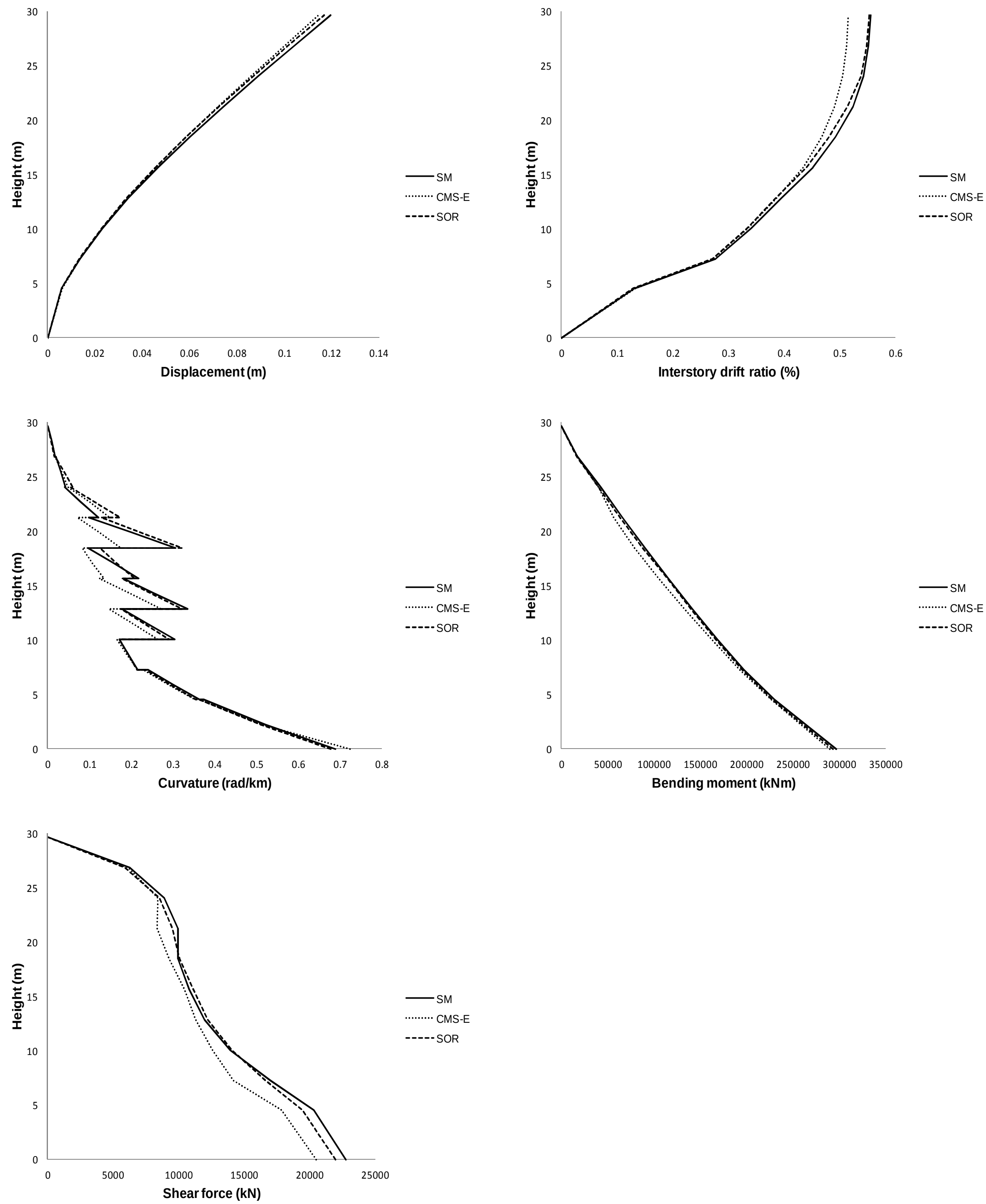

Figure 4.19 Comparison of demand parameters for 10 story wall with R_g = 1.7 using spectrum matched (SM), scaled over range (SOR), and the envelope of results using CMS ground motions (CMS-E).

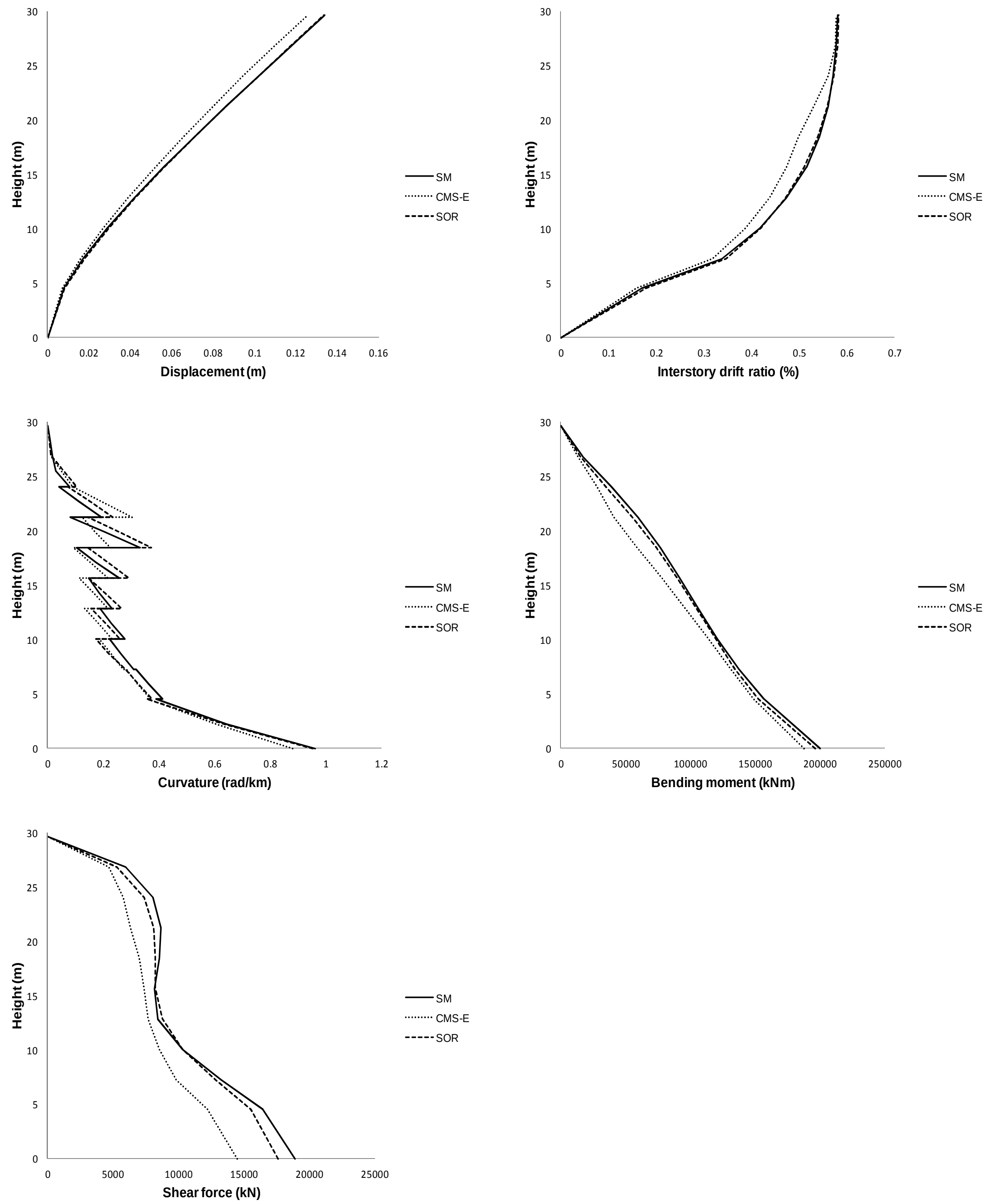

Figure 4.20 Comparison of demand parameters for 10 story wall with R_g = 2.6 using spectrum matched (SM), scaled over range (SOR), and the envelope of results using CMS ground motions (CMS-E).

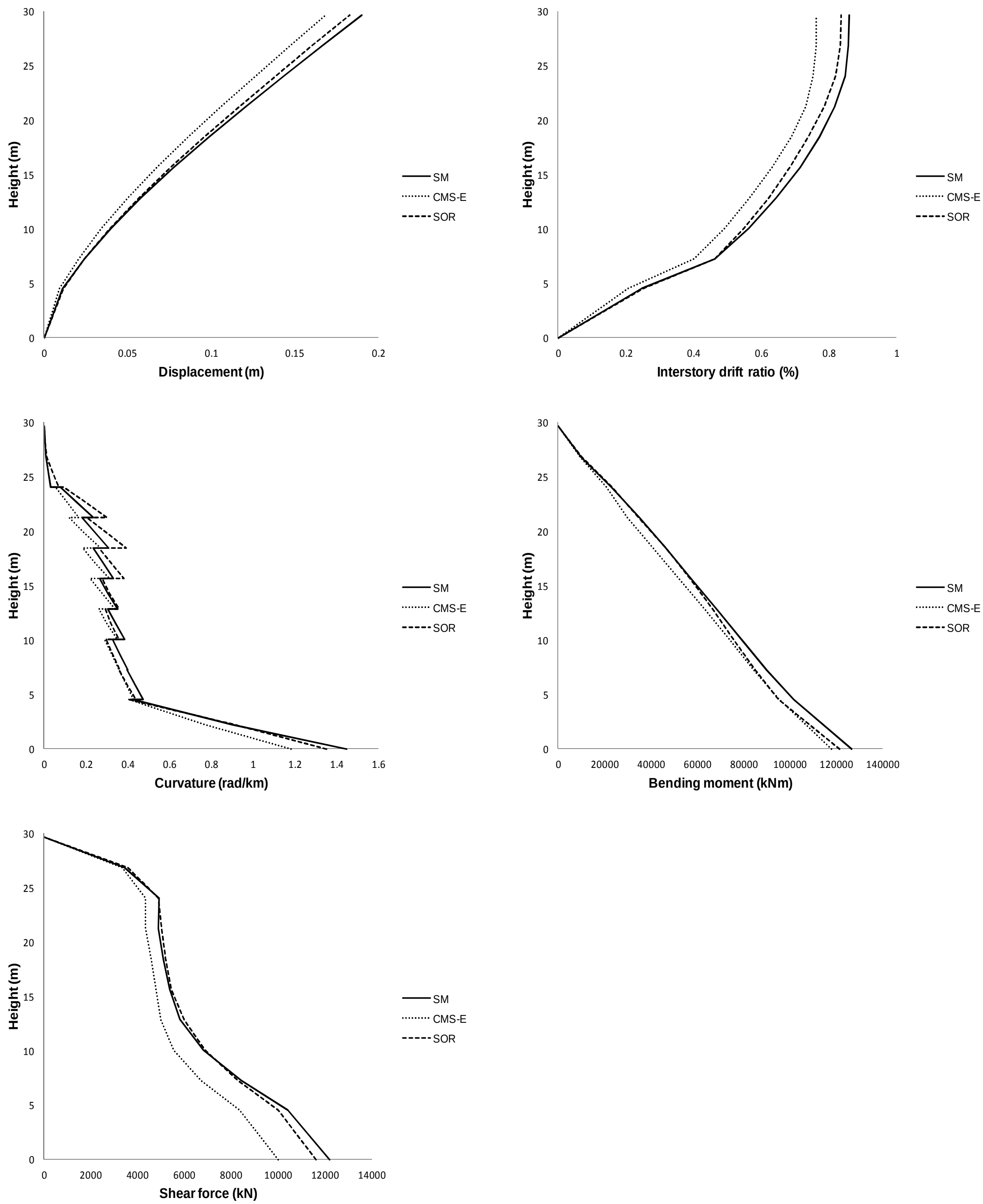

Figure 4.21 Comparison of demand parameters for 10 story wall with R_g = 4.2 using spectrum matched (SM), scaled over range (SOR), and the envelope of results using CMS ground motions (CMS-E).

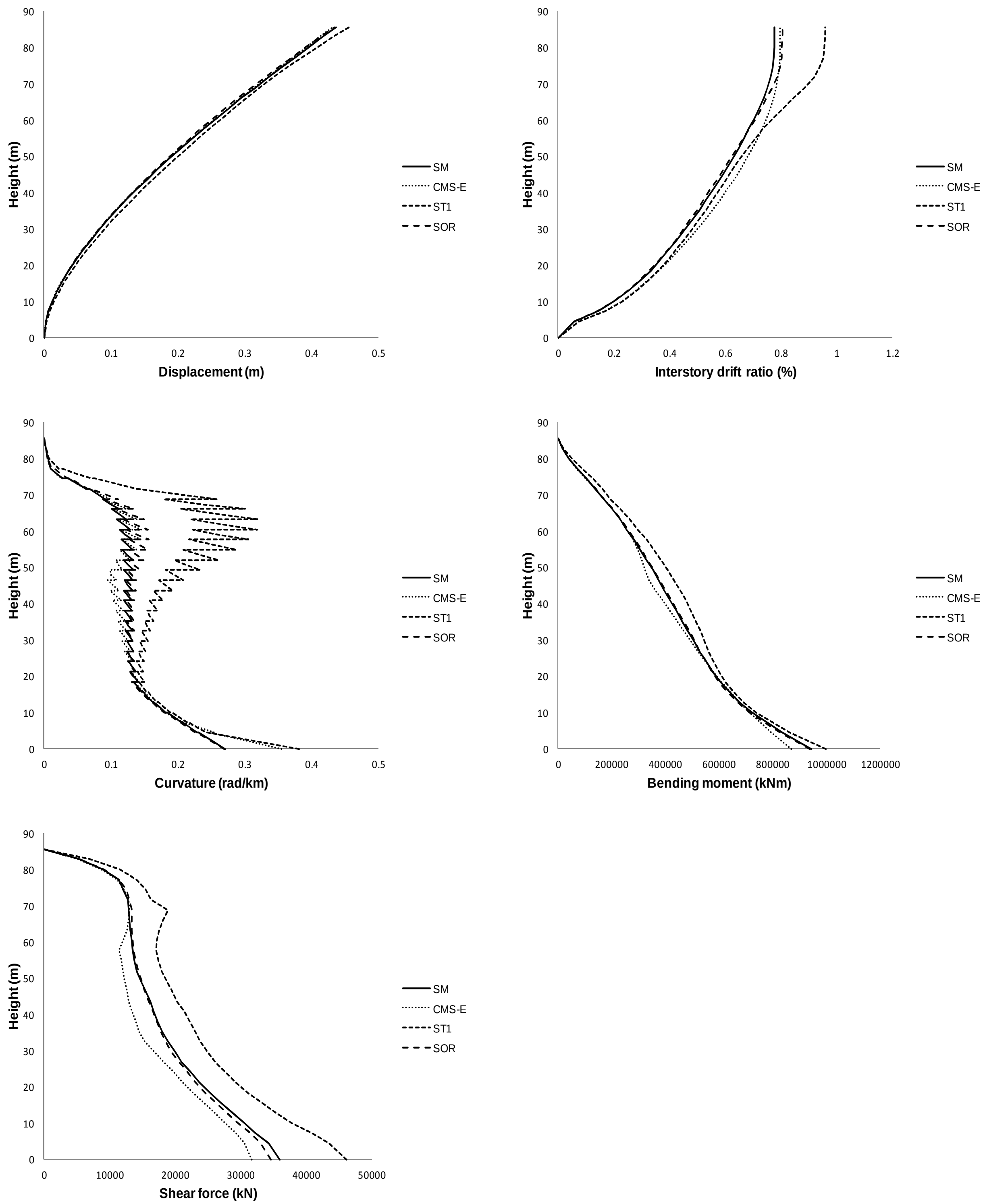

Figure 4.22 Comparison of demand parameters for 30 story wall with R_g = 1.4 using different sets of ground motions.

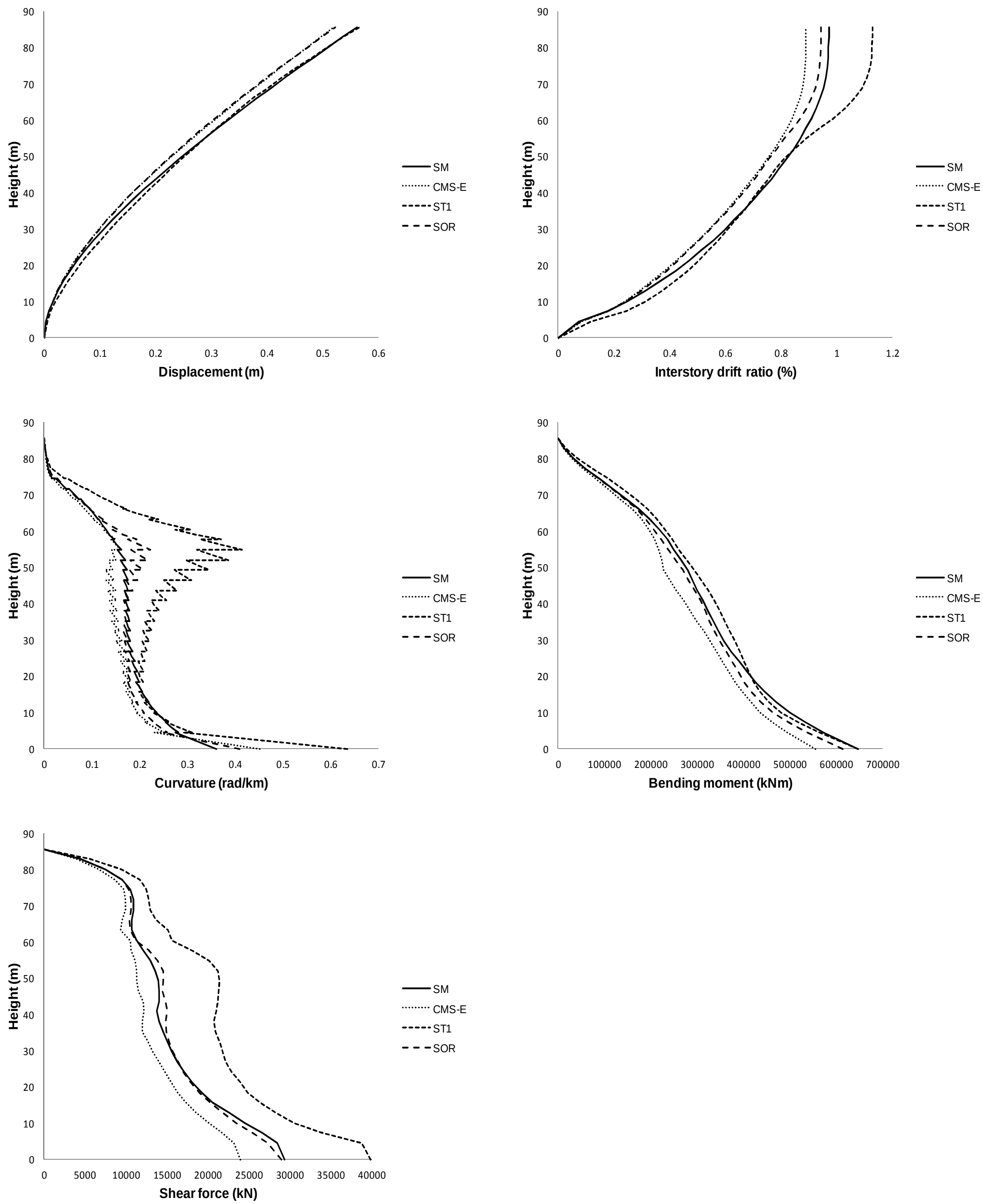

Figure 4.23 Comparison of demand parameters for 30 story wall with R_g = 2.4 using different sets of ground motions.

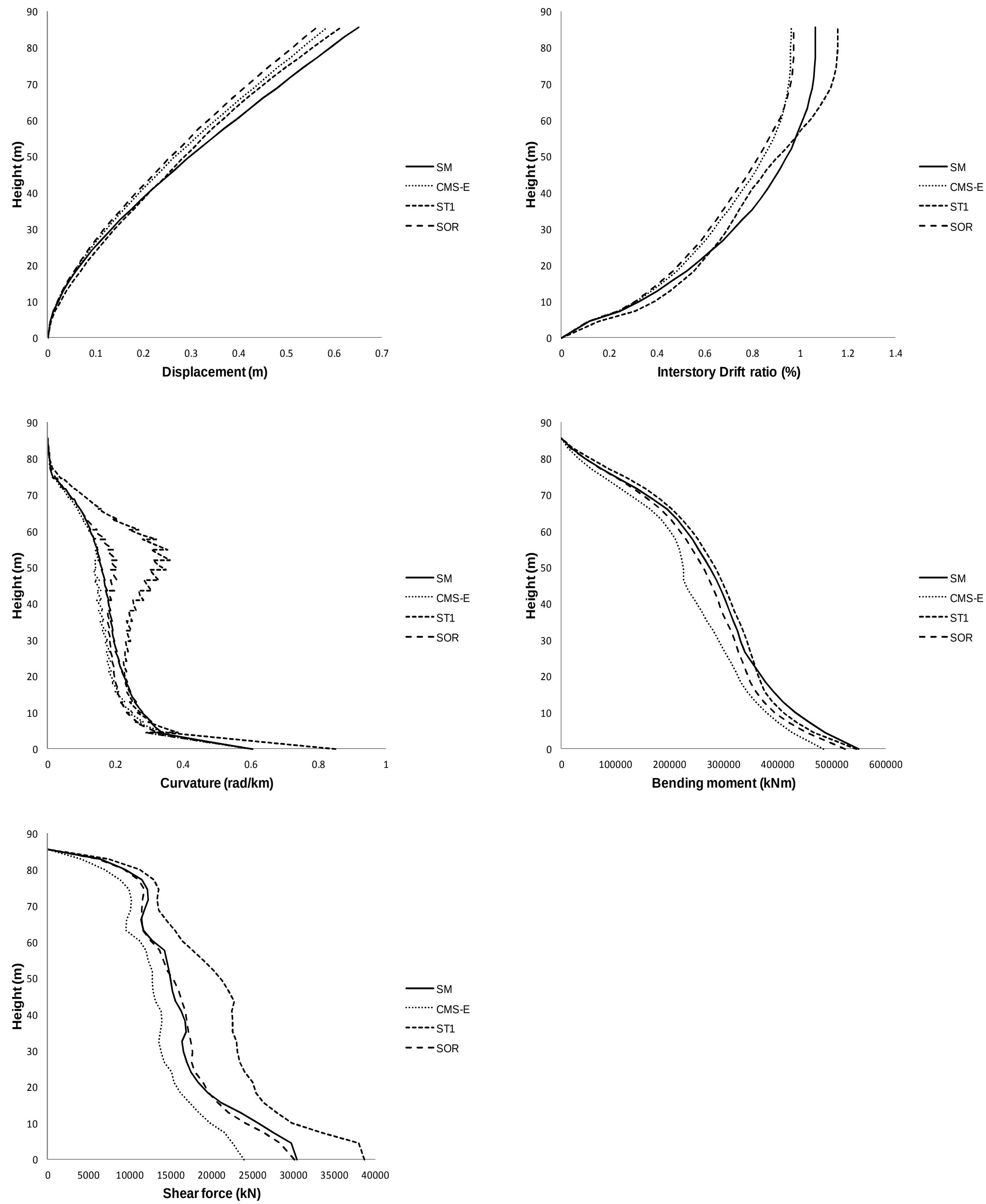

Figure 4.24 Comparison of demand parameters for 30 story wall with R_g = 3.1 using different sets of ground motions.

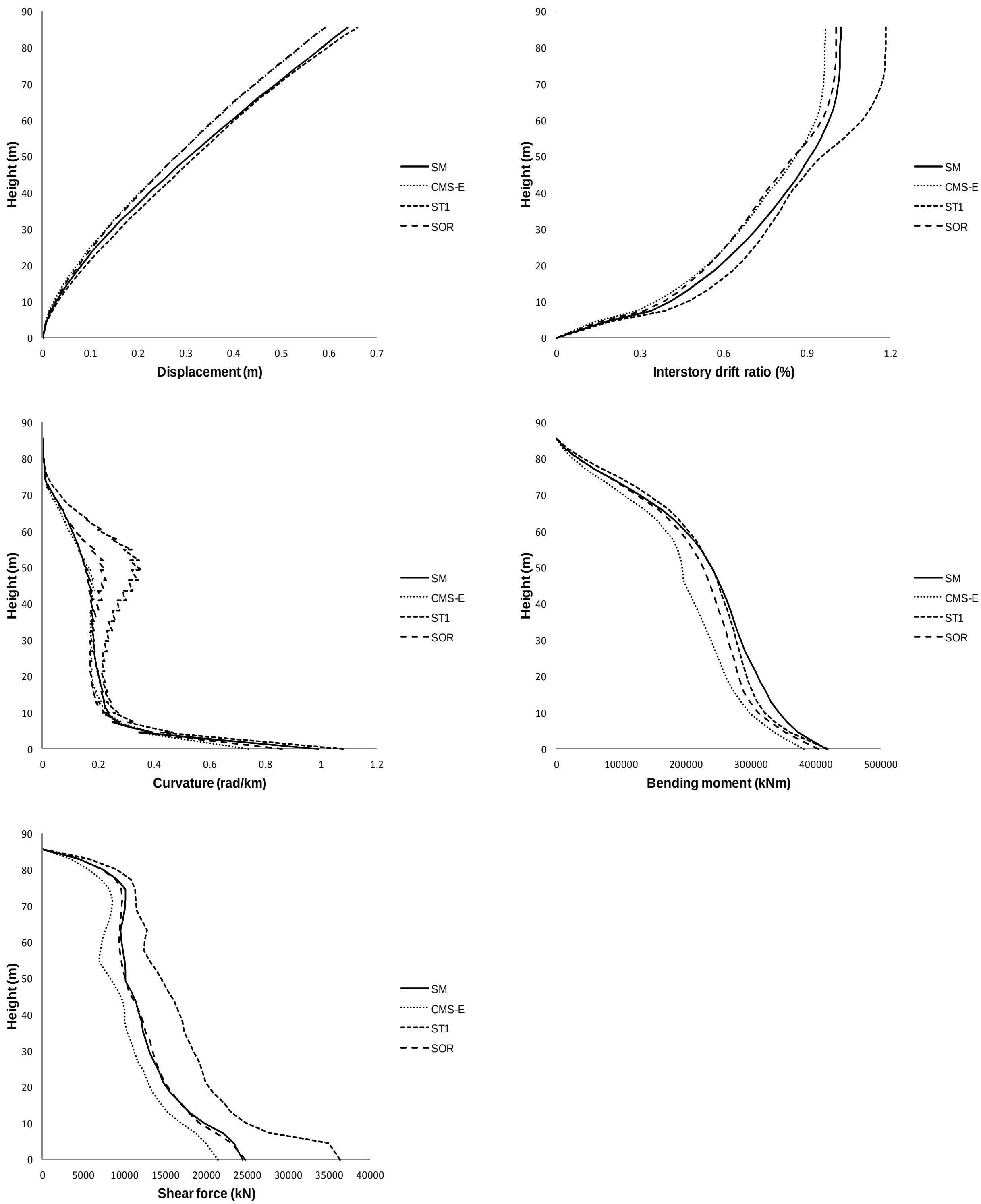

Figure 4.25 Comparison of demand parameters for 30 story wall with R_g = 4.3 using different sets of ground motions.

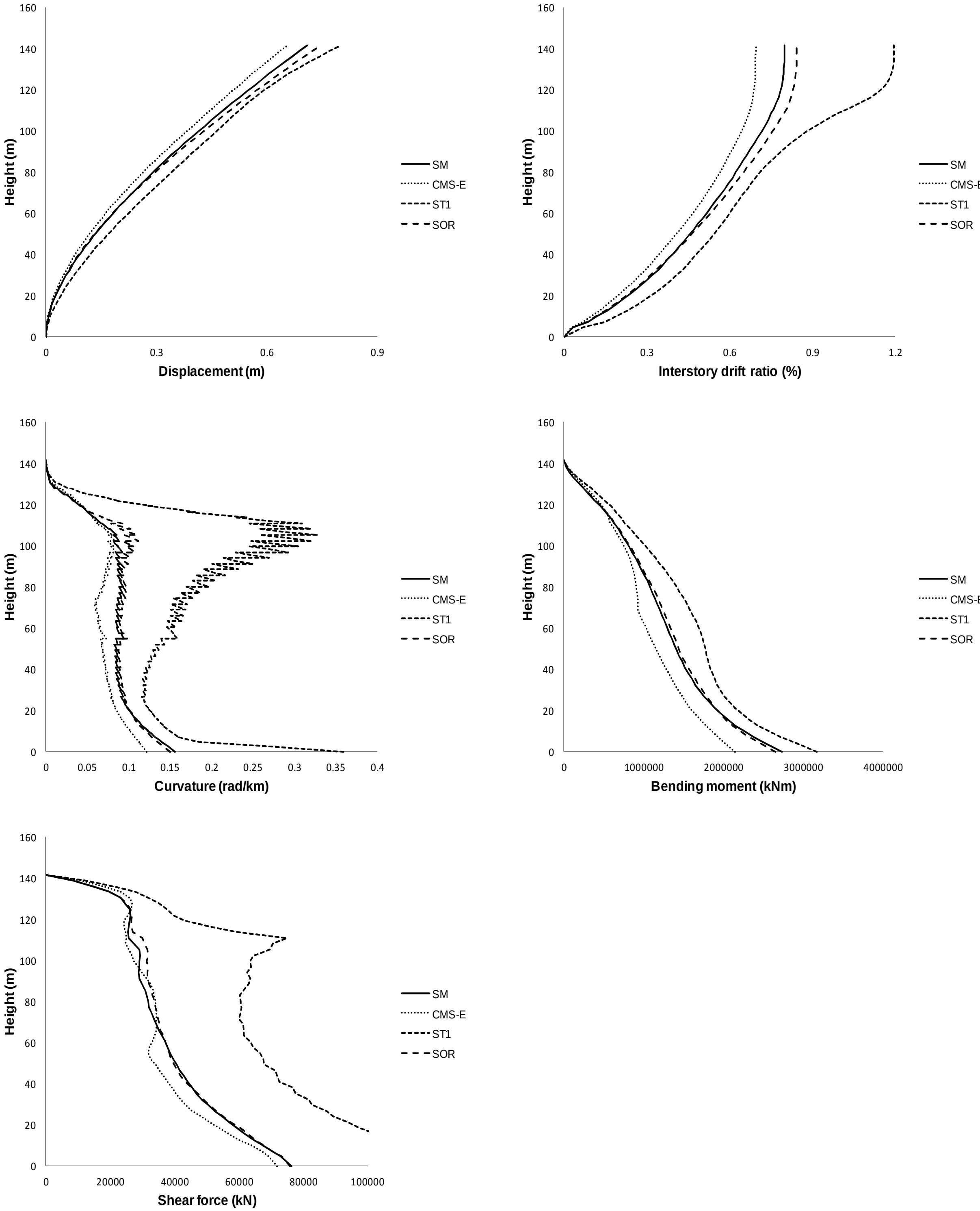

Figure 4.26 Comparison of demand parameters for 50 story wall with R_g = 1.4 using different sets of ground motions.

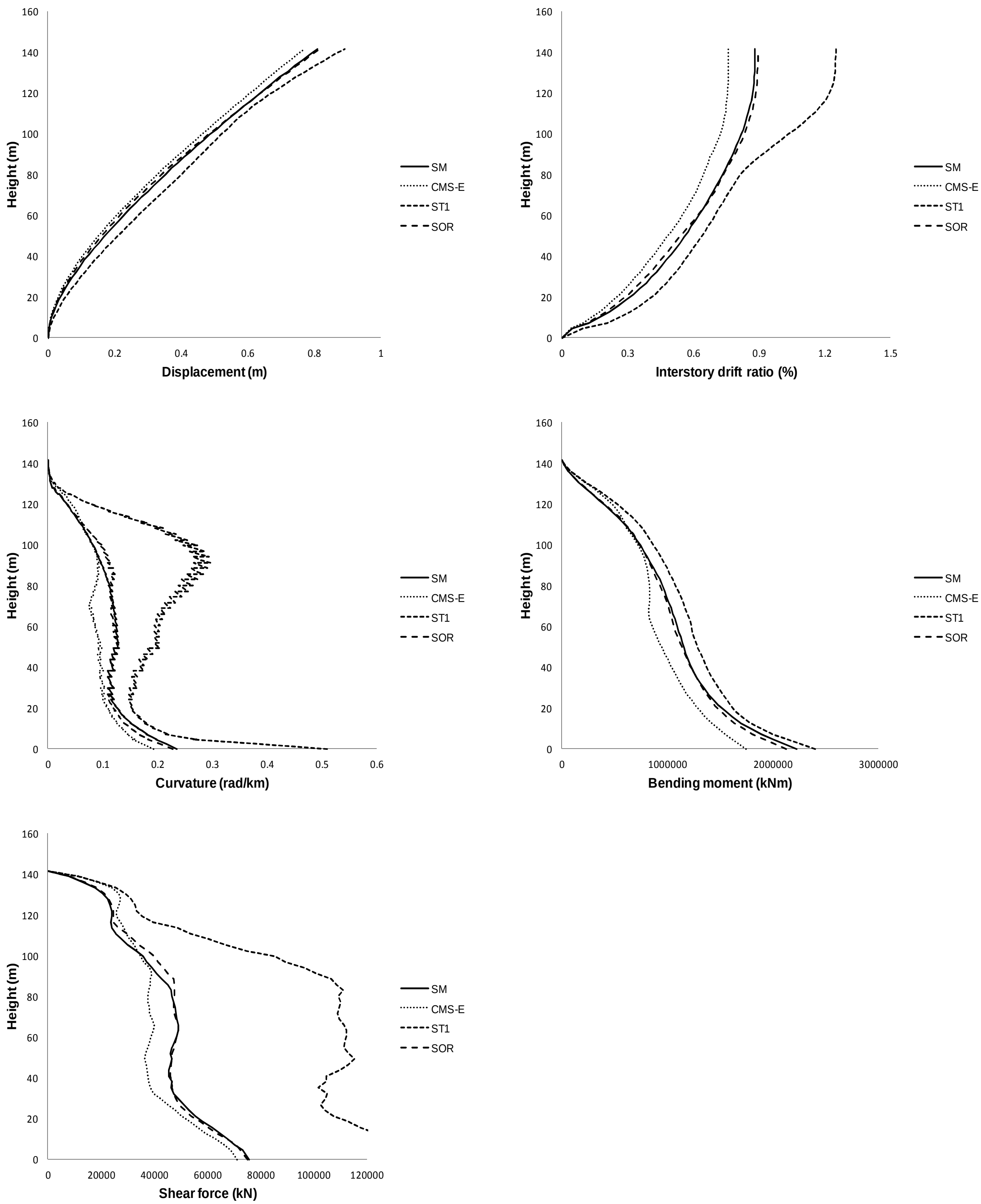

Figure 4.27 Comparison of demand parameters for 50 story wall with R_g = 2.1 using different sets of ground motions.

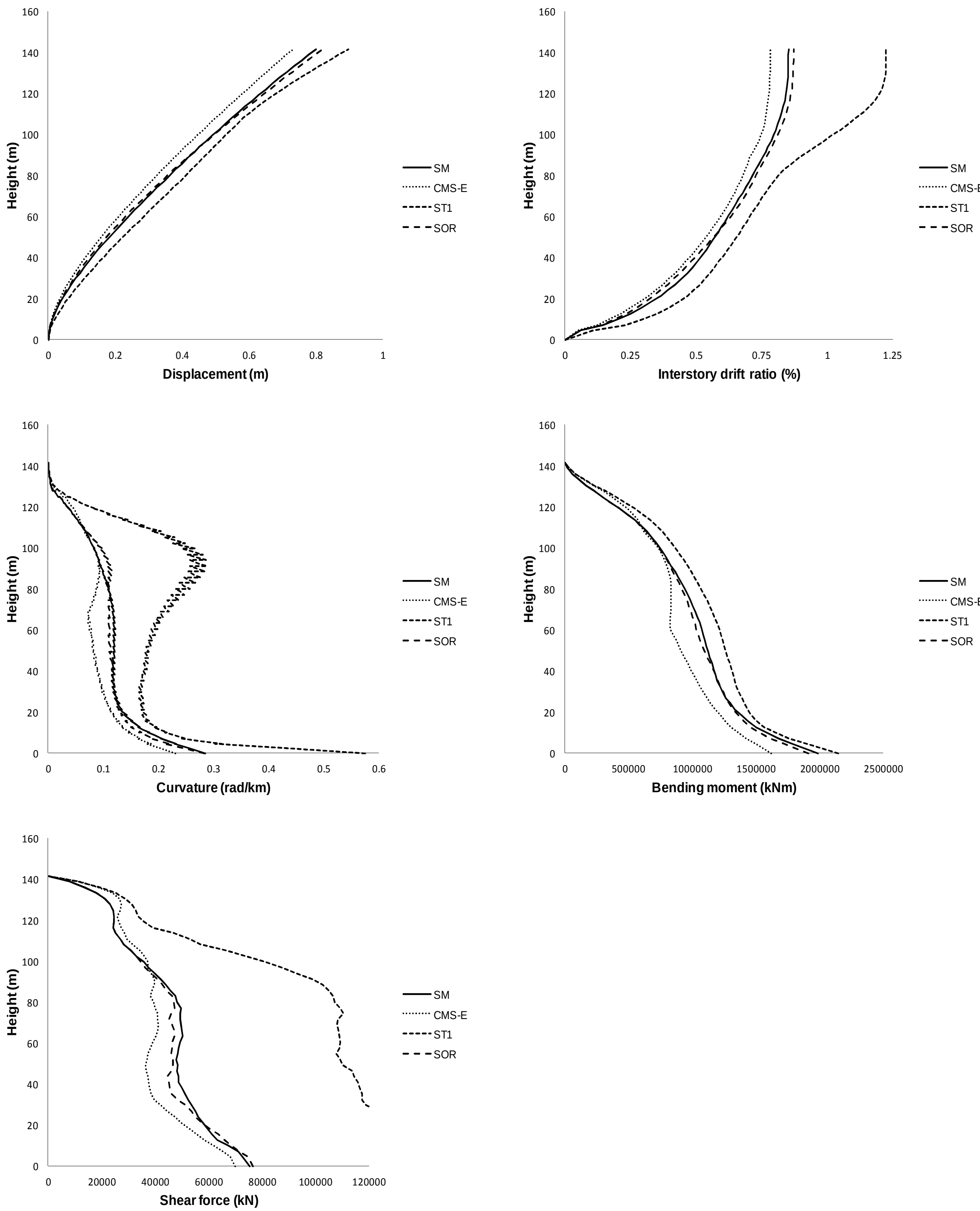

Figure 4.28 Comparison of demand parameters for 50 story wall with R_g = 2.4 using different sets of ground motions.

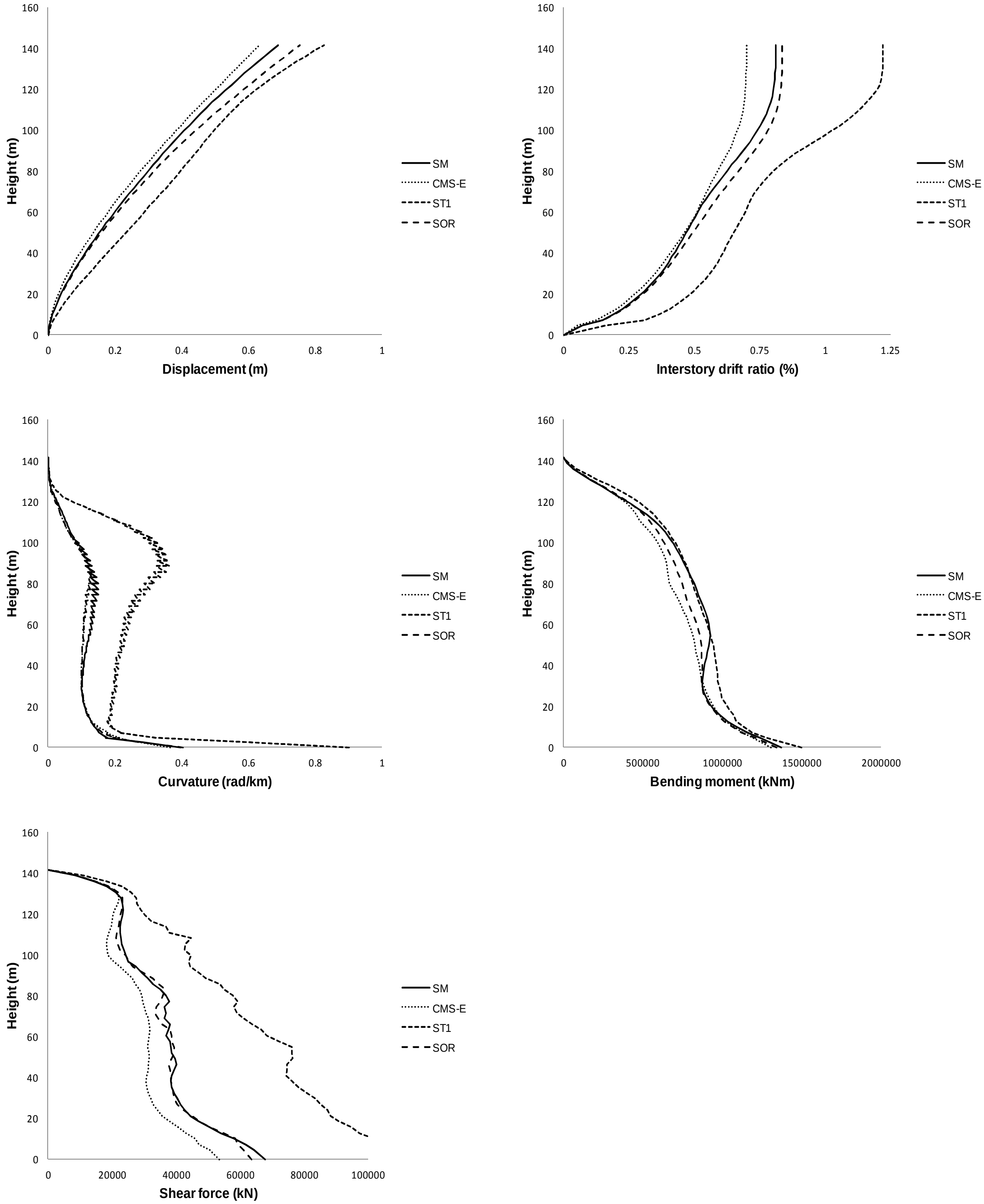

Figure 4.29 Comparison of demand parameters for 50 story wall with R_g = 4.1 using different sets of ground motions.

Table 4.3 Mean roof displacement demand using different sets of ground motions.

Mean Roof displacement (m)										
	R_g	**ST1**	**SM**	**SOR**	**CMS-E**	**CMS**				
Wall						**$2T_1$**	**$1.5T_1$**	**T_1**	**T_2**	**T_3**
10 story	1.7	-	0.119	0.117	0.114	0.088	0.111	**0.114**	0.040	-
	2.6	-	0.134	0.134	0.126	0.093	**0.126**	0.124	0.036	-
	4.2	-	0.190	0.183	0.169	0.138	**0.169**	0.138	0.032	-
30 story	1.4	0.456	0.437	0.434	0.431	-	0.331	**0.431**	0.141	0.055
	2.4	0.565	0.561	0.523	0.520	-	0.457	**0.520**	0.148	0.054
	3.1	0.615	0.651	0.565	0.586	-	0.531	**0.586**	0.158	0.055
	4.3	0.660	0.641	0.593	0.592	-	0.518	**0.592**	0.163	0.058
50 story	1.4	0.800	0.710	0.746	0.656	-	-	**0.656**	0.237	0.095
	2.1	0.891	0.810	0.818	0.771	-	-	**0.771**	0.262	0.103
	2.4	0.898	0.801	0.820	0.731	-	-	**0.731**	0.289	0.105
	4.1	0.830	0.690	0.754	0.635	-	-	**0.635**	0.267	0.095

Table 4.4 Mean interstory drift demand at the top of wall using different sets of ground motions.

Mean top wall interstory drift ratio (%)										
	R_g	**ST1**	**SM**	**SOR**	**CMS-E**	**CMS**				
Wall						**$2T_1$**	**$1.5T_1$**	**T_1**	**T_2**	**T_3**
10 story	1.7	-	0.55	0.55	0.52	0.40	0.50	**0.52**	0.24	-
	2.6	-	0.58	0.58	0.58	0.42	**0.58**	0.53	0.22	-
	4.2	-	0.86	0.84	0.76	0.62	**0.76**	0.65	0.19	-
30 story	1.4	0.96	0.78	0.81	0.80	-	0.56	**0.80**	0.36	0.17
	2.4	1.13	0.97	0.94	0.89	-	0.77	**0.89**	0.38	0.15
	3.1	1.16	1.06	0.97	0.96	-	0.85	**0.96**	0.39	0.15
	4.3	1.18	1.02	1.01	0.97	-	0.82	**0.97**	0.36	0.15
50 story	1.4	1.20	0.80	0.84	0.70	-	-	**0.70**	0.38	0.20
	2.1	1.25	0.88	0.90	0.76	-	-	**0.76**	0.41	0.22
	2.4	1.22	0.85	0.87	0.78	-	-	**0.78**	0.43	0.22
	4.1	1.22	0.81	0.84	0.70	-	-	**0.70**	0.39	0.18

Table 4.5 Mean base curvature demand using different sets of ground motions.

Mean base curvature (rad/km)										
	R_g	ST1	SM	SOR	CMS-E	CMS				
Wall						$2T_1$	$1.5T_1$	T_1	T_2	T_3
10 story	1.7	-	0.69	0.68	0.72	0.53	**0.72**	0.67	0.23	-
	2.6	-	0.96	1.02	0.88	0.59	0.83	**0.88**	0.23	-
	4.2	-	1.45	1.35	1.18	0.90	**1.18**	0.84	0.25	-
30 story	1.4	0.38	0.27	0.27	0.35	-	0.22	**0.35**	0.14	0.07
	2.4	0.63	0.37	0.41	0.45	-	0.29	**0.45**	0.18	0.08
	3.1	0.85	0.60	0.61	0.60	-	0.45	**0.60**	0.22	0.09
	4.3	1.08	0.99	0.86	0.74	-	0.58	**0.74**	0.23	0.09
50 story	1.4	0.36	0.16	0.15	0.12	-	-	**0.12**	0.08	0.06
	2.1	0.51	0.24	0.23	0.19	-	-	**0.19**	0.12	0.08
	2.4	0.57	0.28	0.28	0.23	-	-	**0.23**	0.15	0.09
	4.1	0.90	0.40	0.40	0.36	-	-	**0.36**	0.14	0.08

Table 4.6 Mean base shear demand using different sets of ground motions.

Mean base shear force (kN)										
	R_g	ST1	SM	SOR	CMS-E	CMS				
Wall						$2T_1$	$1.5T_1$	T_1	T_2	T_3
10 story	1.7	-	22747	22001	20531	13763	16129	16601	**20531**	-
	2.6	-	18924	17593	14504	10067	11714	12176	**14504**	-
	4.2	-	12207	11628	10014	7438	8708	8435	**10014**	-
30 story	1.4	46177	35985	34574	31706	-	21680	26077	**31706**	26344
	2.4	39855	29351	28582	23972	-	16055	21516	**23972**	22182
	3.1	38695	30478	29658	23969	-	16012	21069	**23969**	21791
	4.3	36307	24415	23899	21462	-	13895	17055	**21462**	18733
50 story	1.4	136331	76289	75949	71763	-	-	42584	62923	**71763**
	2.1	158176	75532	74984	71072	-	-	41092	61982	**71072**
	2.4	173146	75179	76618	69876	-	-	41020	61277	**69876**
	4.1	141076	67737	63476	53332	-	-	33130	53292	**53332**

4.7 Variability in Demand Parameters

Predicting variability in time history results is important to be considered for particular actions and structural elements. The Tall Building Initiative (PEER TBI 2010) recommends using $\mu+\sigma$ instead of μ for force-controlled actions such as punching shear failure of slabs, shear force demand in shear walls, and compressive strain of concrete in elements that do not have adequate confinement in order to reduce the probability of failure under such actions. Note that μ and σ are the mean and standard deviation of the structural response determined from time history analysis, respectively. The TBI specifies that a large number of records (20 to 30 records) is needed in order to obtain a reliable estimate of the scatter in demand parameters. The ATC 82 (2011), however, indicates that the conditional spectrum (Jayaram et al. 2011) is the only ground motion selection and scaling approach that provides a tool to predict the variability in demand parameters and other record selection schemes - such as record selection based on target magnitude and source to site distance - do not consider the variability in the spectral values.

The intent of this section is to compare the scatter and mean plus one standard deviation results using different ground motion selection and scaling schemes. The spectrum matched (SM) records cannot be used to estimate the dispersion in structural responses since the individual records are altered to match the target spectrum, a procedure which results in reducing dispersion in response parameters. Table 4.7 to 4.10 compares the coefficient of variation ($C_v = \sigma/\mu$) values from ST1 and SOR sets with the CMS envelope from various conditioning periods (denoted as "CMS-E").

Table 4.7 Coefficient of variation for roof displacement demand using different sets of ground motions.

		Coefficient of variation		
Wall	R_g	ST1	SOR	CMS-E
10 story	1.7	-	0.13	0.17
	2.6	-	0.38	0.34
	4.2	-	0.55	0.38
30 story	1.4	0.34	0.27	0.44
	2.4	0.47	0.35	0.33
	3.1	0.54	0.36	0.48
	4.3	0.65	0.44	0.52
50 story	1.4	0.40	0.35	0.38
	2.1	0.52	0.40	0.45
	2.4	0.53	0.39	0.51
	4.1	0.52	0.40	0.47

Table 4.8 Coefficient of variation for interstory drift demand at top of wall using different sets of ground motions.

		Coefficient of variation		
Wall	R_g	ST1	SOR	CMS-E
10 story	1.7	-	0.17	0.16
	2.6	-	0.33	0.36
	4.2	-	0.47	0.34
30 story	1.4	0.38	0.26	0.42
	2.4	0.40	0.32	0.38
	3.1	0.43	0.32	0.50
	4.3	0.50	0.35	0.58
50 story	1.4	0.49	0.33	0.44
	2.1	0.46	0.35	0.51
	2.4	0.47	0.32	0.49
	4.1	0.46	0.35	0.54

Table 4.9 Coefficient of variation for base curvature demand using different sets of ground motions.

		Coefficient of variation		
Wall	R_g	ST1	SOR	CMS-E
10 story	1.7	-	0.25	0.42
	2.6	-	0.71	0.81
	4.2	-	0.97	0.87
30 story	1.4	1.02	0.20	0.50
	2.4	0.91	0.59	0.79
	3.1	0.75	0.60	0.99
	4.3	0.66	0.62	1.07
50 story	1.4	1.30	0.29	0.34
	2.1	0.89	0.41	0.55
	2.4	0.82	0.46	0.62
	4.1	0.82	0.84	0.79

Table 4.10 Coefficient of variation for base shear force demand using different sets of ground motions.

		Coefficient of variation		
Wall	R_g	ST1	SOR	CMS-E
10 story	1.7	-	0.32	0.17
	2.6	-	0.36	0.19
	4.2	-	0.34	0.21
30 story	1.4	0.53	0.33	0.21
	2.4	0.63	0.35	0.30
	3.1	0.63	0.35	0.28
	4.3	0.77	0.34	0.32
50 story	1.4	0.71	0.34	0.21
	2.1	1.11	0.31	0.20
	2.4	1.05	0.33	0.19
	4.1	1.30	0.28	0.25

Tables 4.7 through 4.10 indicate that for the SOR ground motions, the coefficient of variation tend to increase as the force reduction factor increases. For base shear force demand, on the other hand, the C_v coefficient corresponding to the SOR set is relatively constant. The coefficient of variation is around 0.4 for roof displacement, interstory drift at the top of wall, and base shear force demands using the SOR ground motions. The coefficient of variation for base shear force demand determined using the ST1 set is much higher than those from the SOR records, while the lowest C_v values belong to the CMS-E case. Also note that coefficient of variation for base curvature demand is larger than that for other demand parameters.

Figure 4.30 compares mean plus one standard deviation ($\mu+\sigma$) results for four responses determined from the SOR ground motions with those from the CMS-E. It can be seen from Figure 4.30 that for roof displacement and interstory drift demands, the mean plus one standard deviation values for both sets are similar. For the base curvature demand, the $\mu+\sigma$ from the CMS-E is 84%, 110%, and 97% of the results determined using the SOR ground motions for the 10, 30, and 50 story walls with the highest force reduction factors, respectively. The base shear force demand using the CMS-E is consistently lower than the results from the SOR records, especially for the 50 story walls. The mean plus one standard deviation base shear force demands from the CMS-E were found to be between 80% and 90% of the $\mu+\sigma$ base shear force demands using the SOR ground motions.

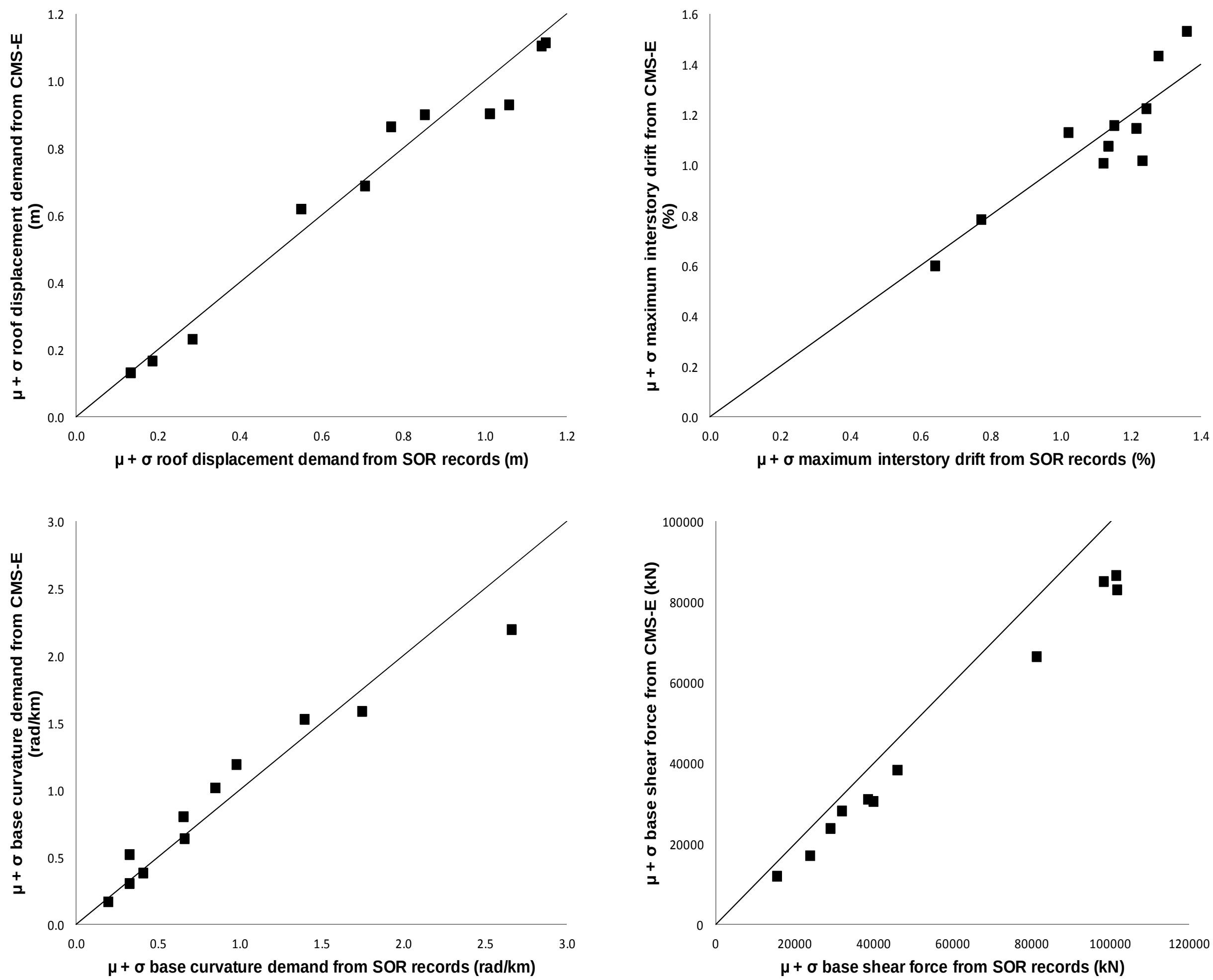

Figure 4.30 Comparison of mean plus one standard deviation results using SOR and envelope of CMS ground motions for roof displacement, interstory drift at top of wall, base curvature, and base shear force demands for 11 shear walls.

Time history results determined using the SOR ground motions will be used in Chapter 5 to develop simplified models for estimating flexural demands on cantilever shear walls. This is due to the fact that the mean demand parameters from the SM and SOR sets were found to be similar, yet the latter can be used to study the variability in different structural responses. It was also observed that for roof displacement, interstory drift, and base curvature demands, the mean plus one standard deviation results from the SOR and CMS sets are similar. The SOR ground motions will also be used in Chapter 6 to study the relationship between base shear force and base rotation demands because as it was observed in Section 4.6.1, different conditioning periods define the CMS envelope of base shear force and base curvature demands. Using the SOR ground motions, on the other hand, is less computational demanding for establishing such interaction diagrams.

4.8 Roof Displacement Demand Using ATC 55 Ground Motions

The purpose of the single-degree-of-freedom study conducted in Chapter 3 was to obtain effective stiffness such that the roof displacement from the linear model would be equal to the roof displacement demand determined from the nonlinear structure. A set of 40 records from ATC 55 project (ATC 2005) recorded on site class B and C was used as the input motions in the SDOF study. The 80 ground motions used in this chapter are more suitable for performing time history analysis of high-rise shear walls as the longest usable period for these ground motions was long enough to accommodate the period elongation of the first mode period of 50 story walls. A comparison of roof displacement demand from different methods for selecting and scaling ground motions showed good agreement (see Table 4.3). It is interesting to compare roof displacement demands of the eleven shear walls using ATC 55 ground motions with those using SM, SOR, and CMS ground motions. For this purpose, the ATC 55 ground motions were scaled to the UHS in two ways: at the fundamental period (denoted as ST1_A) and over a period range of $0.2T_1$ to $1.5T_1$ (denoted as SOR_A). Table 4.11 presents mean roof displacement demands using various sets of ground motions.

Table 4.11 indicates that the mean roof displacement from the SOR_A ground motions varies from 90% to 110% of the mean roof displacement from the SM records. The mean roof displacement results corresponding to the SOR_A set is 2%, 0%, and 4% higher than those associated with the CMS ground motions. Roof displacements from the ST1_A set is generally lower than those determined using the SOR_A set. Similar roof displacement demands from different sets of ground motions listed in Table 4.11 indicates that ATC 55 ground motions can be used in time history analysis if roof displacement is the demand parameter of interest. Determination of other responses such as curvature and shear force demands from time history analysis using ATC 55 ground motions is not recommended for high-rise shear walls with a fundamental period greater than 4.0 seconds since scaling these ground motions to the UHS for longer periods results in high spectral accelerations around higher mode periods. This can influence those structural responses that are dominated by higher mode effects.

Table 4.11 Comparison of mean roof displacement demand from ATC 55 ground motions (denoted as ST1_A and SOR_A) with mean roof displacement demand from other sets of ground motions.

			Mean roof displacement (m)			
Wall	R_g	SM	SOR	CMS-E	ST1_A	SOR_A
10 story	1.7	0.119	0.117	0.114	0.116	0.129
	2.6	0.134	0.134	0.126	0.124	0.153
	4.2	0.190	0.183	0.169	0.129	0.172
30 story	1.4	0.437	0.434	0.431	0.414	0.468
	2.4	0.561	0.523	0.520	0.475	0.587
	3.1	0.651	0.565	0.586	0.516	0.636
	4.3	0.641	0.593	0.592	0.510	0.591
50 story	1.4	0.710	0.746	0.656	0.751	0.735
	2.1	0.810	0.818	0.771	0.790	0.747
	2.4	0.801	0.820	0.731	0.785	0.749
	4.1	0.690	0.754	0.635	0.680	0.658

4.9 Evaluation of the Seven Ground Motion Set for Calculation of Mean Seismic Demands

In this section, the provisions of the ASCE7-05 standard (ASCE 2005) for calculating the design value are studied. According to this standard, if seven or more ground motions are used, the design value is considered to be the mean value of time history results, while if less than seven ground motions are used, the maximum value of response quantities is taken as the design value. It is necessary to evaluate how much the mean value of a given demand parameter varies as different sets of seven records are used as the input motion.

In theory, the possible number of *k* combinations of a set with *n* elements is called binomial coefficient and equals $\frac{n(n-1)(n-2)\ldots(n-k+1)}{k(k-1)(k-2)\ldots1}$ .The *k* factor is equal to 7 and *n* is the number of selected ground motions which is equal to 80, 53, and 35 for the 10, 30, and 50 story shear walls, respectively. In order to reduce the number of possible combinations to a practical number, the following criteria were applied:

1. Equal-area-under-the-curve approach was used to determine the scale factor required to match the individual ground motions to the UHS over a period range between $0.2T_1$ to $1.5T_1$.

2. One ground motion with the scale factor closest to 1.0 was chosen from a given earthquake.

The above criteria reduced the number of selected ground motions *n* to 12, 15, and 11 for the 10, 30, and 50 story walls, respectively. These sets are referred to as Set1, Set2, and Set3 hereafter. Table 4.12 to Table 4.14 presents the ground motion details for the three sets. Note that SF1 in these tables corresponds to the scale factor determined from the equal-area-under-the-curve criterion described above.

Table 4.12 Ground motion details for Set 1.

Event	Station	M_w	R (km)	SF1	SF2	SF
Nahanni, Canada, 1985	Site 1	6.76	9.6	0.76	1.19	0.91
Loma Prieta, 1989	UCSC 14 WAHO	6.93	17.47	0.83	1.19	0.99
Imperial Valley, 1979	Delta	6.53	22.03	1.25	1.19	1.50
Kobe, Japan, 1995	Kakogawa	6.9	22.5	1.57	1.19	1.88
Northridge, 1994	Pacific Palisades – Sunset	6.69	24.08	1.08	1.19	1.29
Landers, 1992	Joshua Tree	7.28	11.03	0.93	1.19	1.11
Hector Mine, 1999	Hector	7.13	11.66	1.28	1.19	1.53
Manjil, Iran, 1990	Abbar	7.37	12.56	0.88	1.19	1.05
Kocaeli, Turkey, 1999	Izmit	7.51	7.21	1.64	1.19	1.96
Duzce, Turkey, 1999	Duzce	7.14	6.58	0.65	1.19	0.78
Cape Mendocino, 1992	Petrolia	7.01	8.18	0.63	1.19	0.75
Tabas, Iran, 1978	Dayhook	7.35	13.94	1.39	1.19	1.66

Table 4.13 Ground motion details for Set 2.

Event	Station	M_w	R (km)	SF1	SF2	SF
Kobe, Japan, 1995	Shin-Osaka	6.9	19.15	1.30	1.05	1.37
Irpinia, Italy, 1980	Sturno	6.9	10.84	0.67	1.05	0.70
Nahanni, Canada, 1985	Site 1	6.76	9.6	1.13	1.05	1.19
Northridge, 1994	Canoga Park - Topanga Can	6.69	14.7	1.04	1.05	1.09
Loma Prieta, 1989	Gilroy Array #3	6.93	12.82	1.61	1.05	1.70
Imperial Valley, 1979	Delta	6.53	22.03	1.09	1.05	1.15
Superstition Hills, 1987	Wildlife Liquef. Array	6.54	23.85	1.13	1.05	1.19
Manjil, Iran, 1990	Abbar	7.37	12.56	1.01	1.05	1.06
Kocaeli, Turkey, 1999	Izmit	7.51	7.21	1.51	1.05	1.59
Duzce, Turkey, 1999	Duzce	7.14	6.58	0.64	1.05	0.68
Cape Mendocino, 1992	Rio Dell Overpass – FF	7.01	14.33	1.04	1.05	1.10
Tabas, Iran, 1978	Dayhook	7.35	13.94	1.87	1.05	1.97
Landers, 1992	Yermo Fire Station	7.28	23.62	0.86	1.05	0.91
Hector Mine, 1999	Amboy	7.13	43.05	1.21	1.05	1.28
St Elias, Alaska, 1979	Icy Bay	7.54	26.46	1.55	1.05	1.63

Table 4.14 Ground motion details for Set 3.

Event	Station	M_w	R (km)	SF1	SF2	SF
Imperial Valley, 1979	El Centro Array #4	6.53	7.05	1.01	1.11	1.12
Northridge, 1994	Tarzana - Cedar Hill A	6.69	15.6	0.70	1.11	0.78
Superstition Hills, 1987	Wildlife Liquef. Array	6.54	23.85	1.06	1.11	1.18
Kobe, Japan, 1995	OSAJ	6.9	21.35	1.74	1.11	1.93
Irpinia, Italy, 1980	Bisaccia	6.9	21.26	1.56	1.11	1.73
Hector Mine, 1999	Hector	7.13	11.66	1.39	1.11	1.54
Manjil, Iran, 1990	Abbar	7.37	12.56	1.16	1.11	1.28
Kocaeli, Turkey, 1999	Duzce	7.51	15.37	0.68	1.11	0.76
Duzce, Turkey, 1999	Duzce	7.14	6.58	0.58	1.11	0.65
Cape Mendocino, 1992	Rio Dell Overpass – FF	7.01	14.33	1.34	1.11	1.48
Landers, 1992	Yermo Fire Station	7.28	23.62	0.79	1.11	0.88

The ASCE7-05 standard also specifies that for 2-dimensional modelling, the mean value corresponding to the 5% damped response spectrum for a set of records should not be less than the target spectrum over the period range from $0.2T_1$ to $1.5T_1$. A similar approach was taken here for matching the mean spectrum of Set1, Set2, and Set3 to the target UHS: an additional scale factor was applied to ensure that the mean spectrum for each set does not fall below the UHS more than 10% at any period over the specified range. This additional scale factor is denoted as "SF2" in Tables 4.12 through 4.14, and is equal to 1.19, 1.05, and 1.11 for Set1, Set2, and Set3, respectively. Also presented in these tables is the total scale factor (denoted as "SF") for individual records, which is the product of SF1 and SF2 factors. Note that the SF factor for the ground motions in Sets1 through 3 is between 0.5 and 2.0. Figure 4.31 compares the mean spectrum of the three sets with the UHS.

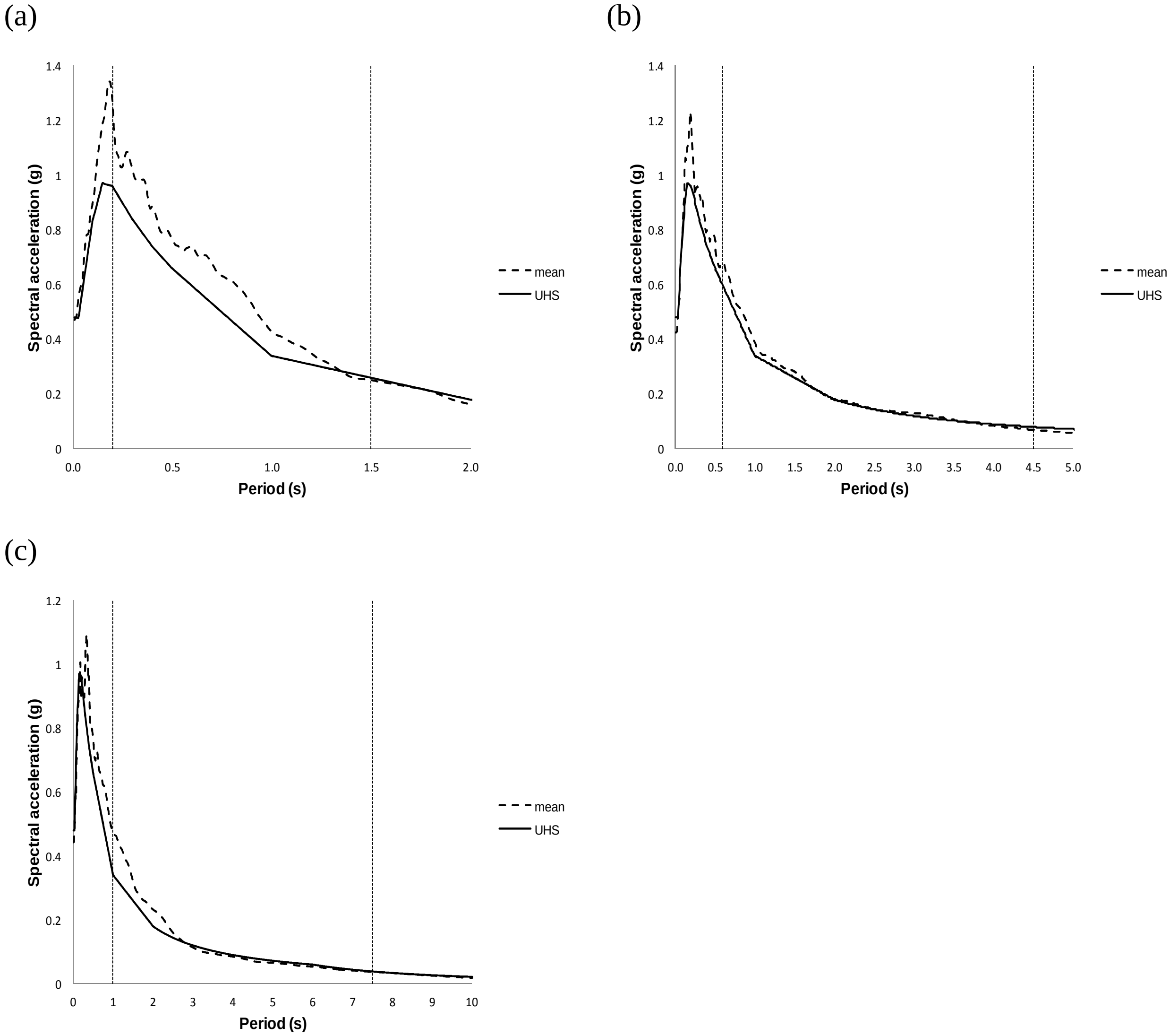

Figure 4.31 Comparison of mean spectrum for: (a) Set1, (b) Set2, and (c) Set3 ground motions with the UHS over the period range of $0.2T_1$ to $1.5T_1$.

The total possible combination of 7 out of 12, 15, and 11 ground motions is 792, 6435, and 330, respectively. Of these possible combinations, those sets of seven ground motions were considered that the corresponding mean spectrum does not fall below the UHS more than 10% at any period between $0.2T_1$ and $1.5T_1$. It turned out that 305, 1094, and 80 sets of seven records satisfied this criteria for the Set1, Set2, and Set3 ground motions, respectively. Time history analysis was conducted for the eleven shear walls using the scale factors presented in Tables 4.12 to 4.14, and the mean value of different demand parameters corresponding to potential sets of seven records was calculated. For each shear wall, the minimum and maximum value of the mean demand parameters from the 305, 1094, and 80 sets of seven records were reported. The results are presented in Figure 4.32. Table 4.15 summarizes the minimum and maximum ratios of demand parameters from different sets of seven ground motions to the mean response from spectrum matched records.

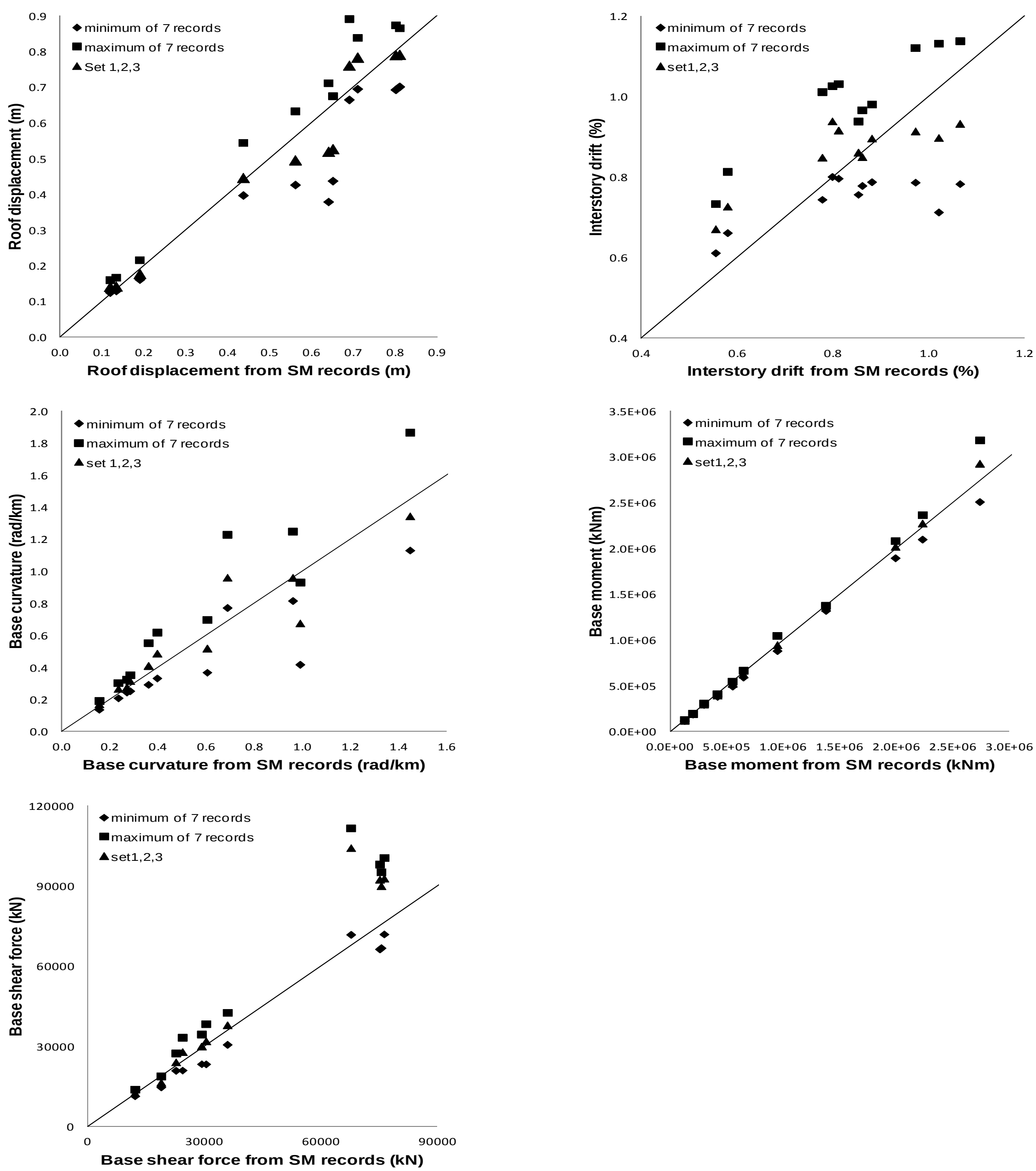

Figure 4.32 Comparison of minimum and maximum demand parameters from the sets of seven ground motions and Set1, Set2, and Set3 with the mean demands from spectrum matched (SM) ground motions.

Table 4.15 Minimum and maximum ratio of the mean response from the set of seven ground motions to the mean response from spectrum matched records (min/max, %).

Wall	R_g	RD[1]	ID[2]	BC[3]	BM[4]	BS[5]
10 story	1.7	105/134	110/132	112/179	99/104	93/121
	2.6	97/125	114/140	85/130	95/100	79/100
	4.2	85/114	90/112	78/129	94/103	94/115
30 story	1.4	91/125	96/130	91/120	94/111	86/119
	2.4	76/113	81/115	82/154	92/103	80/118
	3.1	67/104	74/107	61/116	90/100	77/126
	4.3	59/111	70/111	42/94	92/99	87/137
50 story	1.4	98/118	100/128	89/124	92/116	94/132
	2.1	87/107	89/111	89/129	94/106	89/126
	2.4	87/109	89/110	89/125	95/105	89/131
	4.1	96/129	98/127	84/156	96/100	106/165

[1] roof displacement demand, [2] interstory drift demand at the top of wall, [3] base curvature demand, [4] bending moment demand at the base, [5] base shear force demand.

Figure 4.32 indicates that mean roof displacement demand from the three sets varies between 81% and 110% of the mean roof displacement from the SM ground motions. The mean interstory drift corresponding to the three sets was found to be between 88% and 118% of the mean interstory drift from the SM ground motions. The mean base curvature demand associated with the three sets is between 68% and 123% of the mean base curvature demand using the SM records, while the mean bending moment demand at the base from the three sets varies between 96% and 107% of the mean base bending moment demand from the SM ground motions. Lastly, mean base shear force demand from the three sets is between 88% and 154% of the mean base shear force demand from the SM records. Therefore, reducing the number of ground motions from 80, 53, and 35 to 12, 15, and 11 results in demand parameters that are significantly different from those determined using spectrum matched ground motions.

It is also interesting to compare the average minimum and maximum values reported in Table 4.15 in order to observe how much on average the mean responses from the set of seven ground motions are different from the mean values associated with the SM ground motions. The average minimum ratio for the four response parameters and 11 walls (44 cases) is 88%. All but 9 of the minimum ratios are 80% or higher and only 6 of the minimum ratios are smaller than 75%. The lowest ratio of 42% is for base curvature of the 30 story wall with R_g = 4.3. The other low minimum ratios are for roof displacement and interstory drift for the same 30 story shear wall and base curvature for two other 30 story walls with R_g = 2.4 and 3.1. It was investigated whether the same seven ground motions caused the low minimum ratios; but this was not the case. A comparison of mean spectra from the critical seven ground motions resulting in the minimum ratios and mean spectra of the spectrum matched ground motions revealed a possible explanation only for the low ratio of 42% for the base curvature of the 30 story wall with R_g = 4.3. Figure 4.33 shows that the mean of seven records dropped well below the mean of the SM ground motions at periods less than $0.2T_1$ = 0.6 second. For the other low ratios, no significant difference is visible between the mean spectrum.

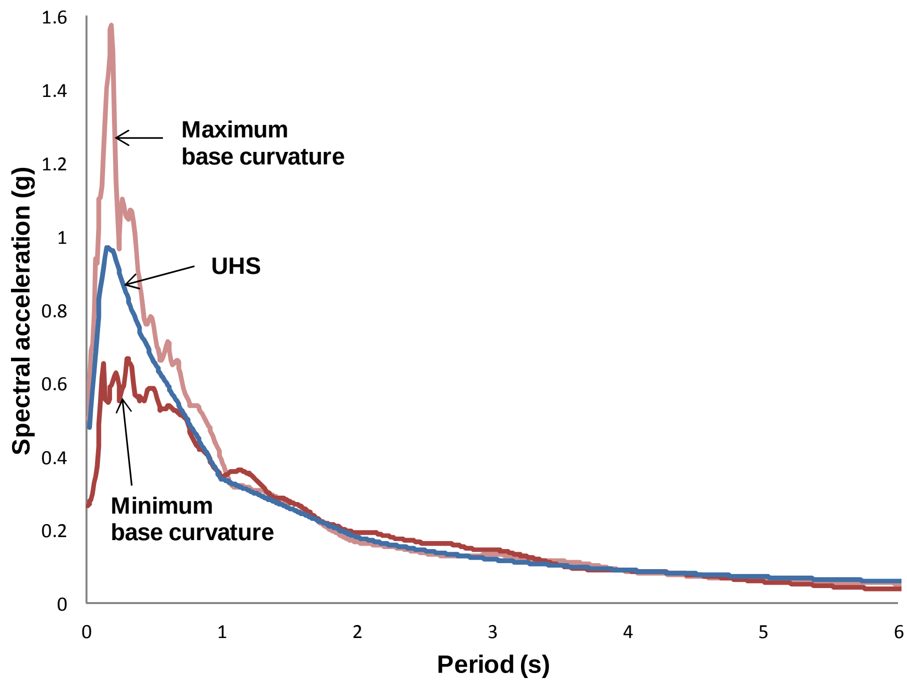

Figure 4.33 Comparison of mean spectrum of seven ground motions associated with maximum and minimum base curvature demand for the 30 story wall with R_g = 4.3 with the UHS.

The maximum ratios of mean response parameters determined using seven ground motions to mean response parameters determined using spectrum matched ground motions have an average value of 120% for the 44 different cases summarized in Table 4.15. All but 12 ratios are less than 130% and only 4 ratios are greater than 140%. The three large maximum ratios are base curvature for the 10 story wall with R_g = 1.7 (179%), base curvature for the 50 story wall with R_g = 4.1 (156%) and base shear force for the 50 story wall with R_g = 4.1 (165%). Examination of the mean spectra from the seven ground motion sets resulting in the large maximum ratios did not provide an explanation for the large ratios. For example, the mean of seven ground motions resulting in base curvature of the 50 story wall with R_g = 4.1 that are 156% of the result determined using spectrum matched ground motions only exceeds the UHS by a maximum of 30% over the range of $0.05T_1$ to $0.2T_1$ (see Figure 4.34).

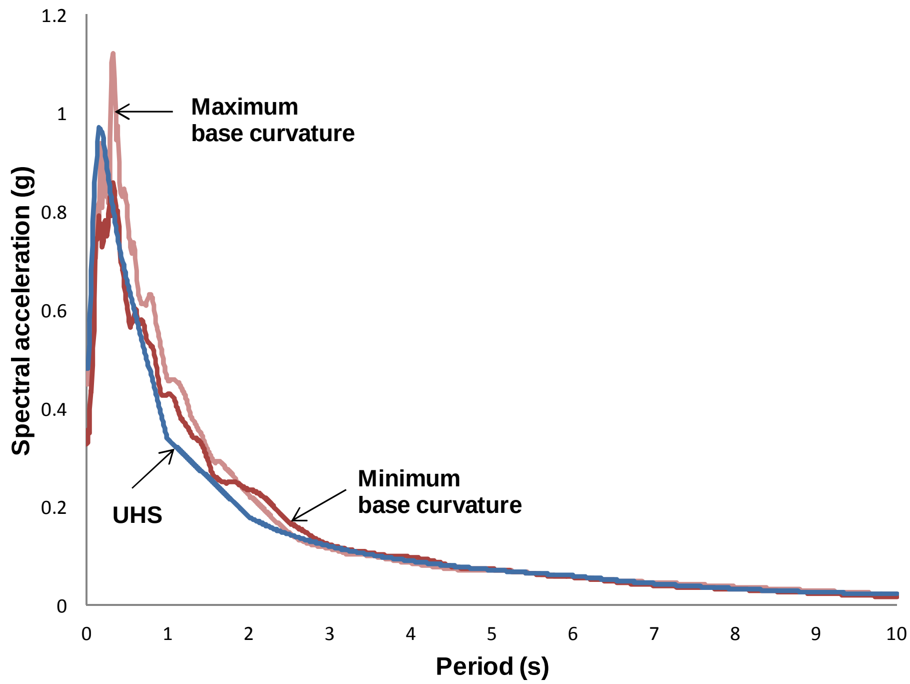

Figure 4.34 Comparison of mean spectrum of seven ground motions associated with maximum and minimum base curvature demand for the 50 story wall with R_g = 4.1 with the UHS.

4.10 Summary and Conclusions

As it was observed, multiple conditioning periods needs to be considered to estimate the largest response depending on the structural characteristics and the structural response under investigation. It was seen that choosing fundamental period as the conditioning period is appropriate for estimating roof displacement, top wall interstory drift, and base curvature demands in taller walls or walls with low force reduction factors, while for shorter walls with high R factors the results from CMS at $1.5T_1$ are larger. Higher mode periods must be considered for estimating midheight curvature and base shear force demands since choosing T_1 as the conditioning period significantly underestimates these parameters in taller buildings. It was also observed that a single conditioning period defined the mean envelope for displacement and interstory drift demands over the height, while multiple conditioning periods defined the mean envelope for curvature and shear force demands. It implies higher computational cost if CMS ground motions are used to develop a design envelope for these structural responses.

It was found that the mean roof displacement and mean interstory drift at the top of walls using ground motions matched to the CMS at different conditioning periods is between 90 and 100% of the mean values from the spectrum matched (SM) records. For base curvature and base shear force demands, on the other hand, the mean results from the CMS ground motions are generally higher than 80% of the base curvature and base shear force demands from the SM records. The results from SM ground motions are very similar to the mean results using the SOR ground motions (with maximum difference of 12%, 8%, 12%, and 7% for roof displacement, interstory drift at the top of wall, base curvature, and base shear force demands, respectively). It was also observed that scaling only at the fundamental period gives mean roof displacement demands that are 20% higher than those associated with the SM records, while it results in a large overestimation of the influence of higher modes on the base shear force and on midheight curvature demands in taller shear wall buildings. Lastly, mean plus one standard deviation roof displacement, interstory drift at the top, and base curvature demands from the ground motions matched to the CMS at different conditioning periods are generally higher than 90% of those associated with SOR ground motions. For base shear force demand, the mean plus one standard deviation results from CMS records were found to be about 80% of the results using SOR ground motions.

The provisions of the ASCE standard 7-05 for calculating the design value were studied. It was shown that the mean design values from a potential set of seven ground motions can vary from about 0.5 to 1.5 times the corresponding mean results from the SM ground motions. This clearly shows that the set of seven ground motions is not adequate for establishing the mean design values. Comparison between the mean spectra resulting the minimum and maximum ratios for a specific demand parameter showed no significant difference.

Findings of this study indicate that using SM ground motions results in demand parameters that are close to the results associated with the SOR records, yet fewer number of input records can be used because using spectrum matched ground motions reduces the variability in the structural responses considerably. The demand parameters corresponding to the records matched to the CMS are generally lower than those from the spectrum matched records; however, it should be noted that the conditioning periods used in this work were limited to the first three modal periods as well as two periods representing the fundamental period elongation due to nonlinearity. Any other period may be considered as the conditioning period with corresponding demand parameters more critical than those associated with conditioning periods considered in this study. Including more conditioning periods will increase the computational cost of the time history analysis.

Chapter 5 : Flexural Demands on Cantilever Shear Walls

5.1 Overview

In this chapter, results from nonlinear time history analysis are used to develop simplified models for estimating flexural demands on cantilever shear walls. Mean roof displacement from time history analysis is used to determine appropriate effective stiffness values to be used in response spectrum analysis as a confirmation of the work done in Chapter 3. The current equations of CSA A23.3 and ACI 318-05 (ACI Committee 2005) codes for estimating base curvature demands are evaluated, and models are developed to estimate mean and mean plus one standard deviation base curvature demand. The intensity of curvature demands around the midheight is evaluated, and a simplified curvature envelope is introduced to predict curvature demands over the height. Also, a simplified envelope is proposed for estimating interstory drift demands over the height. The influence of shear deformation and the flexibility of the base on various response parameters is also studied in this chapter. Time history results determined using the trilinear bending moment - curvature relationship is compared with those using the elastic-perfectly-plastic (EPP) hysteretic model. Lastly, a modified response spectrum analysis is introduced as a method to estimate curvature and interstory drift demands.

5.2 Example Shear Wall Buildings and Ground Motions Used in Time History Analysis

Thirteen cantilever shear walls were included in this chapter. That is, three 10 story walls with R_g = 1.7, 2.6, and 4.2; one 20 story wall with R_g = 4.0; four 30 story walls with R_g = 1.4, 2.4, 3.1, and 4.3; one 40 story wall with R_g = 4.4; and four 50 story walls with R_g = 1.4, 2.1, 2.4, and 4.1. The structural characteristics of these walls were presented in Table 2.2. The 20 and 40 story walls had minimum longitudinal reinforcement and were added to investigate the midheight yielding phenomenon in high-rise shear walls.

Time history results presented in this chapter correspond to the “scaled over the range” ground motions (denoted as SOR in Chapter 4). Using SOR ground motions allows to study the variability in the demand parameters while it resulted in mean responses similar to those determined using spectrum matched (SM) ground motions. To develop scaled over the range ground motions for the 20 and 40 story walls, a subgroup of 62 ground motions for T_1 = 2.0 seconds and 40 ground motions for T_1 = 4.0 seconds were selected from the set of 80 records. Figure 5.1 shows the mean spectrum of the two suites of records. It can be seen from these figures that the mean spectrum matches the UHS over a period range wider than $0.2T_1$ to $1.5T_1$ as recommended by ASCE standard 7-05.

(a) (b)

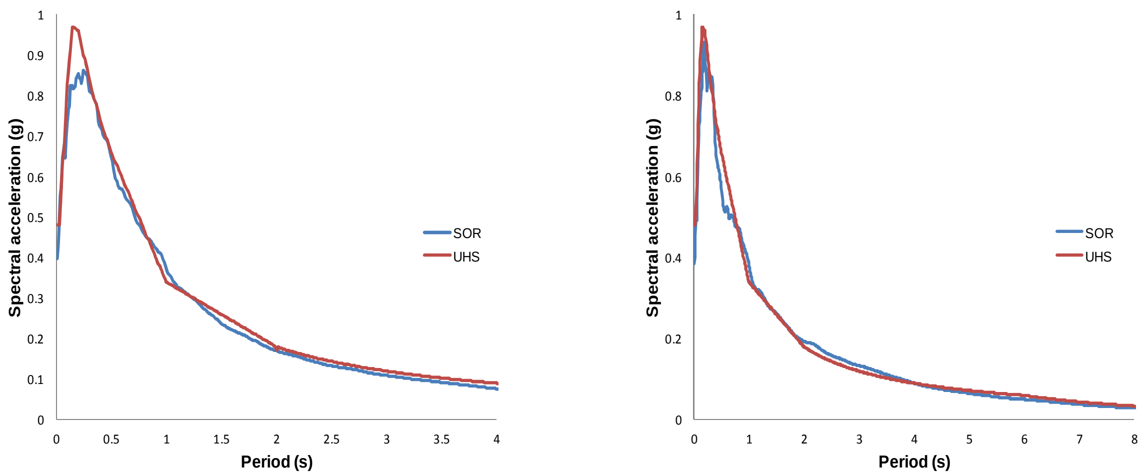

Figure 5.1 Comparison of the mean spectrum of ground motions scaled to the UHS over the period range (denoted as SOR) with the UHS for: (a) a 20 story shear wall with T_1 = 2.0 s, and (b) a 40 story wall with T_1 = 4.0 s.

5.3 Roof Displacement Demands of Shear Walls

Effective stiffness of cantilever shear walls using SDOF oscillators was extensively investigated in Chapter 3. Similar approach is taken in this part in order to determine appropriate effective stiffness values for use in response spectrum analysis (RSA). RSA was used as a potential tool to obtain linear displacements since it is the primary method used by practicing engineers in Canada, yet it requires less computational effort compared to linear time history analysis. The input parameters to perform RSA are the design spectrum, damping, and the structural characteristics of the building. In this work, the UHS shown in Figure 5.1 and 5% damping were considered as the input parameters. The linear displacements from different modes were combined using Complete Quadratic Combination (CQC) method. The first four modes were considered as the potential important modes although the first mode is usually the governing mode for determining roof displacements.

Appropriate effective stiffness values are determined such that the roof displacement from RSA matches the mean roof displacement from the time history analysis. A stiffness reduction factor of 1.0 was assumed as the first guess and it was reduced iteratively until the best match for roof displacement was achieved. Lower reduction factors must be used for walls with higher nonlinear action. Figures 5.2 through 5.5 compare the mean displacement profile from time history analysis with the displacement profile from RSA for the 13 shear walls. Note that the force reduction factor shown in these figures is the ratio of elastic bending moment corresponding to effective stiffness EI_e at the base of the wall to the wall flexural strength M_n. Table 5.1 compares the force reduction factors corresponding to uncracked flexural stiffness EI_g and effective flexural stiffness EI_e. Force reduction factors corresponding to effective flexural stiffness are denoted as R hereafter. Also shown in Figures 5.2 through 5.5 are the displacement envelopes from RSA using stiffness reduction factors proposed by CSA A23.3-04, which can be determined from the following equation:

$$\alpha = \frac{EI_e}{EI_g} = 0.6 + \frac{P}{f_c' A_g} \qquad Eq\ 5.1$$

where P is the axial force at the base of the wall due to gravity loads.

Table 5.1 Force reduction factor corresponding to uncracked and effective flexural stiffnesses.

Wall	R_g[1]	R[2]
10 story	1.7	1.7
	2.6	2.3
	4.2	3.2
20 story	4.0	2.7
30 story	1.4	1.4
	2.4	2.0
	3.1	2.3
	4.3	3.1
40 story	4.4	3.6
50 story	1.4	1.3
	2.1	1.8
	2.4	2.0
	4.1	3.7

[1] based on gross (uncracked) flexural stiffness EI_g, [2] based on effective stiffness EI_e which results in roof displacement demand equal to the mean roof displacement demand from time history analysis.

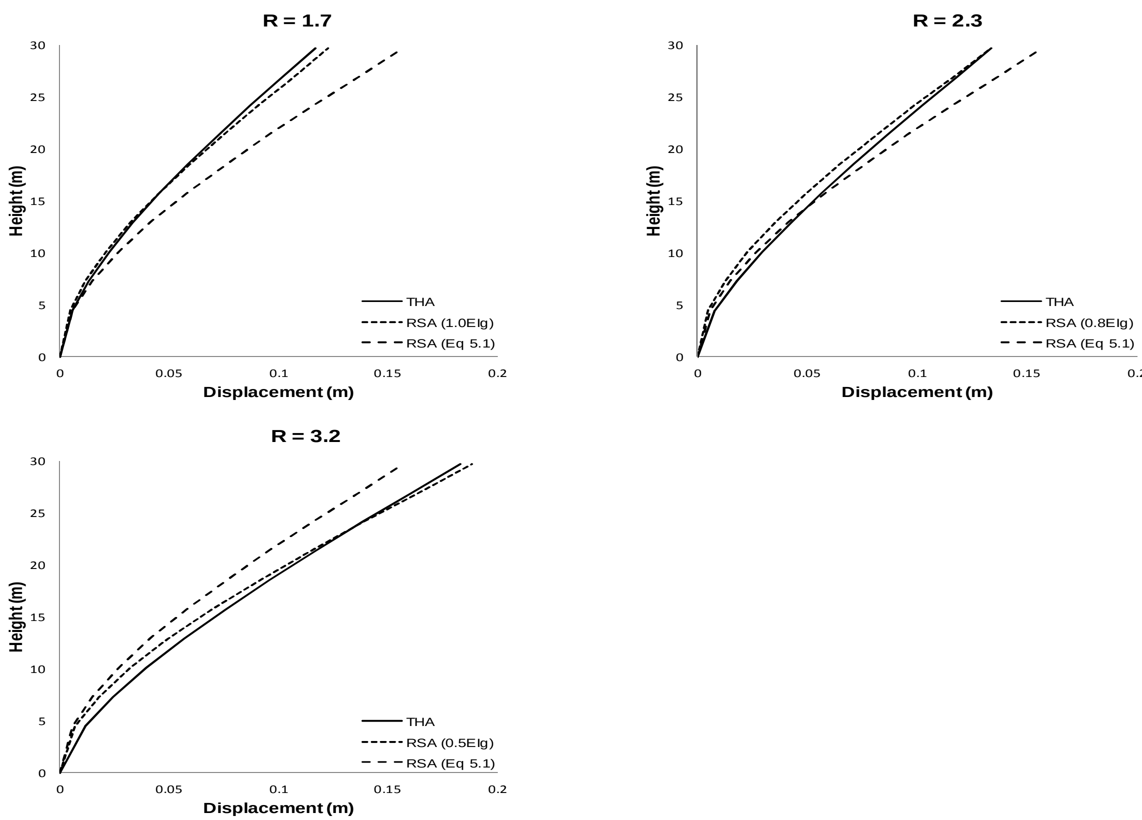

Figure 5.2 Comparison of mean displacement profile determined from time history analysis (denoted as THA) with displacement envelope from response spectrum analysis (denoted as RSA) for 10 story walls with different force reduction factors.

(a) (b)

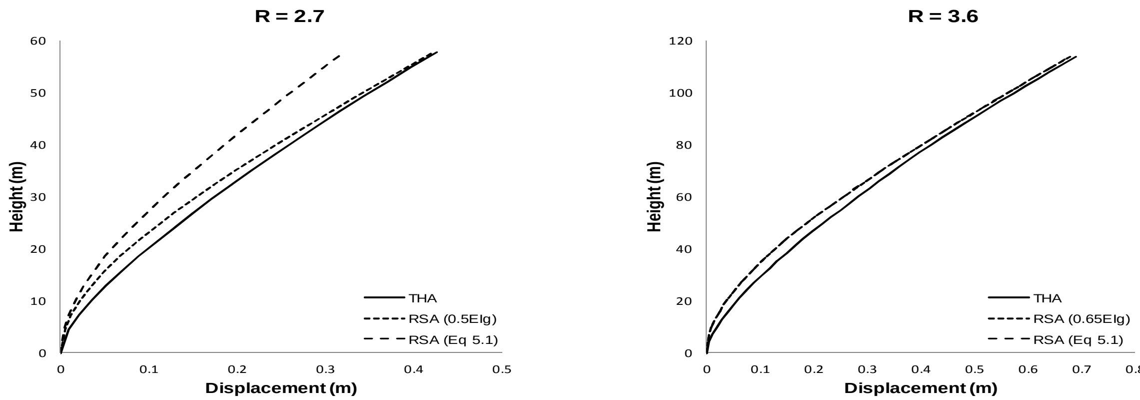

Figure 5.3 Comparison of mean displacement profile determined from time history analysis (denoted as THA) with displacement envelope from response spectrum analysis (denoted as RSA) for: (a) 20 story wall with R = 2.7, and (b) 40 story wall with R = 3.6.

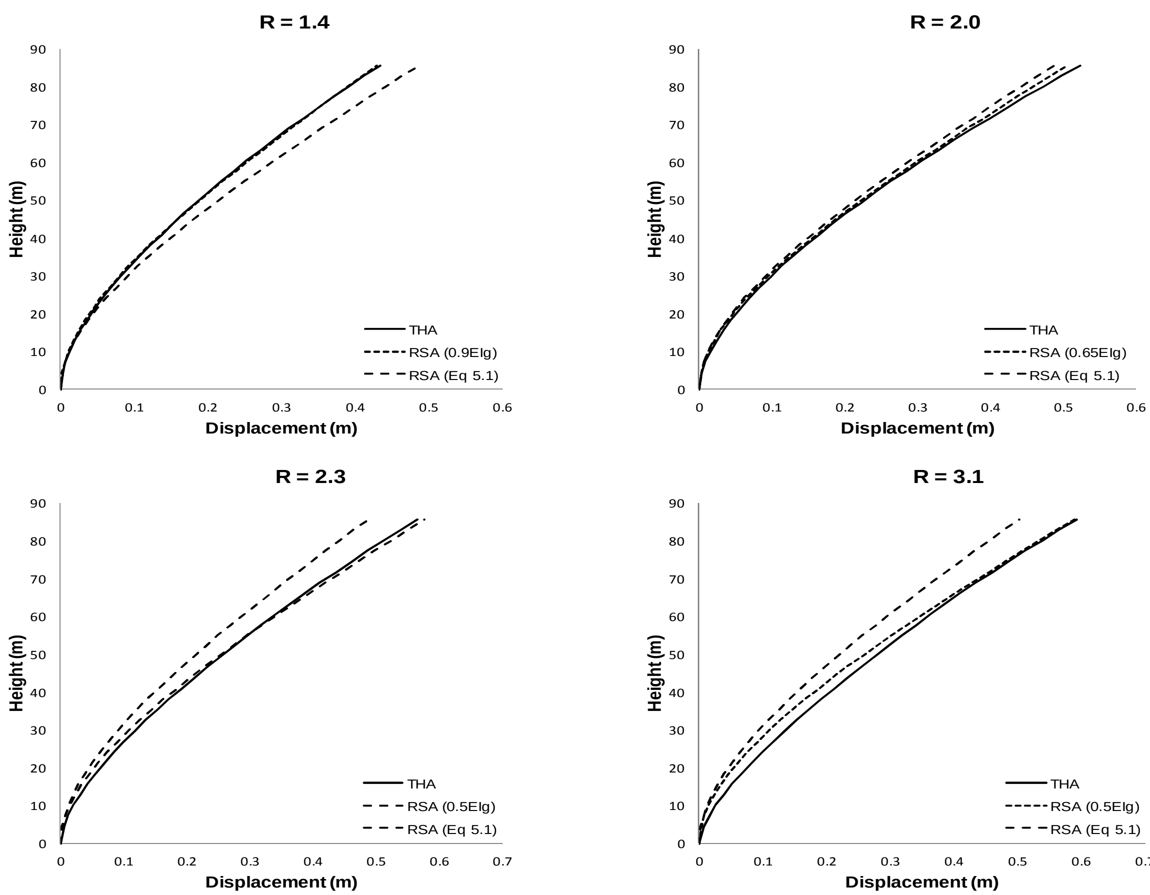

Figure 5.4 Comparison of mean displacement profile determined from time history analysis (denoted as THA) with displacement envelope from response spectrum analysis (denoted as RSA) for 30 story walls with different force reduction factors.

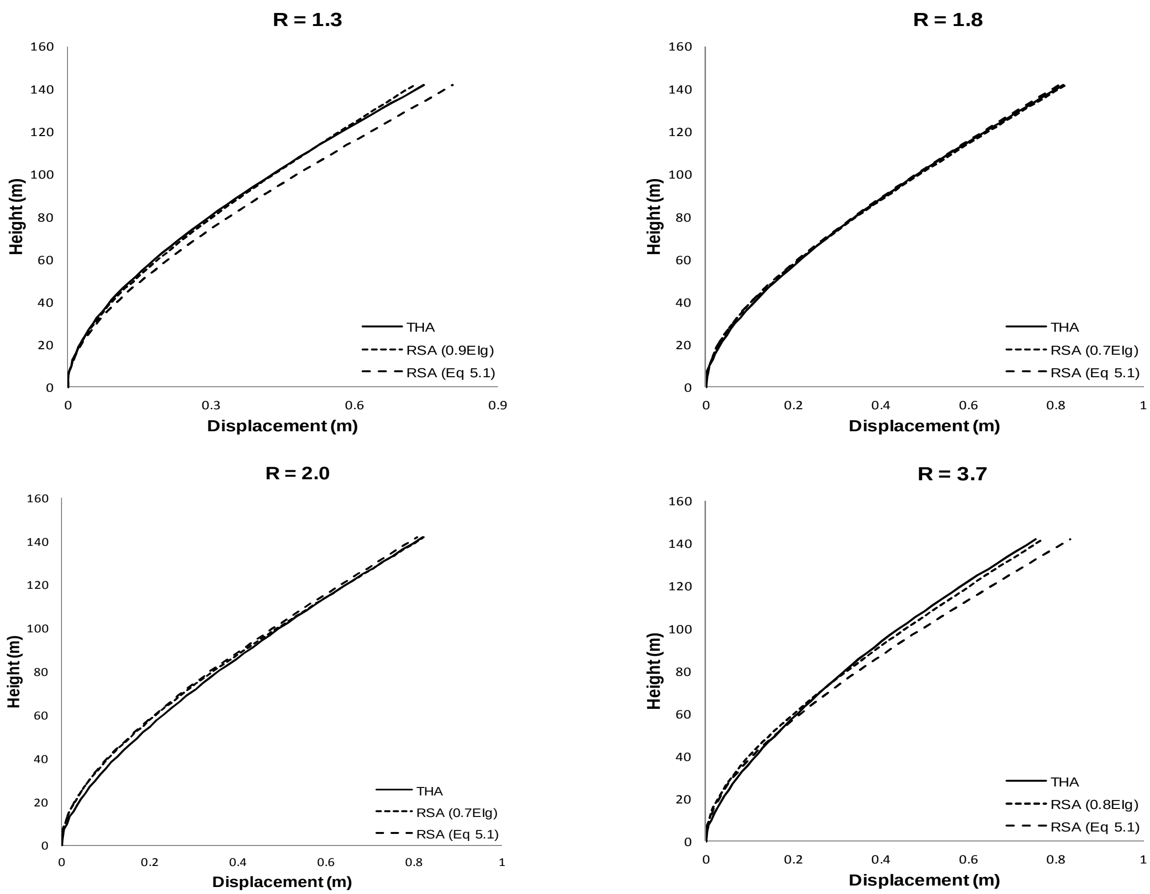

Figure 5.5 Comparison of mean displacement profile determined from time history analysis (denoted as THA) with displacement envelope from response spectrum analysis (denoted as RSA) for 50 story walls with different force reduction factors.

Figures 5.2 to 5.5 indicate that stiffness reduction factor generally drops from 1.0 to 0.5 as the force reduction factor increases. Stiffness reduction factors from the CSA approach result in higher roof displacement demands for walls with lower force reduction factors but lower roof displacement demand for walls with higher *R* values. Also, the CSA approach is based on the axial compression force and therefore it gives equal roof displacement demand for the 10 story walls with different force reduction factors. Stiffness reduction factor for the 40 story wall and 50 story wall with $R = 3.7$ is higher than those associated with 10 to 30 story walls with highest *R* factor. It means that the mean roof displacement of the nonlinear structure is approximately equal to the roof displacement demand of the linear structure, which is consistent with the equal displacement principle.

It should be noted that although response spectrum analysis can predict roof displacements accurately, it still underestimates the displacements at lower floors. It is mainly attributed to the fact that using RSA is restricted to linear structures, while the actual deformation profile from time history analysis is affected by yielding over the base plastic hinge region which results in higher rotations and deformation at lower floors.

Figure 5.6 plots the stiffness reduction factor α as a function of force reduction factor R for the 13 shear walls. The following equation was proposed for estimating stiffness reduction factor:

$$\alpha = \frac{EI_e}{EI_g} = 1.4 - 0.4R \geq 0.5 \qquad Eq\ 5.2$$

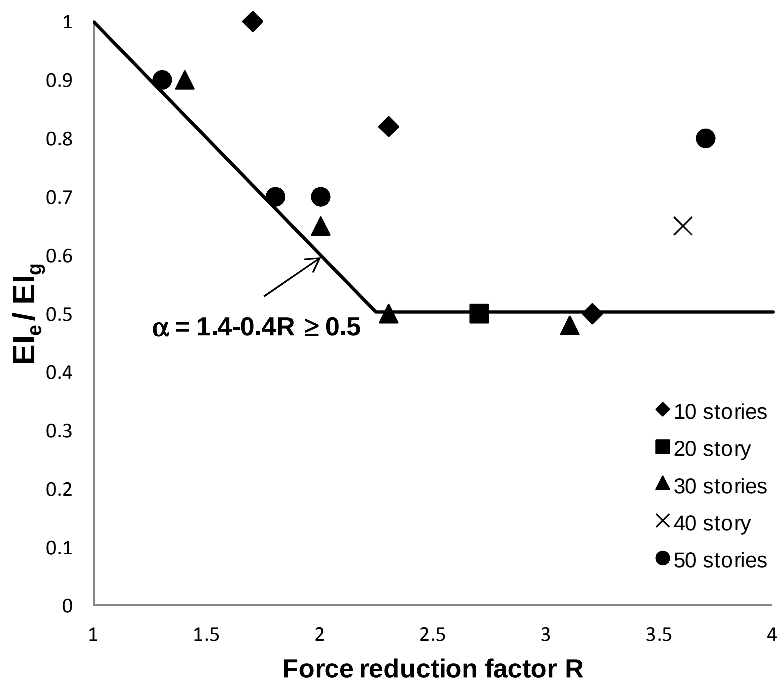

Figure 5.6 Stiffness reduction factor as a function of R for the thirteen walls.

5.4 Curvature Demands of Shear Walls

In this section, the CSA A23.3-04 approach for predicting base curvature demand is reviewed. The ACI 318-05 provision on limiting compression strain depth to avoid confinement steel is converted to a simple equation for predicting base curvature demand. Revised equations for estimating base curvature corresponding to the mean and mean plus one standard deviation response will be introduced. A new model for predicting midheight curvature will be presented. The section ends with the introduction of a curvature profile that addresses the realistic distribution of curvature demands over the height of cantilever shear walls.

5.4.1 Base Curvature Demands

5.4.1.1 Estimating Base Curvature Demand Using CSA and ACI Approaches

According to CSA A23.3-04 provisions, the ductility of concrete shear walls is evaluated by ensuring that the inelastic rotational capacity of wall, θ_{ic}, is greater than the inelastic rotational demand, θ_{id}. The inelastic rotational capacity can be determined from the following equation:

$$\theta_{ic} = (\phi_c - \phi_y) l_p \qquad Eq\ 5.3$$

where ϕ_c is the curvature capacity and is equal to the ratio of maximum compressive strain of concrete (0.0035 for unconfined concrete) to neutral axis depth c, ϕ_y is the yield curvature and is assumed to be the ratio of 0.004 to the wall length l_w, and l_p is the plastic hinge length and is assumed to be $0.5 l_w$. The inelastic rotational demand of concrete walls can be estimated from the following equation:

$$\theta_{id} = \frac{\Delta_{id}}{h_w - 0.5 l_p} \qquad Eq\ 5.4$$

where h_w is the wall height and the inelastic displacement demand Δ_{id} equals the total displacement demand Δ_t minus the elastic displacement demand Δ_e. According to CSA A23.3-04 provisions, the elastic displacement demand can be taken as the ratio of total displacement demand to the force reduction factor R, i.e. $\Delta_e = \Delta_t / R$ (Adebar et al. 2004). Base curvature demands ϕ_d can be determined by equating Equation 5.3 and 5.4:

$$\phi_d = \phi_y + \frac{2}{l_w} \frac{\Delta_t (1 - \frac{1}{R})}{h_w - 0.25 l_w} \qquad Eq\ 5.5$$

Another possible approach is to relate base curvature demands to global drift ratio Δ_t / h_w. According to ACI 318-05, confinement steel must be provided if the compression strain depth c exceeds:

$$c \geq \frac{l_w}{600(\frac{\Delta_t}{h_w})} \qquad Eq\ 5.6$$

Setting a maximum compressive strain of 0.003 for unconfined concrete and substituting c with $0.003/\phi_d$ gives:

$$\phi_d = \frac{1.8 \Delta_t}{h_w l_w} \qquad Eq\ 5.7$$

Note that Equation 5.7 is an implied equation in ACI 318-05 for predicting base curvature demand. The predictions from Equation 5.7 is referred to in this study as ACI 318.

5.4.1.2 Relationship Between Base Curvature and Roof Displacement Demands

Both CSA and ACI approaches (i.e. Equations 5.5 and 5.7) relate maximum base curvature demand to maximum roof displacement demand. Although this assumption is valid for first mode elastic response, the response quantities determined from nonlinear time history analysis can be affected by structural as well as ground motion characteristics. Consequently, the relationship between various demand parameters determined from nonlinear time history analysis can be different from that determined using elastic analysis, a phenomenon associated with the influence of higher modes on structural response quantities. To investigate higher mode effects in cantilever shear walls, roof displacement and base curvature time histories for three 10, 30, and 50 story walls were examined. The R factor corresponding to these walls is 3.2, 3.1, and 3.7, respectively. Only 30 records out of 80 ground motions were studied for the 10 story wall, while all ground motions were considered for the 30 and 50 story walls. Figures 5.7 to 5.9 summarize the results.

Figure 5.7 indicates that base curvature demands at the instant of maximum roof displacement are very close to the maximum base curvature for the majority of ground motions. Also, maximum base curvatures tend to increase as the roof displacement demand at the instant of maximum base curvature increases. The displacement profile over the height at the time when maximum base curvature occurs is similar to the first mode displacement profile. The plots for the 30 and 50 story walls, on the other hand, are significantly different. That is, base curvature demands at the instant of maximum roof displacement are much lower than the maximum base curvature demands. There is no correlation between the roof displacement demand at the instant of maximum base curvature and maximum base curvature demand. Also, for the 30 and 50 story walls, the shape of displacement profiles at the instant of maximum base curvature are influenced by higher mode response for some ground motions.

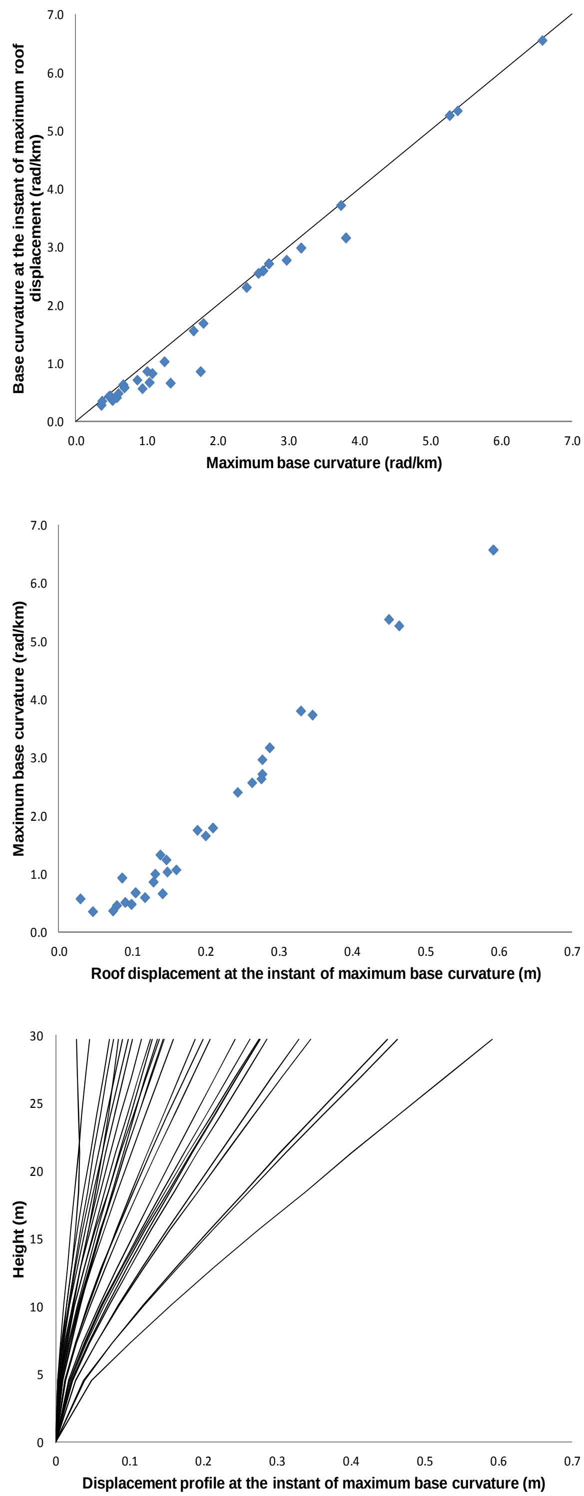

Figure 5.7 Relationship between base curvature and roof displacement demands for the 10 story wall with R = 3.2.

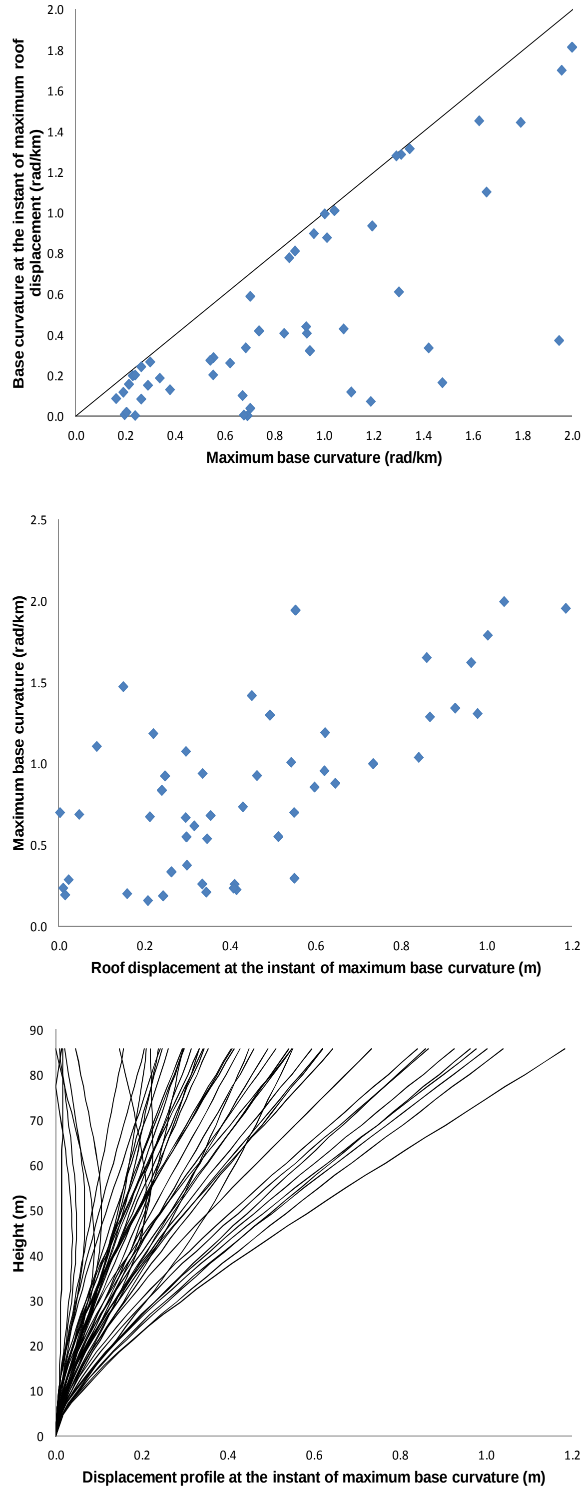

Figure 5.8 Relationship between base curvature and roof displacement demands for the 30 story wall with R = 3.1.

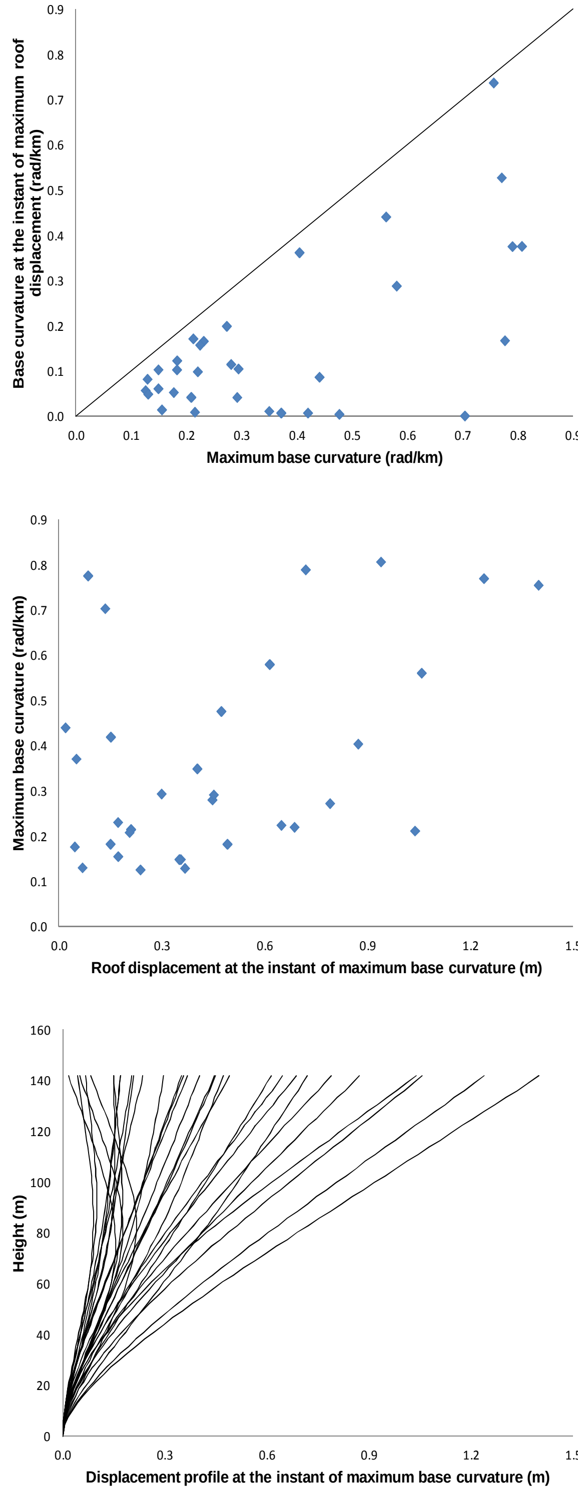

Figure 5.9 Relationship between base curvature and roof displacement demands for the 50 story wall with R = 3.7.

Time history results shown in Figures 5.7 through 5.9 indicate that for 30 and 50 story walls, the influence of higher modes caused maximum base curvature and roof displacement demands occur at different instants. For the 10 story wall, on the other hand, maximum base curvature and maximum roof displacement occur simultaneously, which indicates that first mode is the dominant mode of vibration. It is necessary to mention that the CSA and ACI approaches to estimate base curvature demands is relatively straightforward since it relates base curvature demand to the roof displacement demand, a parameter that can be determined accurately if appropriate stiffness reduction factors, such as those presented in Figure 5.6, are used in response spectrum analysis. This makes using roof displacement as the input parameter to estimate base curvature demands appealing. This approach will be adopted in Section 5.4.1.4, in which a refined model will be developed for predicting base curvature demands.

5.4.1.3 Evaluation of CSA A23.3-04 Approach for Predicting Base Curvature Demands

There are three pieces of information required to estimate the base curvature demand from the CSA approach (see Equation 5.5): yield curvature ϕ_y, elastic displacement demand Δ_e, and also total displacement demand itself. The focus in this section is on the yield curvature and elastic displacement demand, as the method to determine roof displacement demands was already discussed in Section 5.3.

5.4.1.3.1 Estimating Yield Curvature

There are different recommendations for the yield curvature of concrete shear walls. Paulay (2001) estimated the curvature at first yield of reinforcement is about $0.0026/l_w$ in walls with small flexural compression zone, while Wallace (2007) used $0.0025/l_w$ to $0.003/l_w$ for estimating yield curvature. Englekirk (2007) chose $0.0033/l_w$, and Adebar et al. (2005) concluded that $0.004/l_w$ is a upper bound estimate of the yield curvature.

One of the input parameters for the trilinear hysteretic bending moment - curvature relationship used to perform time history analysis is the upper-bound yield curvature $\phi_{y,UB}$, a parameter that represents the yield curvature for a wall that is loaded monotonically to yield without having been previously cracked (Adebar and Ibrahim 2002). The upper bound yield curvature is a function of axial compression force and longitudinal reinforcement, and it accounts for the influence of tension stiffening on the response of uncracked walls. Table 5.2 summarizes this parameter for the 13 shear walls.

Table 5.2 Upper-bound yield curvature times wall length for the range of walls used in time history analysis.

Wall	R	$P/(f_c^{'}A_g)$	$\phi_{y,UB}l_w$
10 story	1.7	0.059	0.0032
	2.3	0.059	0.0029
	3.2	0.059	0.0028
20 story	2.7	0.087	0.0026
30 story	1.4	0.101	0.0031
	2.0	0.101	0.0031
	2.3	0.101	0.0033
	3.1	0.061	0.0023
40 story	3.6	0.062	0.0024
50 story	1.3	0.127	0.0033
	1.8	0.127	0.0035
	2.0	0.127	0.0042
	3.7	0.062	0.0023

Table 5.2 indicates that the upper bound yield curvature is generally greater than $0.003/l_w$ for most walls, except those with minimum amount of vertical reinforcement and low axial compression force, e.g. 20, 30, 40, and 50 story walls with the highest force reduction factors. These walls yield at lower curvatures because high tension stiffening in such walls causes the bending demands reach the nominal bending moment capacity M_n at lower curvatures. Based on the values shown in Table 5.2, the value of $0.0026/l_w$ proposed by Paulay (2001) seems to underestimate the yield curvature for the majority of walls, while the recommended value of $0.004/l_w$ by Adebar et al. (2005) is a safe upper bound. It should be noted that CSA A23.3-04 uses $0.004/l_w$ as the yield curvature in Equation 5.5.

5.4.1.3.2 Estimating Elastic Displacement

One of the assumptions of CSA A23.3-04 approach for estimating base curvature demands is that the elastic potion of total roof displacement demand is equal to the ratio of total displacement demand to force reduction factor R. In this section, the results from time history analysis will be used to compute elastic portion of total displacement demand at the roof. Equation 5.5 was rearranged in order to obtain elastic portion of roof displacement:

$$\Delta_e = \Delta_t - (\phi_d - \phi_y) l_p (h_w - 0.5 l_p) \qquad Eq\ 5.8$$

Elastic displacement for individual records was calculated using maximum base curvature ϕ_d and maximum roof displacement Δ_t demands determined from time history analysis. Two values of $0.0025/l_w$ and $0.004/l_w$ were considered as the lower bound and upper bound estimates for the yield curvature. Plastic hinge length l_p was found to vary between 0.47 and 0.72 times the wall length using the Bohl and Adebar (2011) equation:

$$l_p = 0.2 l_w + 0.05 h_w \qquad Eq\ 5.9$$

Therefore, two values of $0.5l_w$ and $0.7l_w$ were considered as the lower bound and upper bound estimate of the plastic hinge length for the thirteen walls. The elastic displacement was computed from Equation 5.8 for two cases of (1) $0.0025/l_w$ for the yield curvature and $0.5l_w$ for the plastic hinge length, and (2) $0.004/l_w$ for the yield curvature and $0.7l_w$ for the plastic hinge length. Figure 5.10 presents the ratio of elastic to total displacement for individual motions. Also shown in this figure are the mean and mean minus one standard deviation values for the 13 walls.

Figure 5.10(a) indicates that CSA A23.3-04 assumption for predicting elastic portion of roof displacement demand (i.e. $\frac{\Delta_e}{\Delta_t} = \frac{1}{R}$) gives elastic displacements that are consistently lower than μ-σ values from time history analysis. This implies that the approach taken by CSA A23.3-04 for estimating base curvature demands gives conservative results for most cantilever walls, especially for taller walls if Equation 5.5 is computed based on yield curvature and plastic hinge length equal to $0.004/l_w$ and $0.5l_w$, respectively. The results in Figure 5.10(b) indicate that the CSA approach gives elastic displacements that are closer to μ-σ ratios from time history analysis for the majority of walls.

There are some data points in Figure 5.10 with negative elastic displacements or elastic displacement demands that are greater than the total roof displacement demand. Negative elastic displacements correspond to ground motions that cause significant higher mode effects with small roof displacement and high base curvature demand. The data points with elastic displacements larger than total displacement correspond to ground motions with base curvature demands less than the yield curvature. It should be noted that the number of data points with $\Delta_e \geq \Delta_t$ is higher in Figure 5.10(a) than in Figure 5.10(b).

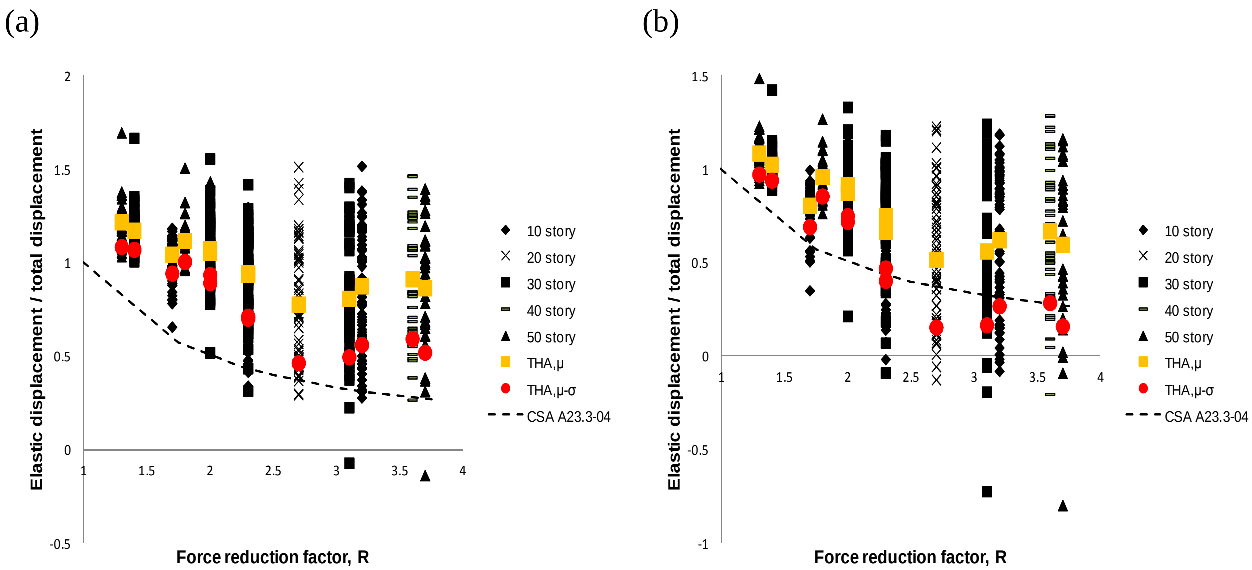

Figure 5.10 Comparison of the ratio of elastic to total displacement demand from CSA A23.3-04 with the mean (denoted as THA,μ) and mean minus one standard deviation (denoted as THA,μ-σ) results from time history analysis for: (a) yield curvature of $0.004/l_w$ and plastic hinge length of $0.5l_w$, and (b) yield curvature of $0.0025/l_w$ and plastic hinge length of $0.7l_w$.

It can be seen from Figure 5.10 that the CSA approach underestimates the elastic portion of the roof displacement demand for most cases. Underestimating elastic displacement is equivalent to overestimating base curvature demand (see Equation 5.5). It is necessary to develop separate models to estimate mean and mean plus one standard deviation base curvature demands determined from time history analysis. The details of the model are presented hereafter. A comparison between base curvature demands from time history analysis with the predictions using Equations 5.5 and 5.7 will be presented in section 5.4.1.4.

5.4.1.4 Refined Model for Predicting Base Curvature Demands

In this section a refined model for predicting base curvature demands will be developed. For this purpose, the base curvature demand is expressed as a function of roof displacement demand as follows:

$$\phi_d = C\frac{\Delta_t}{h_w l_w} \qquad Eq\ 5.10$$

The parameter C was calculated for individual records using maximum base curvature demand obtained from time history analysis and roof displacement demand from response spectrum analysis using stiffness reduction factors presented in Figure 5.6. Figure 5.11 shows the computed mean and mean plus one standard deviation of coefficient C as a function of the force reduction factor, wall height, and the ratio of wall height to force reduction factor h_w/R.

Figure 5.11 indicates that the C coefficient is not correlated to the wall height and the force reduction factor, while it decreases as the ratio of wall height to force reduction factor, h_w/R, increases. For two walls with equal height, the wall with higher force reduction factor has higher C factor than the wall with lower force reduction factor. This is similar to the CSA approach (Equation 5.5), which correlates the base curvature demand to $1/R$. For two walls with equal R values but different heights, the wall with larger height has lower C factor than the shorter wall. Again, this is similar to the CSA approach because the length of plastic hinge increases as the wall height increases (see Equation 5.9), which results in lower inelastic rotational demands (see Equation 5.4) and consequently lower base curvature demands. The constant C factor of 1.8 in Equation 5.7 is also shown in Figure 5.11 with a solid line. Equation 5.11 and Equation 5.12 are proposed to calculate the C coefficient corresponding to the mean and mean plus one standard deviation time history results:

$$C = 1.8 - 0.017\frac{h_w}{R} \geq 0.8 \qquad Eq\ 5.11$$

$$C = 2.8 - 0.022\frac{h_w}{R} \geq 1.0 \qquad Eq\ 5.12$$

Figure 5.12 compares base curvature predictions from Equations 5.10 & 5.11 (denoted as M1 model) and Equations 5.10 & 5.12 (denoted as M2 model) with the mean and mean plus one standard deviation base curvature demands determined from time history analysis. Also shown in this figure are the predictions from CSA A23.3-04 (Equation 5.5) and ACI 318 (Equation 5.7). Note that the input roof displacement in all models is the roof displacement determined from response spectrum analysis using stiffness reduction factors shown in Figure 5.6.

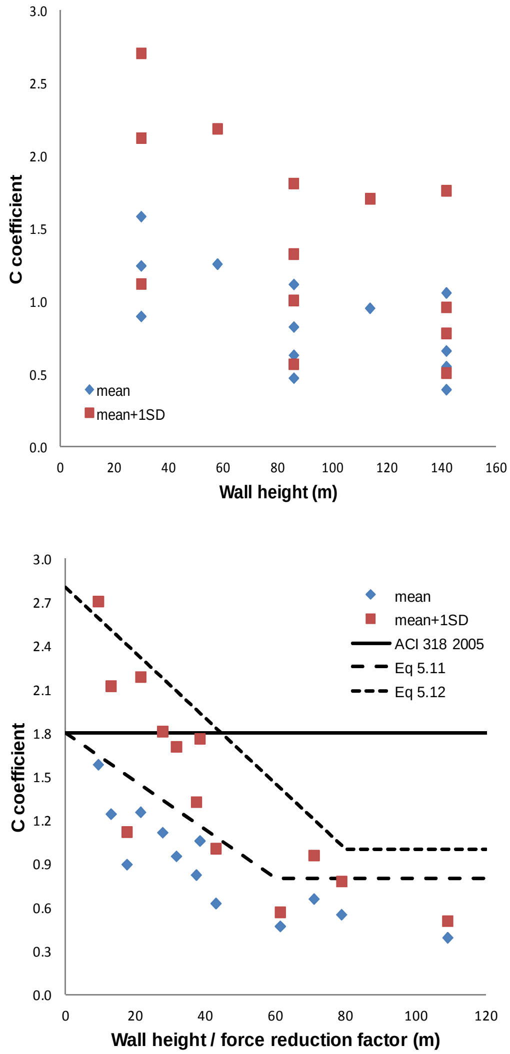

Figure 5.11 Variation of *C* coefficient corresponding to the mean and mean plus one standard deviation of results from time history analysis as a function of wall height, force reduction factor, and the ratio of wall height to force reduction factor.

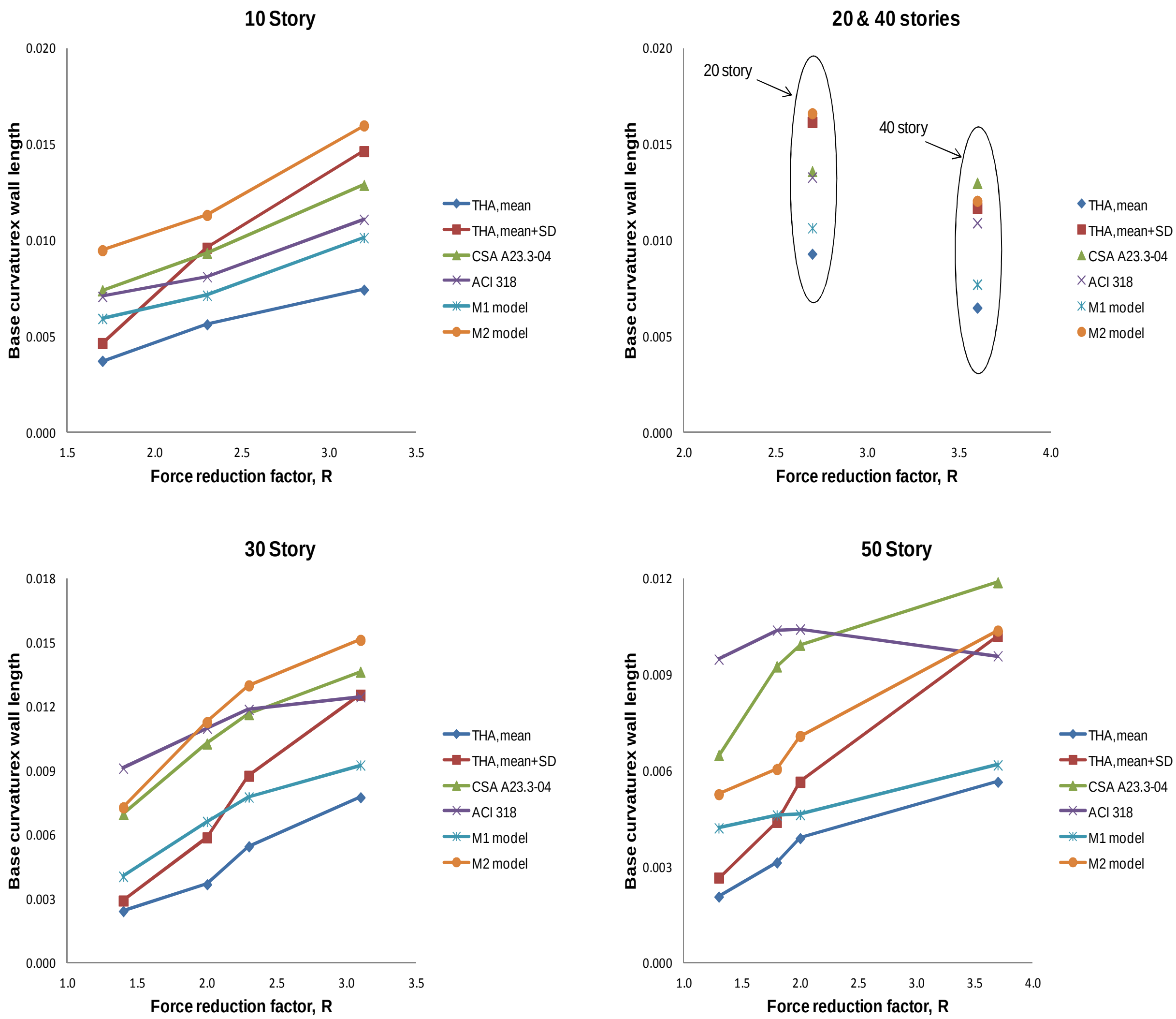

Figure 5.12 Comparison of base curvature demands from different models with mean and mean plus one standard deviation results for time history analysis (denoted as THA) for 10 to 50 story walls.

Figure 5.12 indicates that the M1 model provides the best prediction of the mean response. Base curvature demands predicted from the CSA and ACI approaches are consistently higher than the mean time history results for all walls and also higher than the mean plus one standard deviation results for 30, 40, and 50 story walls. CSA and ACI prediction of base curvature demand for 10 story walls with *R* factors of 2.3 and 3.2 and also the 20 story wall is lower than mean plus one standard deviation time history results. Base curvature predictions from the M2 model are consistently higher than the mean plus one standard deviation results.

5.4.1.5 Prediction of Base Curvature Demand for Individual Ground Motions

In Figure 5.12, base curvature demands predicted from different models were compared with the mean and mean plus standard deviation of results obtained from time history analysis. In this part, the CSA (Equation 5.5), ACI (Equation 5.7), and M1 (Equations 5.10 & 5.11) models are used to predict the base curvature demand for each ground motion using the maximum roof displacement obtained from time history analysis. The results are shown in Figures 5.13 through 5.16.

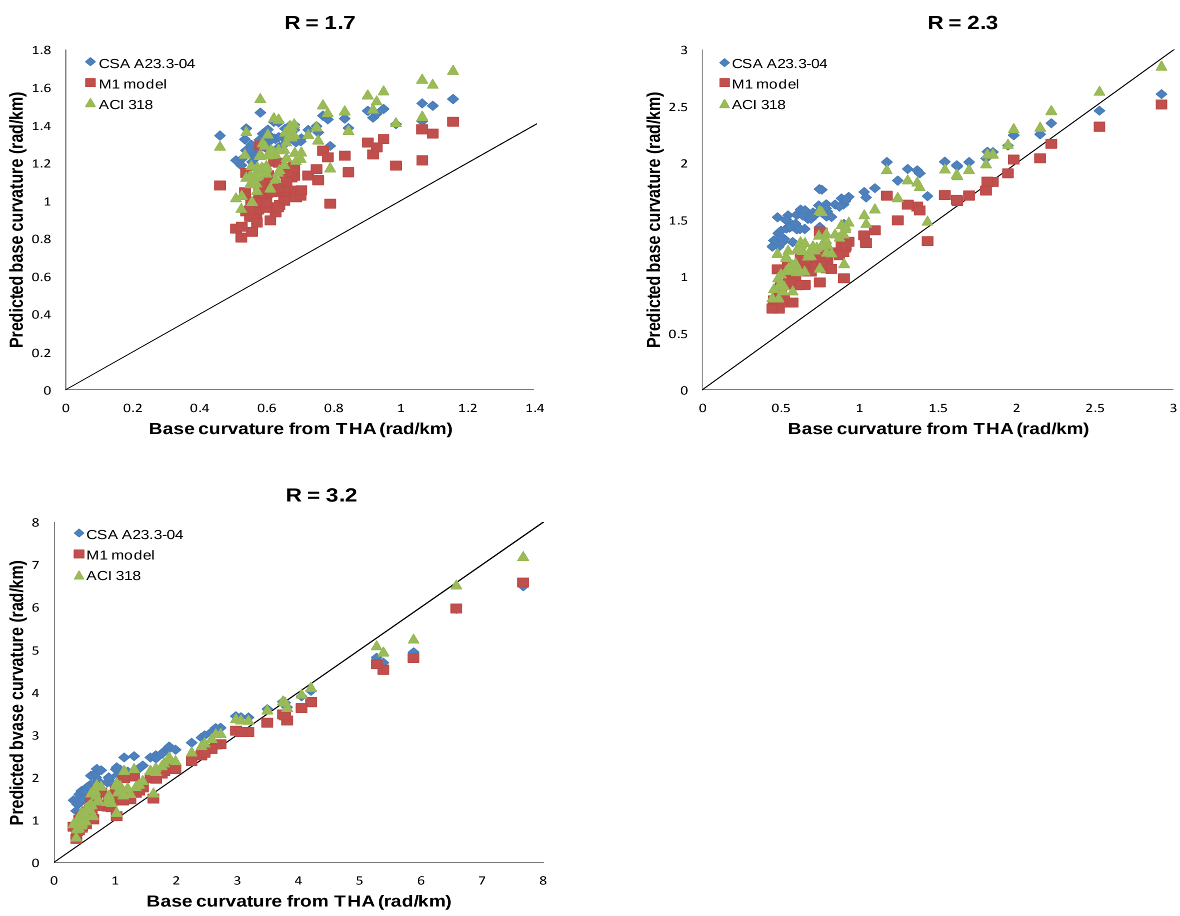

Figure 5.13 Comparison of maximum base curvature demand for individual ground motions determined from time history analysis (denoted as THA) with the predictions from different models for 10 story walls with different force reduction factors.

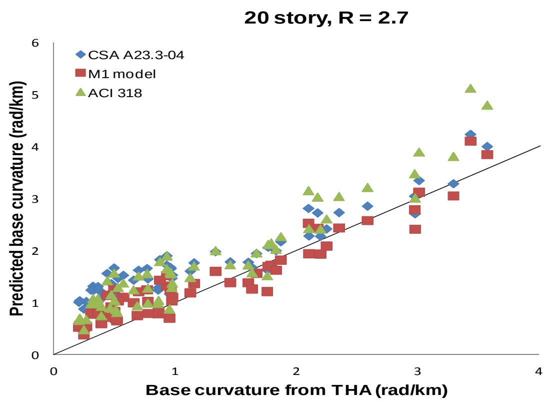

Figure 5.14 Comparison of maximum base curvature demand for individual ground motions determined from time history analysis (denoted as THA) with the predictions from different models for 20 and 40 story walls.

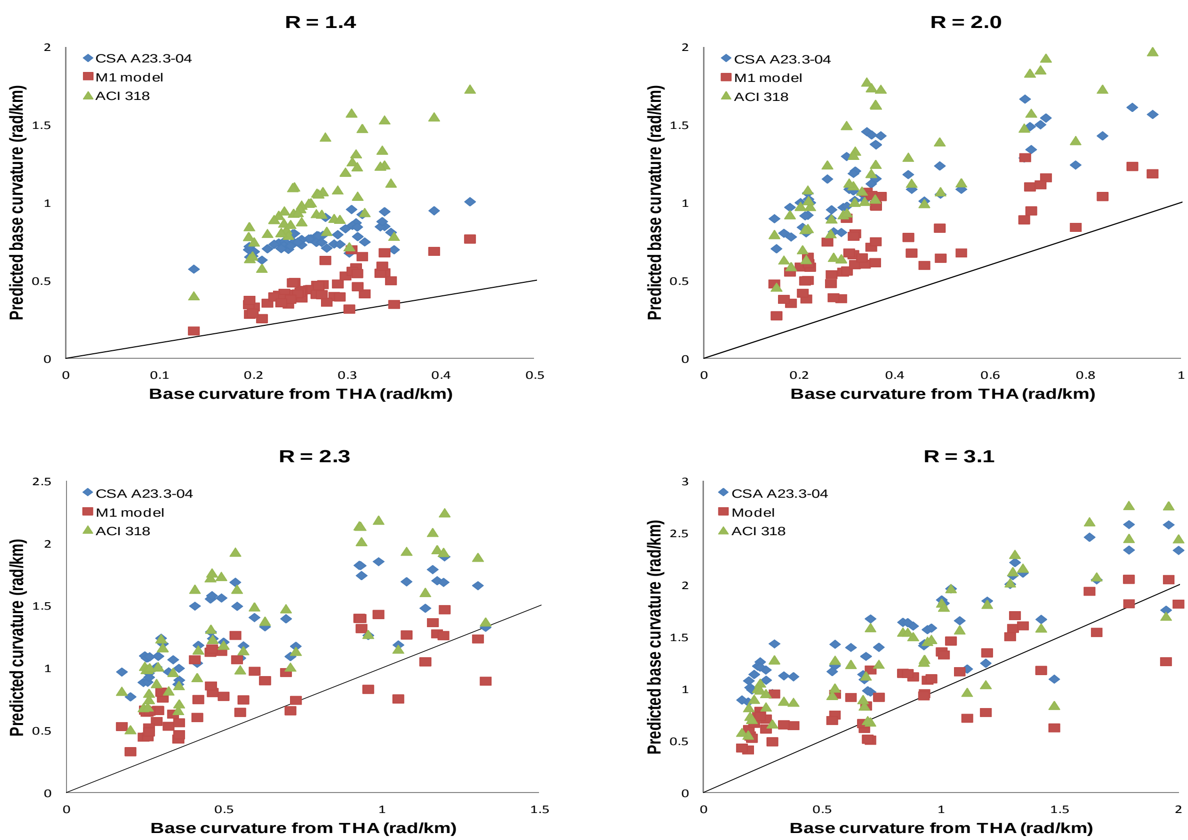

Figure 5.15 Comparison of maximum base curvature demand for individual ground motions determined from time history analysis (denoted as THA) with the predictions from different models for 30 story walls with different force reduction factors.

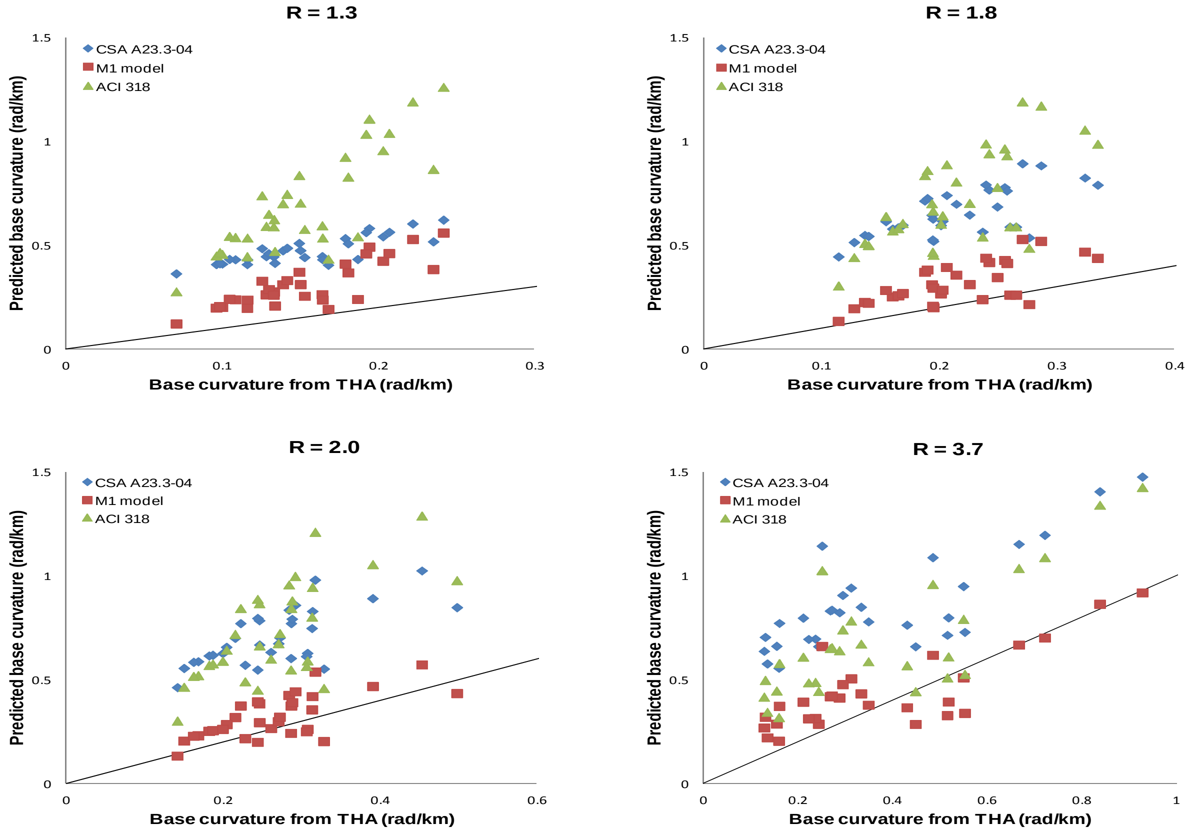

Figure 5.16 Comparison of maximum base curvature demand for individual ground motions determined from time history analysis (denoted as THA) with the predictions from different models for 50 story walls with different force reduction factors.

Figures 5.13 through 5.16 indicate that the three models give base curvature demands that are generally higher than those from time history analysis. The CSA and ACI models over predict the curvature demands for taller walls especially those with lower force reduction factors, while the M1 model predictions are generally closer to time history results. For some ground motions, the three models underestimate the base curvature demand because higher mode effects result in base curvature demands that are larger than those determined from the first mode assumption. It should be noted that base curvature models are developed to predict base curvature demands for a suite of ground motions not for individual records.

5.4.1.6 Discussion of Mean and Mean Plus One Standard Deviation Results

As it was observed in Figure 5.12, mean plus one standard deviation base curvature demands are very different from the mean results especially for walls with high force reduction factors. The question that arises is that which one should be considered to evaluate the seismic demands on shear walls?

In order to answer this question, it is necessary to compare the base curvature demand with the curvature capacity of the 13 walls. Most walls constructed in the west coast of Canada have no confinement to vertical reinforcement, so curvature capacity of a concrete shear wall can be considered to be 0.0035/*c*, where 0.0035 is the compressive strain capacity for unconfined concrete and *c* is the compression strain depth. Table 5.3 summarizes compression strain depth and curvature capacity of the 13 walls.

Table 5.3 Compression strain depth and curvature capacity for the range of shear walls.

Wall	R	c (mm)	c/l_w	ϕ_{cap} (rad/km)[1]	$\phi_{max,THA}$ (rad/km)[2]
10 story	1.7	547	0.099	6.4	1.45
	2.3	341	0.062	10.3	4.29
	3.2	233	0.042	15.0	7.67
20 story	2.7	308	0.041	11.4	3.57
30 story	1.4	748	0.083	4.7	0.43
	2.0	514	0.057	6.8	1.37
	2.3	443	0.049	7.9	1.58
	3.1	298	0.033	11.7	2.00
40 story	3.6	297	0.027	11.8	1.92
50 story	1.3	1014	0.074	3.5	0.24
	1.8	754	0.055	4.6	0.33
	2.0	700	0.051	5.0	0.50
	3.7	389	0.028	9.0	1.07

[1] curvature capacity of unconfined concrete at the base, [2] maximum base curvature demand from a single ground motion.

Table 5.3 indicates that maximum base curvature demands from time history analysis are significantly lower than the curvature capacity of the walls at the base. It implies that unconfined concrete has adequate curvature capacity to tolerate earthquake induced deformations. Consequently, no concrete crushing in compression occurs in the shear wall itself regardless of using mean or mean plus one standard deviation results to compute the curvature demands at the base.

Base curvature demands on the shear walls can be used to assess the performance of other structural members. CSA A23.3-04 requires that the structural components that are not part of the Seismic Force Resisting System (SFRS) must have adequate ductility to undergo the displacement demands on the SFRS. Gravity-load columns, for instance, must be designed such that the curvature capacity of these elements is greater than or equal to the curvature demands in SFRS. The new requirement of CSA A23.3-04 (CSA August 2009 update) specifies that the compression strain depth c of columns should satisfy the following equation:

$$c \leq \frac{\varepsilon_{cu} l_w}{2\theta_{id} + 0.004} \qquad Eq\ 5.13$$

where ε_{cu} is assumed to be 0.0035 and inelastic rotational demand θ_{id} on SFRS is:

$$\theta_{id} = \phi_{id}.l_p = \left(\phi_d - \phi_y\right) * 0.5 l_w \qquad Eq\ 5.14$$

Gravity-load columns in high rise structures in the west coast of Canada usually have elongated rectangular cross sections (Adebar et al. 2010). This special configuration together with the fact that most columns do not have confinement limits the curvature capacity of such elements. Therefore, in order to provide a greater margin against crushing of concrete in gravity-load columns, it is suggested that mean plus one standard deviation base curvature demands from time history analysis be used to compute inelastic rotational demand in Equation 5.14, i.e. Equations 5.10 and 5.12 be used to predict induced curvature demands in gravity-load columns. Note that using Equation 5.14 implies that the maximum base curvature in gravity-load columns is equal to the maximum base curvature demand in the shear wall.

5.4.2 Midheight Curvature Demands

Current design codes such as CSA A23.3 and ACI 318 provide detailing provisions at the base of concrete walls to ensure that they have adequate ductility to undergo the deformations induced by seismic actions. The length of ductile detailing is called plastic hinge length l_p, and the rest of the wall is assumed to remain elastic, so the walls are not provided with ductile detailing outside the base plastic hinge region. This approach does not consider the formation of a plastic hinge near midheight due to the influence of higher modes. Moehle et al. (2007) concluded that a second plastic hinge near midheight can be developed in addition to the base plastic hinge in tall walls subjected to high seismic loads. Panneton et al. (2006) pointed out that plastic hinges can occur above the base of an 8 story shear wall located in Eastern Canada although the considered wall had enough ductility to undergo such plastic deformations. Priestley et al. (2007) proposed a design bending moment envelope in which the design bending moment at the midheight increases as the displacement ductility and the fundamental period of the wall increases. This approach is in contrast with the CSA A23.3-04 approach in which the design bending moment decreases from factored moment at the top of the plastic hinge region to zero at the top of the wall. Panagiotou (2008) introduced Dual Plastic Hinge model in which a second plastic hinge located at midheight is considered in addition to the conventional plastic hinge at the base. The model was examined for three 10, 20, and 40 story walls subjected to three near fault ground motions with high spectral accelerations over a period range that covered second mode period of the walls. Panagiotou observed large curvature ductility around the midheight, and he concluded increasing flexural strength at the midheight can prevent midheight yielding.

In this part, the sensitivity of midheight curvature demand to the bending moment capacity at the midheight and spectral acceleration at second mode period will be investigated. The relationship between midheight curvature and global drift ratio will be also examined. Lastly, a simple model for estimating midheight curvature demands will be proposed.

5.4.2.1 Sensitivity of Midheight Curvature to Flexural Strength

To limit flexural yielding at the midheight, some researchers have proposed design envelopes, which is equivalent to design for higher bending moment demands around the midheight. It should be noted that since the walls have much reduced axial compression near midheight, very significant increases in vertical reinforcement is needed to prevent yielding near midheight. It is necessary to compare the mean curvature envelope from time history analysis with the flexural strength envelopes in order to observe how much the variation of flexural strength would change the mean curvature demands around the mid-height. Figure 5.17 presents mean curvature profiles for 11 different shear walls. Also shown in this figure are the bending moment capacity envelopes for individual walls. For the 11 walls, the base curvature demand increases significantly as the flexural strength of the wall is reduced. The mean midheight curvature is less sensitive to the flexural strength of the walls. For example, maximum midheight curvatures for 50 story walls with R = 1.8 and R = 3.7 are identical (0.133 rad/km for R = 1.8 versus 0.132 rad/km for R = 3.7). At the location that the maximum curvatures occur for R = 1.8, flexural strength of the wall with R = 1.8 is 1.5 times the flexural strength of the wall with R = 3.7. Therefore, it seems that increasing flexural strength slightly reduces midheight curvature demands, while it significantly reduces base curvature demands.

(a)

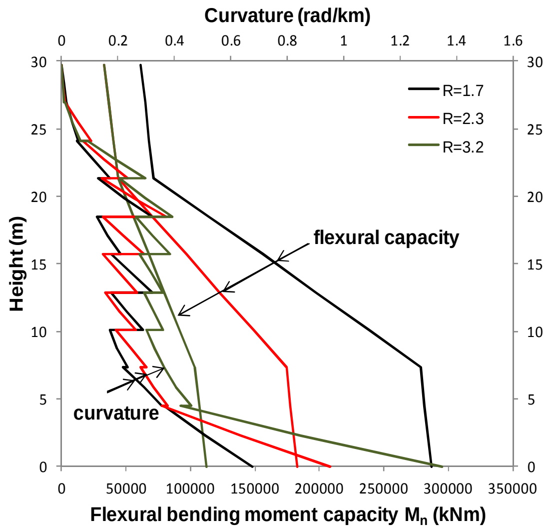

(b)

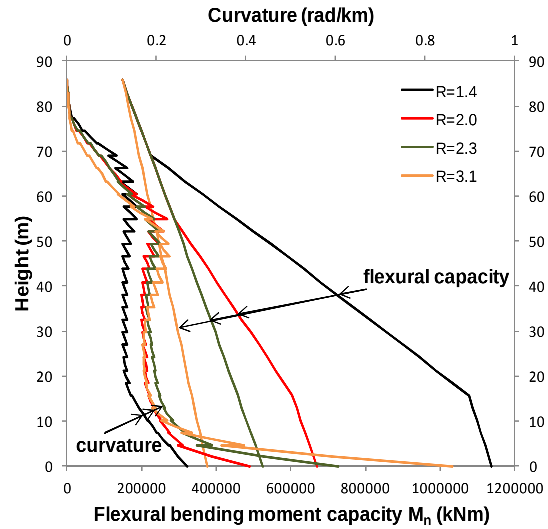

(c)

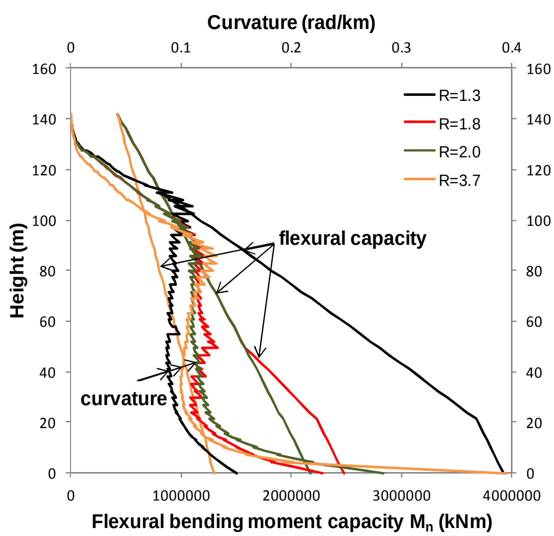

Figure 5.17 Relationship between midheight curvature demand and flexural capacity at midheight for: (a) 10 story, (b) 30 story, and (c) 50 story walls.

5.4.2.2 Sensitivity of Midheight Curvature to Characteristics of Ground Motions

The influence of ground motion characteristics on various demand parameters was investigated in Chapter 4. The sensitivity analysis carried out on conditioning period T^* revealed that base shear force and in some cases midheight curvature demands from the ground motions matched to the CMS computed at $T^* = T_2$ were higher than those associated with the records matched to the CMS computed at $T^* = T_1$. Also, it was observed that ST1 ground motions (ground motions matched to the UHS only at the fundamental period) gave highest midheight curvatures in taller walls. Note that the ST1 ground motions had higher spectral accelerations at shorter periods than other sets of records. These observations indicate that midheight curvature demands are influenced by the characteristics of the ground motions around higher mode periods. Figure 5.18 plots midheight curvature demand as a function of spectral acceleration at second mode period for 10 to 50 story walls. Figure 5.18 indicates that midheight curvature generally increases as the spectral accelerations at the second mode increases. The correlation seems to be stronger for 10 to 30 story walls. For 50 story walls, midheight curvature demand is insensitive to the variation of the spectral accelerations at T_2. Therefore, it can be concluded that ground motions with higher spectral accelerations around second mode period tend to induce higher midheight curvature demands in cantilever shear walls.

5.4.2.3 Midheight Curvature versus Global Drift Ratio

In order to develop a simple model for predicting midheight curvature demands, midheight curvatures corresponding to walls with different heights but similar force reduction factors were plotted as a function of the ratio of the roof displacement demand to the wall height, Δ_t / h_w. Figure 5.19 shows this variation for the thirteen walls and individual ground motions. Note that curvature values shown in Figure 5.19 are the maximum curvatures occurring at any location along the height ranging from $h = l_w$ to the top of the walls. The mean and mean plus one standard deviation of midheight curvature demands shown in Figure 5.19 are presented in Table 5.4.

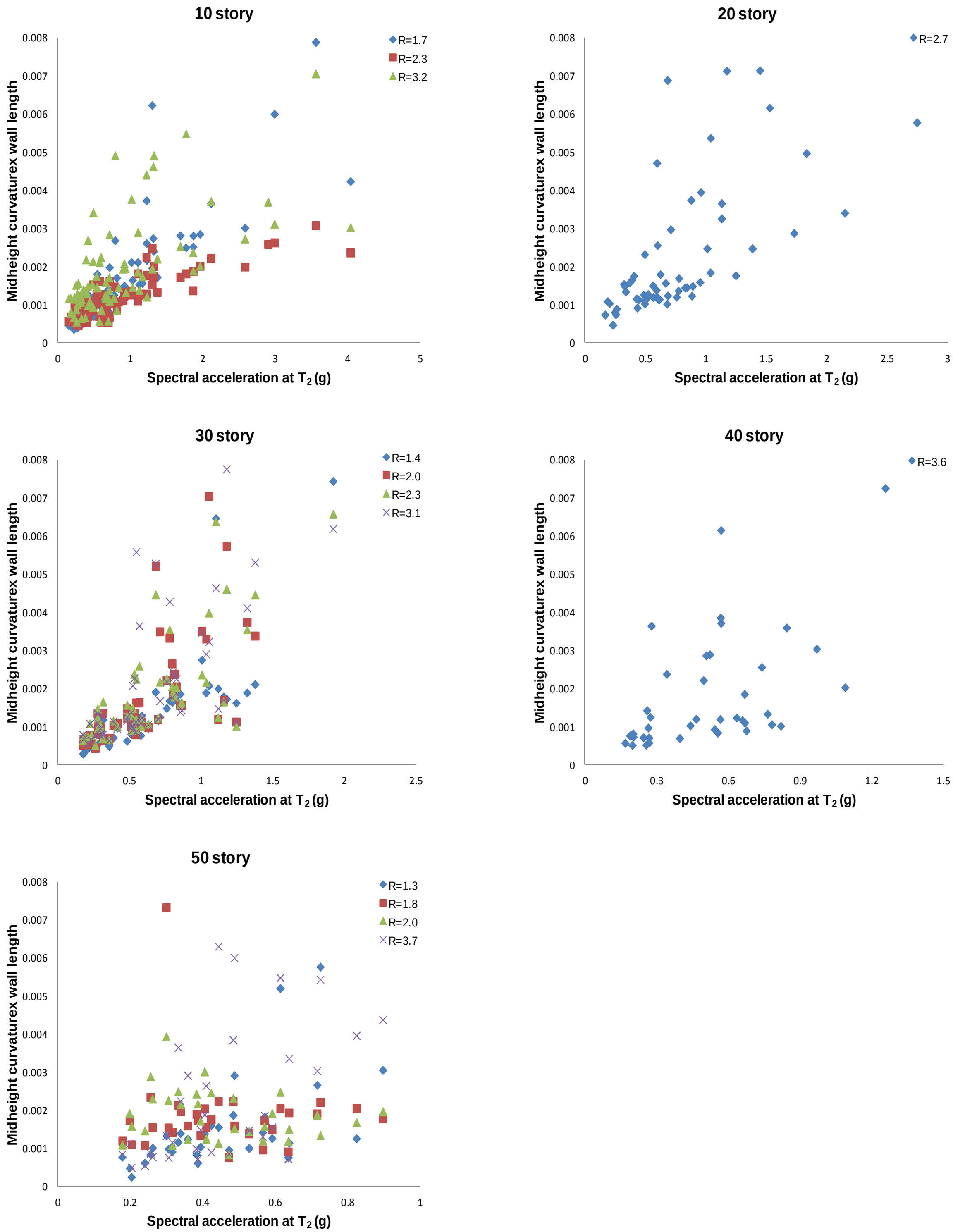

Figure 5.18 Variation of midheight curvature versus spectral acceleration at second mode for 10 to 50 story walls.

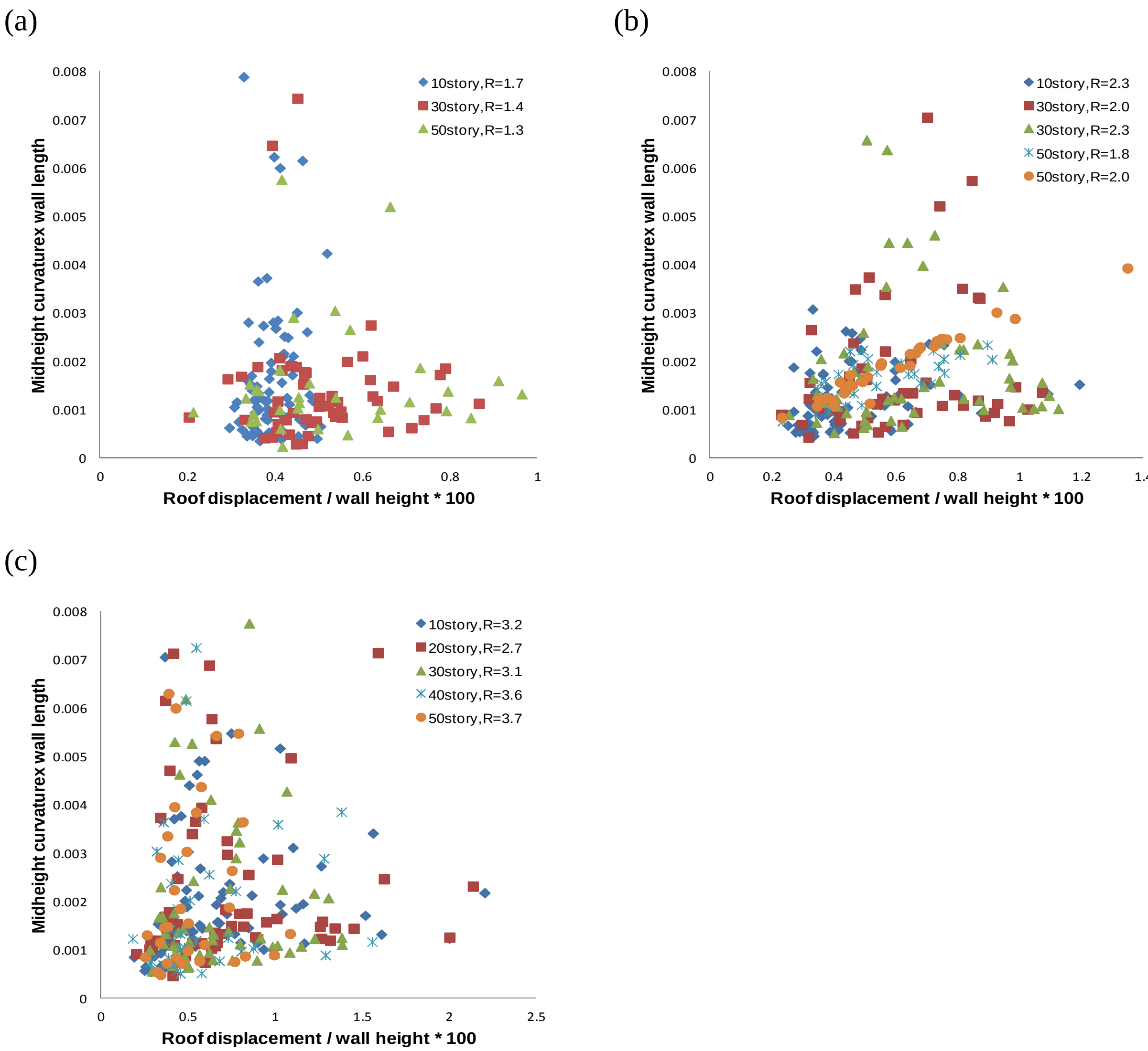

Figure 5.19 Variation of midheight curvature demand as a function of global drift ratio for (a) low, (b) medium, and (c) high force reduction factors.

Table 5.4 Mean (μ) and mean plus one standard deviation ($\mu + \sigma$) results for midheight curvature times wall length.

		$\phi_{mid} \cdot l_w$	
Wall	R	μ	μ+σ
10 story	1.7	0.0018	0.0035
	2.3	0.0020	0.0037
	3.2	0.0021	0.0037
20 story	2.7	0.0023	0.0042
30 story	1.4	0.0014	0.0027
	2.0	0.0020	0.0039
	2.3	0.0019	0.0032
	3.1	0.0021	0.0037
40 story	3.6	0.0018	0.0033
50 story	1.3	0.0015	0.0027
	1.8	0.0018	0.0029
	2.0	0.0019	0.0025
	3.7	0.0023	0.0040
	Average	**0.0019**	**0.0034**

Figure 5.19 shows that there is no correlation between midheight curvature demand and global drift ratio. The majority of the data on the vertical axis are below 0.004 for the thirteen walls indicating that maximum midheight curvature is less than the yield curvature as proposed by Adebar et al. (2005). Table 5.4 indicates that the product of maximum midheight curvature times the wall length varies from 0.0014 to 0.0023 for the mean results and from 0.0025 to 0.0042 for the mean plus one standard deviation results. The mean value of the midheight curvature demand times the wall length for the thirteen walls corresponding to the mean and mean plus one standard deviation results is 0.0019 and 0.0034, respectively. Therefore, $0.002/l_w$ and $0.0035/l_w$ are appropriate values for midheight curvature demands depending whether mean or mean plus one deviation of time history results are used. Comparing these two values with the recommendations for the yield curvature (see Section 5.4.1.3.1) reveals that midheight curvature demands in concrete shear walls are approximately equal to the yield curvature, and therefore, there is no need to prevent flexural yielding of cantilever shear walls near midheight by trying to increase the flexural capacity of the walls. Relatively few detailing rules are needed to ensure that shear walls have adequate ductility to undergo the induced midheight curvature demands.

5.4.3 Simplified Design Envelope for Curvature Demands

A simplified design envelope for predicting curvature demands over the height is proposed in Figure 5.20 based on the general shape of curvature envelopes determined from time history analysis.

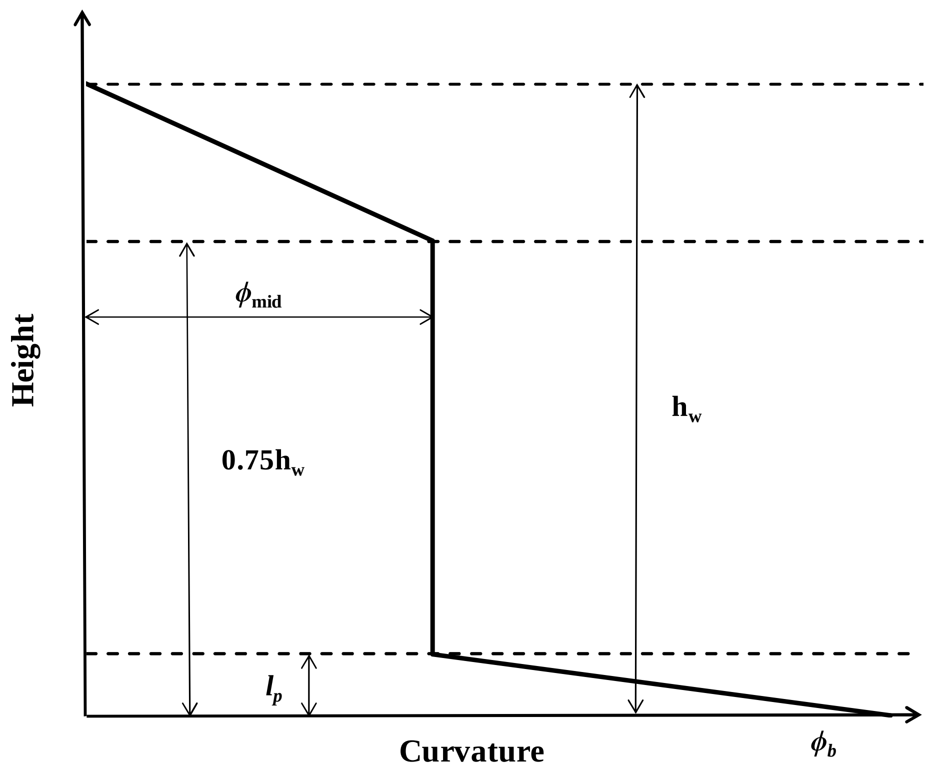

Figure 5.20 Simplified design envelope for predicting curvature demands in cantilever shear walls.

ϕ_{mid} in Figure 5.20 refers to midheight curvature demand and can be determined from the following equations:

$$(\phi_{mid})_{mean} = \frac{0.002}{l_w} \qquad Eq\ 5.15$$

$$(\phi_{mid})_{mean+SD} = \frac{0.0035}{l_w} \qquad Eq\ 5.16$$

where $(\phi_{mid})_{mean}$ and $(\phi_{mid})_{mean+SD}$ are midheight curvature demand corresponding to the mean and mean plus one standard deviation values from time history analysis, respectively. Also, ϕ_b refers to the base curvature demand and can be determined from Equations 5.10

through 5.12. The length of plastic hinge region, l_p, was calculated using Equation 5.9 and Bohl and Adebar (2011) model, and it was observed that wall length l_w is an appropriate upper bound to approximate this parameter. Figure 5.21 through Figure 5.24 compares curvature envelopes corresponding to the mean and mean plus one standard deviation results from time history analysis with the simplified models. Note that in these figures, the M1 envelope uses Equations 5.10, 5.11, and 5.15, while the M2 envelope uses Equations 5.10, 5.12, and 5.16.

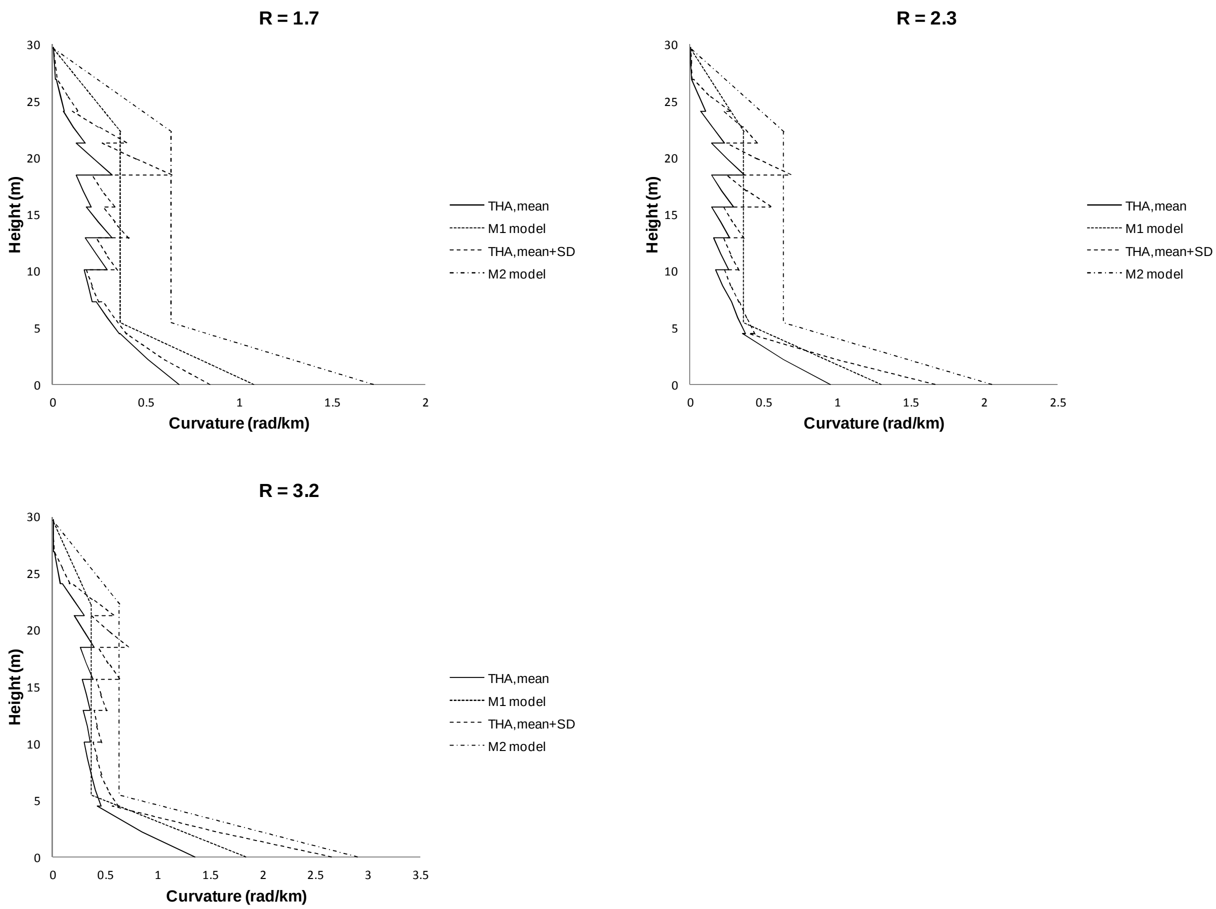

Figure 5.21 Comparison of mean (denoted as THA,mean) and mean plus one standard deviation (denoted as THA,mean+SD) curvature envelopes determined from time history analysis with the simplified models for 10 story walls.

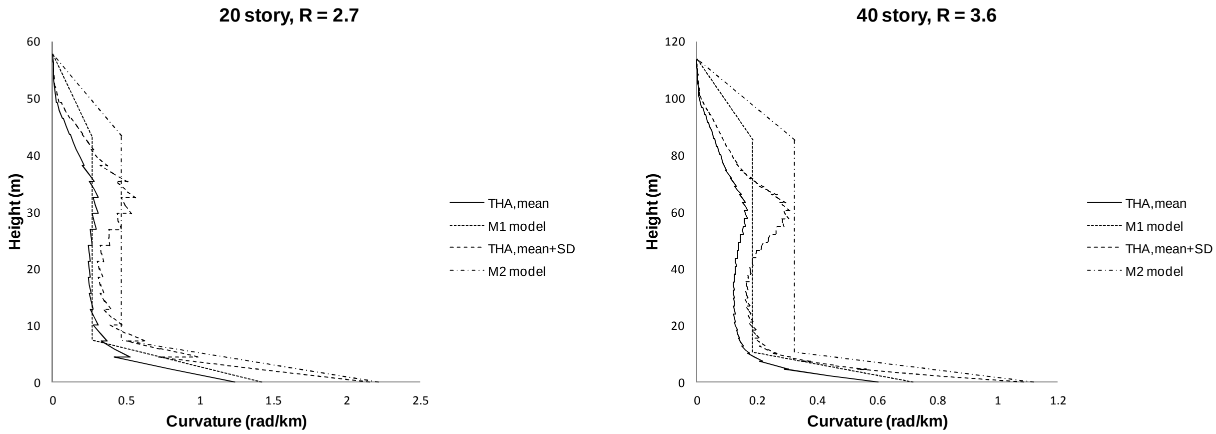

Figure 5.22 Comparison of mean (denoted as THA,mean) and mean plus one standard deviation (denoted as THA,mean+SD) curvature envelopes determined from time history analysis with the simplified models for 20 and 40 story walls.

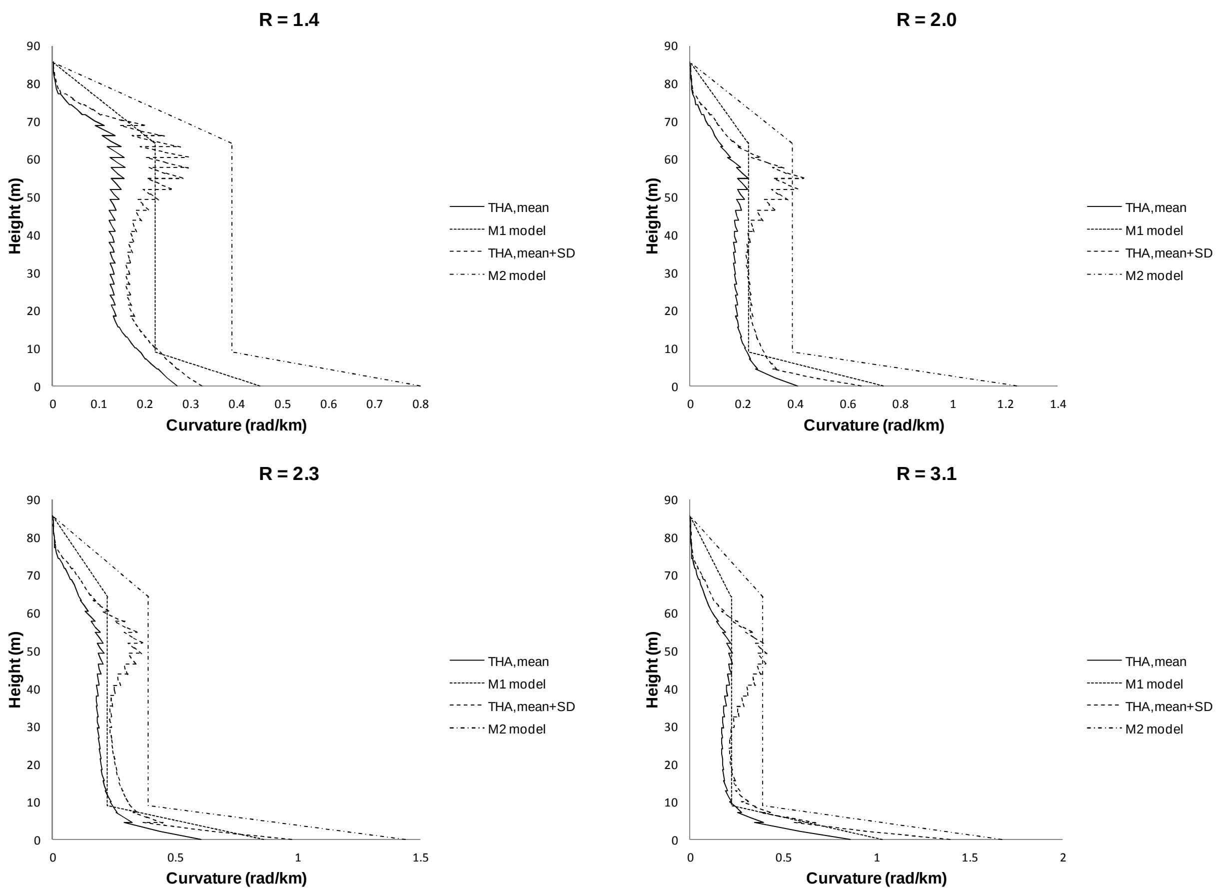

Figure 5.23 Comparison of mean (denoted as THA,mean) and mean plus one standard deviation (denoted as THA,mean+SD) curvature envelopes determined from time history analysis with the simplified models for 30 story walls.

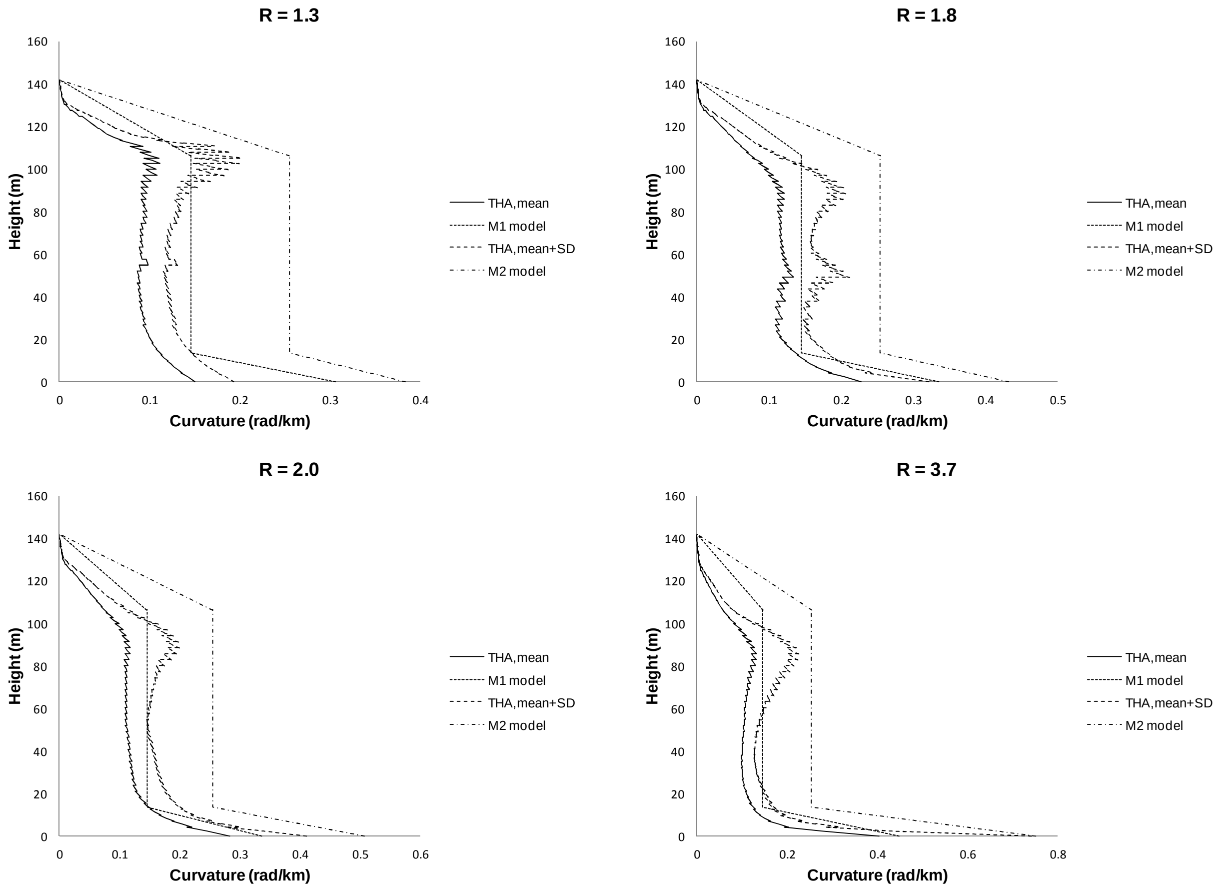

Figure 5.24 Comparison of mean (denoted as THA,mean) and mean plus one standard deviation (denoted as THA,mean+SD) curvature envelopes determined from time history analysis with the simplified models for 50 story walls.

5.5 Interstory Drift Demands of Shear Walls

Estimating base curvature demands on gravity-load columns was discussed in Section 5.4.1.6. Slab-column connection is another component of the gravity-load resisting system that must have adequate ductility to undergo seismic displacement demands. According to CSA A23.3-04 guidelines, shear reinforcement must be provided in the slab if the shear stress from gravity loads exceeds R_E times the limiting shear stress for gravity loads. The reduction factor R_E is determined from the following equation:

$$R_E = (\frac{0.005}{\delta_i})^{0.85} \leq 1.0 \qquad Eq\ 5.17$$

where δ_i is the interstory drift demand; therefore, an accurate estimate of interstory drift is necessary to calculate the resistance of slab-column connections.

In this section, two methods of obtaining interstory drift from response spectrum analysis will be compared. The correlation of maximum interstory drift (at the top of wall) and midheight interstory drift demands with the roof displacement demand will be investigated. Lastly, a simplified design envelope for estimating interstory drifts over the height of shear walls will be introduced.

5.5.1 Calculation of Interstory Drift from Response Spectrum Analysis

The displacement demands determined from RSA can be used to calculate interstory drift demands. One method is to compute interstory drifts corresponding to each mode and then combine the results using Complete Quadratic Combination (CQC) method. The second method is to calculate interstory drift from the displacement envelope profile, which is essentially the combination of the displacement demands from different modes. The shortcoming of the second approach is that the maximum displacements at each floor do not obtain their peak values at the same time, i.e. it is not correct to estimate interstory drift demands from a vector summation.

Figure 5.25 shows the interstory drift envelope from the two approaches for the 50 story wall with R = 3.7. Displacement demands were determined from RSA using a stiffness reduction factor of 0.5. Figure 5.25 indicates that the two methods result in similar interstory drift values, except that the first method gives slightly higher interstory drifts at upper floors. Since obtaining interstory drift demands from displacement envelope profile is easier than from individual modes, yet it gives reasonably accurate results, it will be used hereafter to determine interstory drift demands from response spectrum analysis.

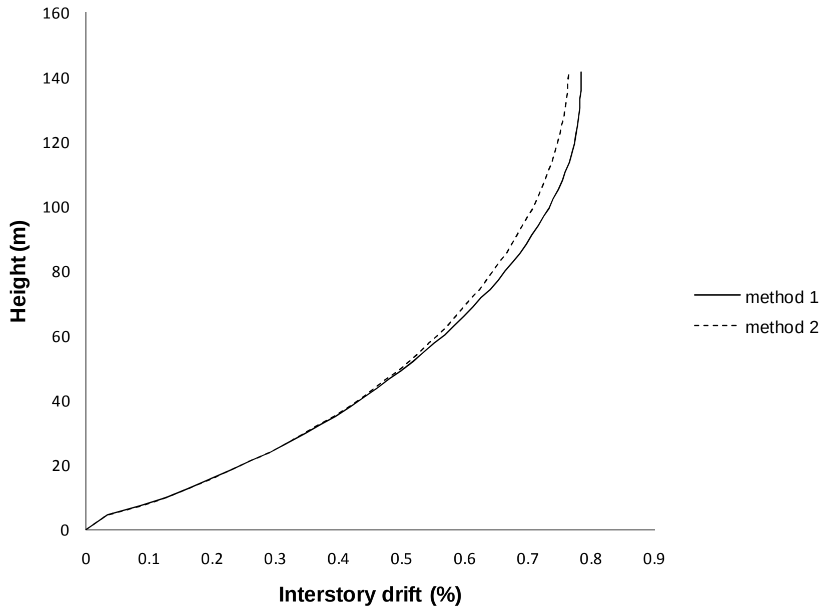

Figure 5.25 Comparison of interstory drift envelopes from the two approaches for the 50 story wall with R = 3.7.

5.5.2 Correlation of Roof and Midheight Interstory Drift Demands with Maximum Roof Displacement

Establishing a simple model for estimating interstory drift demands requires relating interstory drifts at key points to another demand parameter. In this work, roof and midheight interstory drift demands are expressed as a function of roof displacement demand since the latter, as it was shown in Section 5.3, can be predicted accurately if appropriate effective stiffness values are used in response spectrum analysis. The relationship between maximum roof and midheight interstory drifts with the roof displacement demand can be illustrated by examining time history plots of the three demand parameters for individual ground motions. This was done for three 10, 30, and 50 story walls with force reduction factors of 3.2, 3.1, and 3.7, respectively. Only 30 records out of 80 ground motions were investigated for the 10 story wall, while all motions were considered for the 30 and 50 story walls. Figure 5.26 shows the results.

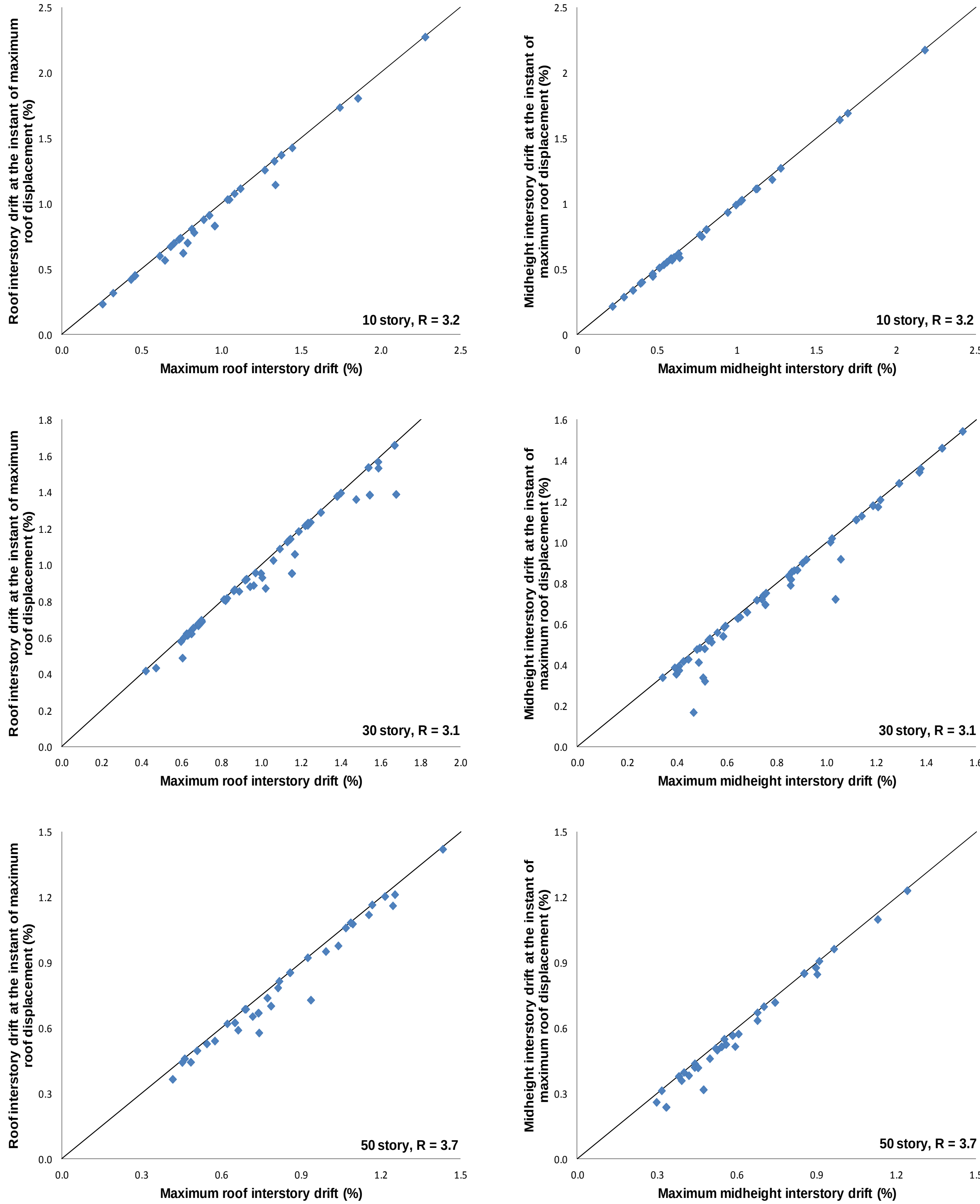

Figure 5.26 Roof and midheight interstory drifts at the instant of maximum roof displacement for the 10, 30, and 50 story walls.

It can be inferred from Figure 5.26 that roof and midheight interstory drift demands at the instant of maximum roof displacement are very close to the corresponding maximum values for the majority of records. The scatter is higher for the 30 and 50 story walls than for the 10 story one, e.g. for several ground motions, maximum roof displacement and maximum interstory drifts at the top of wall occur at different instants. However, it can be inferred from Figure 5.26 that both roof and midheight interstory drifts are well correlated to the roof displacement demand. This finding will be used to develop a simplified model for predicting interstory drift demands at the roof and at the midheight.

5.5.3 Simplified Design Envelope for Predicting Interstory Drift Demands

In this section, a simplified model for predicting interstory drift demands will be developed based on the results from time history analysis. According to this model, roof interstory drift and midheight interstory drift – denoted as $(ID)_r$ and $(ID)_m$, respectively – are expressed as a function of global drift ratio Δ_t / h_w , as follows:

$$(ID)_r = A_r \frac{\Delta_t}{h_w} \qquad Eq\ 5.18$$

$$(ID)_m = A_m \frac{\Delta_t}{h_w} \qquad Eq\ 5.19$$

where parameters A_r and A_m were calculated for individual records using $(ID)_r$ and $(ID)_m$ values obtained from time history analysis and roof displacement demand Δ_t from response spectrum analysis using stiffness reduction factors presented in Figure 5.6. Figure 5.27 shows the computed mean and mean plus one standard deviation values of A_r and A_m as a function of the force reduction factor R for the thirteen walls.

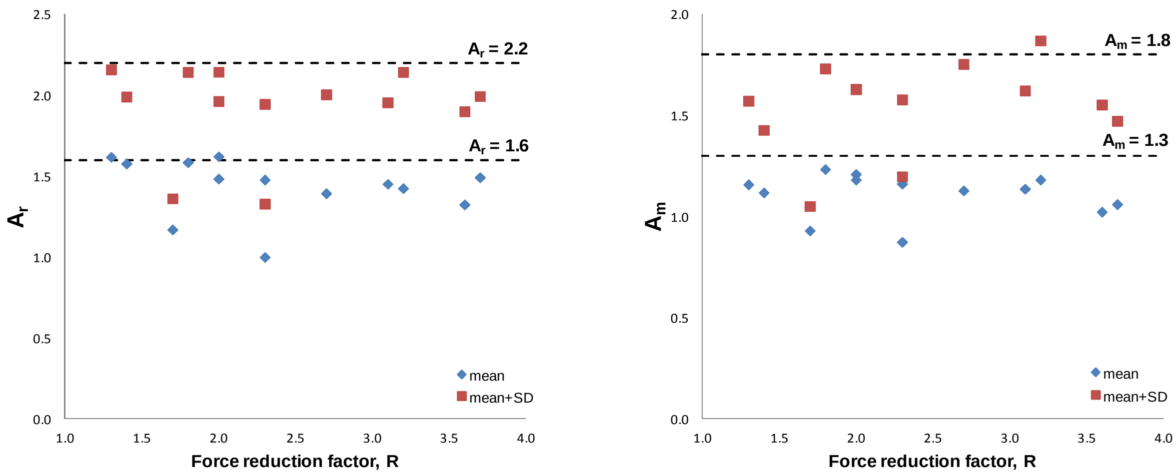

Figure 5.27 Variation of A_r and A_m corresponding to the mean and mean plus one standard deviation results from time history analysis as a function of force reduction factor R for the thirteen walls.

Figure 5.27 indicates that both A_r and A_m are relatively independent of R factor regardless whether mean or mean plus one standard deviation results were used. The dashed lines in these figures represent upper bound estimates of the two parameters, that is 1.6 and 2.2 for A_r and 1.3 and 1.8 for A_m corresponding to mean and mean plus one standard deviation results, respectively. Having known A_r and A_m, one can calculate roof and midheight interstory drift demands from Equations 5.18 and 5.19 respectively.

A simplified design envelope for predicting interstory drift demands over the height is proposed in Figure 5.28. It should be noted that $(ID)_b$ in Figure 5.28 reflects the amount of rotation at the base of shear walls with flexible foundation or those with several floors below grade which are usually used for parking or commercial space. Having determined $(ID)_r$ and $(ID)_m$ from Equations 5.18 and 5.19, respectively, one can obtain $(ID)_b$ from the geometry. For example, using A_r = 1.6 and A_m = 1.3 results in the following equation for base rotational demands:

$$(ID)_b = 0.7\frac{\Delta_t}{h_w} \qquad Eq\ 5.20$$

and, base rotational demand corresponding to A_r = 2.2 and A_m = 1.8 can be determined from:

$$(ID)_b = 1.0\frac{\Delta_t}{h_w} \qquad Eq\ 5.21$$

The adequacy of Equations 5.20 and 5.21 will be examined in Section 5.6.2 for a 30 story shear wall with base support stiffness varying from infinite (fixed) to a very low value.

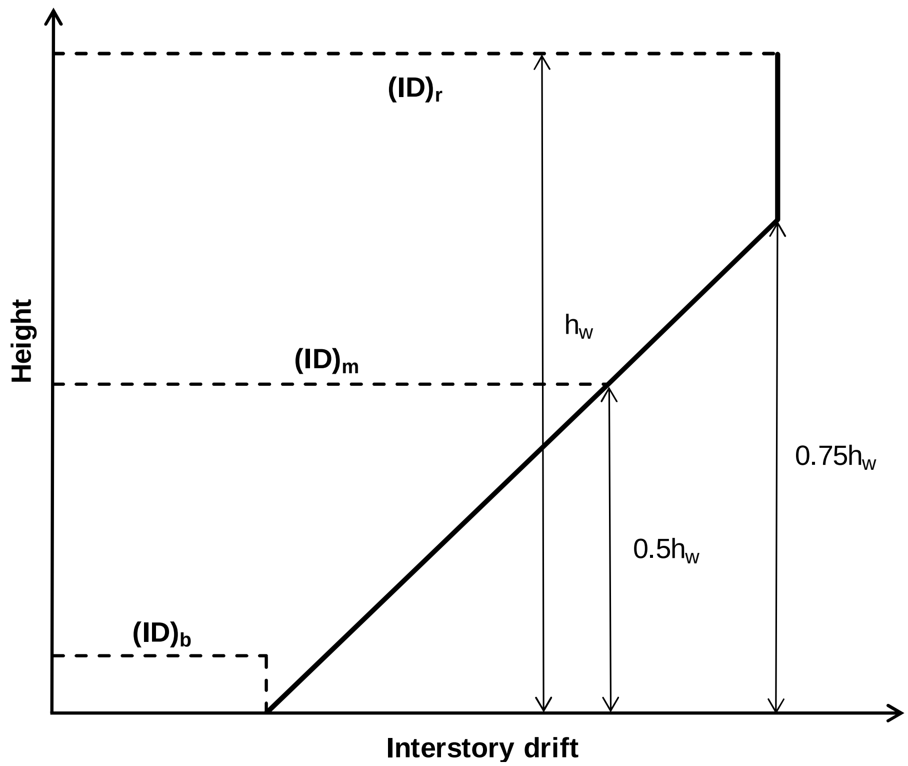

Figure 5.28 Simplified design envelope for predicting interstory drift demands in cantilever shear walls.

Figures 5.29 through 5.32 compare mean and mean plus one standard deviations interstory envelopes from time history analysis with the predictions from response spectrum analysis and simplified model using A_r = 2.2 and A_m = 1.8 (denoted as D2 model) and A_r = 1.6 and A_m = 1.3 (denoted as D1 model) for the thirteen walls. As it can be seen from these figures, response spectrum analysis underestimates interstory drifts at lower floors compared to the mean demands from time history analysis, while it gives a good estimate of roof interstory drifts for 10 and 20 story walls. For 30 to 50 story walls, roof interstory drifts from RSA are lower than those obtained from time history analysis. The D1 and D2 models, on the other hand, provide a reasonably conservative estimate of interstory drift demands over the height for all walls. Predicted interstory drift values from D1 or D2 models can be used in Equation 5.17 to compute the R_E factor in order to calculate the shear resistance of slab-column connection in gravity-load resisting system. Using D2 model provides a greater margin against punching shear failure of slab-column connections. Note that using D1 and D2 models to assess the safety of slab-column connection in the gravity-load resisting system implies that interstory drifts in the gravity-load resisting system are equal to those in the shear wall.

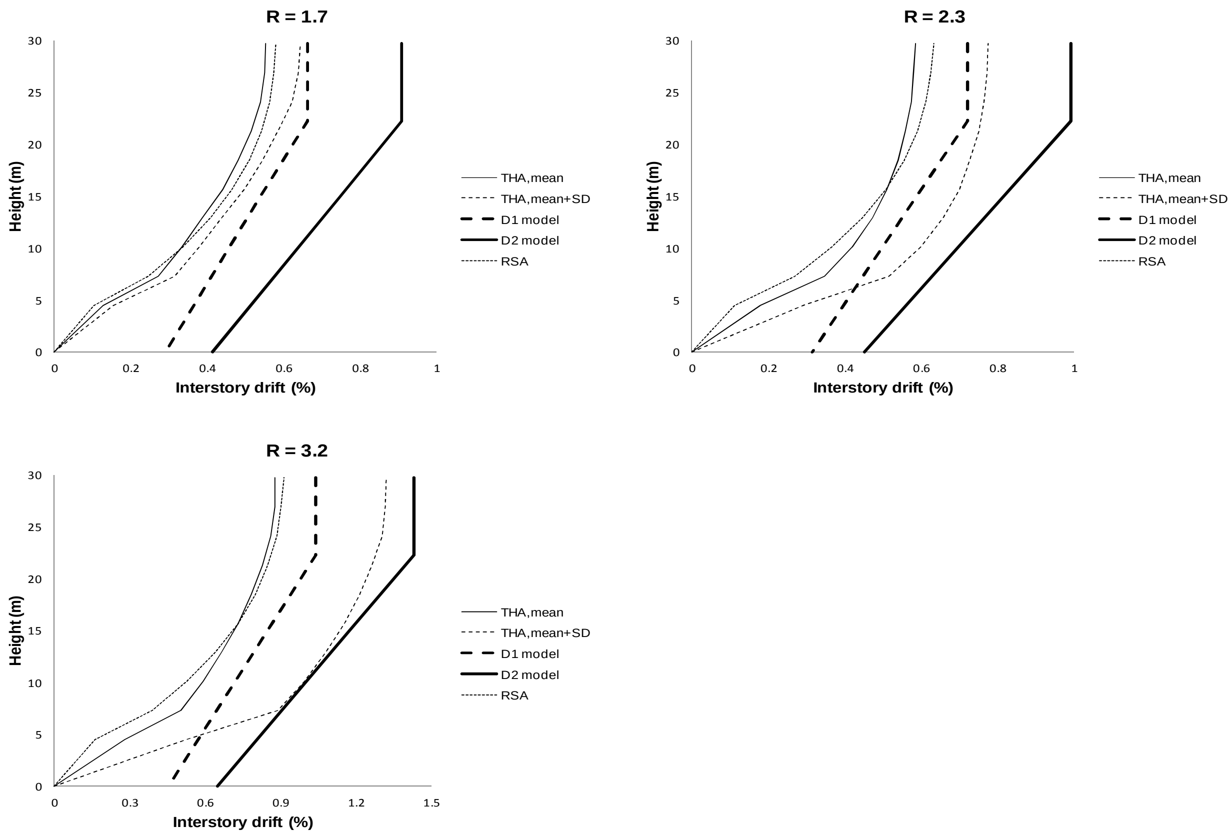

Figure 5.29 Comparison of mean (denoted as THA,mean) and mean plus one standard deviation (denoted as THA,mean+SD) interstory drift envelopes from time history analysis with the predictions from RSA and simplified models for 10 story walls with different force reduction factors.

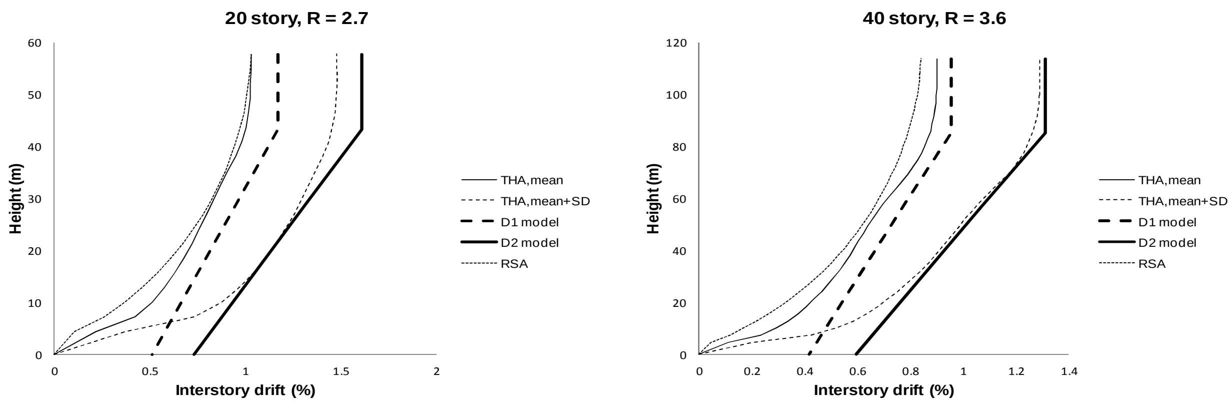

Figure 5.30 Comparison of mean (denoted as THA,mean) and mean plus one standard deviation (denoted as THA,mean+SD) interstory drift envelopes from time history analysis with the predictions from RSA and simplified models for 20 and 40 story walls.

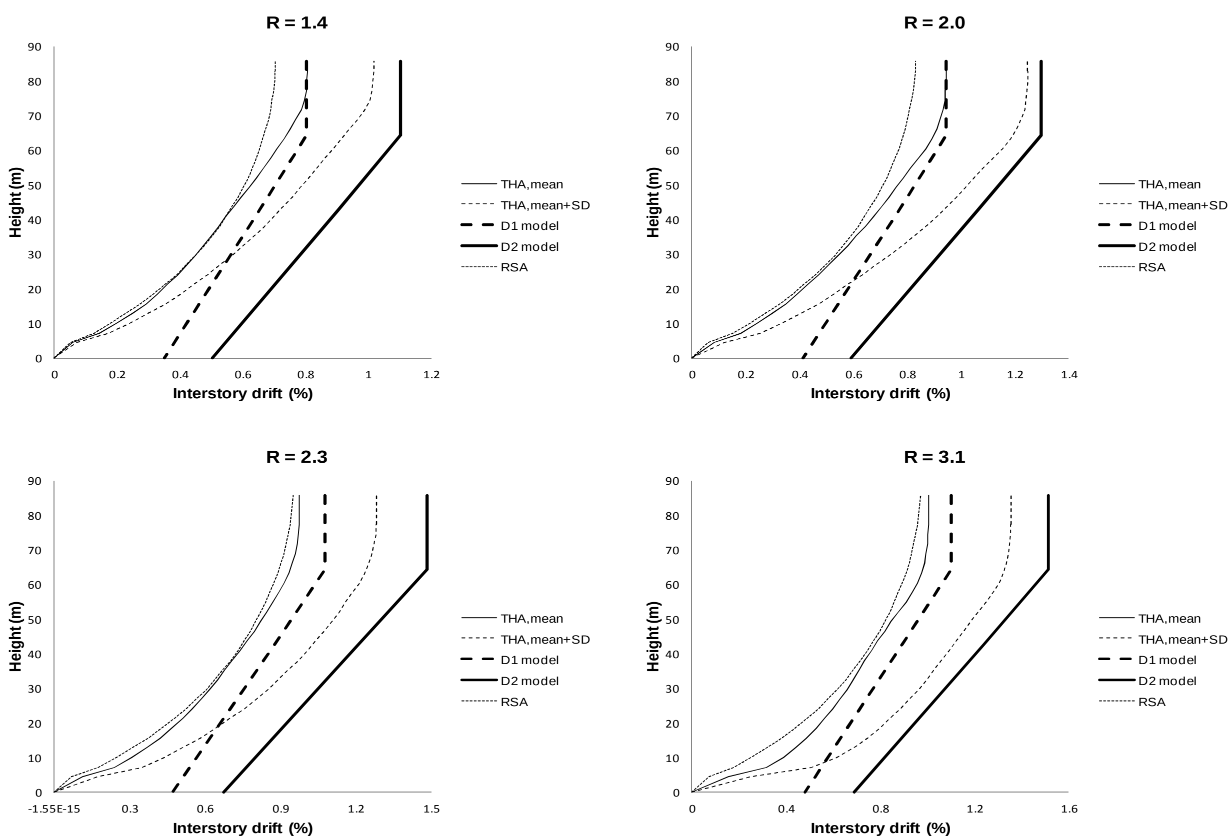

Figure 5.31 Comparison of mean (denoted as THA,mean) and mean plus one standard deviation (denoted as THA,mean+SD) interstory drift envelopes from time history analysis with the predictions from RSA and simplified models for 30 story walls with different force reduction factors.

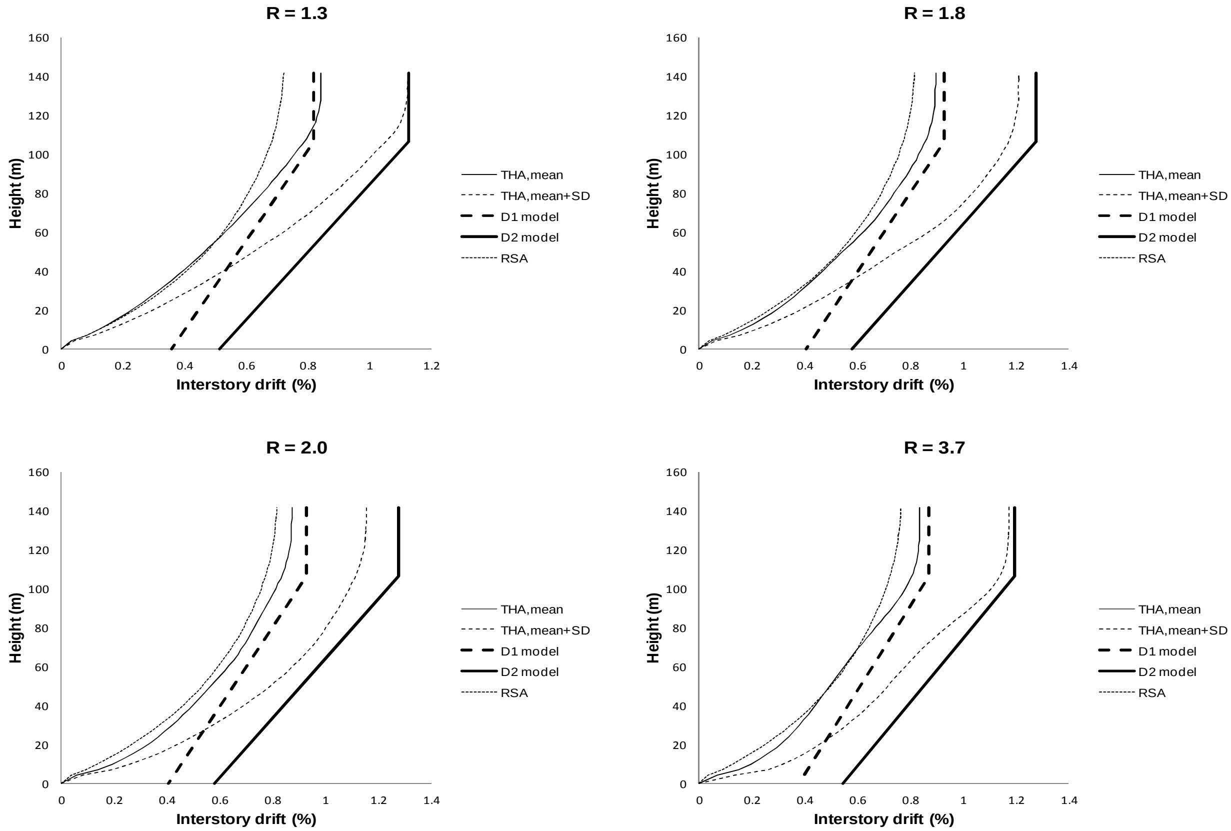

Figure 5.32 Comparison of mean (denoted as THA,mean) and mean plus one standard deviation (denoted as THA,mean+SD) interstory drift envelopes from time history analysis with the predictions from RSA and simplified models for 50 story walls with different force reduction factors.

5.6 Influence of Shear Deformation and Base Rotational Stiffness on Seismic Demands of Shear Walls

The demand parameters presented thus far correspond to flexural deformation of cantilever shear walls with a fixed base support. Other possible sources of deformation would be shear deformation and base support flexibility. In this section, the influence of shear deformation on demand parameters such as roof displacement, base curvature, and interstory drift at the top of wall will be investigated. Also, a case study will be carried out to examine the influence of base rotational stiffness on various demand parameters.

5.6.1 Influence of Shear Deformation

Modeling shear response of reinforce concrete members requires complicated hysteretic models which accounts for initial uncracked shear stiffness, reduction in shear stiffness due to the formation of diagonal cracking, and also accumulation of residual strain. It is well established that large shear deformations can develop after the formation of diagonal cracking and reinforcement yielding if the reinforced concrete has adequate shear reinforcement (Gerin and Adebar 2004; Rajaee Rad and Adebar 2009; and Gerin and Adebar 2009).

The shear response of reinforced concrete slender walls is usually assumed to be elastic (Boivin and Paultre 2010). The stiffness of the linear model varies from gross shear stiffness G_cA_{vg} to cracked shear stiffness $G_{cr}A_{vg}$, where G_c is gross shear modulus and is equal to $0.4E_c$ and G_{cr} is cracked shear modulus, which is defined as the secant stiffness to the yield point and is a function of the percentage of transverse reinforcement. Also, A_{vg} is the cross sectional area effective in shear, and can be taken as the web area of the cross section. In this work, shear deformations are assumed to be linearly elastic with shear stiffness equal to $G_{cr}A_{vg}$. Gerin and Adebar (2004) concluded that crack shear stiffness is about 0.1 times the gross shear stiffness. Selecting lower bound shear stiffness results in higher shear deformation demands, which allows to examine how much shear stiffness can potentially influence roof displacement demands. Figure 5.33 plots mean roof displacement demands from time history and response spectrum analysis. Note that the term “w shear def.” in Figure 5.33 refers to the case with shear deformations included in the analytical model, while the term “w/o shear def.” corresponds to the case without shear deformations.

Figure 5.33 indicates that including shear deformation has negligible influence on the roof displacement demand of taller walls. The increase is not more than 5% for 30 and 50 story walls. For 10 story walls, on the other hand, including shear deformation results in 20%, 16%, and 10% increase in mean roof displacement for force reduction factors of 1.7, 2.3, and 3.2, respectively. Also shown in Figure 5.33 are roof displacement demands obtained from response spectrum analysis using stiffness reduction factors depicted in Figure 5.6 .Response spectrum analysis was repeated for two cases of with and without shear deformation scenarios. It can be concluded from Figure 5.33 that response spectrum analysis with shear deformation gives roof displacement demands that are in good agreement with those determined from time history analysis with shear deformation scenario.

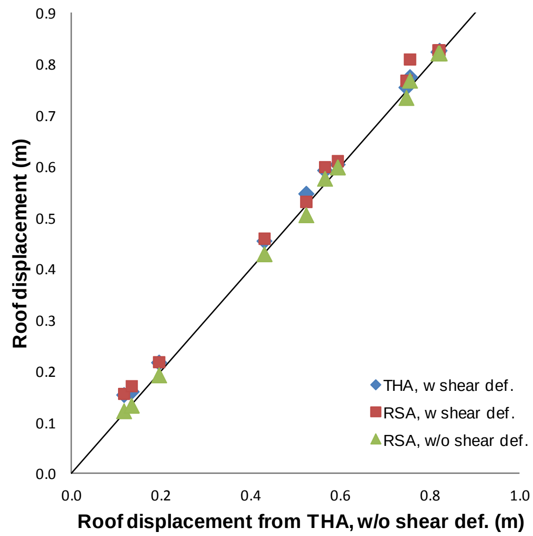

Figure 5.33 Comparison of roof displacement demands from flexure only with flexure plus shear deformation components determined using time history (THA) and response spectrum (RSA) analysis.

Table 5.5 compares mean base curvature and mean roof interstory drift demands for two analytical models from time history analysis. Table 5.5 indicates that the ratio of base curvature and roof interstory drift demands for the walls with shear deformation to those without shear deformation varies from 0.91 to 1.15 and from 1.01 to 1.34, respectively. Including shear deformation generally results in an increase in interstory drift demands. The amount of increase is higher for the 10 story walls than for the 30 and 50 story walls.

Table 5.5 Comparison of mean base curvature and mean roof interstory drift demands from time history analysis corresponding to models with and without shear deformation component.

		Base curvature (rad/km)		Roof interstory drift (%)	
Wall	R	w shear	w/o shear	w shear	w/o shear
10 story	1.7	0.78	0.68	0.73	0.55
	2.3	0.99	1.02	0.78	0.58
	3.2	1.37	1.35	0.96	0.84
30 story	1.4	0.26	0.27	0.84	0.81
	2.0	0.41	0.41	1.00	0.94
	2.3	0.61	0.61	1.04	0.97
	3.1	0.78	0.86	1.02	1.01
50 story	1.3	0.15	0.15	0.90	0.84
	1.8	0.23	0.23	0.94	0.90
	2.0	0.28	0.28	0.89	0.87
	3.7	0.33	0.40	0.88	0.84

5.6.2 Influence of Base Rotational Stiffness

Time history results presented in Sections 5.3 to 5.5 correspond to fixed base cantilever shear walls. Evaluating the stiffness of base support is a complicated task since it depends on the stiffness of floor diaphragms below grade, stiffness of foundation wall, and also soil type. The influence of foundation rocking, floor diaphragms, and the uplifting of the core walls due to the rocking mechanism on the seismic response of concrete shear walls has been investigated by Anderson (2003), Rajaee Rad and Adebar (2009), and Nielsen et al. (2010). The concern in this section is not modeling all possible parameters that would influence the boundary condition at the base, but is to evaluate the impact of base rotational stiffness on the behavior of cantilever shear walls and compare time history results with those for a fixed base support wall. It was assumed that buildings with fixed and flexible base supports are located on firm soil class (e.g. soil site class C according to NBCC 2005); therefore, the influence of soft soil on the seismic demands are not investigated. For this purpose, fixed support was replaced with a rotational spring with infinite axial and shear stiffnesses, while the rotational stiffness of the elastic spring was varied in order to achieve different levels of rotation at the base. The analysis was carried out for the 30 story walls with R = 3.1, and the base rotational stiffness was reduced in three steps. Table 5.6 compares modal periods of the wall with different base rotational stiffnesses.

Table 5.6 Modal periods of 30 story walls with fixed and flexible base supports.

Wall	T_1 (s)	T_2 (s)	T_3 (s)
Fixed base	2.97	0.47	0.17
Case 1	4.61	0.73	0.26
Case 2	5.74	0.82	0.28
Case 3	6.91	0.87	0.29

It can be inferred from Table 5.6 that the Case 3 wall possesses a very soft base spring since the fundamental period has elongated from 2.97 s for the fixed base wall to 6.91 s. Note that the third mode period is not as sensitive as the first mode period to the base rotational stiffness.

Table 5.7 shows the mean roof displacement demand determined from time history analysis (THA) and response spectrum analysis (RSA) for walls listed in Table 5.6. The displacement demands from RSA correspond to the stiffness reduction factor of 0.5, which gives a roof displacement demand that is equal to the mean roof displacement for the wall with a fixed base support.

Table 5.7 indicates that the displacement demand increases as the rotational stiffness of the base spring decreases. Also, RSA gives higher roof displacement demands than time history analysis for Case 2 and Case 3, i.e. using a stiffness reduction factor of 0.5 for walls with flexible base generally gives higher roof displacement demands than those determined from time history analysis.

Table 5.7 Comparison of mean roof displacement demand determined from THA and RSA for 30 story walls with different base stiffnesses.

	Roof displacement (m)	
Base support	THA	RSA
Fixed	0.59	0.59
Case 1	0.61	0.63
Case 2	0.66	0.78
Case 3	0.69	0.81

Figure 5.34 shows the mean curvature and bending moment envelopes for the four walls listed in Table 5.6. It can be seen that as the base rotational stiffness reduces, base curvature and base moment demands tend to decrease, while midheight curvature and midheight moment demands remain relatively constant. It was also observed that reducing base rotational stiffness

increases roof displacement demand up to 17%, while it reduces base curvature and base moment demands up to 49% and 19%, respectively.

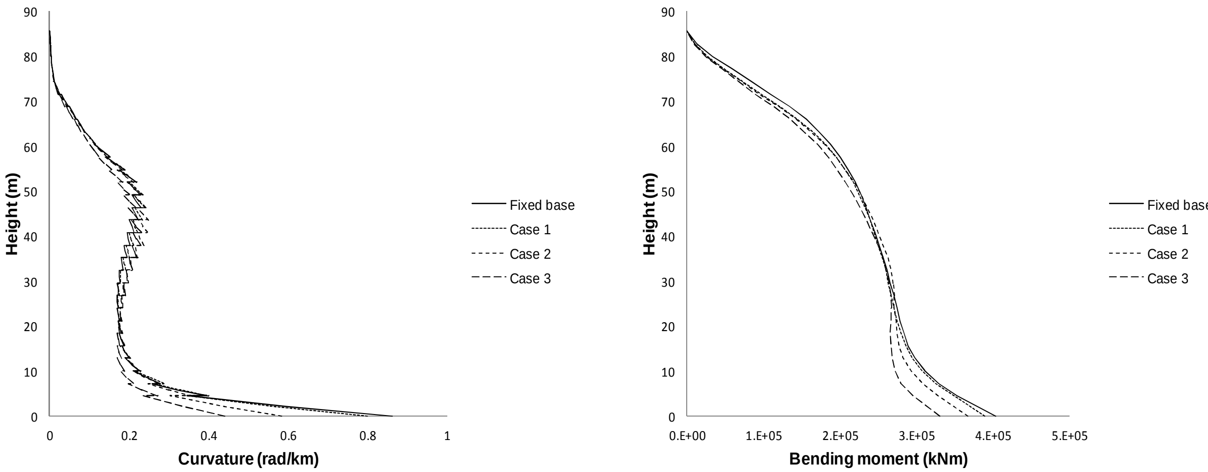

Figure 5.34 Comparison of mean curvature and bending moment profiles for 30 story walls with different base support stiffnesses determined from time history analysis.

Comparison between mean and mean plus one standard deviation interstory drift envelopes for the four walls and the predictions from D1 and D2 models is presented in Figure 5.35. Since roof displacement demands corresponding to time history analysis are lower than those from response spectrum analysis for Case 2 and Case 3 walls, the former was used to compute the key parameters of the simplified models. This was done to ensure that the models still predict accurate base rotations even if lower roof displacements are used. Figure 5.35 indicates that the simplified models give a reasonably accurate prediction of interstory drift demands over the height for walls with a flexible base support.

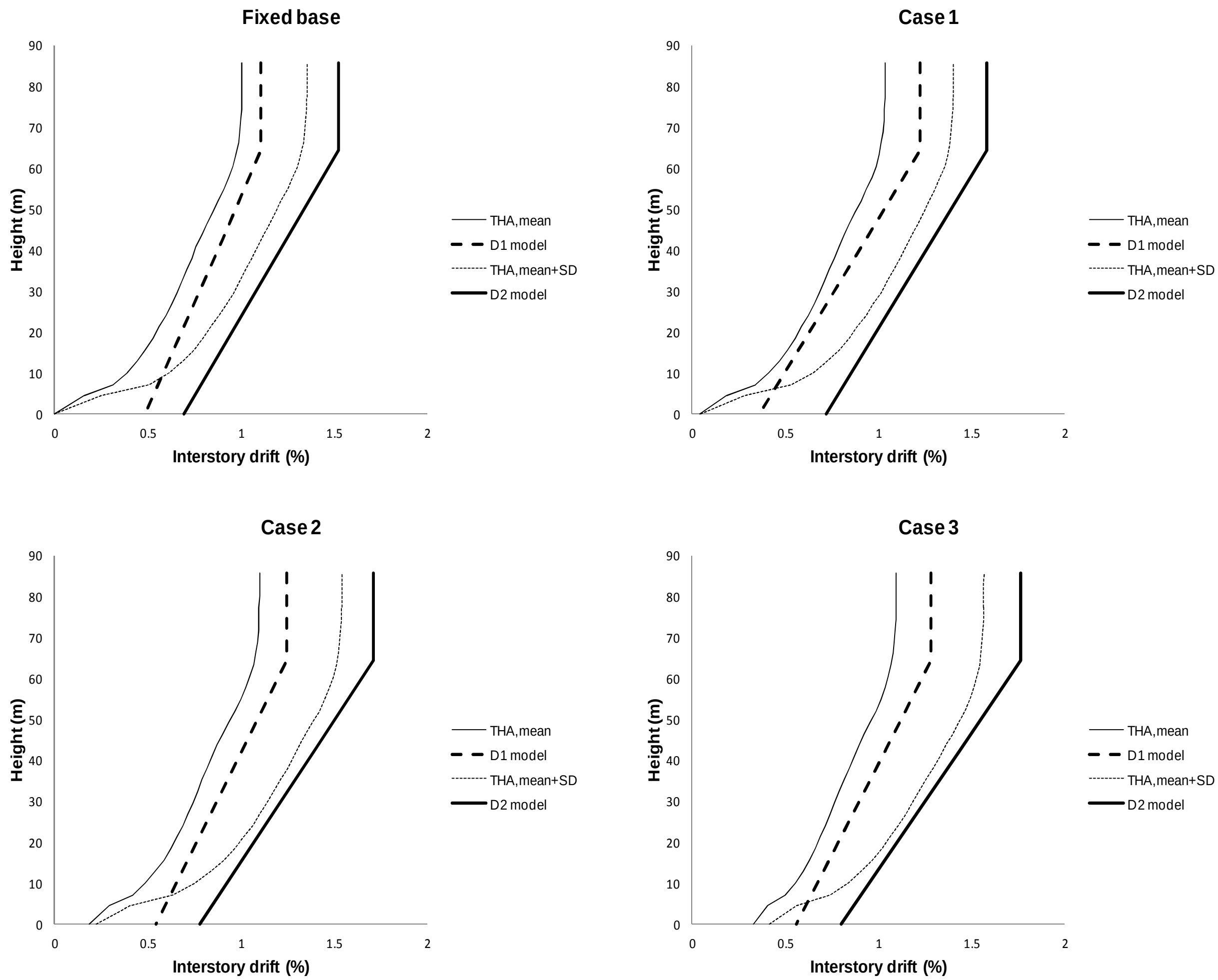

Figure 5.35 Comparison of mean (denoted as THA,mean) and mean plus one standard deviation (denoted as THA,mean+SD) interstory drift envelopes from time history analysis with the D1 and D2 models for 30 story walls with various base support stiffnesses.

5.7 Elastic-perfectly-plastic versus Trilinear Bending Moment - Curvature Relationship

The bending moment - curvature model used in this work features a trilinear backbone curve which accounts for uncracked response as well as tension stiffening of concrete. The Trilinear model also exhibits more pinching and less residual curvatures. These properties are very different from those of Elastic-perfectly-plastic (EPP) model, which has a bilinear backbone curve with larger hysteretic loops. The EPP model was used by Rutenberg and Nsieri (2006) to conduct time history analysis for estimating shear force demands in concrete shear walls. It is interesting to compare demand parameters from the trilinear model with those from the EPP relationship in order to observe how much the details of the hysteretic model influences the results. For this purpose, three 10, 30, and 50 story walls with force reduction factors of, respectively, 3.2, 3.1, and 3.7 were modeled using the EPP relationship. The EPP model can be defined by knowing three parameters: the initial slope of the backbone curve, bending moment capacity M_n, and post yield stiffness. The bending moment capacity is identical to those used for the trilinear model, and post yield stiffness is assumed to be 0.5% of the gross flexural stiffness EI_g. Two initial slopes of EI_g and $0.5EI_g$ were assumed for each wall. The fundamental period for the 10, 30, and 50 story walls is 1.0 s, 3.0 s, and 5.0 s for the initial slope of EI_g, and 1.34 s, 4.20 s, and 7.01 s for the initial slope of $0.5EI_g$, respectively. Figure 5.36 compares the trilinear and EPP bending moment - curvature models at the base of the three walls. The mean time history results are presented in Figures 5.37 through 5.39.

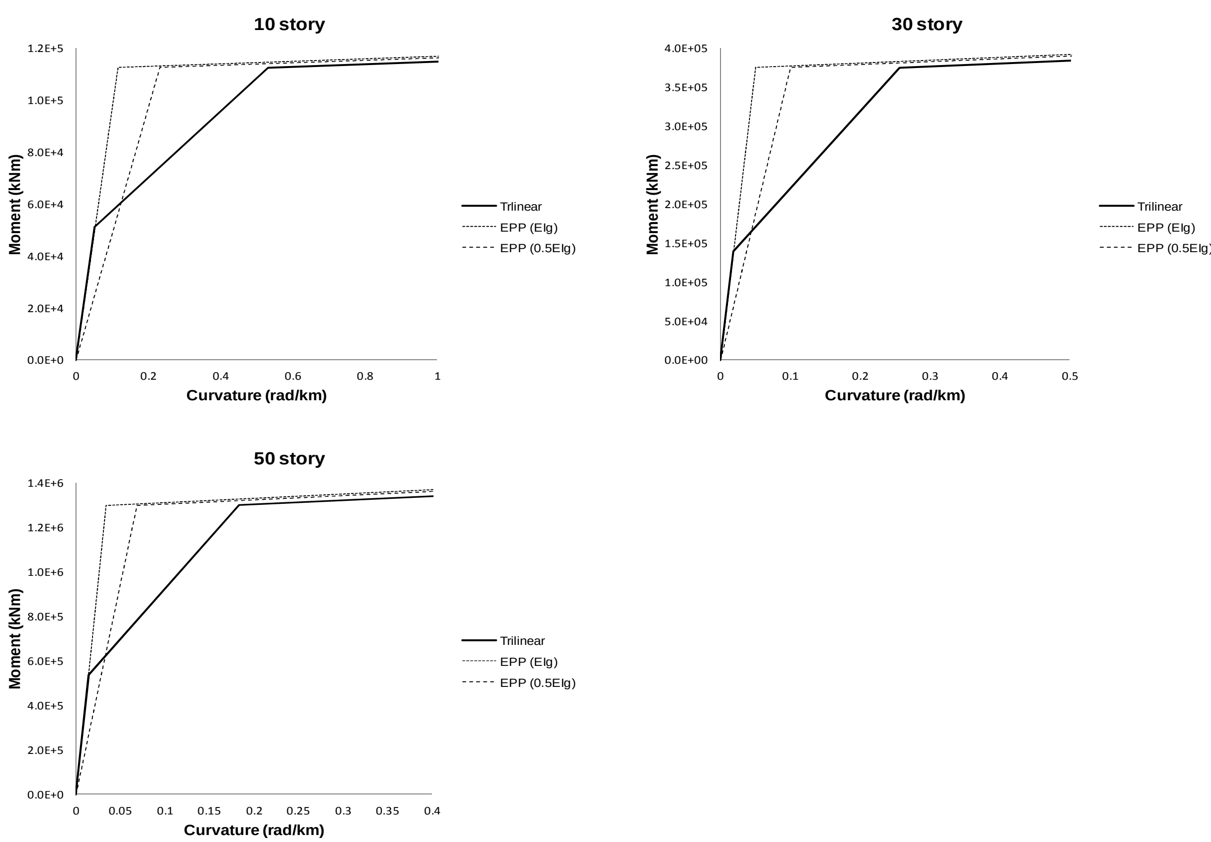

Figure 5.36 Bending moment - curvature relationship at the base for 10 story wall with R = 3.2, 30 story wall with R = 3.1, and 50 story wall with R = 3.7.

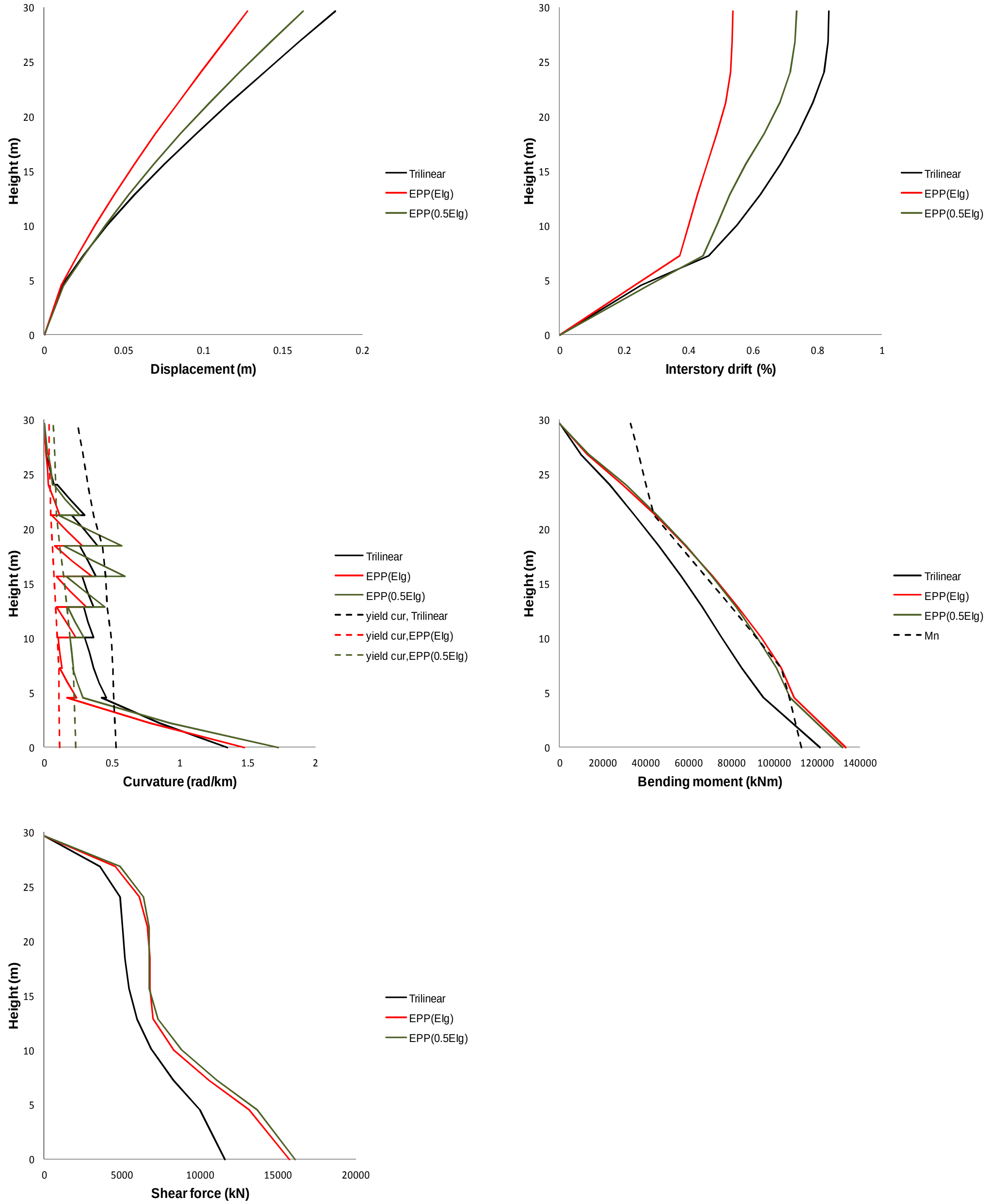

Figure 5.37 Comparison of mean demand parameters using trilinear and EPP models for the 10 story wall with R = 3.2.

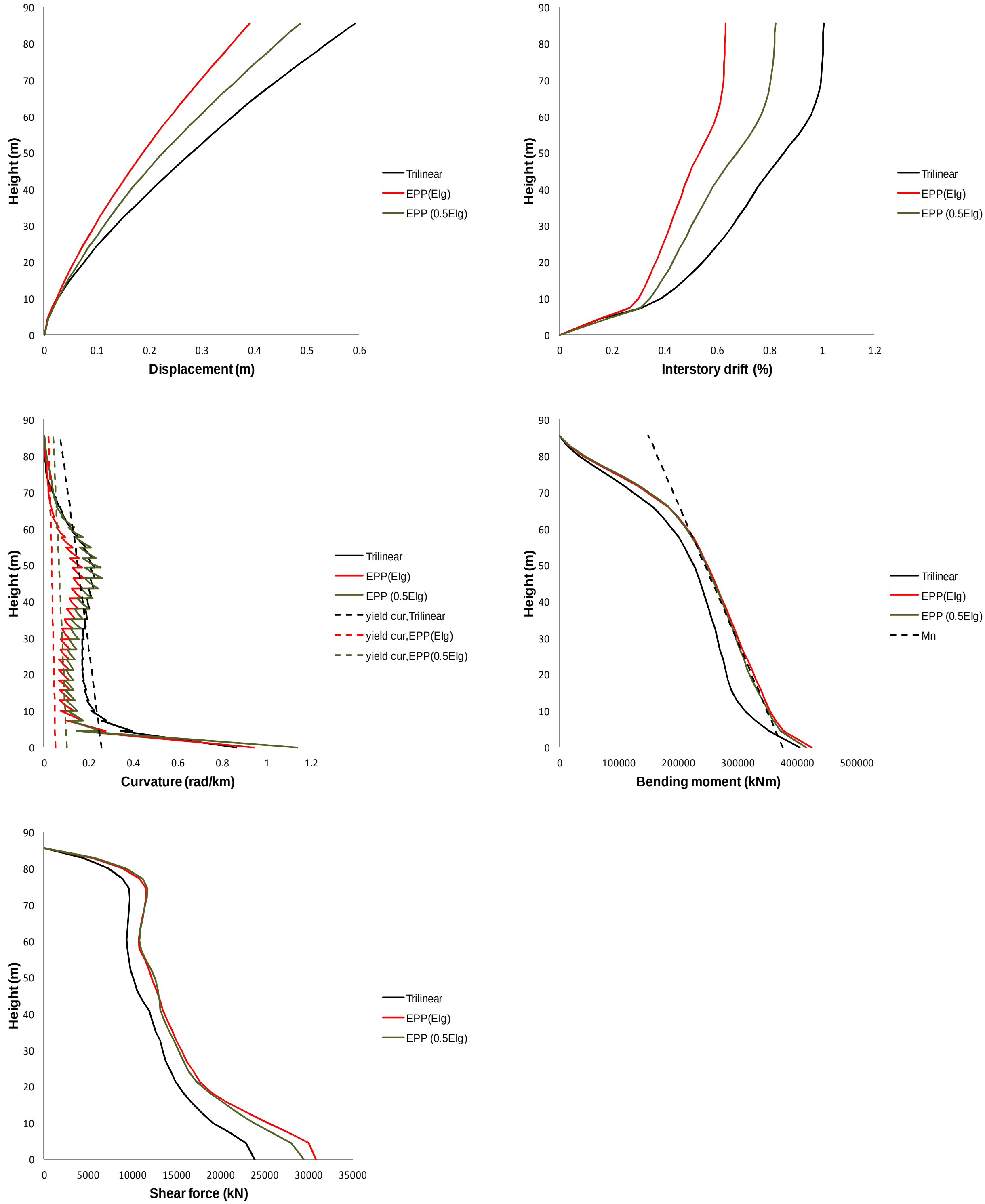

Figure 5.38 Comparison of mean demand parameters using trilinear and EPP models for the 30 story wall with R = 3.1.

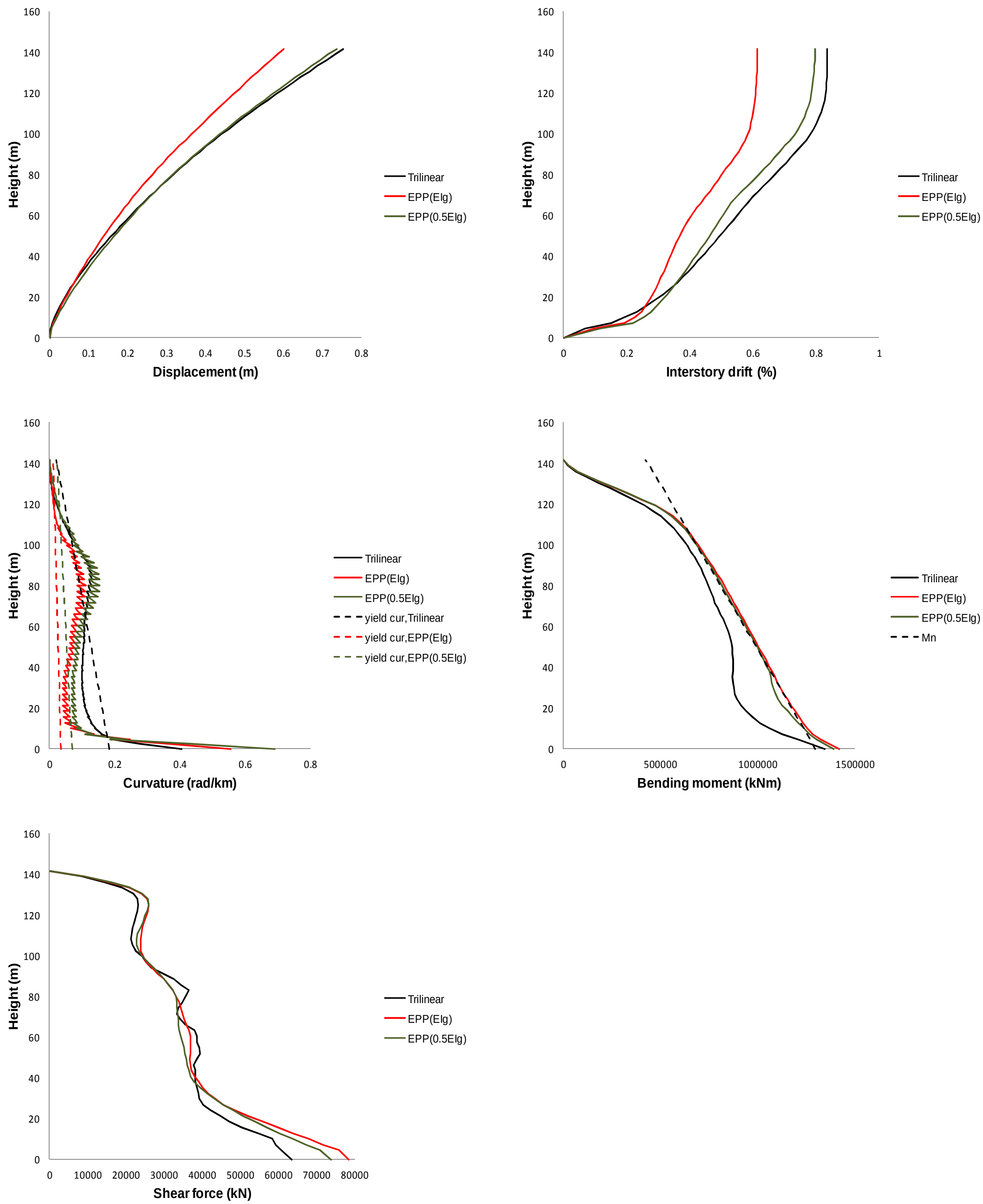

Figure 5.39 Comparison of mean demand parameters using trilinear and EPP models for the 50 story wall with R = 3.7.

Figures 5.37 through 5.39 indicate that roof displacement demands from the EPP model with $0.5EI_g$ initial stiffness are 11%, 18%, and 3% lower than those associated with the trilinear model for 10, 30, and 50 story walls, respectively. Mean interstory drifts at the top of the wall from EPP relationship with $0.5EI_g$ initial stiffness are 12%, 18%, and 5% lower than those corresponding to the trilinear model. Base curvature demands corresponding to the EPP model with $0.5EI_g$ initial stiffness are 27%, 32%, and 70% higher than those from the trilinear model for the 10, 30, and 50 story wall, respectively. The difference exacerbates if nonlinear behavior is expressed in terms of curvature ductility. Curvature ductility is defined as the ratio of mean base curvature determined from time history analysis to the yield curvature. Curvature ductility at the base for the trilinear model is 2.5, 3.4, and 2.2 for, respectively, 10, 30, and 50 story walls, while it is 12.8, 18.6, 16.2 for the EPP model with EI_g initial stiffness and 7.4, 11.3, and 10.1 for the EPP model with $0.5EI_g$ initial stiffness. Midheight curvature demands from the trilinear model are similar to those determined using the EPP relationship with $0.5EI_g$ initial stiffness. In terms of curvature ductility at the midheight, using the trilinear model results in no midheight yielding for the 10 story wall and moderate yielding for the 30 and 50 story walls. Comparison of mean midheight curvature demands with the yield curvature for the EPP models shows a curvature ductility of 3.0, 2.5, and 4.6 for EI_g and 2.6, 1.5, and 3.1 for $0.5EI_g$ initial stiffnesses for 10, 30, and 50 story walls, respectively. The difference between the curvature ductility at the base and at the midheight from the trilinear and EPP models is mostly attributed to the difference between the yield curvature predicted by these models rather than the difference between mean curvature demands from time history analysis.

Figures 5.37 to 5.39 also indicate that the mean base shear force demands from the trilinear model are consistently lower than those associated with the EPP models. The mean base shear force demand from the trilinear model is 28%, 19%, and 14% lower than that from the EPP model with $0.5EI_g$ initial stiffness, while it is 26%, 23%, and 20% lower than the mean base shear force demand corresponding to the EPP model with EI_g initial stiffness.

5.8 Using RSA to Estimate Curvature Envelope

As it was shown in Section 5.3, a good estimate of roof displacement can be obtained if appropriate stiffness reduction factors are used in response spectrum analysis. Applying a constant stiffness reduction factor implies that the shear wall possesses uniform stiffness distribution over the height. Results from time history analysis, on the other hand, indicated that largest curvature demands occur at the base of the wall, and curvature demands tend to increase around the midheight. Seismic demands at other elevations are less than these critical regions; therefore, the idea of applying uniform stiffness reduction factor does not capture the actual distribution of stiffness over the height of cantilever shear walls. To address this, Panagiotou (2008) proposed the Dual Plastic Hinge model, in which flexural rigidity at the base and at the midheight was reduced to rEI_e, while flexural stiffness at other sections was assumed to be EI_e. The r factor was defined as the ratio of post yield stiffness to initial stiffness EI_e and was assumed to be 2%. Also, effective stiffness EI_e was assumed to be 0.5 times the gross flexural stiffness EI_g. The length over which flexural rigidity was reduced at the base and midheight was considered to be 0.1 times the wall height h_w. Panagiotou (2008) concluded that applying dual plastic hinge concept in the design of cantilever shear walls results in lower amount of vertical reinforcement and easing of detailing along the height.

A modified response spectrum analysis similar to the Dual Plastic Hinge model is proposed in this section in order to better predict curvature demands in cantilever shear walls. Figure 5.40(a) shows a general schematic of the model. According to this model, plastic hinge length at the base and midheight was assumed to be $0.5l_w$ and $3l_w$, respectively. Stiffness reduction factors α, β, and γ were determined such that base curvature and midheight curvature demands predicted from RSA match the mean values from time history analysis, yet it gives an accurate prediction of mean roof displacement demands. This was done in two steps as follows:

1. For the first step, effective stiffness at the base was reduced from EI_e (Figure 5.40(b)) to αEI_g (Figure 5.40(c)) to give base curvature demands equal or greater than mean base curvature demands from time history analysis. Since reducing stiffness at the base increases roof displacement demands, the effective stiffness above the plastic hinge region at the base was increased in order to obtain roof displacement demands equal to mean roof displacement demands from time history analysis. A reduction factor of 0.9 was considered for these regions,

i.e. β = γ = 0.9 (Figure 5.40(c)). Figure 5.41(a) shows the variation of the reduction factor α as a function of force reduction factor R for the thirteen walls.

2. For the second step, effective stiffness at midheight was reduced from EI_e (Figure 5.40(b)) to γEI_g (Figure 5.40(d)) to give midheight curvature demands equal to or greater than mean midheight curvature demands from time history analysis. The effective stiffness outside the midheight plastic hinge region was adjusted to obtain roof displacements equal to the mean roof displacement demand from time history analysis. Figure 5.40(b) and Figure 5.40(c) show the variation of stiffness reduction factor at the midheight plastic hinge region (denoted as γ) and outside this region (denoted as β) as a function of R for the thirteen walls.

3. Final curvature and interstory drift demands for a wall can be calculated by taking the maximum of curvature and interstory drift envelopes determined from steps one and two.

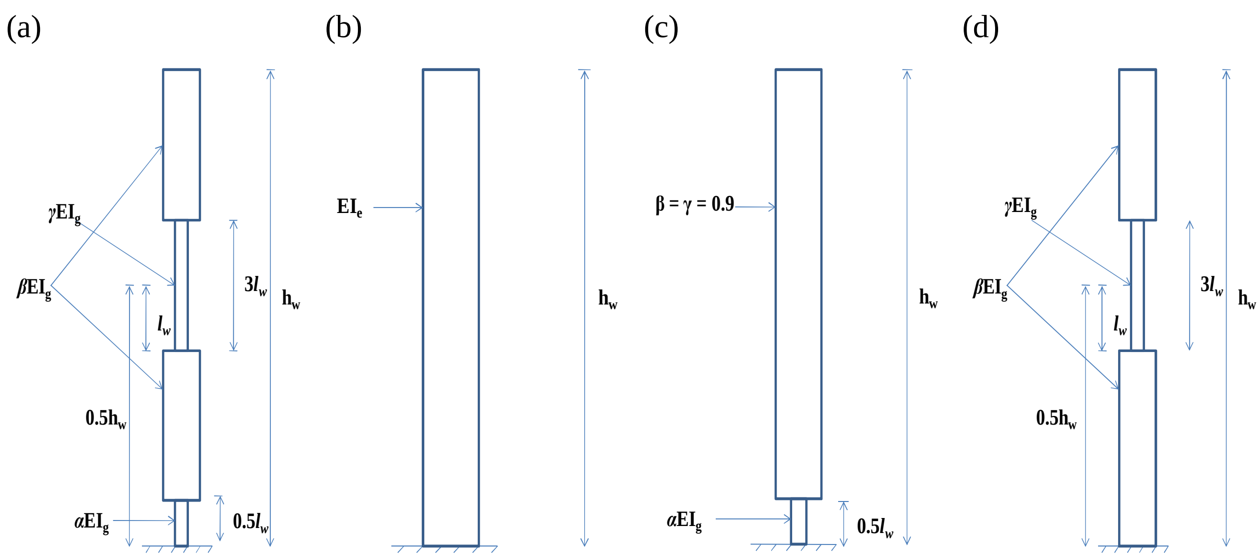

Figure 5.40 General schematic of (a) RSA with variable stiffness reduction factor, (b) RSA with uniform reduction factor to estimate roof displacement demand, (c) RSA with reduced stiffness reduction factor at the base to estimate base curvature demand, and (d) RSA with reduced stiffness reduction factor at the midheight to estimate midheight curvature demand.

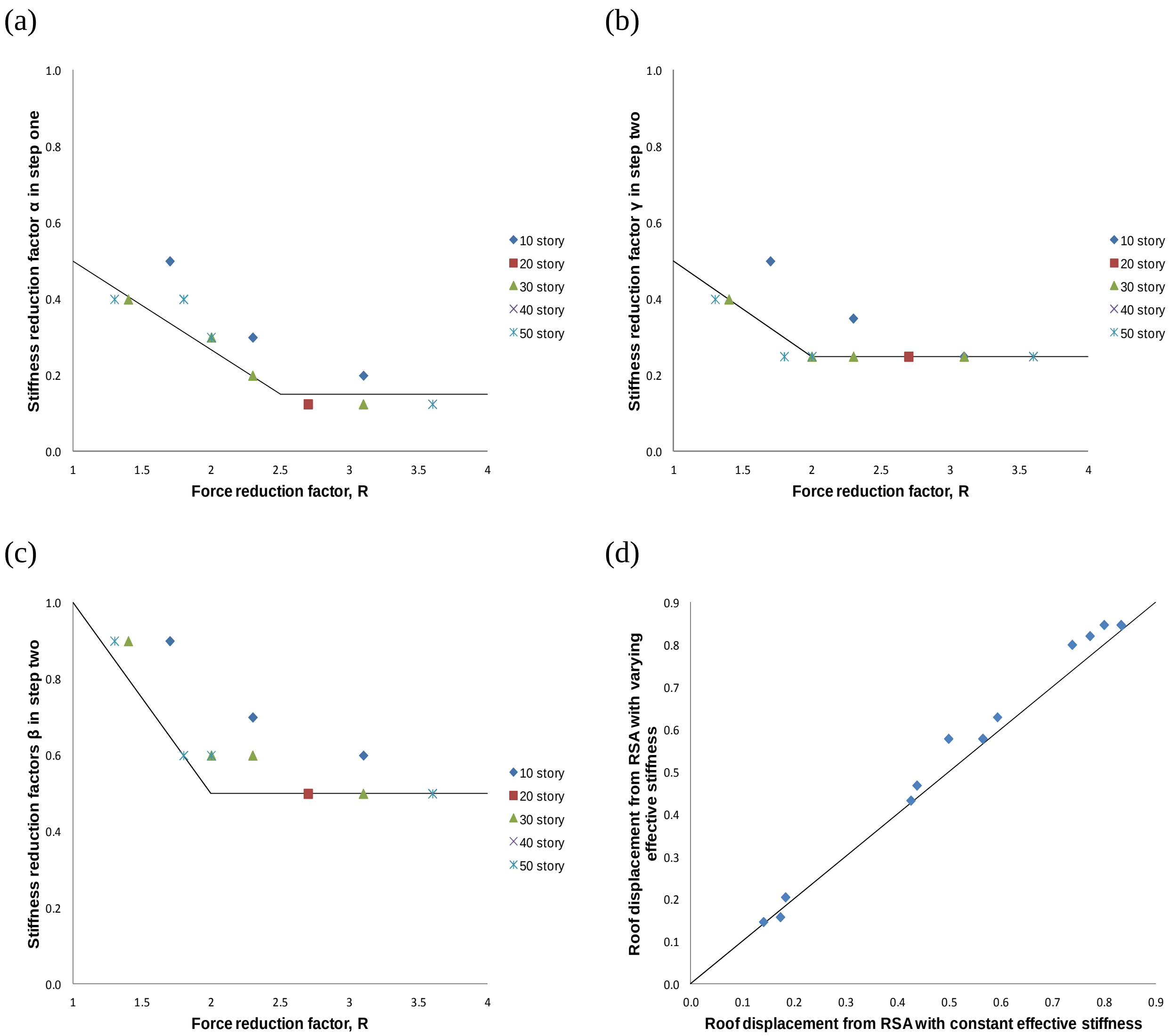

Figure 5.41 Variation of: (a) α determined in step 1, (b) γ determined in step 2, (c) β determined in step 2; (d) comparison of roof displacement demand from step 1 and 2 with roof displacement demand using a constant effective stiffness over the height.

Figure 5.41(d) compares roof displacement demands from RSA using stiffness reduction factors presented in Figures 5.41(a) to (c) with those determined from RSA using constant stiffness reduction factors over the height. It can be seen that roof displacement demand from the two approaches are very similar.

Figures 5.42 to 5.45 compare curvature and interstory drift envelopes determined from Step 3 with the mean envelopes from time history analysis. Also shown in these figures are the curvature and interstory drift profiles from RSA using constant stiffness reduction factors. As it can be seen from these figures, the traditional RSA with constant effective stiffness over the height gives poor estimate of base and midheight curvature demands, while the modified RSA with varying stiffness reduction factors gives a reasonable estimate of these demands. Note that the idea of developing RSA with varying effective stiffness over the height was to predict mean curvature envelopes from time history analysis, yet it can be seen from Figures 5.42 through 5.45 that the interstory drift envelopes corresponding to the modified RSA are a reasonable upper bound to the interstory drifts envelopes determined from time history analysis.

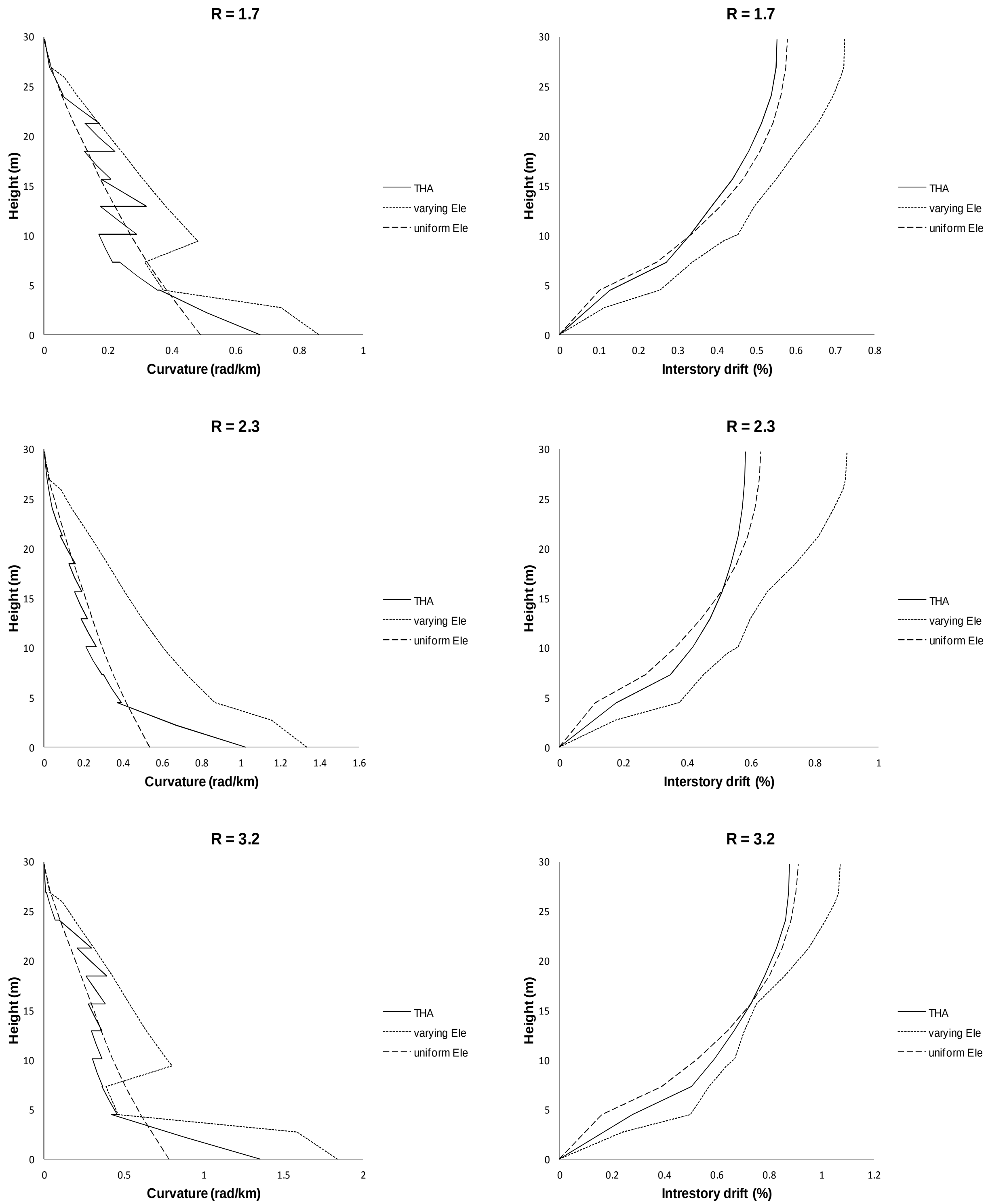

Figure 5.42 Comparison of mean curvature and interstory drift envelopes from time history analysis (THA) with predictions from RSA using varying and uniform stiffness reduction factors for 10 story walls.

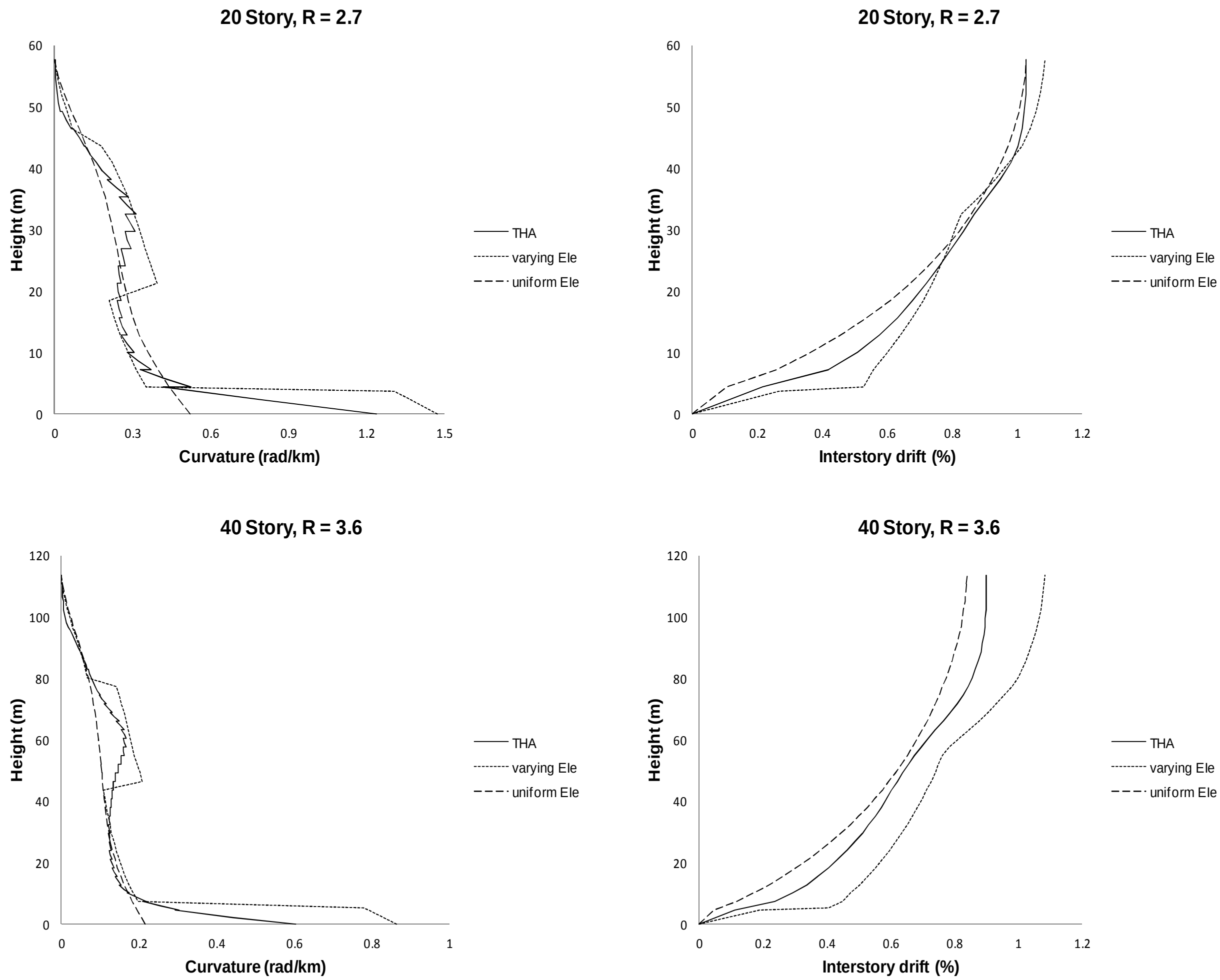

Figure 5.43 Comparison of mean curvature and interstory drift envelopes from time history analysis (THA) with predictions from RSA using varying and uniform stiffness reduction factors for 20 and 40 story walls.

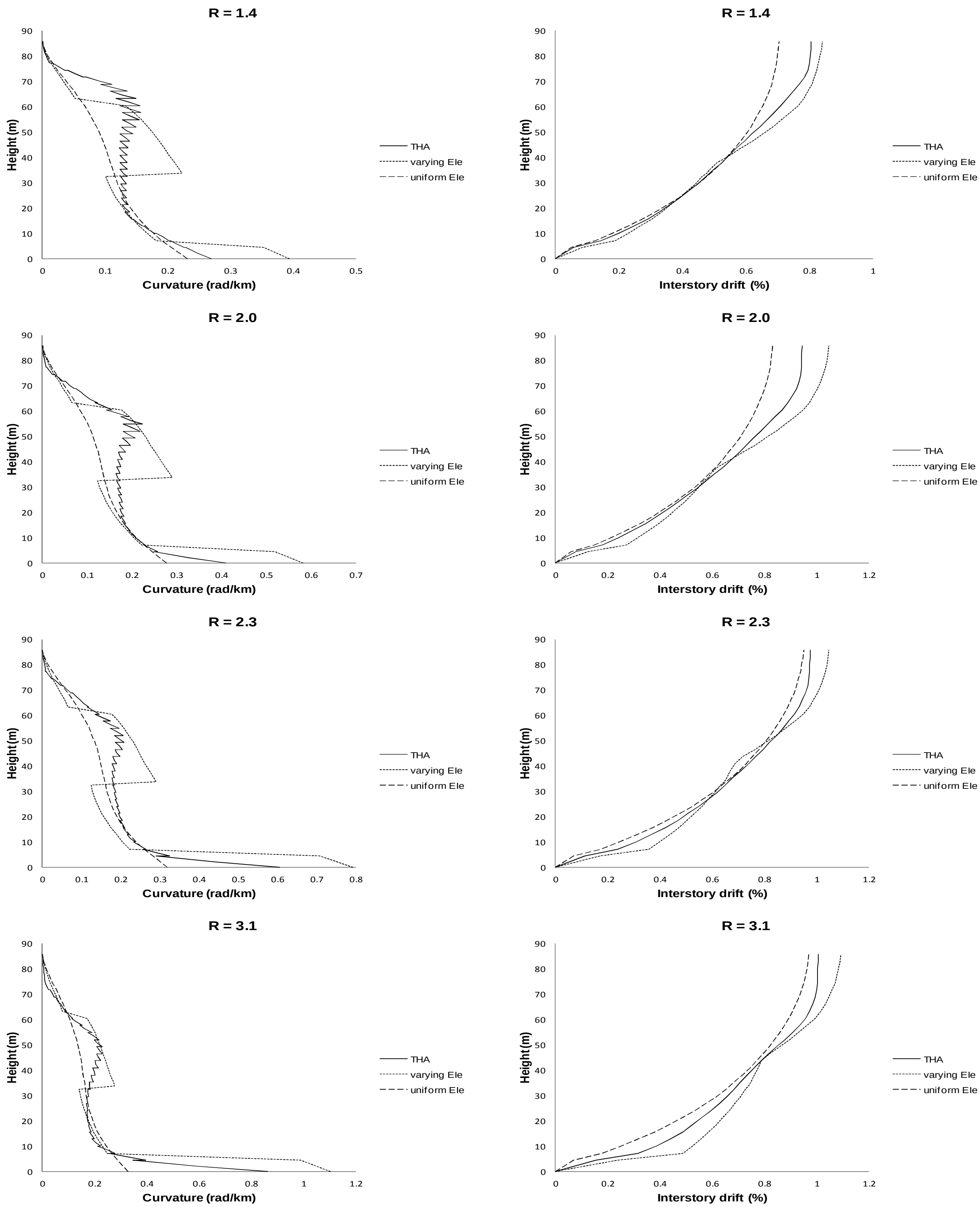

Figure 5.44 Comparison of mean curvature and interstory drift envelopes from time history analysis (THA) with predictions from RSA using varying and uniform stiffness reduction factors for 30 story walls.

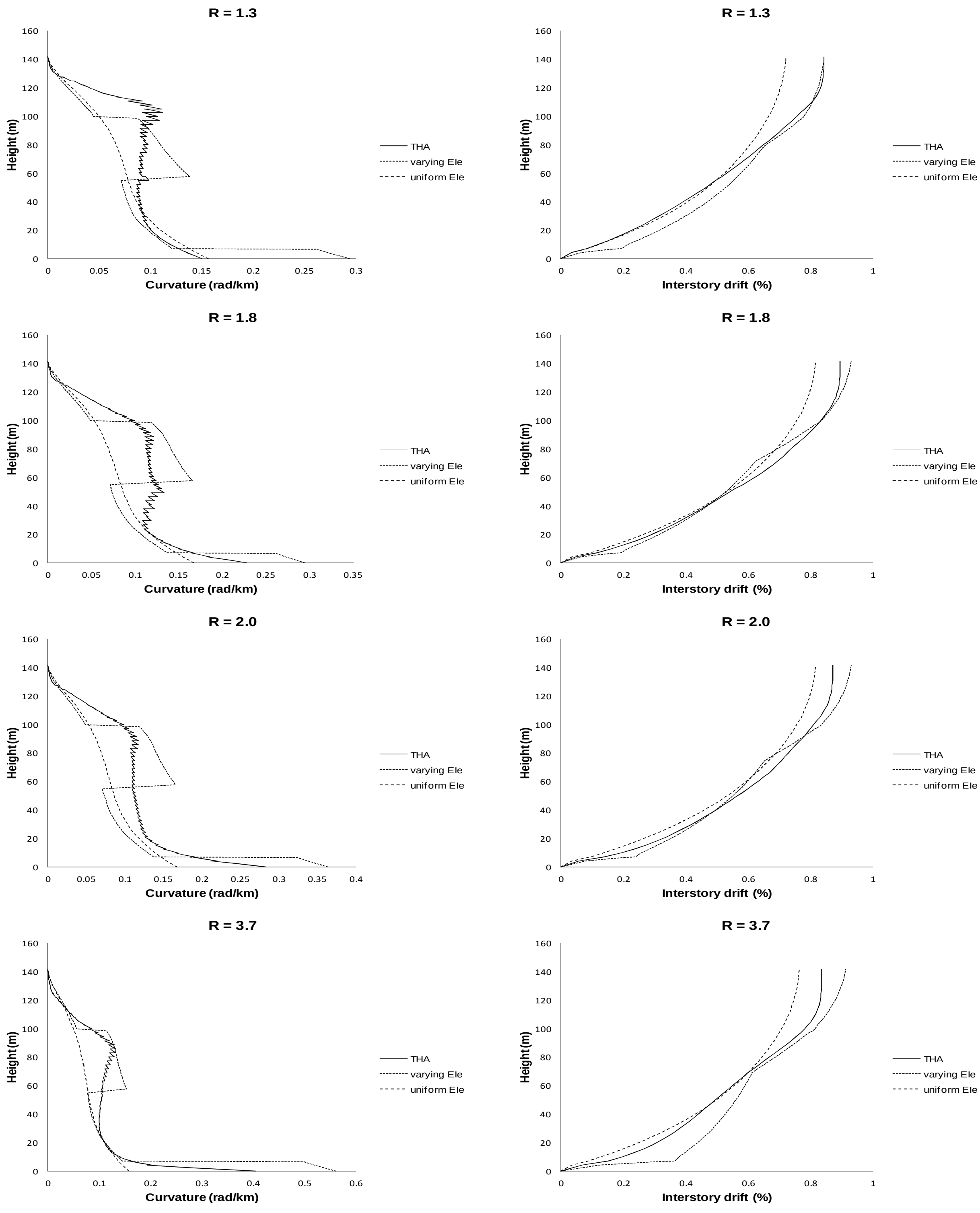

Figure 5.45 Comparison of mean curvature and interstory drift envelopes from time history analysis (THA) with predictions from RSA using varying and uniform stiffness reduction factors for 50 story walls.

5.9 Summary and Conclusions

Time history analysis was used to develop simplified models to predict flexural response of cantilever shear walls. The study included 13 different cantilever shear walls that were 10 to 50 stories high, and had a wide range of longitudinal reinforcement percentages and axial compression force levels. Mean roof displacement demands from time history analysis was used to determine effective stiffness of cantilever shear walls. It was observed that stiffness reduction factor drops from 1.0 to 0.5 as the force reduction factor increases. Using the recommended reduction factors in a linear analysis such as response spectrum analysis (RSA) results in roof displacement demands that are similar to the mean displacement demands from time history analysis.

The relationship between base curvature and roof displacement demands was investigated for three walls. It was observed that these demands did not occur at the same instant in taller walls due to the influence of higher modes. It was also observed that the CSA A23.3-04 approach underestimates the elastic portion of the roof displacement demand, which implies that this approach overestimates base curvature demands especially in taller walls. A model was proposed in order to predict base curvature demands corresponding to mean and mean plus one standard deviation results determined from time history analysis. The proposed model relates base curvature demands to the global drift demand through a term, which is a function of the wall height and force reduction factor. Also, a new model for predicting midheight curvature demands was developed. It was observed that the intensity of midheight curvature demand is relatively independent of the wall flexural strength, and midheight curvature demand vary between $0.002/l_w$ and $0.0035/l_w$, where l_w is the wall length. Midheight yielding can be well tolerated by providing minimum detailing over the elevation range from above the plastic hinge region at the base to $0.75h_w$, where h_w is the wall height. Lastly, a simplified design envelope for predicting curvature demands over the height was proposed. The input parameters for this model are the base curvature demand, midheight curvature demand, and the plastic hinge length at the base.

This study introduced a new model for predicting interstory drift demands in cantilever shear walls. Accurate estimate of this parameter is of particular importance in assessing the strength of slab-column connections. Roof and midheight interstory drifts were expressed in terms of the global drift ratio. It was observed that both roof and midheight interstory drift demands are relatively independent of the force reduction factor. Two models were proposed for estimating interstory drift demands corresponding to mean and mean plus one standard deviation results determined from time history analysis. Both models feature residual drift demands at the base to represent the additional rotation at the base of walls with a flexible support. A simplified design envelope was then proposed to estimate interstory drift demands over the height. The accuracy of the model was demonstrated for walls with fixed and flexible base supports.

The influence of shear deformation on roof displacement demands of cantilever shear walls was studied. It was concluded that including shear deformation does not impact demand parameters on cantilever shear walls significantly even though a lower-bound shear stiffness is used in the analytical model.

Time history results using trilinear and Elastic-perfectly-plastic (EPP) hysteretic models were also compared in this study. It was observed that except roof displacement and interstory drift at the top of wall, other demand parameters from the EPP models are higher than those associated with the trilinear model. It was observed that the reason the two models resulted in very different base and midheight curvature ductility ratios is due to the fact that the two analytical models offer very different estimate of the yield curvature.

This study introduced a modified response spectrum analysis with varying stiffness reduction factor in order to predict the mean curvature envelope. It was observed that although using constant stiffness reduction factors in RSA results in good prediction of roof displacement demands, it gives a poor estimate of base and midheight curvature demands. The modified RSA is accomplished in two steps: in the first step the stiffness of the wall at the base in reduced to estimate mean base curvature demands, while in the second step the wall stiffness is reduced at the midheight in order to estimate mean midheight curvature demands from time history analysis. Final curvature envelope for a wall would be the maximum of the envelopes determined from steps one and two. It was also observed that using the modified RSA results in interstory drifts that are an upper-bound to the mean interstory drift demands determined from time history analysis.

Chapter 6 : Shear Demands on Cantilever Shear Walls

6.1 Overview

In this chapter, time history results are used to estimate shear force demands on cantilever shear walls. Previous recommendations on shear amplification factor are reviewed. The relationship between base shear force and base rotation demands and the influence of higher mode period elongation on midheight shear force demands are investigated. Lastly, shear force profiles corresponding to mean time history results are used to develop simple design envelopes for predicting shear force demands over the height.

6.2 Dynamic Shear Amplification Factor

Estimating shear force demands is of particular interest in the seismic design of cantilever shear walls in order to ensure these structures will have a ductile response. Due to the influence of higher modes, the shear force demands from nonlinear time history analysis are considerably larger than those from linear analysis. The difference between shear force demands from the two approaches is often called dynamic shear amplification factor. Many previous studies have been carried out in order to estimate this parameter. A brief review of these studies is presented in this section.

Blakely et al. (1975) observed that base shear force demands from time history analysis of 6 to 20 story shear walls are larger than those determined from the static code procedure. Only five unscaled ground motions were used in the study, and a bilinear bending moment - curvature relationship was used to model the shear walls. Blakely et al. proposed the following equation to amplify shear force demands from the code procedure:

$$\omega_v = \begin{cases} 0.9 + \dfrac{n}{10}, & n \leq 6 \\ 1.3 + \dfrac{n}{30}, & n > 6 \end{cases} \qquad Eq\ 6.1$$

where n is the number of stories. It should be noted that the shear amplification factor ω_v in Equation 6.1 is limited to 1.8, i.e. this parameter is constant for buildings with the number of floors n equal to or greater than 15. Also implied in Equation 6.1 is that ω_v is proportional to the fundamental period of the structure since the latter is usually a function of number of stories. Rutenberg and Nsieri (2006) conducted time history analysis on a series of 5 to 25 story shear walls with fundamental periods ranging from 0.3 to 3.0 s. These walls were subjected to 2 suites of records, each containing 20 ground motions, developed for SAC project (Somerville 1997). The elastic-perfectly-plastic hysteretic model was used in the analytical model, and the following equation was proposed based on the mean base shear force demands:

$$V_a = \big(0.75 + 0.22(T + q + Tq)\big)V_d \qquad Eq\ 6.2$$

where T and q are the fundamental period and behaviour factor (similar to force reduction factor which is defines as the ratio of elastic bending moment demand to the wall capacity, both calculated at the base of the wall), respectively. Note that V_d is the shear force demand at the base determined from static analysis using an inverted triangular lateral load pattern and is equal to $\frac{M_n}{\frac{2}{3}H(1+\frac{1}{2n})}$, where M_n is the bending moment at flexural yielding, and H and n are the total height and number of stories, respectively. The ratio of V_a/V_d in Equation 6.2 is essentially the shear amplification factor ω_v. Rutenberg and Nsieri also introduced a simple model to estimate shear force distribution over the height of the building. According to this model, shear force is constant over a length equal to $0.1H$, and then it decreases to 0.5 times the base shear force determined using Equation 6.2. The elevation at which shear force is dropped to $0.5V_a$ is ξH, where ξ is equal to $1.0\text{-}0.3T$ and is greater than or equal to 0.5.

Keintzel (1990) used the SRSS modal combination method to estimate base shear force demands from time history analysis. He assumed that only the first and second modes are the dominant modes of vibration, and he proposed the following equation for predicting base shear force demand V_{ED}:

$$V_{ED} = \sqrt{(V_{ED1})^2 + (qV_{ED2})^2} \qquad Eq\ 6.3$$

where V_{ED1} and V_{ED2} are the design base shear forces corresponding to the first and second modes, respectively. Equation 6.3 indicates that the design shear force from the second mode is increased by the behaviour factor q in order to account for the influence of higher modes. Keintzel simplified Equation 6.3 by assuming that the ratio of the base shear force from the second mode to the base shear force from the first mode is equal to $\sqrt{0.1}\frac{S_a(T_2)}{S_a(T_1)}$, where $S_a(T_1)$ and $S_a(T_2)$ are the spectral accelerations corresponding to the first and second modes, respectively. Implementing this assumption in Equation 6.3 and considering the influence of flexural overstrength on the first mode shear force gives the following equation, which has also been used in the Eurocode 8-EC 8 (CEN 2004):

$$\omega_v = q.\sqrt{(\frac{\gamma_{Rd}}{q}\frac{M_{Rd}}{M_{Ed}})^2 + 0.1(\frac{S_a(T_c)}{S_a(T_1)})^2} \qquad Eq\ 6.4$$

where ω_v is shear amplification factor and should be applied to the design shear force determined from the first mode, γ_{Rd} is the overstrength associated with reinforcing steel strain hardening, M_{Rd}/M_{Ed} is the ratio of design flexural strength to the design bending moment demand at the base of the wall, and $S_a(T_c)$ is the maximum spectral acceleration. According to EC 8 provisions, the minimum and maximum value for ω_v is 1.5 and the q factor, respectively.

Priestley and Amaris (2003) studied the seismic response of 6 cantilever shear walls with the number of stories from 2 to 20 and fundamental period ranging from 0.34 to 3.65 s. Five spectrum matched ground motions compatible with the EC 8 design spectrum were used as the input motion, and the walls were modelled using the Takeda hysteretic model. Similar to the approach taken by Keintzel, Priestley and Amaris proposed a so called Modified Modal Superposition (MMS) method, in which the shear force at a given floor i, V_i, can be determined from the following equation:

$$V_i = (V_{1i}^2 + V_{2Ei}^2 + V_{3Ei}^2 + \cdots)^{0.5} \qquad Eq\ 6.5$$

where V_{1i} is the design shear force from the first mode and the other terms are the elastic shear forces corresponding to higher modes. Equation 6.5 implies that nonlinear response only limits the shear force from the first mode response, and shear forces from higher modes are not affected by ductility in the same manner as the first mode response is.

The MMS method described above has been modified by several researchers. Sullivan et al. (2008) compared base shear force demands from Equation 6.5 with time history results for two groups of frame-wall structures using the Takeda hysteretic model subjected to only five real (not spectrum matched) ground motions. They observed that the MMS method gives considerably higher base shear forces than the mean base shear force from time history analysis. A so called Transitory Inelastic Modal Superposition (TIMS) method was introduced, which accounts for the period lengthening of higher modes due to the inelastic behaviour. The base shear force from this method can be determined from the following equation:

$$V_{bTIMS} = (V_{b1}^{o^2} + V_{bTIMS2}^2 + V_{bTIMS3}^2 + \cdots + V_{bTIMSn}^2)^{0.5} \qquad Eq\ 6.6$$

where V_{b1}^{o} is the ductile first mode base shear force (identical to V_{1i} term in Equation 6.5), and V_{bTIMSn} is the base shear force corresponding to the n^{th} mode of a structure with a very soft spring at the base. Sullivan et al. (2008) indicated that the stiffness of the spring at the base is possibly close to the post yield stiffness. Performing eigen value analysis of a structure with a softened base results in very long fundamental period, which essentially represents the hinge mechanism at the base due to the flexural yielding.

Pennucci et al. (2010) followed a similar approach to estimate shear force demands in tall concrete shear walls. They carried out time history analysis on a series of walls with fundamental periods varying from 1 to 10 seconds. The ratio of elastic bending moment at the base to the flexural strength (denoted as R_M) ranged from 1 to 5. The Takeda hysteretic model was used to model the plastic hinge region at the base, and the rest of the wall was assumed to remain elastic. Eleven spectrum matched ground motions were used in time history analysis, and a damping of only 0.5% was set to the first and third modes. Pennucci et al. observed that for a wall with fundamental period of 4 s and R_M = 4, the ratio of elastic shear force demand at the base to the mean base shear force demand from time history analysis is considerably less than 4.0. Consequently, using traditional response spectrum analysis leads to underestimation of shear force demands in taller walls with higher force reduction factors. Lastly, the following equation was proposed to predict base shear force demand:

$$V_a = \frac{V_{Ed,1}}{R_m} + \frac{\sqrt{(V_{pin,2})^2 + (V_{pin,3})^3 + \cdots}}{R_p} \qquad Eq\ 6.7$$

where $V_{Ed,1}$ is the elastic base shear force form the first mode of a wall with a fixed support, and $V_{pin,i}$ (i = 2, 3,…) is the elastic base shear force from higher modes of response of a wall with a pinned support. The authors found that the R_p factor is related to R_M: for R_M = 1, R_p goes to infinity, while for very flexible structures ($R_M = \infty$) R_p goes to 1.0.

Calugaru and Panagiotou (2011) studied the seismic response of cantilever shear walls subjected to pulse type loading. The study included 10, 20, and 40 story walls with fundamental periods ranging from 2.2 to 6.6 s, and three force reduction factors of 2, 4, and 6 were considered for each wall. The Clough hysteretic relationship was used to model the nonlinear response over the plastic hinge region at the base of walls, and the remainder of the wall was modelled with elastic elements with an effective stiffness equal to $0.4EI_g$. Calugaru and Panagiotou proposed the following equation to estimate a given response quantity (such as shear force or bending moment demand) at floor i:

$$Q^i = \sqrt{(Q_1^i \frac{\Omega_{b,o}}{R_1})^2 + \frac{(Q_2^i)^2 + (Q_3^i)^3}{(R_H)^2}} \qquad Eq\ 6.8$$

where, Q^i_1, Q^i_2, and Q^i_3 are the elastic quantities corresponding to the first, second and third modes at floor i, R_1 is the force reduction factor applied to the first mode response, $\Omega_{b,o}$ is the overstrength factor, and R_H is the reduction factor associated with higher modes. The authors found that R_H is generally much smaller than R_1. It was found that for base shear force demand, R_H varies from about 1 to 2 for pulse loads with periods between second and third mode periods of the shear wall.

CSA A23.3-04 Clause 21 defines shear force demand and shear resistance of ductile walls in order to ensure that the ductile response (flexural yielding at the base plastic hinge region) occurs prior to shear failure. Clause 21.6.9 states that the shear force demands determined from linear analysis must be increased by the ratio of probable moment capacity to the applied factored moment at the base of the wall. Also, the shear force demand is limited to shear demands determined from linear analysis. Boivin and Paultre (2010) performed nonlinear time history analysis on a 12-story cantilever shear wall located in Montreal and they concluded that shear force demand from time history analysis was greater than the predicted shear force demand from the CSA A23.3 prediction.

In terms of shear strength, CSA A23.3-04 defines concrete shear strength V_c as a function of the parameter β. The β parameter reduces as the longitudinal strain increases, which is an indicator of the diagonal crack width. Bentz et al. (2006) observed that β varied from 0.3 to about 0.15 as longitudinal strain ε_x increased from 0 to $2.5\text{x}10^{-3}$. Clause 21 of CSA A23.3-04, on the other hand, recommends a lower-bound value for 0.18 for β for regions of plastic hinging, and then reduces this parameter further to account for the reduction in aggregate interlock shear resistance due to the increase in the width of diagonal cracks. The inelastic rotation at the base plastic hinge region θ_{id}, is used as an indicator of diagonal crack width. The same analogy was taken by Krolicki et al. (2011) to relate concrete shear resistance to displacement ductility based on experimental results.

Most of the researchers focused on estimating shear force demands by using a small number of ground motions (five by Priestley and Amaris; five by Sullivan et al. ,and eleven by Pennucci et al.) to conduct time history analysis. The relationship between base rotation and base shear force demands during ground motion shaking still needs to be examined in order to understand the intensity of base rotations at the instant of high base shear force demands. Lastly, it is necessary to correlate shear force demands determined from time history analysis to the results from response spectrum analysis, as the latter is the method that is used in practice to estimate seismic demands on cantilever shear walls. A simplified design envelope for predicting shear force demands over the height is also proposed in this chapter.

6.3 Shear Force - Base Rotation Relationship

In order to understand the relationship between base rotation and base shear force demands, time history results for three 10, 30, and 50 story walls were examined. The force reduction factor corresponding to these walls is 3.2, 3.1, and 3.7, respectively. The number of input ground motions is 80, 53, and 35 for 10, 30, and 50 stories high walls, respectively. These records are referred to as “SOR” ground motions in Chapter 4.

Figure 6.1 shows the variation of base curvature and base bending moment demands at the instant of maximum base shear force demand for the three walls. Note that the vertical axis in the left figures is normalized by the mean base curvature demand, which is essentially the mean value of the largest base curvature demand recorded for individual ground motions. Figure 6.1 indicates that the base curvature demands are relatively small at the time when maximum base shear force occurs. The ratios are bigger for the 10 story wall, and it gets smaller for the 30 and 50 story walls. In terms of bending moment demand at the base, it can be seen that bending moments at the instant of maximum base shear force are relatively large for the 10 story wall – all moments are higher than the bending moment at crack opening M_{co}. For the 30 and 50 story walls, on the other hand, bending moments corresponding to half of ground motions are less than M_{co} indicating that bending moments are relatively low when maximum base shear force occurs.

The main drawback of Figure 6.1 is that it only shows base curvature at the instant when maximum base shear force occurs. Other possible critical instants might be the instants at which base curvature demand is significantly higher than the curvature demands at the instant of maximum base shear force, while the corresponding base shear force is slightly lower than the maximum base shear force for that ground motion. Figure 6.2 shows an example of such case.

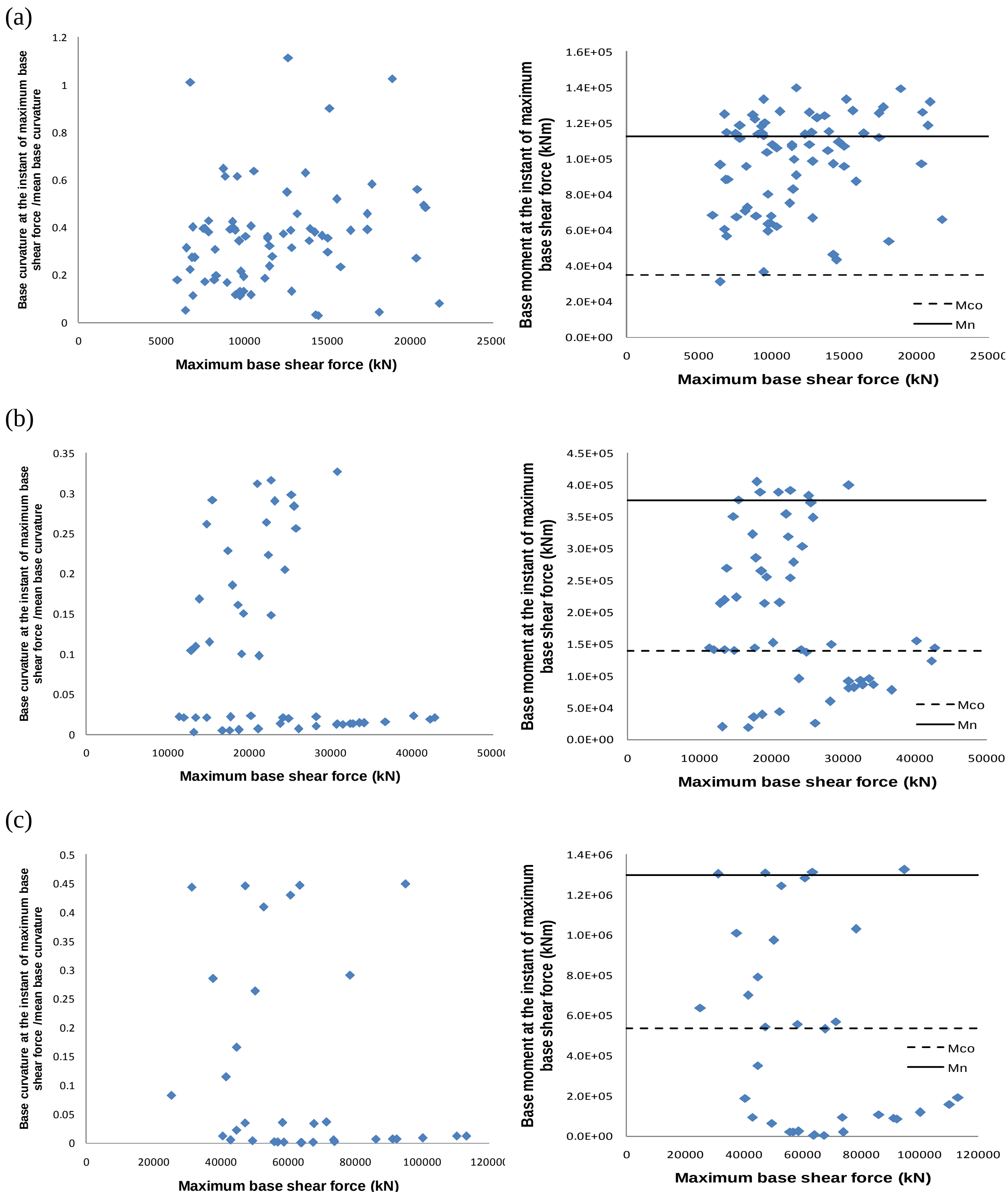

Figure 6.1 Variation of base curvature and base bending moment at the instant of maximum base shear force for (a) 10 story, (b) 30 story, and (c) 50 story walls.

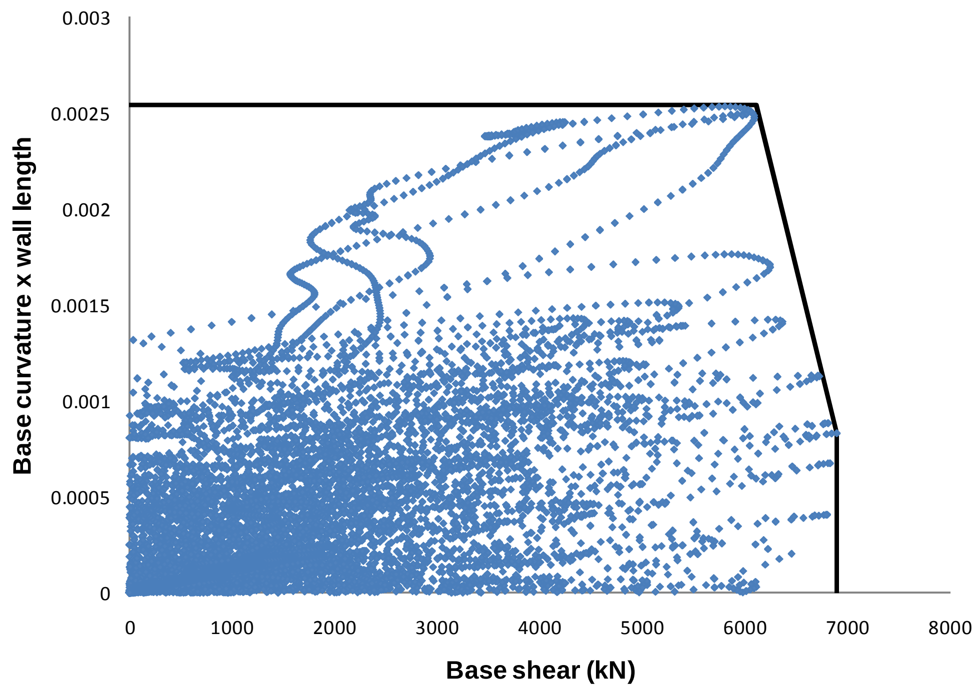

Figure 6.2 Variation of base rotation versus base shear force for one ground motion for the 10 story wall with $R = 3.2$.

Figure 6.2 shows that at the instant of maximum base shear (6891 kN), base rotation is only 0.0008. Maximum base rotation, on the other hand, is 0.0025, and the base shear force corresponding to this instant is 6102 kN. Therefore, in order to establish the base shear - base rotation interaction diagram (as shown with a thick line in Figure 6.2), it is necessary to consider more data points as potential critical points rather than only considering the instant of maximum base shear force. For this purpose, base rotations corresponding to base shear force demands equal to or greater than 50% of the maximum base shear force were considered for individual ground motions. For each ground motion, the instant with maximum base shear force demand was identified (labelled as point (1) in Figure 6.3). The point having maximum base rotation within time steps with shear force demands equal to or greater than 50% of maximum base shear force is also identified as point (2). Note that base rotation for point (2) can be different from the maximum base curvature for a given earthquake. All data points above a straight line connecting point (1) and (2) are considered to define the contour of the base shear - base rotation interaction plot. A point is selected within these points so that the interaction diagram includes all data points above the straight line connecting point (1) to (2) (labelled as point (3) in Figure 6.3). Also, point (4) in this figure represents data points with maximum base curvature demand over the entire record and the corresponding base shear force demand at the instant of maximum base curvature demand. The interaction diagram for a given ground motion passes through points (1) to (4). This procedure was repeated for all ground motions for the three shear walls. Figure 6.4 shows the results.

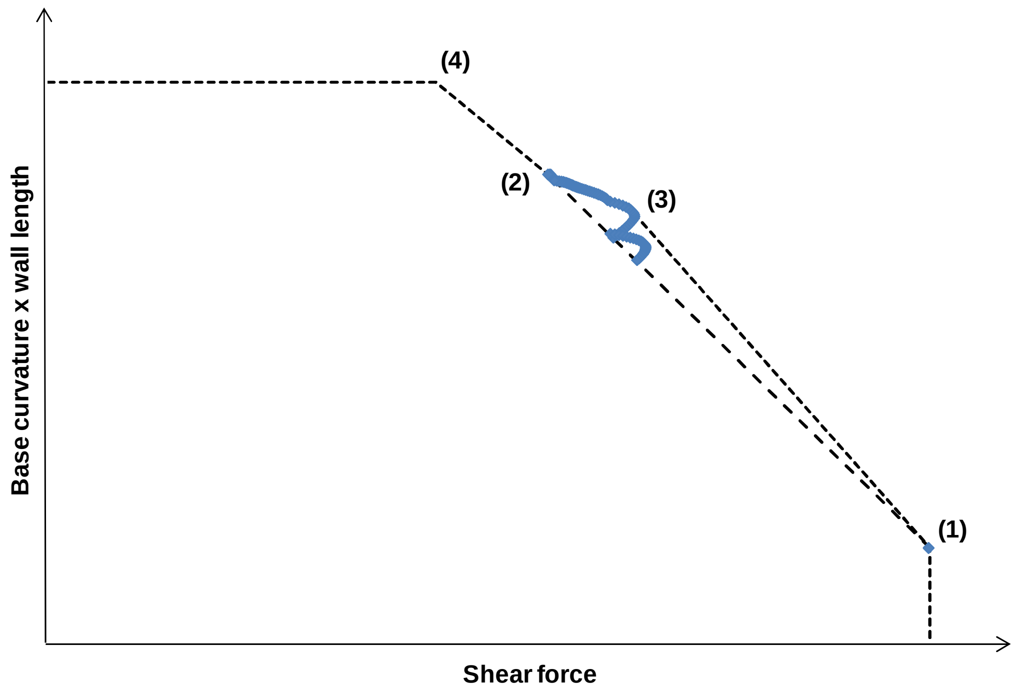

Figure 6.3 Base shear - base rotation interaction diagram.

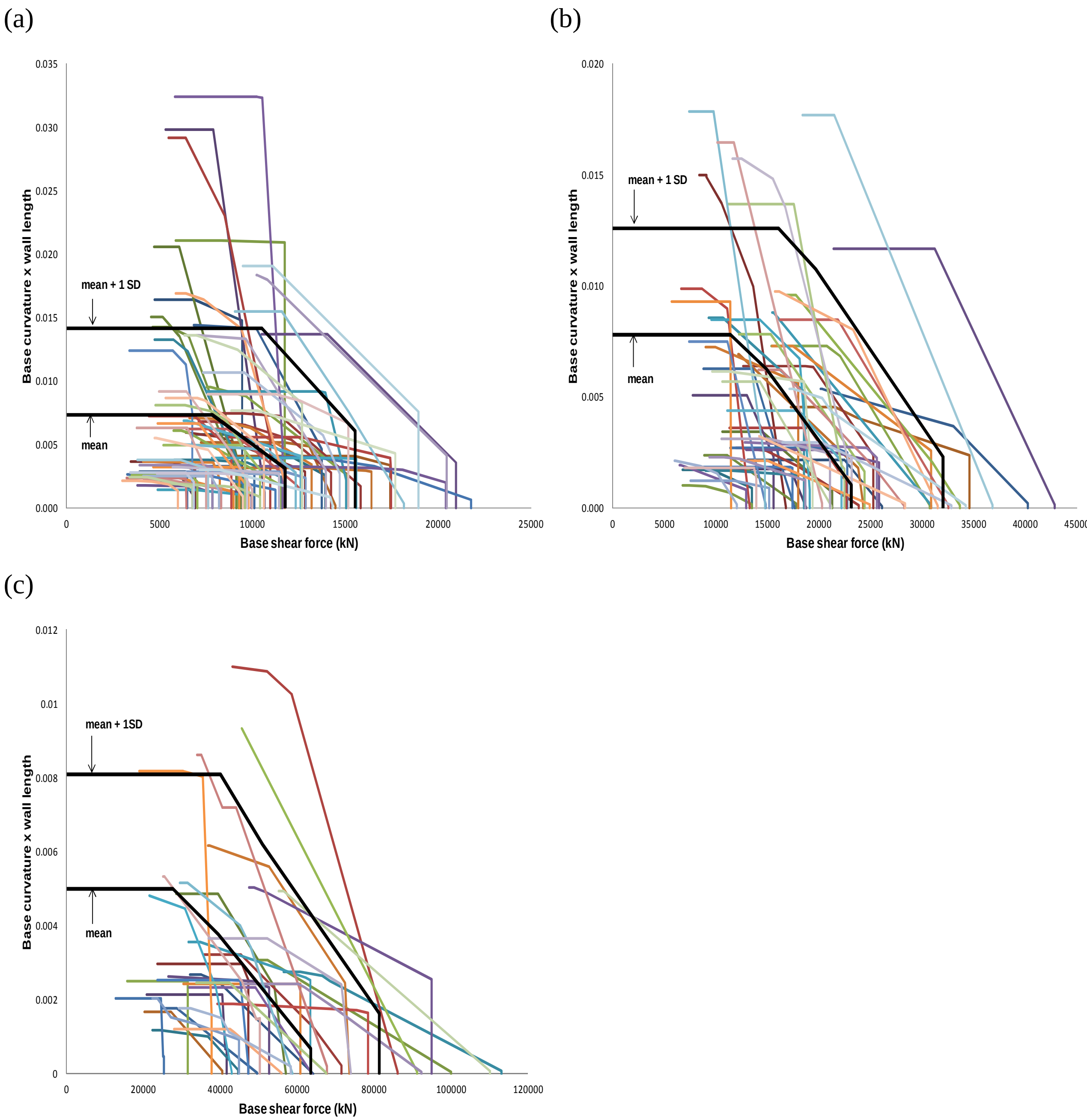

Figure 6.4 Base shear - base rotation interaction diagrams for (a) 10 story, (b) 30 story, and (c) 50 story walls.

The interaction plots in Figure 6.4 were cut off since the interaction diagram shown in Figure 6.3 was developed for base shear force demands between 50 and 100% of the maximum base shear force for each ground motion. Also shown in Figure 6.4 are the mean and mean plus one standard deviation interaction diagrams. Note that for the 10 story wall, points (2) and (4) have equal base rotations, which indicates that the maximum base curvature occurs within time steps with base shear demand equal to or greater than 50% of the maximum value. For 30 and 50 story walls, on the other hand, base rotations for point (4) are larger than those associated with point (2), which means that for these walls, the maximum base curvature occurs at base shear forces that are less than 50% of the maximum base shear force.

Figure 6.4 shows that base rotations associated with mean base shear forces are generally small. Base rotation corresponding to the mean base shear force (point (1) in Figure 6.3) is 0.003, 0.001, and 0.0006 for 10, 30, and 50 story walls, respectively. On the other hand, the base shear forces at high base rotations (point (4) in Figure 6.3) are lower than the corresponding mean base shear force demands. The ratio of mean base shear force for point (4) to that for point (1) is 0.60, 0.49, and 0.43 for 10, 30, and 50 story walls, respectively. This observation is contrary to CSA A23.3-04 design provisions, which uses maximum base shear force and maximum base rotation simultaneously to design horizontal reinforcement. Interaction plots shown in Figure 6.4 indicate that base rotations at high base shear force were relatively lower than the corresponding maximum values. Consequently, concrete shear strength is expected to be higher since lower base rotation is associated with smaller diagonal cracking and less reduction in the aggregate interlock shear resistance.

6.4 Mean versus Mean Plus One Standard Deviation Base Shear Force

Comparisons between base shear force demands corresponding to mean and mean plus one standard deviation results were discussed in Chapter 4. It was shown that the coefficient of variation is approximately 0.3 for SOR ground motions, which indicates that mean plus one standard deviation base shear force demands are 30% higher than those associated with the mean results. The Tall Building Initiative (PEER TBI 2010) and SEAONC recommended procedure (SEAONC 2007) recommended using mean plus one standard deviation results for actions with low ductility such as punching shear failure of slabs and shear force in walls. Gerin and Adebar (2009) studied the shear response of reinforced concrete walls and they concluded that concrete walls can have considerable ductility after the horizontal reinforcement yields. As a result, considering dispersion in order to achieve higher conservatism in the shear design of concrete shear walls may not be necessary as the wall failure mode is not brittle when shear force demand exceeds the shear capacity at a given instant.

It is interesting to plot peak base shear force demands for various ground motions and compare them with the maximum base shear force demand. In this way, reduction in base shear demand can be determined as a function of number of cycles. For this purpose, peak shear force demands for all cycles were determined for three 10, 30, and 50 story walls with force reduction factors of 3.2, 3.1, and 3.7, respectively. For each ground motion, peak base shear force at various cycles was normalized to the maximum base shear force over the entire ground motion, and a curve was determined that related the normalized base shear force to the number of cycles. For a given number of cycles, the mean value for a suite of ground motions shows how much on average the base shear force drops compared to the maximum value. Figure 6.5 shows the mean plots for the three walls.

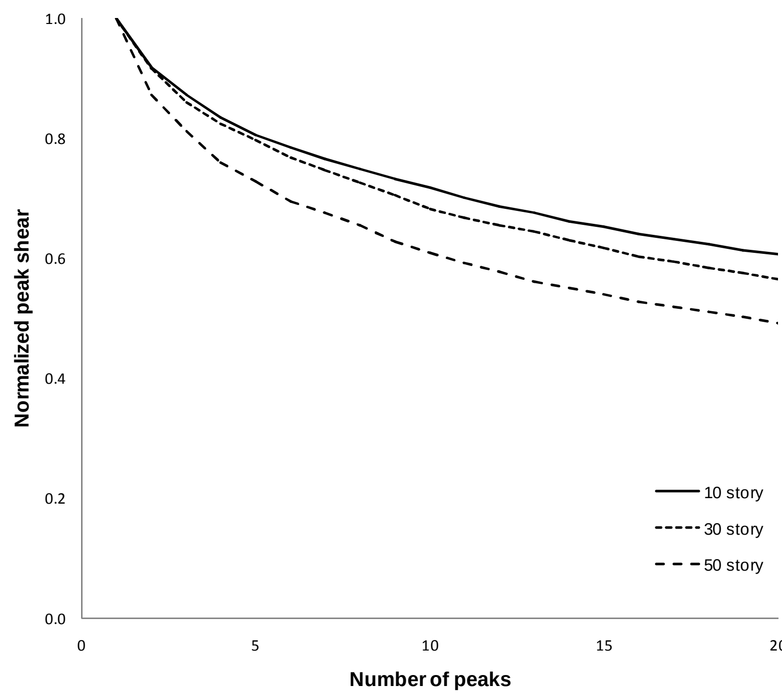

Figure 6.5 Normalized base shear force demand as a function of number of peaks.

It should be mentioned that the cycles associated with maximum shear forces do not necessarily occur in order, and Figure 6.5 merely shows the mean ratio of maximum base shear force at the n^{th} biggest cycle to the maximum base shear force. Figure 6.5 indicates that after 5 cycles, base shear force drops to 80% for 10 and 30 story walls and to 73% of the maximum value for the 50 story wall. If there is no shear failure at the instant of maximum base shear force, the mean base shear demand reduces by 20% after only 5 cycles. For the rest of cycles, the base shear force is less than 80% of the maximum value. Therefore, it seems that considering mean shear demands is adequate for estimating shear demands on cantilever walls since after few cycles, the base shear force drops by approximately 20%. Mean shear force demands will be used in this chapter to develop simplified models for estimating shear force demands in cantilever shear walls.

6.5 Shear Force Profile over the Height

Figure 6.6 compares the mean shear force enveloped for 10 to 50 story walls with different force reduction factors using the SOR ground motions. It can be seen from Figure 6.6 that the shape of the mean shear force envelope changes as the height of the wall increases. Mean shear force for 10 story walls reduces gradually over the height, while for 30 and 50 story wall, mean shear force envelope has a bulge near midheight. For 50 story walls, shear force demand around midheight for two R values of 1.8 and 2.0 is higher than the corresponding values for R factors of 1.3 and 3.7 (48000 kN for R = 1.8 and 2.0 as opposed to 34700 kN for R = 1.3 and 3.7). These observations need further examination.

Although shear force profiles shown in Figure 6.6 correspond to walls with nonlinear behaviour, performing response spectrum analysis can give insight into the influence of higher modes on the shear force distribution over the height. Figure 6.7 shows the shear force profiles from the first to fourth modes of vibration and the envelope of these profiles using CQC method for 10 to 50 story walls. Note that elastic shear force demands shown in this figure correspond to $0.5EI_g$ flexural stiffness.

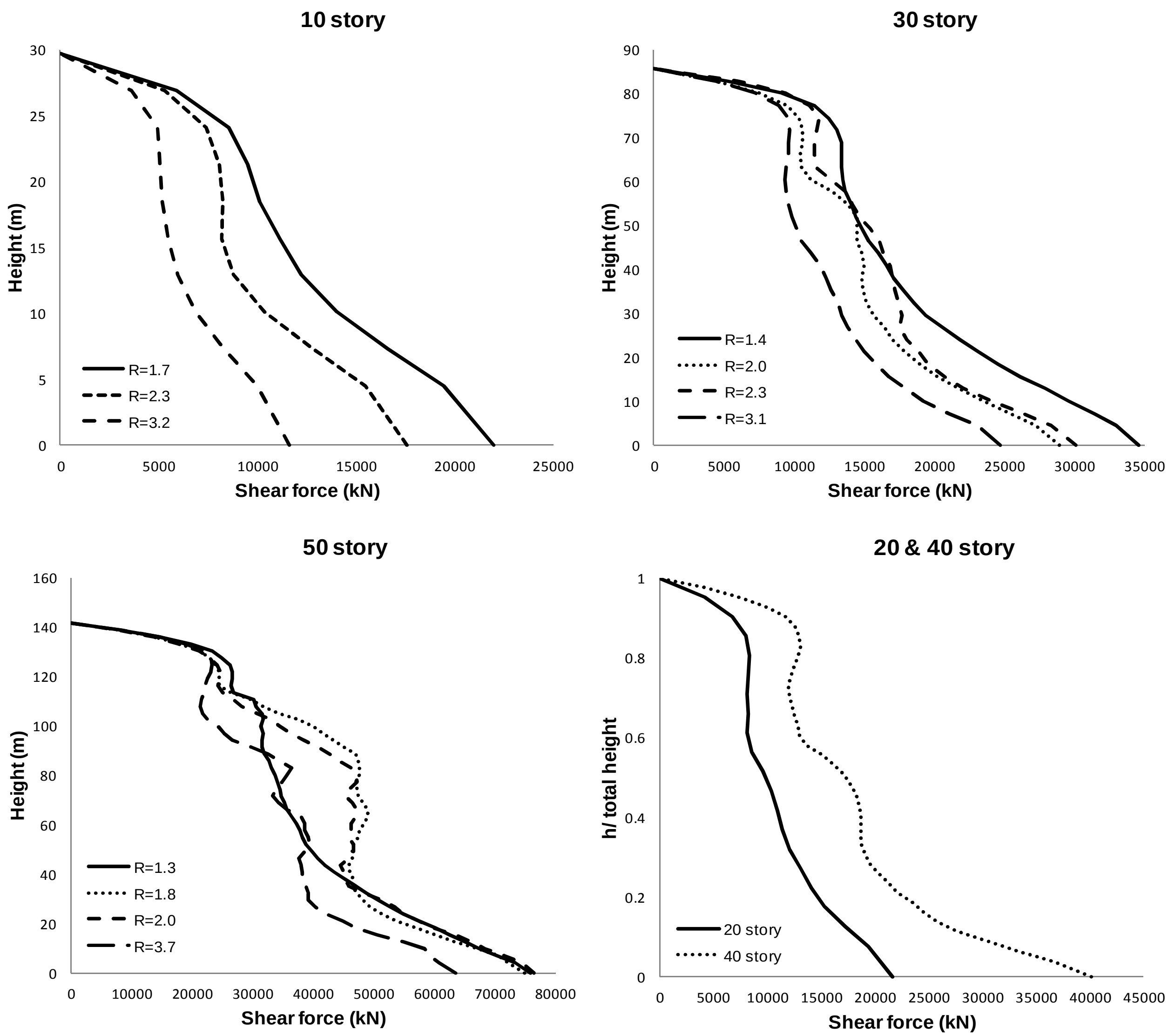

Figure 6.6 Variation of mean shear force profile over the height of 10 to 50 story walls with different force reduction factors.

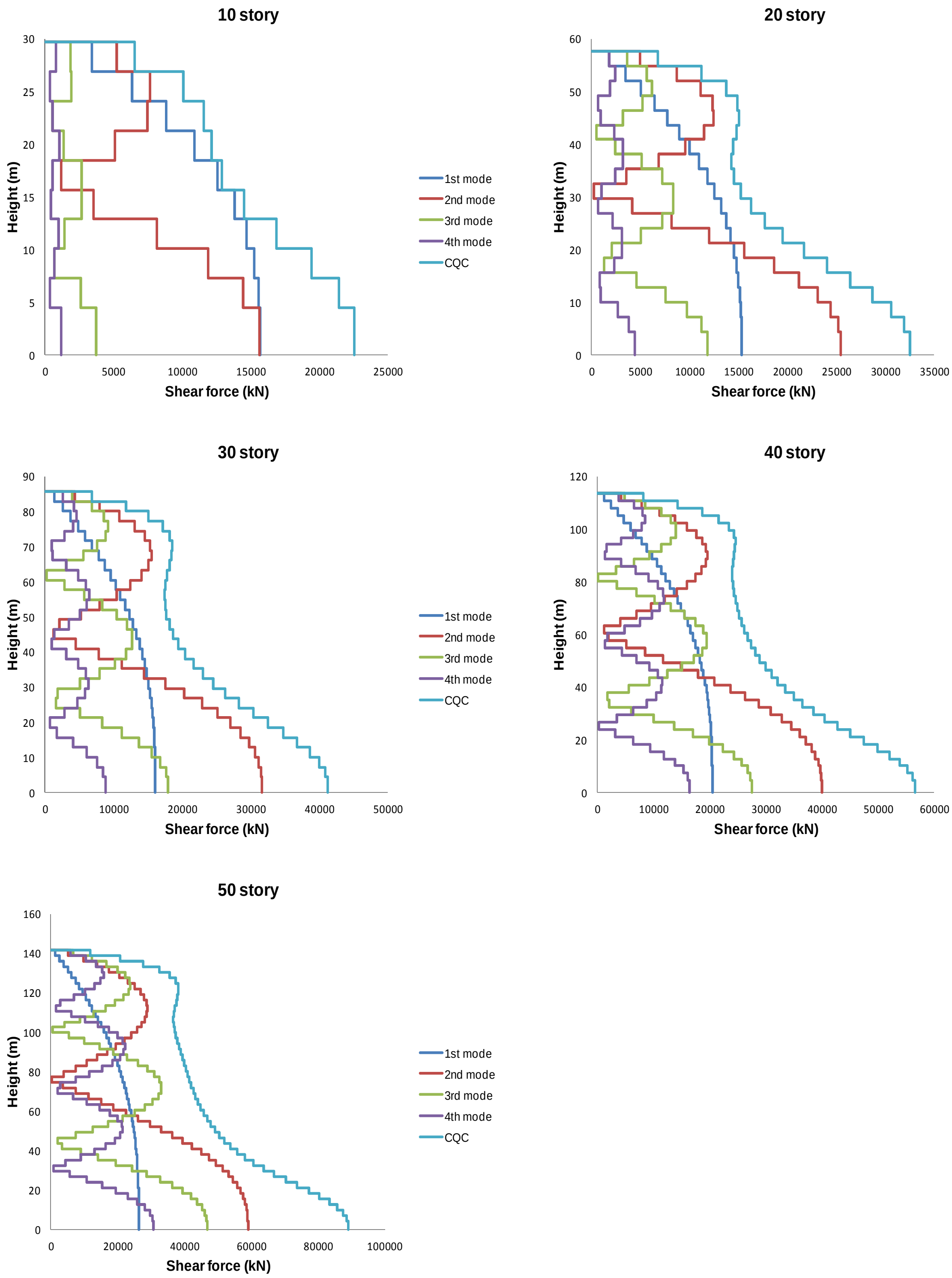

Figure 6.7 Shear force profile corresponding to different modes for 10 to 50 story walls.

Figure 6.7 shows that for the 10 story wall, the shape of the shear force envelope is highly influenced by the first mode shear force profile over the height. The shear force envelope at the base, however, is influenced by the first and second modes. As the wall height increases, shear force from the second mode dominates the envelope above the midheight, while at the midheight, the contribution of the third mode becomes higher. As a result, shear force envelopes for 20 to 50 story walls remain constant over a region starting around the midheight. This observation is consistent with the general shape of the shear force envelopes for the 50 story walls with intermediate force reduction factors, as shown in Figure 6.6.

It is also important to examine why there are large midheight shear force demands for 50 story walls with force reduction factors of 1.8 and 2.0. A possible explanation for this observation would be to compare shear force envelopes corresponding to CMS ground motions using different conditioning periods. In this way, it is possible to determine which conditioning period defines the envelope of the shear force demand near the midheight. This was done for five shear walls: 10 story wall with R = 3.2, 30 story walls with R = 2.3 and R = 3.1, and 50 story walls with R = 2.0 and R = 3.7. Selected conditioning periods for the 10 story wall are $2T_1$, $1.5T_1$, T_1, $1.5T_2$, and T_2, while $2T_1$, T_1, $1.5T_2$, T_2, and T_3 are selected for 30 story walls. For 50 story walls, T_1, T_2, $2T_3$, and T_3 are considered. Note that $1.5T_2$ and $2T_3$ represent the period elongation of the second and third modes for the 10 (as well as 30) and 50 story walls, respectively. Figure 6.8 shows the results. The following observations can be made:

1. For the 10 story wall, the CMS at $1.5T_1$ defines the shear force envelope around the midheight. The shear force demand reduces gradually around the midheight as $1.5T_1$ is the conditioning period that is associated with the elongation of first mode period. Also, changing conditioning period from T_2 to $1.5T_2$ did not change the mean shear force envelope, which indicates that the elongation of higher mode has no effect on shear force distribution over the height.

2. For the 30 story walls, the CMS at $1.5T_2$ defines the shear force envelope over the elevation range from 50 to 60 m for R = 2.3 and from 7 to 22 m for R = 3.1. Over these regions, mean shear forces from the CMS at $1.5T_2$ is very close to those determined using SOR ground motions. It was observed that period elongation of the second mode has no effect on base shear force demand since mean base shear force demands corresponding to T_2 and $1.5T_2$ are similar. Also note that the CMS at T_3 controls the shear force envelope over the elevation range from 40

to 55 m for R = 3.1, while for R = 2.3, the shear force near midheight corresponding to this conditioning period is considerably lower than those associated with T_2 or $1.5T_2$.

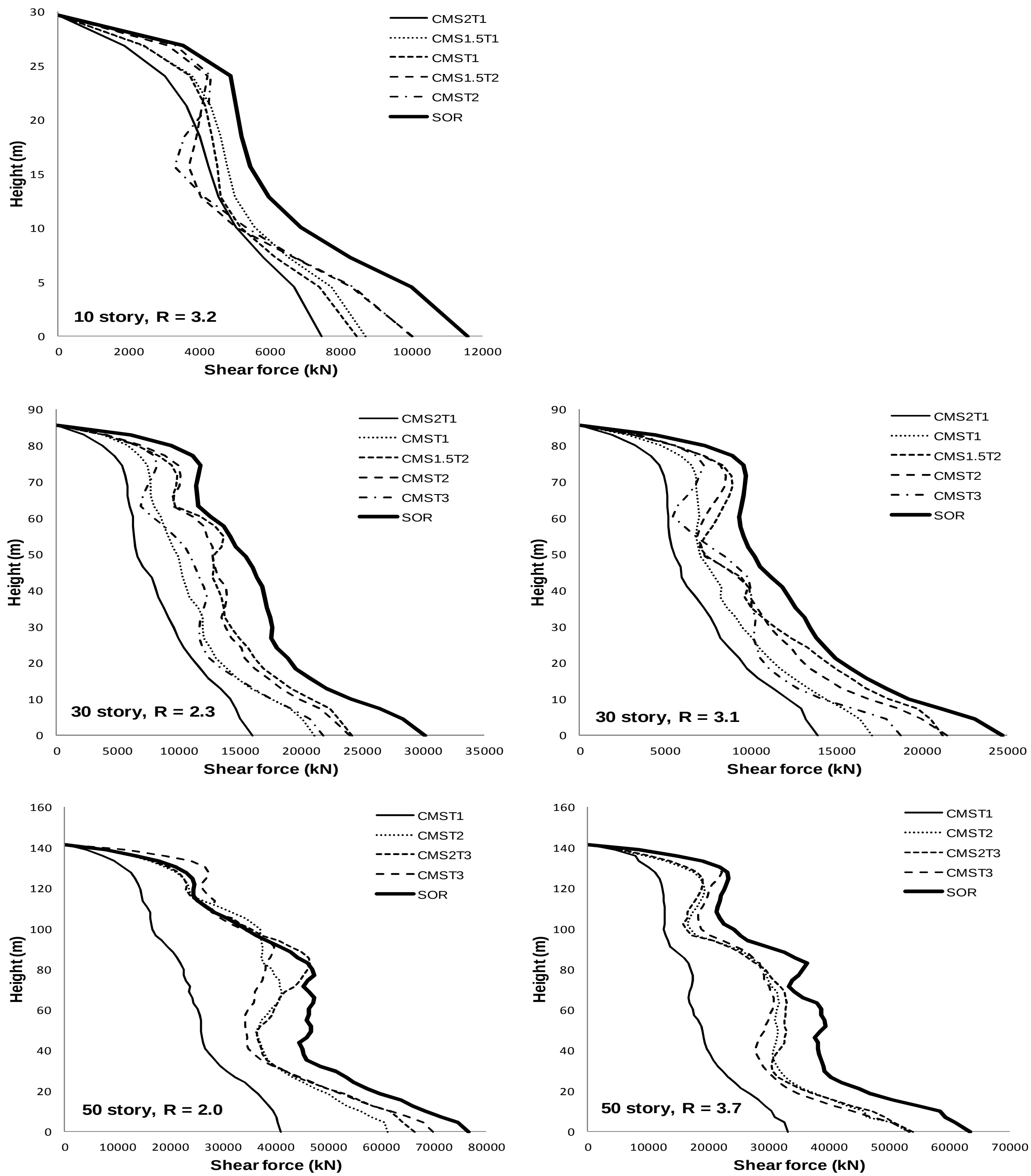

Figure 6.8 Shear force envelope for 10, 30 and 50 story walls using CMS ground motions with different conditioning periods.

3. For the 50 story wall with R = 2.0, the CMS at $2T_3$ defines the shear force envelope over the elevation range from 70 to 90 m. The mean shear force near midheight from this conditioning period is very similar to those determined using SOR ground motion, which indicates that high midheight shear forces for the 50 story wall with R = 2.0 are derived by the elongation of the third mode period. For R = 3.7, the CMS at $2T_3$ defines the shear force envelope from h = 40 to 80 m; however, the difference between mean shear forces using T_3 and $2T_3$ is insignificant. Similar to what was observed for 30 story walls, elongation of higher mode periods has no effect on the mean base shear force demand for 50 story walls.

The sensitivity analysis shown in Figure 6.8 demonstrates that midheight shear forces in the 10 story wall are derived by the elongation of the first mode period, while in 30 and 50 story walls, the elongation of higher mode generally defines the shear force envelope over different regions along the height. It was shown that high midheight shear forces for the 50 story wall with R = 2.0 are derived by the elongation of third mode period. Also, second mode period elongation defines the shear force envelope over some portion of the height of the 30 story walls. Determining which conditioning period defines the shear force envelope of taller walls with high force reduction factor requires significant computational effort. The investigation conducted in this section with a limited number of conditioning periods cannot be generalized to other walls, rather it gives some insight into the influence of higher mode period lengthening on midheight shear force demands in high-rise cantilever shear walls.

6.6 Simplified Design Envelope for Predicting Shear Force Demands

In this section, mean shear force demands from time history analysis are used to establish a simplified design envelope for predicting shear force demand over the height. Time history analysis was carried out for 13 shear walls (three 10 story, one 20 story, four 30 story, one 40 story, and four 50 story) using the SOR ground motions. The details are presented hereafter.

6.6.1 Estimating Base Shear Force

Figure 6.9 compares the predicted base shear force demand from different models with the mean and mean plus one standard deviation base shear force demands determined from time history analysis. The predicted base shear forces were calculated using Equation 6.5 (Priestley and

Amaris), Equation 6.6 (Sullivan et al.), Equation 6.3 (Keintzel), and Equation 6.2 (Rutenberg and Nsieri). Elastic modes 1 to 4 were considered in Eq. 5 and Eq.6. Two stiffness reduction factors of 1.0 and 0.5 were used to compute elastic shear forces and the corresponding force reduction factor. These values are considered as the upper-bound and lower-bound stiffness reduction factors.

(a) (b)

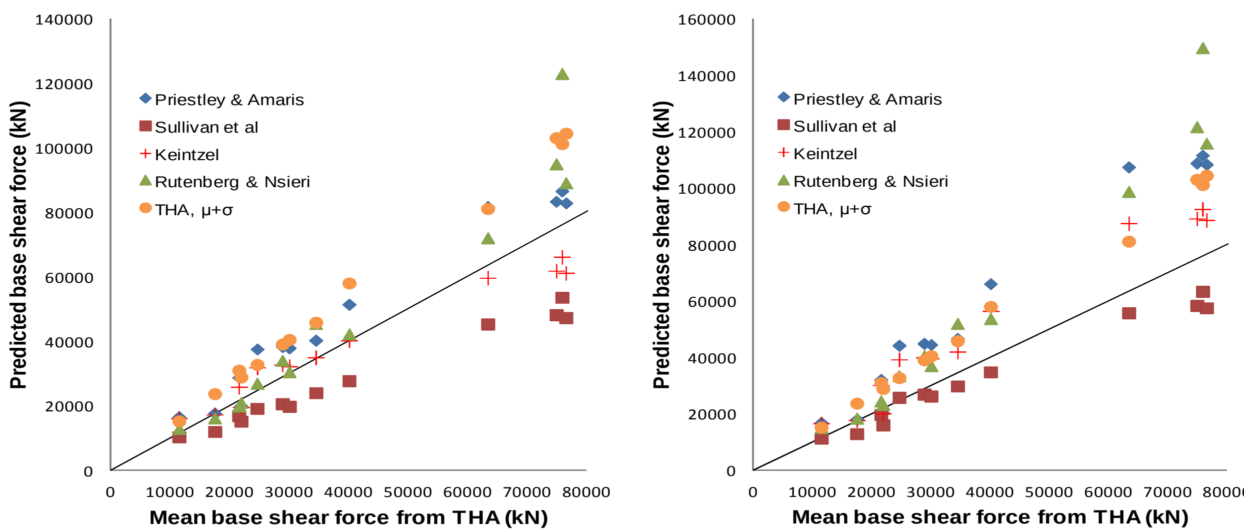

Figure 6.9 Comparison of base shear force demand from different models using stiffness reduction factors of (a) 0.5, and (b) 1.0 with the mean and mean plus one standard deviation ($\mu + \sigma$) results from time history analysis (denoted as THA).

Figure 6.9 indicates that Sullivan et al. approach gives base shear forces that are consistently lower than the mean results from time history analysis. For this method, the results corresponding to stiffness reduction factor of 1.0 are closer to the mean results. The base shear forces predicted by Priestley and Amaris approach using stiffness reduction factor of 1.0 are higher than the mean plus one standard deviation results for 20 to 50 story walls; however, using an effective stiffness of $0.5EI_g$ gives base shear forces that are generally lower than $\mu + \sigma$ results. Note that Sullivan et al. method requires performing response spectrum analysis for both fixed base and pinned base walls, while Priestley and Amaris approach requires performing response spectrum analysis for only fixed base walls. Yet, it can be seen from Figure 6.9 that Priestley and Amaris method gives better prediction of mean base shear force demands. Base shear forces predicted by Keintzel approach are very close to the mean results except that they are lower than the mean results for 50 story walls (Figure 6.9(a)), which indicates that considering only second mode is not adequate for predicting base shear force demands for tall walls.

It can be seen from Figure 6.9(a) that Rutenberg and Nsieri approach gives closest values to the mean time history results for most walls. The predictions from Priestley and Amaris method is better than Rutenberg and Nsieri and also Keintzel approaches for 50 story walls. Therefore, it seems that either Priestley and Amaris or Rutenberg and Nsieri approaches provide a good prediction of mean base shear force demand. A comparison between mean shear force envelopes from time history analysis with those from these approaches will be presented in section 6.6.2.

In design, the base shear force determined using response spectrum analysis is reduced by the same ratio that the elastic bending moments are reduced to account for flexural ductility of the structure. The shear amplification factor is the amount these design shear forces (reduced from the elastic analysis) need to be increased again. In order to establish a simple model for shear amplification factor, mean base shear forces from time history analysis were compared with base shear forces from response spectrum analysis for fixed base cantilever walls. Elastic modes 1 to 4 and an effective stiffness of $0.5EI_g$ were used to compute the elastic bending moments and shear forces. Elastic shear forces from different modes were combined using the CQC method. To obtain design shear forces, elastic shear forces were reduced by the ratio of elastic bending moment at the base corresponding to $0.5EI_g$ to wall flexural strength M_n (denoted as $R(0.5EI_g)$). Table 6.1 compares force reduction factors associated with different effective stiffness values. The shear amplification factors are also shown in Figure 6.10.

Table 6.1 Force reduction factor R corresponding to different stiffness effective stiffness values.

Wall	R_g [1]	R [2]	$R_{(0.5EIg)}$ [3]
10 story	1.7	1.7	1.3
	2.6	2.3	2.0
	4.2	3.2	3.2
20 story	4.0	2.7	2.7
30 story	1.4	1.4	1.0
	2.4	2.0	1.8
	3.1	2.3	2.3
	4.3	3.1	3.1
40 story	4.4	3.6	3.2
50 story	1.4	1.3	0.9
	2.1	1.8	1.4
	2.4	2.0	1.6
	4.1	3.7	2.6

[1] based on gross flexural stiffness EI_g, [2] based on effective stiffness which results in roof displacement demand equal to the mean roof displacement demand from time history analysis, [3] based on $0.5EI_g$.

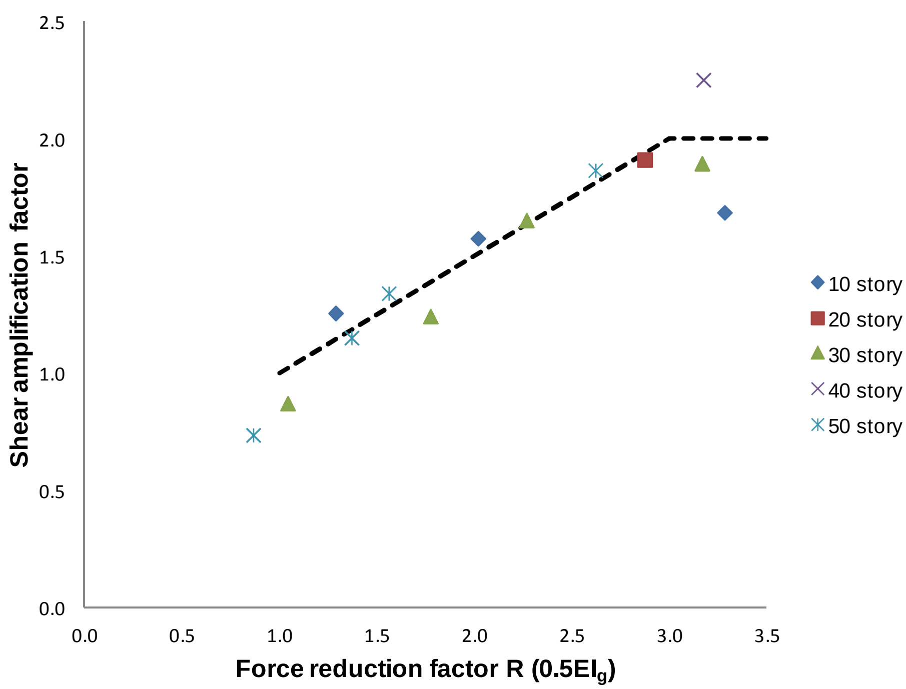

Figure 6.10 Shear amplification factor as a function of force reduction factor corresponding to $0.5EI_g$.

Figure 6.10 indicates that shear amplification factor generally varies from 1.0 to 2.0 as the force reduction factor increases. For 10 story walls, shear amplification factor varies from 1.3 to 1.7, while the highest shear amplification factor for 20. 30, and 50 story walls is 1.9. The only exception is the 40 story wall, which has a shear amplification factor of 2.3. Also shown in Figure 6.10 is the proposed equation for calculating shear amplification factor for cantilever shear walls:

$$\omega_v = 0.5\left(R_{0.5EI_g} + 1\right), 1 \leq \omega_v \leq 2 \qquad Eq\ 6.9$$

A comparison between the predicted base shear force from Equation 6.9 with mean time history results will be presented in Section 6.6.2

6.6.2 Estimating Shear Force Demands near Midheight

Figures 6.11 through 6.14 compare the shear force envelope from different models with mean shear force envelopes obtained from time history analysis. Note that the R factor in these Figures corresponds to an effective stiffness of $0.5EI_g$.

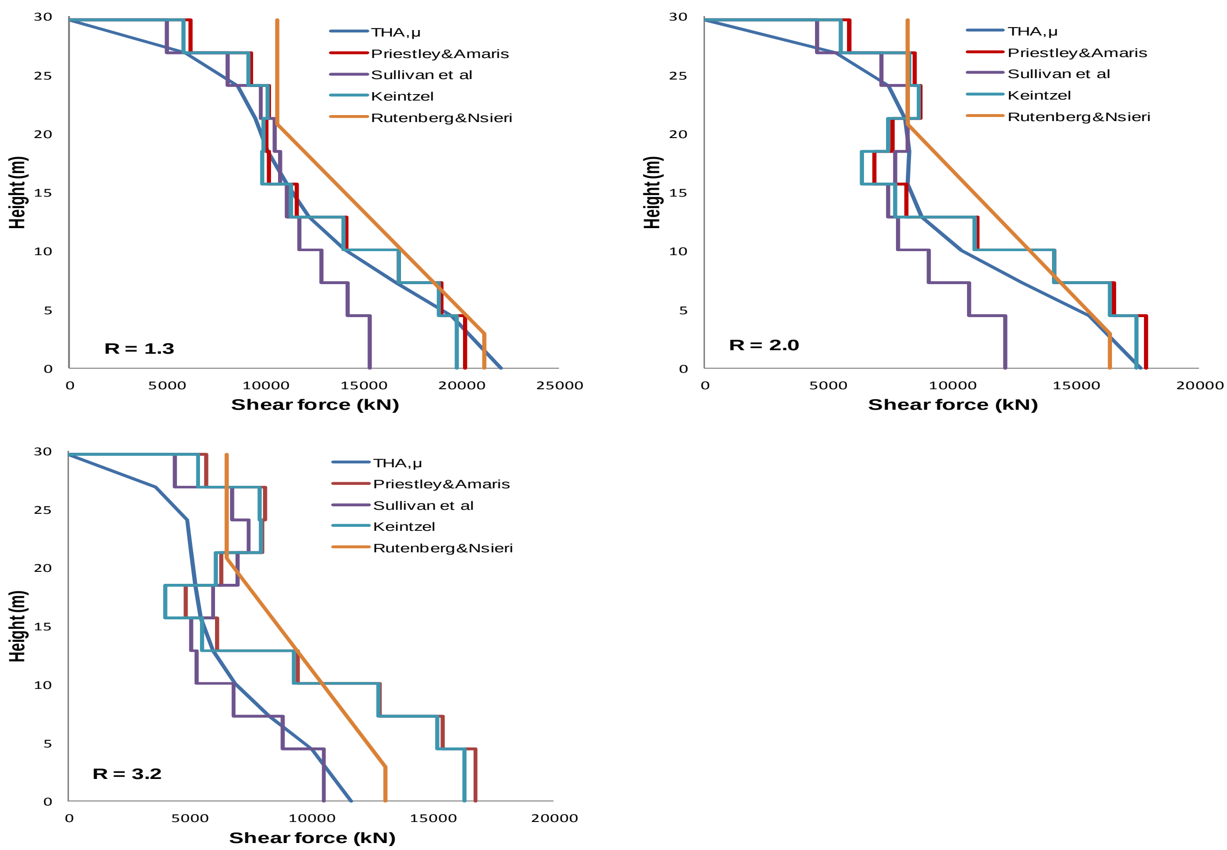

Figure 6.11 Comparison of shear force envelope from different models with the mean shear force envelope from time history analysis (denoted as THA) for 10 story walls with different force reduction factors.

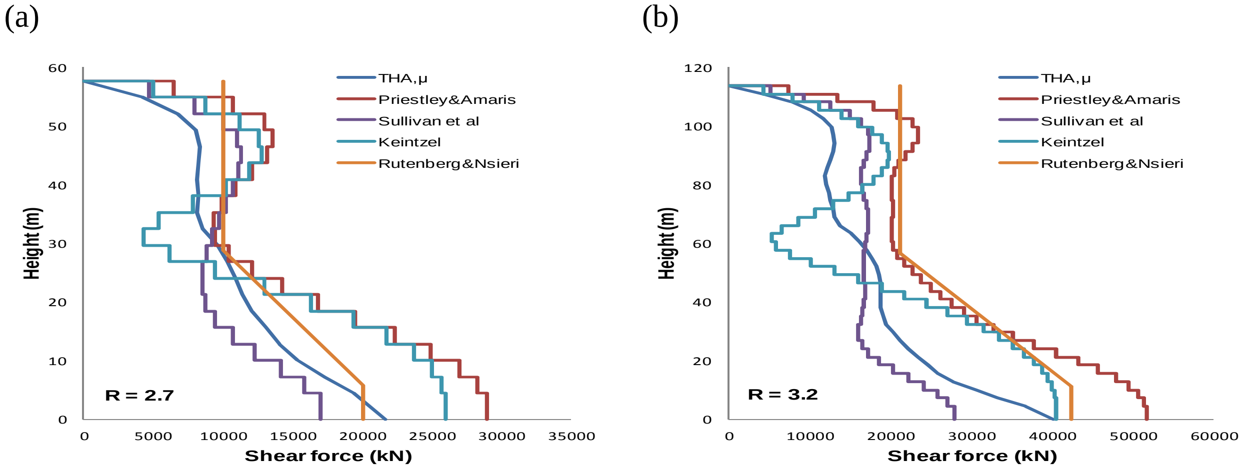

Figure 6.12 Comparison of shear force envelope from different models with the mean shear force envelope from time history analysis (denoted as THA) for: (a) 20 story wall, and (b) 40 story wall.

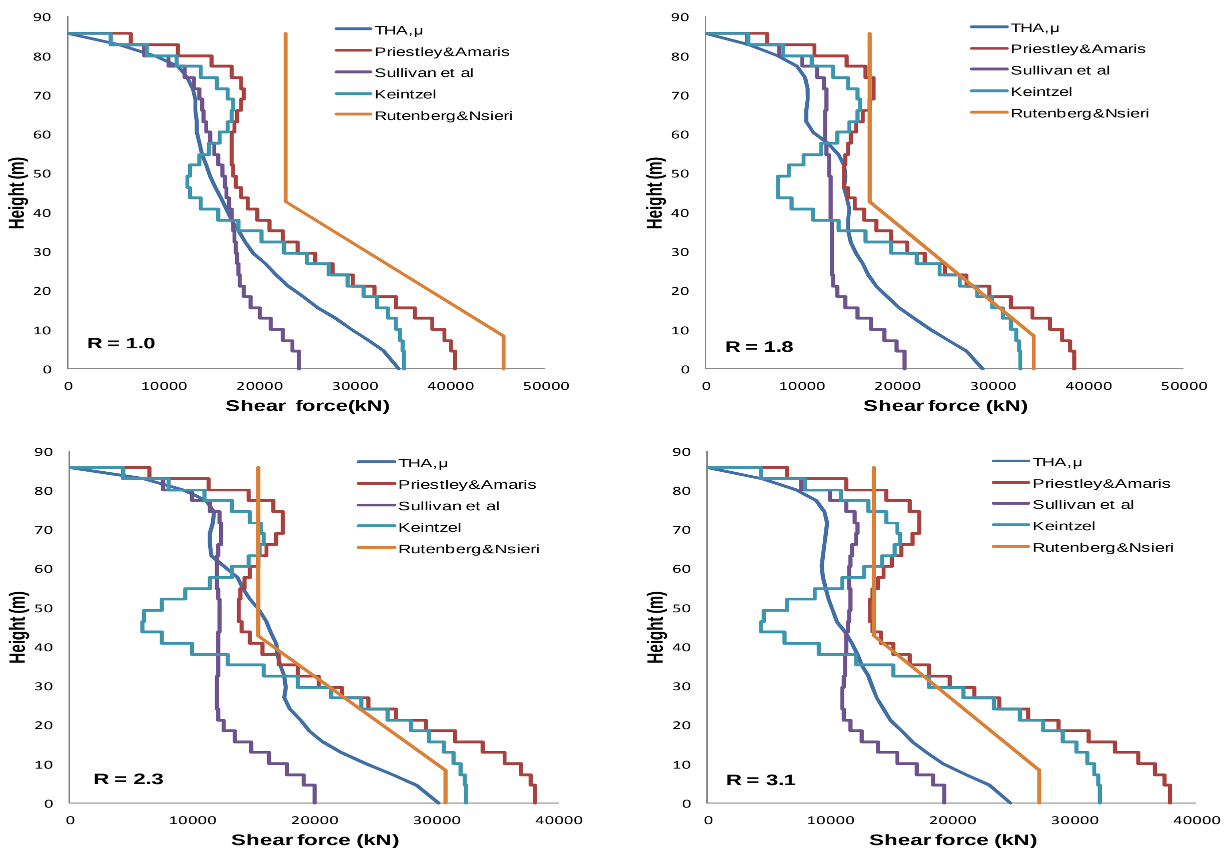

Figure 6.13 Comparison of shear force envelope from different models with the mean shear force envelope from time history analysis (denoted as THA) for 30 story walls with different force reduction factors.

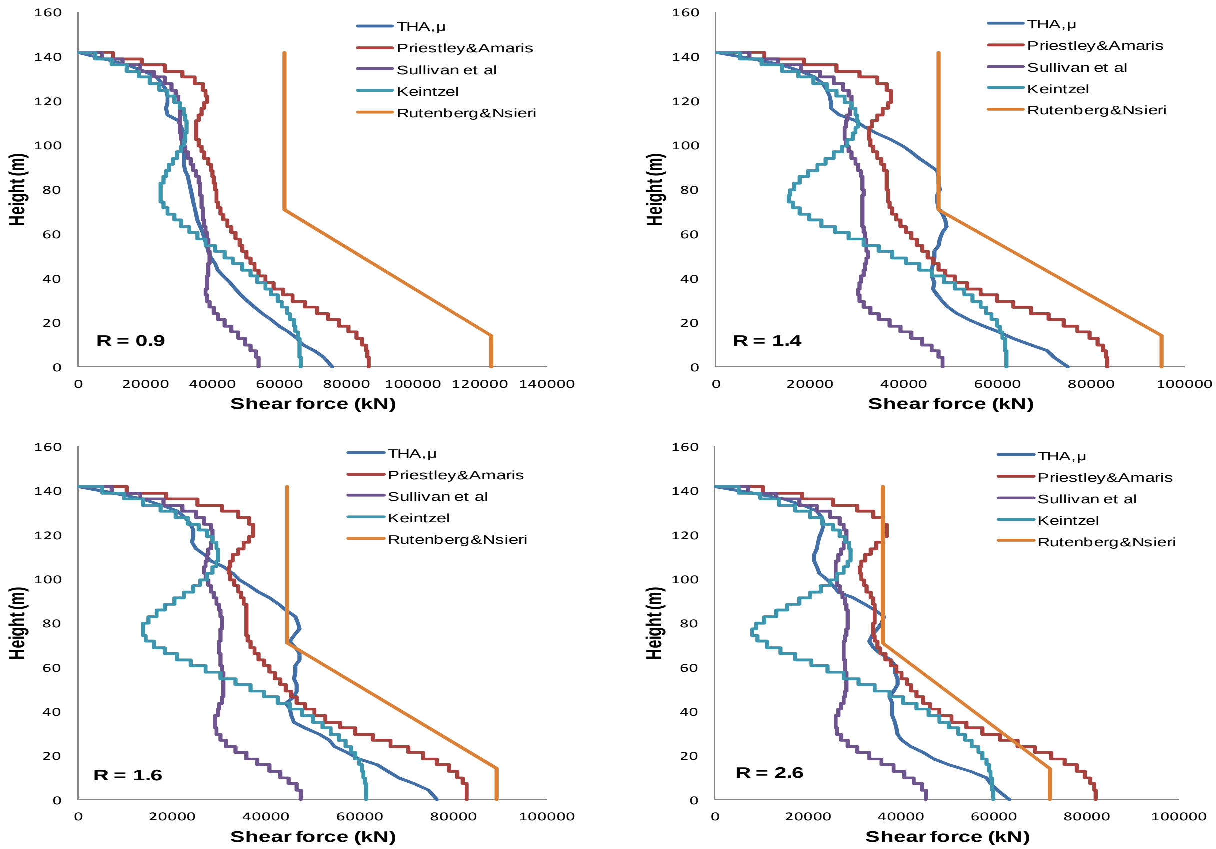

Figure 6.14 Comparison of shear force envelope from different models with the mean shear force envelope from time history analysis (denoted as THA) for 50 story walls with different force reduction factors.

Figures 6.11 to 6.14 indicate that Sullivan et al. method generally underestimates midheight shear forces for most shear walls. The Keintzel approach underestimates shear force demands around the midheight for all walls except for 10 story walls. On the other hand, Priestley and Amaris model generally provides a reasonable estimate of midheight shear force demands. The only exception are the 50 story walls with force reduction factors of 1.4 and 1.6, in which the mean shear force results around the midheight are greater than the predictions from Priestley and Amaris approach. A comparison of envelopes determined from the Keintzel with Priestley and Amaris approach shows that including elastic shear forces from the third and fourth modes in Equation 6.3 improves the midheight shear force prediction significantly for taller walls. This is due to the fact that elastic shear forces corresponding to the third and fourth modes are relatively small for 10 story walls, while as it can be seen from Figure 6.7, the intensity of these forces tend to increase as the wall height increases.

Figures 6.11 through 6.14 also show that Rutenberg and Nsieri approach provides a reasonable estimate of mean shear force results for the thirteen walls. Although this method can be readily used to estimate shear force demands in cantilever walls, it overestimates mean base shear force demands in 50 story walls. One reason for this observation is that Rutenberg and Nsieri equation is based on time history results for 5 to 25 story cantilever shear walls. The other possible reason is that Rutenberg and Nsieri used elastic-perfectly-plastic (EPP) bending moment - curvature relationship for performing time history analysis. As it was observed in Figures 5.37 through 5.39, using trilinear moment - curvature relationship results in lower base shear force demands than using the EPP model. In addition, for 50 story walls, the ratio of midheight shear force to base shear force is greater than the 0.5 factor proposed by Rutenberg and Nsieri. To refine this approach, a simple design envelope was developed with key parameters that can be obtained from RSA with fixed base support using $0.5EI_g$ effective stiffness. Figure 6.15 shows a schematic of this model.

$(V_f)_{RSA}$ shown in Figure 6.15 is shear force from RSA using an effective stiffness of $0.5EI_g$. The ω_v factor is the shear amplification factor and can be determined from Equation 6.9, while h_w and l_w are the wall height and wall length, respectively. The ξ parameter controls the shape of the envelope at upper levels and is equal to 0.5 for number of floors $n \leq 30$ and it reduces linearly to 0.3 for $n = 50$. Comparison between mean shear force enveloped from time history analysis with the predictions from the design envelope is shown in Figure 6.16. As it can be seen from Figure 6.16, the design envelope generally gives a reasonable upper-bound estimate of the mean shear force envelopes.

Figure 6.16 also compares mean shear force envelopes from time history analysis with those determined from RSA. Note that RSA was performed using an effective stiffness of $0.5EI_g$, and shear force envelopes were then scaled using shear amplification factor obtained from Equation 6.9. Figure 6.16 indicates that the envelopes from RSA are generally an upper-bound to the mean shear force envelopes from time history analysis. The only exceptions are the 30 story wall with $R = 2.3$ and 50 story walls with force reduction factors of 1.4 and 1.6. For these walls, scaled envelopes from RSA underestimate the shear force demand around the midheight. For 50 story walls, midheight shear forces from scaled RSA are approximately 25% lower than those determined from time history analysis. This observation suggests that using RSA to predict midheight shear force demands for tall shear walls must be done cautiously. The design envelope shown in Figure 6.15 can be used in such cases.

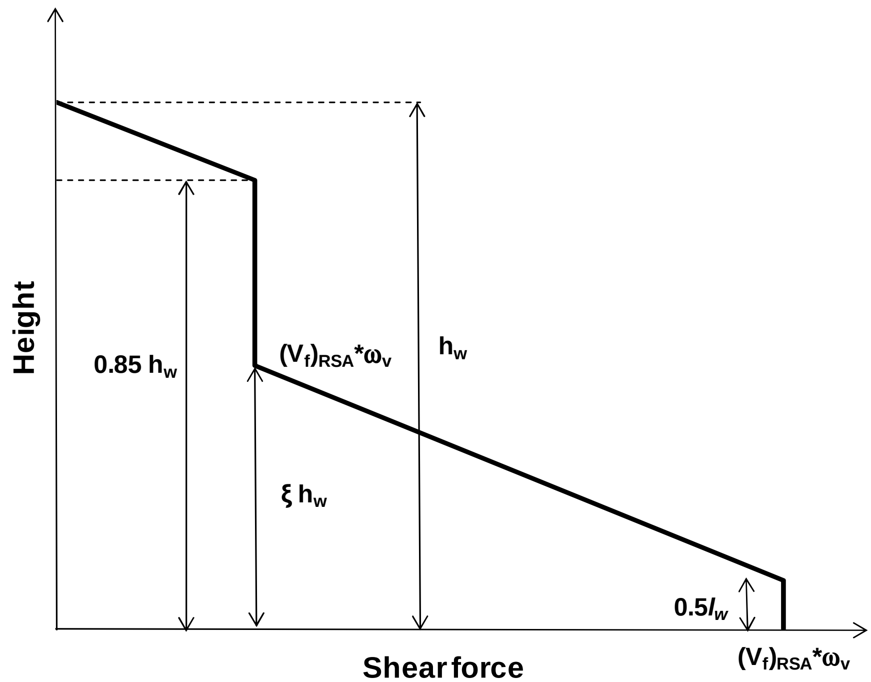

Figure 6.15 Simplified design envelope for predicting shear force demands in cantilever shear walls.

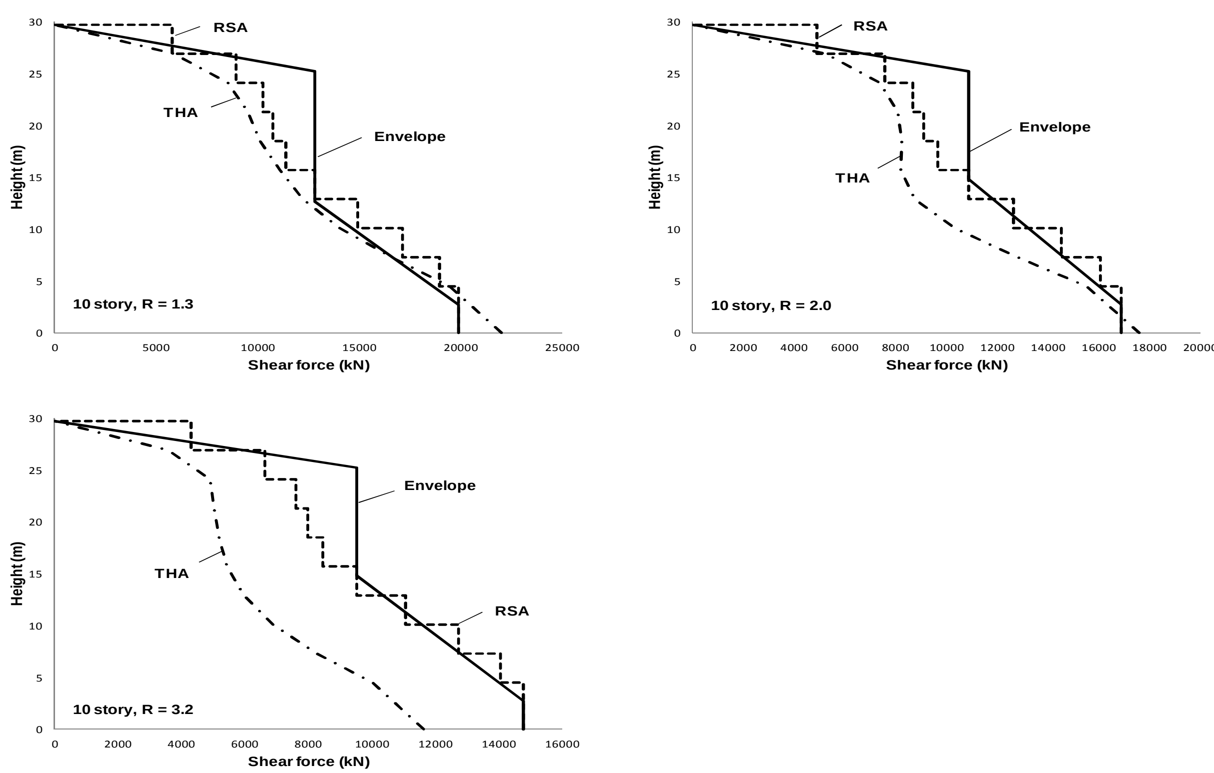

Figure 6.16 Comparison of mean shear force envelope from time history analysis (denoted as THA) with the envelope shown in Figure 6.15 and scaled shear force envelope from RSA.

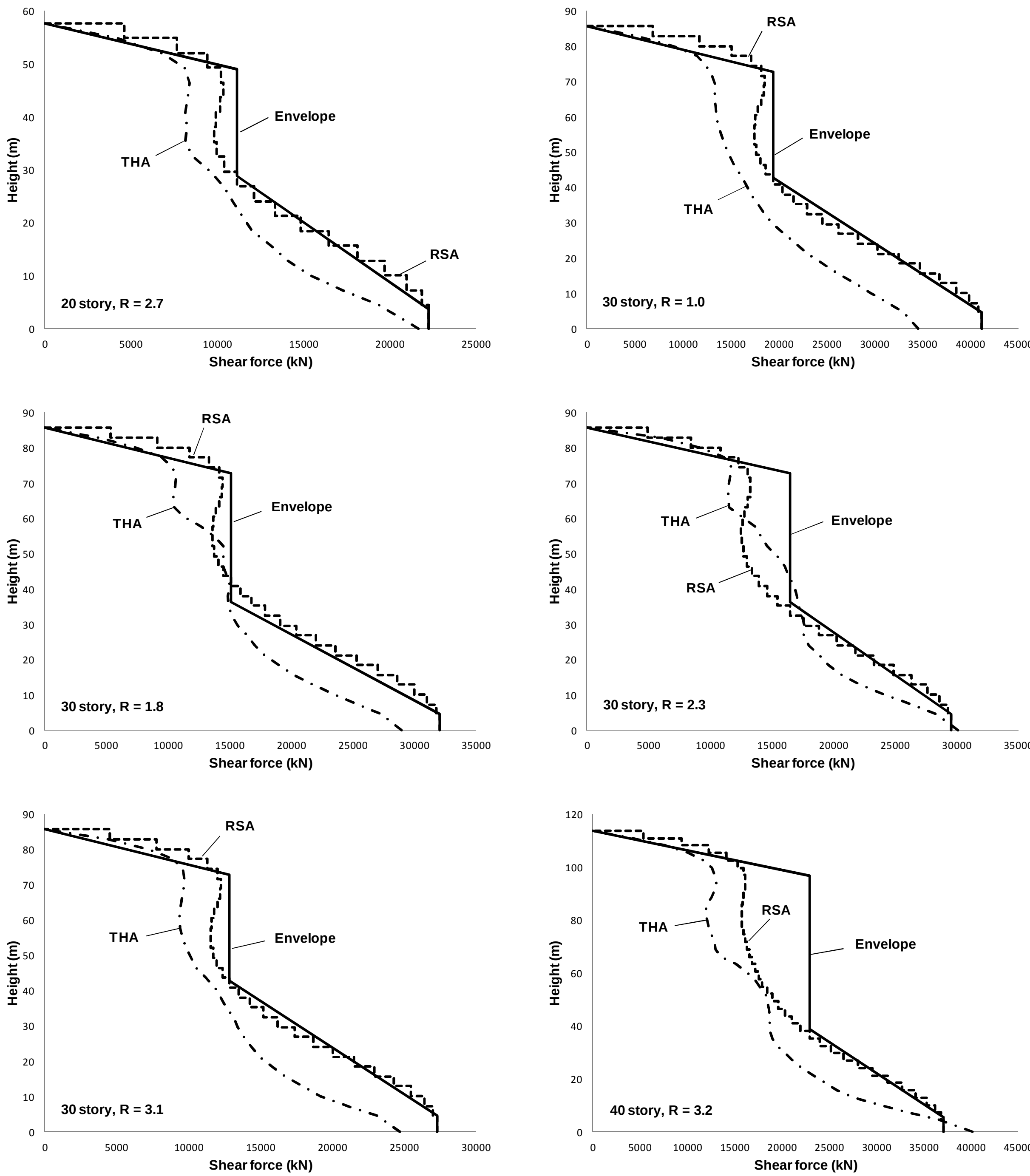

Figure 6.16 Cont'd.

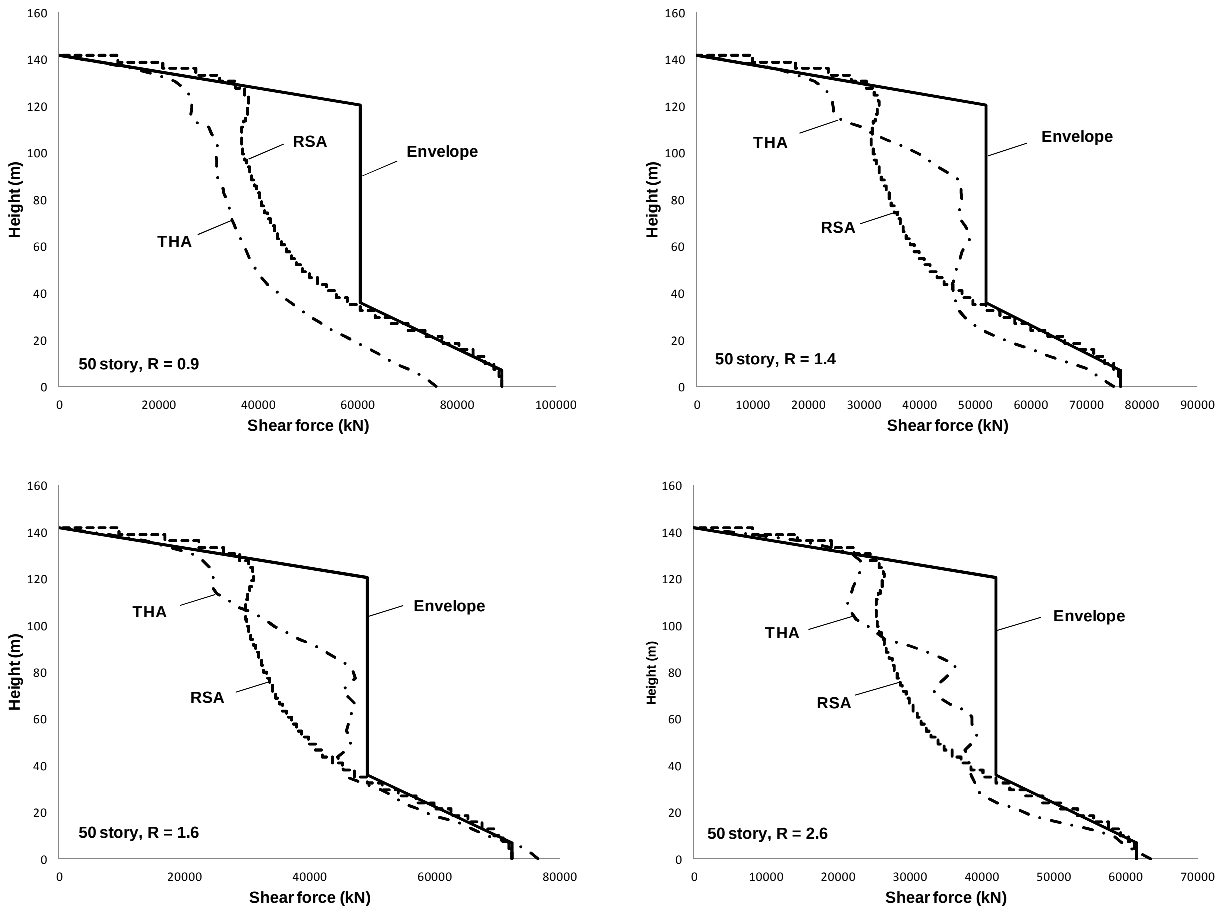

Figure 6.16 Cont'd.

6.7 Summary and Conclusions

Time history results were used to estimate shear force demands in cantilever shear walls. A simple base shear - base rotation interaction diagram was developed to study the intensity of base rotations at the instant of maximum base shear force demand. It was observed that the base rotation associated with the maximum base shear force was smaller than the maximum base rotation for individual ground motions. Low base rotation corresponding to high base shear force demand results in smaller diagonal cracking, which increases concrete shear strength.

An investigation was carried out to understand the intensity of shear force demands near the midheight. Time history results showed that large shear force demands were developed around the midheight for 50 story walls with intermediate force reduction factors. It was observed that period lengthening of higher modes caused high midheight shear force demands in such walls. For shorter walls, on the other hand, period lengthening of the first mode derived high shear force demands near the midheight.

Mean shear force envelopes from time history analysis were compared with the shear force demands determined from available recommendations on shear amplification factor. The Rutenberg and Nsieri method provided the best envelope although this method overestimated the base shear force demand in 50 story walls. A simple envelope was proposed based on Rutenberg and Nsieri model to estimate the design shear force over the height of cantilever shear walls. The proposed envelope can be easily determined by performing response spectrum analysis for walls with a fixed base support using $0.5EI_g$ flexural stiffness. Comparison of mean time history results with the proposed envelope showed good agreement. Also, it was observed that RSA can be used for estimating mean shear force demands if they are scaled by appropriate shear amplification factors. For very tall walls, however, midheight shear force demands from scaled RSA were found to be 25% lower than those determined form time history analysis.

Chapter 7 : Validation of Flexural Models with Shake Table Results

7.1 Overview

Shake table test results of a 7-story shear wall at the University of California at San Diego (UCSD) are used in this section to validate the simplified models developed for estimating roof displacement, base curvature, and interstory drift demands. A 3-dimensional linear model of the wall was developed in SAP and the stiffness of the linear model was adjusted to match roof displacement demands obtained from the experiment. The peak interstory drift profile recorded during the test was compared with the simplified interstory drift model. Lastly, base curvature demands predicted from simplified models were compared with those measured during the test.

7.2 Description of the Specimen

Figure 7.1 shows the elevation and floor plan view of the shear wall specimen (Panagiotou 2008). The specimen is a seven story building designed using displacement-based approach for a site located in Los Angeles. The total height of the specimen is 19.2 m. The main lateral force resisting system for the building is a 3.66 m long rectangular shear wall (so called web wall). The thickness of the web wall is 0.2 m at levels 1 and 7 and 0.15 m at other elevations. The longitudinal reinforcement ratio for the web wall is 0.66% at levels 1 and 7 and 0.81% elsewhere. The specimen includes two additional walls, which provide lateral and torsional stability. The flange wall is 4.87 m long, and is 0.2 m thick at level 1 and 0.15 m thick elsewhere. The third wall is a precast segmental wall which is connected to the slabs at each elevation with pin-pin horizontal trusses. The simply supported slab is 0.2 m thick, and is supported by the web wall and four steel gravity columns with pinned ends. The web wall is connected to the flange wall via a slotted connection. This connection is 0.61 m wide and 4.88 m wide, and has two slots on both ends. The slots are 51 mm wide and 140 mm thick to minimize the coupling between the web and flange walls. The concrete had a compressive strength of 37.9 MPa, and the yield strength for the reinforcing steel was 455 MPa. The total seismic weight of the specimen is 2045 kN, and the mass distribution over the height is evenly distributed over the height.

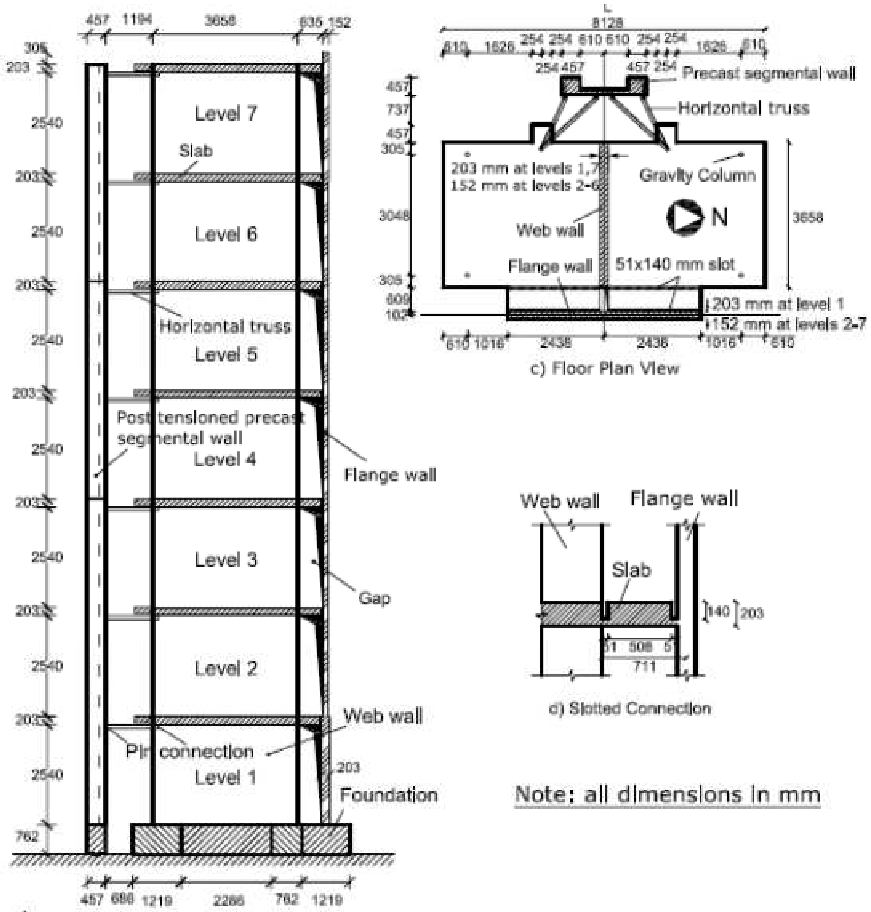

Figure 7.1 Elevation and plan view of the seven-story wall specimen (from Panagiotou 2008, © Ph.D. thesis, by permission).

7.3 Test Program and Experimental Results

The specimen was subjected to four earthquakes in the direction parallel to the web wall. Figure 7.2 shows the acceleration and displacement spectra corresponding to 5% damping for the four ground motions. Also shown in this figure is the spectral acceleration and spectral displacement for the UHS used in this thesis as the target spectrum for scaling ground motions. Note that EQ1 and EQ4 represented records with 63.7% and 5.8% probability of exceedance in 50 years for the period of 0.5 s, respectively. White noise tests were performed to measure the period of the building prior and after each earthquake. The fundamental period of the building at the beginning of the experiment was measured to be 0.51 s. This period increased to 0.59 s because the specimen was subjected to 25 white noise tests prior to EQ1. The fundamental period shifted to 0.65, 0.82, 0.88, and 1.16 s after EQ1, EQ2, EQ3, and EQ4, respectively. The fundamental period of the specimen prior to each earthquake is shown in Figure 7.2 with a dashed line. The experimental results are summarized in Table 7.1.

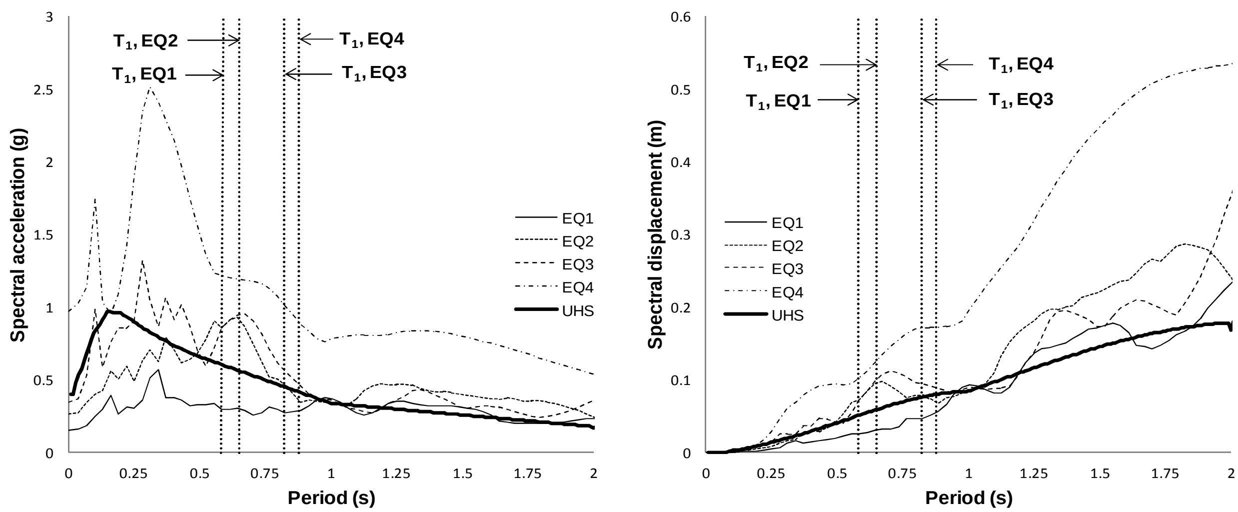

Figure 7.2 Spectral acceleration and spectral displacement spectra corresponding to 5% damping for the input ground motions (Note: fundamental period of the specimen prior to each motion is shown in dotted lines).

Table 7.1 Maximum values of different demand parameters recorded in the experiment.

	EQ1	**EQ2**	**EQ3**	**EQ4**
Global drift ratio (%)	0.28	0.75	0.83	2.06
Base curvature times wall length	0.002	0.0107	0.0114	0.0282
Tensile strain in long. steel	0.0061	0.0173	0.0178	0.0285
Compressive strain in concrete	-0.0007	-0.0017	-0.0018	-0.0039
Interstory drift at the top of wall (%)	0.35	0.89	1.03	2.36

A considerable difference was observed between the measured base bending moment demand and the web wall flexural strength. The measured base bending moment demand was 5368 kNm, 8351 kNm, 8353 kNm, and 11495 kNm for EQ1 to EQ4, while the flexural strength of the web wall was 6368 kNm (Panagiotou 2008). This increase of the flexural capacity of the wall is associated with the slotted slab connecting the web and flange walls. The slab was slotted to reduce the coupling between the two walls. The moment capacity of the slotted connection was 6.22 kNm and 10.2 kNm per unit length of the connection for the side connecting to the flange wall and for the side connecting to the web wall, respectively. Although these moments are low, the shear force from the yielding of the slotted connection caused significant axial force variation in the web and flange walls when it is summed over seven stories. This variation leads to considerable increase in the moment capacity of the specimen. This observation was verified by comparing bending moment and shear force demands from experiment with those determined from nonlinear time history analysis using the trilinear hysteretic bending moment - curvature relationship shown in Figure 2.20. The results from this study indicated that roof displacement, base curvature, and maximum interstory drift at the roof vary between 85% and 120% of the experimental results, while the predicted base shear and bending moment demands are significantly less than those determined from the experiment, especially for the EQ4. Similar observations were found by Martinelli and Filippou (2009). Panagiotou et al. (2007) indicated that such overstrength may not be observed in real buildings since the configuration of gravity columns and slabs in practice are different from those of the specimen, therefore the development of such overstrength seems to be questionable to apply for a real structure.

7.4 Linear Analysis of the Specimen for Predicting Effective Stiffness

The purpose of this section is to obtain appropriate effective stiffness values to be used in the linear analysis in order to predict roof displacement demands from the shake table test. A 3-dimensional linear model of the specimen was set up in SAP (Computers & Structures Inc. 2010). The model included the web wall, flange wall, precast segmental wall, gravity columns, and slabs. The flexibility of the foundation was modelled using rotational springs at the base of the web wall and flange wall. Fundamental period of the analytical model using EI_g for the three concrete walls and $0.2EI_g$ for the slab was 0.52 s, which nearly matched the fundamental period of 0.51 s measured from white noise test at the beginning of the experiment. Wong (2010) observed that reducing slab stiffness from $0.2EI_g$ to $0.1EI_g$ does not change roof displacement demand from the linear model more than 10% for EQ1 and EQ4. As a result, an effective stiffness of $0.2EI_g$ was considered to model cracking of the slab during the experiment. Note that Elastic Modulus of concrete E_c and self weight of concrete was assumed to be $4500\sqrt{f_c'}$ and 2400 kN/m^3, respectively.

For each earthquake, appropriate effective stiffness was determined in two steps. In the first step, the stiffness of the walls was calibrated such that the fundamental period of the linear model matched the period obtained from the white noise tests prior to each earthquake. The stiffness reduction factor associated with this step is denoted as β. In the second step, the stiffness of the wall is further reduced so that the roof displacement from response spectrum analysis matched the maximum roof displacement from the experiment. The stiffness reduction factor associated with this step is denoted as α. It should be noted that the fundamental period of the specimen shifted from 0.51 s to 0.59 s prior to EQ1 due to applying 25 white noise tests. A reduction factor of β = 0.8 was required to increase the fundamental period of the analytical model from 0.52 s to 0.59 s. The input spectrum for performing response spectrum analysis is the acceleration spectrum for individual earthquakes as shown in Figure 7.2. Table 7.2 shows the reduction factors α and β associated with the two steps.

Table 7.2 Stiffness reduction factors to estimate the period and roof displacement of the specimen using the acceleration spectrum for individual earthquakes.

	WN[3]	**EQ1**	**EQ2**	**EQ3**	**EQ4**
Reduction factor in the first step (β)[1]	0.8	0.8	0.64	0.4	0.30
Reduction factor in the second step (α)[2]	-	0.8	0.9	1.3	0.53
Product ($\alpha\beta$)	-	0.64	0.58	0.52	0.16
R_1	-	1.43	2.22	2.32	3.54
R_2	-	1.32	3.22	3.70	3.22
Fundamental period from white noise prior to earthquake (s)	0.51	0.59	0.65	0.82	0.88
Fundamental period of linear model prior to earthquake (s)	0.52	0.59	0.65	0.81	0.88
Fundamental period from white noise after earthquake (s)	0.59	0.65	0.82	0.88	1.16
Fundamental period of linear model after earthquake (s)	0.59	0.65	0.69	0.68	1.16
Roof displacement / wall height (%)	-	0.28	0.75	0.83	2.06

[1]as a fraction of stiffness prior to EQ1, [2]as a fraction of stiffness prior to each earthquake, [3]white noise applied prior to EQ1.

Force reduction factors R_1 and R_2 in Table 7.2 refer to the ratio of the elastic bending moment demand to the nominal flexural capacity of the specimen: the R_1 factor was calculated using stiffness of the specimen prior to each earthquake, while the R_2 factor corresponds to the stiffness of the wall after each earthquake, i.e. effective stiffness that gives a roof displacement demand equal to the roof displacement demand obtained from the experiment. Reduction factors associated with EQ2 and EQ3 are similar since these motions have similar spectral accelerations for periods greater than 0.5 s.

The α values required to match roof displacement demand is 0.9 and 1.3 for EQ2 and EQ3, respectively. This is because of the fact that spectral displacement tends to decrease between 0.67 s and 0.8 s for EQ2 and between 0.7 s and 0.95 s for EQ3 (see Figure 7.2). The fundamental period of the specimen is 0.65 and 0.82 s prior to EQ2 and EQ3, respectively. Therefore, stiffness reduction factor must be close to 1.0 for EQ2 and greater than 1.0 for EQ3 in order to reduce the effective period and hence increase the roof displacement demand. To remedy this, it was decided to perform response spectrum analysis using a smooth spectrum instead of the spectrum for individual earthquakes. The UHS shown in Figure 7.2 was scaled such that it gives area-under-the-curve equal to those corresponding to EQ1 to EQ4 over a period range from T_1 to $2T_1$. Periods lower than T_1 were not considered since higher modes do not contribute to roof displacement demand in an elastic analysis. Also, $2T_1$ was considered as an upper bound for the elongation of period due to nonlinear behaviour. Figure 7.3 compares the scaled UHS with the displacement spectrum for individual earthquakes. Stiffness reduction factors using scaled UHS are shown in Table 7.3.

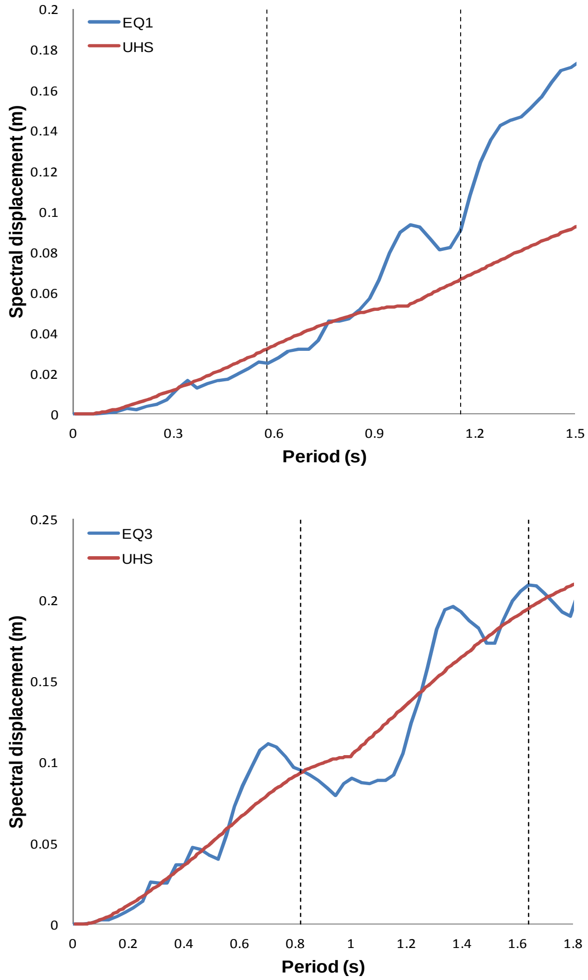

Figure 7.3 Comparison of scaled UHS with the displacement spectra for individual earthquakes.

Table 7.3 Stiffness reduction factors to estimate the period and roof displacement of the specimen using the scaled UHS.

	WN[3]	**EQ1**	**EQ2**	**EQ3**	**EQ4**
Reduction factor in the first step (β)[1]	0.8	0.8	0.64	0.39	0.34
Reduction factor in the second step (α)[2]	-	0.84	0.65	0.75	0.55
Product ($\alpha\beta$)	-	0.67	0.42	0.29	0.19
R_1	-	1.45	2.73	2.32	3.44
R_2	-	1.38	2.44	1.98	3.16
Fundamental period from white noise prior to earthquake (s)	0.51	0.59	0.65	0.82	0.88
Fundamental period of linear model prior to earthquake (s)	0.52	0.59	0.65	0.82	0.88
Fundamental period from white noise after earthquake (s)	0.59	0.65	0.82	0.88	1.16
Fundamental period of linear model after earthquake (s)	0.59	0.64	0.80	0.93	1.17
Roof displacement / wall height (%)	-	0.28	0.75	0.83	2.06

[1]as a fraction of stiffness prior to EQ1, [2]as a fraction of stiffness prior to each earthquake, [3]white noise applied prior to EQ1.

Table 7.3 shows that using smooth UHS results in α values that vary from 0.84 to 0.55 as the force reduction factor R_2 increases from 1.38 to 3.44. Stiffness reduction factor of 0.84 refers to EQ1, when the specimen had limited yielding (base curvature demand times web wall length = 0.002), while stiffness reduction factor of 0.55 refers to EQ4, when the specimen had significant yielding (base curvature demand times web wall length = 0.0282). Therefore, it can be concluded that stiffness reduction factor reduced from 0.84 for an earthquake that caused limited yielding to 0.55 for an event which resulted significant yielding at the base of the specimen.

7.5 Comparison of Base Curvature and Interstory Drift Demands from Experiment with Simplified Models

Figure 7.4 compares the maximum recorded interstory drift corresponding to each earthquake with the predictions from the D1 model. Roof and midheight interstory drifts for the D1 model are equal to $1.6\Delta_t/h_w$ and $1.3\Delta_t/h_w$, respectively. Figure 7.4 indicates that the D1 model provides a reasonably conservative estimate of interstory drift demands for the four earthquakes.

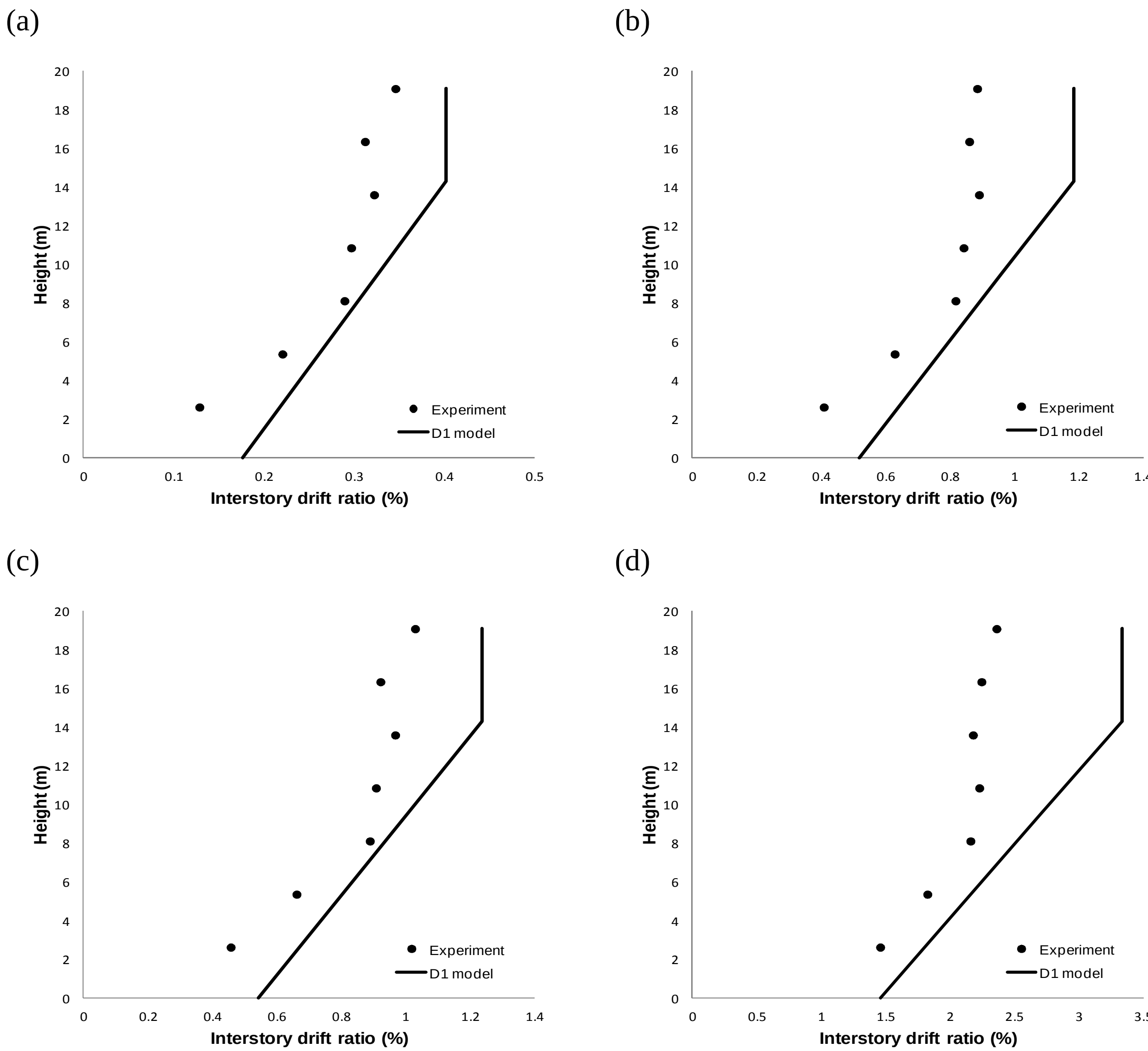

Figure 7.4 Comparison of interstory drift profile from experiment with the prediction from the D1 model for (a) EQ1, (b) EQ2, (c) EQ3, and (d) EQ4.

Figure 7.5 compares the base curvature demand for the web wall from different analytical models with the maximum recorded base curvature demand. Note that the R_2 values shown in Table 7.3 were used to compute the base curvature demand for the CSA and M1 models. The predictions from the M1 model are lower than those form the ACI 318 approach since the C factor in the M1 model (see Equation 5.11) is less than 1.8 depending on the ratio of the wall height to the force reduction factor. The CSA method also provides a reasonable estimate of the recorded base curvature demand.

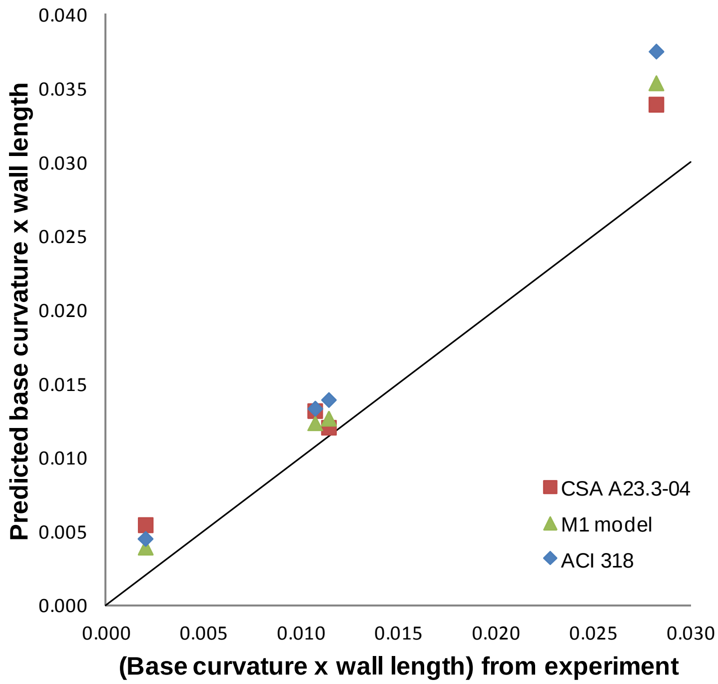

Figure 7.5 Comparison of the predicted base curvature of the web wall from different analytical models with the experimental results.

7.6 Summary and Conclusions

Shake table test results of a 7-story shear wall building were used to assess the accuracy of simplified models developed in Chapter 5 for predicting roof displacement, base curvature, and interstory drift demands. A 3-dimensional linear model was constructed in SAP, and the stiffness of the model was calibrated to match the fundamental period and roof displacement demand recorded during the experiment. It was observed that stiffness reduction factor dropped from 0.84 to 0.53 as the force reduction factor increased from 1.4 to 3.2. Figure 7.6 plots the stiffness reduction factors determined from this study as well as the stiffness reduction factors obtained from nonlinear time history analysis of the 13 shear walls as described in Chapter 5. Figure 7.6 indicates that stiffness reduction factors determined from the experiment are consistent with the results obtained from time history analysis.

It was also observed that the simplified models for predicting base curvature and interstory drift demands provide a reasonable estimate of the maximum recorded values from the experiment.

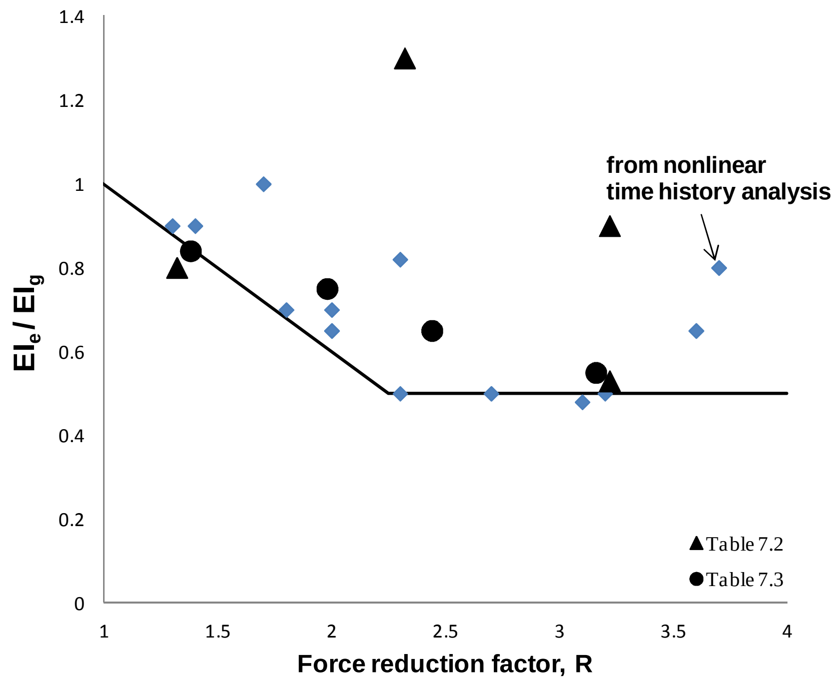

Figure 7.6 Comparison of stiffness reduction factor for the 7-story shear wall specimen determined from linear analysis (i.e. α versus R_2 as shown in Table 7.2 and Table 7.3) with the stiffness reduction factor of 10 to 50 story shear walls using nonlinear time history analysis.

Chapter 8 : Contributions and Recommendations for Future Work

8.1 Contributions

Nonlinear time history analysis was used to investigate the seismic response of cantilever concrete shear walls. The research involved the modeling and design of 15 slender shear walls that were 10 to 50 stories high. The findings and contributions for each chapter is summarized hereafter.

8.1.1 Trilinear Hysteretic Bending Moment - Curvature Relationship

The objective of Chapter 2 was to develop a transparent hysteretic bending moment - curvature model as an analytical tool for performing time history analysis of cantilever shear walls. The experimental results from two shear walls with rectangular and flanged cross sections showed that the flanged wall with a high axial compression force and low percentage of longitudinal reinforcement had less residual displacements and smaller hysteretic loops than those for the rectangular cross section. In addition, it was observed that the loading segment of the force - displacement relationship for the flanged wall resembled a trilinear curve rather than the conventional bilinear backbone curves used in most hysteretic model such as the Clough hysteretic model. It was observed that the fiber model provides a reasonable prediction of the force - displacement relationship of both specimens. The fiber model was used to develop a rational model for the softening of reinforced concrete sections subjected to reverse cyclic loads. The influence of reinforcing steel constitutive relationship on the yield curvature was examined. A rational model was developed to estimate residual curvatures in shear walls subjected to reverse cyclic loads. The trilinear hysteretic model proved to accurately estimate the general response of both flanged and rectangular specimens.

8.1.2 Effect of Ground Motion Selection on Demand Parameters

The objective of Chapter 4 was to investigate the influence of ground motions selection and scaling on the seismic response of cantilever shear walls. The input ground motions in this study were selected and scaled to the UHS and CMS. The ground motions were scaled to the UHS in two ways: scaling at the fundamental period and over a range of periods. T_1, T_2, T_3 as well as $1.5T_1$ and $2T_1$ were considered as possible conditioning periods. Time history results indicated that a single conditioning period defined the envelope response for displacement and interstory drift demands over the height of the walls, while different conditioning periods contributed to the envelope of the curvature and shear force demands. It was observed that maximum values for roof displacement, roof interstory drift, and base curvature demands were associated with T_1 or $1.5T_1$ conditioning periods, while maximum base shear and midheight curvature were caused by the ground motions matched to the CMS computed at T_2 or T_3. For 10 story walls, using conditioning period of $1.5T_1$ gave higher roof displacement demands than $2T_1$, indicating that the period lengthening due to the nonlinear action was closer to $1.5T_1$.

It was observed that the mean roof displacement and mean interstory drift at the roof from the envelope of the ground motions matched to the CMS at different conditioning periods varied between 90 and 100% of the mean values from the spectrum matched ground motions. This difference is considerably less than the reported 29% difference between maximum interstory drift from ground motions scaled to the UHS and the CMS computed at T_1 for the 12 story shear wall analyzed by PEER GMSM program (Haselton et al. 2009). The base curvature and base shear force demands from the ground motions matched to the CMS were not lower than 80% of the mean results from the spectrum matched records. The difference between the base curvature and base shear force demands using CMS and spectrum matched ground motions did not always increase as the force reduction factor increased.

In most cases, the structural responses from the two sets of spectrum matched records and ground motions matched to the UHS over a range of periods (SOR) were similar. Using spectrum matched ground motions reduced the dispersion of the response, meaning a fewer number of ground motions can be used without influencing the mean value of the structural response. A reasonable similarity between the roof displacement and roof interstory drift demands from spectrum matched and CMS ground motions was observed. For curvature and shear force demands, a maximum difference of 20% was reported between the spectrum matched and the envelope of results using various sets of CMS ground motions. This difference could be reduced if more conditioning periods were used, but this would entail considerable computational effort.

The findings of Chapter 4 indicated that using spectrum matched ground motions is the best method for establishing mean response for cantilever shear walls. Since the variability of the responses from individual records was minimal, the mean structural envelopes from spectrum matched ground motions were more stable than the SOR ground motions. It was also concluded that using additional conditioning periods provides closer responses to those obtained from the spectrum matched ground motions; however, specifying a single period as the conditioning period that governs the maximum responses such as shear force and curvature demands might not be evident in tall shear walls with high nonlinear action. Period lengthening of higher modes can contribute to maximum response over the height of the wall. Using a set of spectrum matched ground motions, on the other hand, establishes a mean response with minimal computational effort.

8.1.3 Effective Stiffness

This study dealt with the estimating of roof displacement demands in cantilever shear walls. Roof displacement demands from time history analysis were used to define appropriate effective stiffness values to be used in a linear analysis such as response spectrum analysis. This method of estimating effective stiffness ensures that the linear analysis yields an accurate estimate of the mean roof displacement demands determined from time history analysis. Both single-degree-of-freedom (SDOF) and multi-degree-of-freedom (MDOF) approaches were used for estimating effective stiffness. The SDOF study included a higher number of periods and force reduction factors due to low computational costs associated with the time history analysis of SDOF systems. In both studies the stiffness reduction factor was expressed as a function of force reduction factor rather than axial compression force.

Time history results indicated that the stiffness reduction factor dropped from 1.0 to about 0.5 as the force reduction factor increased from 1.0 to 5.0. As opposed to current recommendations for effective stiffness - Ibrahim and Adebar (2004), CSA A23.3 (2004), Paulay and Priestley (1992) - it was found that the variation of axial compression force had less influence on effective stiffness. In fact, walls with high axial compression force and low longitudinal reinforcement ratio tend to have lower effective stiffness. This is due to the fact that such walls have a flag-shaped force - displacement relationship with smaller hysteretic loops. It was proven that walls with lower hysteretic dissipation capacity had lower effective stiffness since the mean displacement demands corresponding to these walls were higher than those with larger hysteretic loops.

8.1.4 Flexural Demands on Cantilever Concrete Shear Walls

The main contribution from this section of thesis was the determination of curvature and interstory drift demands in cantilever shear walls. A comparison of roof displacement and base curvature time histories for three walls with different heights showed that for taller walls, the maximum value for these response quantities do not occur at the same instant for individual ground motions. This observation is an indication of the influence of higher mode response in high-rise shear walls with considerable nonlinear action. It was demonstrated that the CSA A23.3-04 approach for estimating base curvature demands underestimates the elastic portion of the total roof displacement demand for most walls especially for taller walls, which leads to an overestimation of base curvature demands in tall cantilever shear walls. To address this issue, a simple equation was developed to predict the base curvature demand associated with the mean and mean plus one standard deviation results determined from time history analysis. The equation relates the base curvature demand to the global drift ratio using a term which is a function of wall height, length, and force reduction factor.

The findings from an investigation of midheight curvature demands indicated that this demand parameter is less sensitive to the flexural strength of the wall around midheight. It was demonstrated that the location at which maximum midheight curvature occurs varied along the height as the force reduction factor increased. Consequently, providing additional flexural strength around midheight is ineffective in reducing curvature demands along the height of concrete shear walls. It was observed that midheight curvature demand corresponding to mean plus one standard deviation results from time history analysis was $0.0034/l_w$, where l_w is the wall length. This value is similar to the recommended values for yield curvature. Therefore, midheight curvatures can be tolerated by providing minimum detailing for ductility around midheight. A simple design envelope was proposed for predicting curvature demands over the height of cantilever shear walls.

Another contribution from Chapter 5 was to develop a design envelope for predicting interstory drift demands over height. A comparison of mean interstory drift profiles from time history analysis with those determined using response spectrum analysis showed that linear analysis underestimated interstory drifts at lower floors even if appropriate effective stiffness values were used to accurately estimate mean roof displacement demands from time history analysis. The design envelope developed in Chapter 5, however, provides a reasonable upper bound to interstory drift profile determined from time history analysis. The predicted interstory drift values from this simplified model can be used to assess the likelihood of punching shear failure of slabs in gravity-load columns. Lastly, the accuracy of the proposed interstory drift profile for a shear wall with flexible base support was demonstrated.

8.1.5 Shear Demands on Cantilever Concrete Shear Walls

The objective was to develop a simple base shear - base rotation interaction diagram for three cantilever shear walls with high force reduction factors. Results from this study showed that base rotations were relatively low when base shear force was high. Low base rotation is equivalent to lower strain in longitudinal reinforcement, a parameter that influences the width of diagonal cracks and concrete shear strength. The fact that the maximum values of base shear force and base rotation demands did not occur simultaneously due to the influence of higher mode response increases the shear strength of shear walls in earthquakes. This observation contrasts current seismic design guidelines which entail the shear design of concrete walls for maximum shear force and maximum rotation demands. Reducing concrete shear strength for maximum base rotation leads to an underestimation of concrete shear strength since rotations corresponding to high base shear force demands were considerably lower than the maximum base rotations.

The findings from time history analysis indicated that mean base shear forces from time history analysis were higher than those resulting from linear analysis reduced by force reduction factor, which is defined as the ratio of elastic bending moment demand to the wall nominal capacity - both calculated at the base of the building. The ratio of base shear force demands from time history analysis to the base shear force from linear analysis is generally referred to as shear amplification factor. It was observed that for most walls, the shear amplification factor increased from 1.0 to 2.0 as the force reduction factor increased from 1.0 to 3.5. Also, shear amplification factors for 10 story walls were lower than those for taller walls.

Another contribution was the determination of shear force demands around the midheight in tall cantilever shear walls. It was observed that the ratio of midheight to base shear force demands in 50 story walls with intermediate force reduction factors was higher than those for other shear walls. A sensitivity analysis using different conditioning periods showed that for 30 and 50 story walls, elongation of higher mode periods resulted in midheight shear force demands that were higher than those from higher mode periods. For a 10 story wall, on the other hand, elongation of the first mode period defined the shear force envelope around midheight. It was also observed that as the force reduction factor increased, the elongation of higher mode periods defined the shear force envelope at different elevations, while the shear force demand corresponding to these conditioning periods decreased around the midheight. Lastly, it was observed that base shear force demand was rather insensitive to the elongation of the higher mode period, which indicated that higher mode period elongation mainly influenced midheight shear force demands in tall cantilever shear walls.

8.2 Future Work

The analytical results presented in this research correspond specifically to cantilever concrete shear walls. Further investigation needs to be undertaken on seismic response of coupled shear walls, which consist of cantilever shear walls connected through coupling beams. The behavior of coupled wall structures may deviate from those observed in this thesis depending on the level of coupling between individual walls. The trilinear bending moment - curvature relationship developed in this work to perform time history analysis accounts for constant axial compression force from gravity loads. The axial load on coupled wall structures, however, is not constant during seismic loads since the shear forces developed in the coupling beams influence the axial compression force in individual shear walls. Research on coupled wall structures provides insight into curvature and shear force distribution in coupled wall systems as well as the end rotations of coupling beams.

This thesis focused on the flexural modeling of cantilever shear walls. This analytical model can be further extended by developing a model for shear response of such systems. Although an insignificant interaction between shear force and rotation demands was observed at the base of cantilever walls, the inclusion of a shear model results in a more realistic estimate of shear forces over the height of walls. In addition, an estimate of shear deformations at lower floors is critical for evaluating the safety of gravity load columns.

The main intent of this thesis was to investigate the seismic response of cantilever shear walls. Time history results for shear walls were also used to develop simple models to estimate seismic demands on gravity-load columns. It was assumed that maximum curvature and interstory drift demands in gravity-load columns were equal to those in the shear wall. This assumption requires further examination and could be refined by performing time history analysis on structural systems including both shear wall and gravity load resisting systems. Using this method, the interaction between seismic and gravity force resisting systems can be further researched.

This study dealt with the 2-dimensional modeling of cantilever shear walls. This method of modeling does not take into account the additional seismic demands on structural components resulting from torsion. Both shear walls and gravity load columns can undergo additional demands in buildings with plan irregularity. A 3-dimensional model could address additional demands on both shear wall and gravity-load columns since the 2-dimensional modeling did not account for the influence of torsion on seismic demand parameters.

References

Abrahamson, N. A. (1992). “Non-stationary spectral matching”, Seismological Research Letters, Vol. 63, No. 1.

ACI 318 (2005). Building code requirements for structural concrete (ACI 318-05) and Commentary (ACI 318R-05), ACI Committee, 318. American Concrete Institute, Farmington Hills. MI.

Adebar, P., and Ibrahim, A. M. M. (2002). “Simple nonlinear flexural model for concrete shear walls”, Earthquake Spectra, 18(3), 407-426.

Adebar, P., Mutrie, J., and DeVall, R. (2005). “Ductility of Concrete Walls: the Canadian Seismic Design Provisions 1984 to 2004”, Canadian Journal of Civil Engineering, 32(6): 1124-1137.

Adebar, P., Ibrahim, A. M. M., and Bryson, M. (2007). “Test of high-rise core wall: effective stiffness for seismic analysis”, ACI Structural Journal, 104(5), 549-559.

Adebar, P., Bazargani, P., Mutrie, J., and Mitchell, D. (2010). “Safety of Gravity-load Columns in Shear Wall Buildings Designed to Canadian Standard CSA A23.3”, Canadian Journal of Civil Engineering, 37(11): 1451-1461.

Anderson, D. L. (2003) “Effect of Foundation Rocking on the Seismic Response of Shear Walls”, Canadian Journal of Civil Engineering, 30(2): 360-365.

ASCE 7 (2005). Minimum Design Loads for Buildings and Other Structures. American Society of Civil Engineers, Reston, VA.

Atkinson, G. M. (2010). Personal communication, October.

Atkinson, G. M. (2009). “Earthquake time histories compatible with the 2005 National building code of Canada uniform hazard spectrum”, Canadian Journal of Civil Engineering, 36(6): 991-1000.

ATC 55 (2005). “Improvement of nonlinear static seismic analysis procedures”, Applied Technology Council, Redwood City, California.

ATC 72 (2010). “Modeling and acceptance criteria for seismic design and analysis of tall buildings”, Applied Technology Council, Redwood City, California.

ATC 82 (2011). “Selection and scaling earthquake ground motions for performing response-history analyses”, NEHRP Consultants Joint Venture.

Baker, J. W., and Cornell, C. A. (2005). “A vector-valued ground motion intensity measure consisting of spectral acceleration and epsilon”, Earthquake Engineering & Structural Dynamics, 34(10), 1193-1217.

Baker, J. W., and Cornell, C. A. (2006). "Spectral shape, epsilon, and record selection", Earthquake Engineering & Structural Dynamics, 35(9), 1077-1095.

Baker, J. W. (2011). "The conditional mean spectrum: A tool for ground motion selection", Journal of Structural Engineering, 137(3), 322-331.

Bentz, E. C., Vecchio, F. J., and Collins, M. P. (2006). "Simplified modified compression field theory for calculating shear strength of reinforced concrete element", ACI Structural Journal, 103(4): 614-624.

Blakeley, R.W.G, Cooney, R.C., and Megget, L.M. (1975). "Seismic shear loading at flexural capacity in cantilever wall structures", Bulletin of the New Zealand Society for Earthquake Engineering, 8, 278-290.

Bohl, A., and Adebar, P. (2011). "Plastic Hinge Lengths in High-Rise Concrete Shear Walls", ACI Structural Journal, 108(2): 148-157.

Boivin, Y., and Paultre, P. (2010). "Seismic Performance of a 12-story Ductile Concrete Shear Wall System Designed According to the 2005 National Building Code of Canada and the 2004 Canadian Standard Association Standard", Canadian Journal of Civil Engineering, 37(1): 1-16.

Boore, D. M., and Atkinson, G. M. (2008). "Ground-motion prediction equations for the average horizontal component of PGA, PGV, and 5%-damped PSA at spectral periods between 0.01 s and 10.0 s", Earthquake Spectra, 24(1), 99-138.

Carr, A. J. (2002). Computer program RUAUMOKO, Department of Civil Engineering, University of Canterbury, Christchurch, New Zealand.

Calugaru, V., and Panagiotou, M. (2011). "Response of tall cantilever wall building to strong pulse type seismic excitation", Earthquake Engineering & Structural Dynamics, published online, December.

CEN (2004). Eurocode 8 - Earthquake resistant design of structures. Pt. 1.3 General rules - specific rules for various materials and elements, Brussels, Belgium.

Chopra, A. K., Goel, R. K., and Chintanapakdee, S. M. (2003). "Statistics of single-degree-of-freedom estimate of displacement for pushover analysis of buildings", Journal of Structural Engineering, 129(4): 459-469.

CSA Committee A23.3 "Design of Concrete Structures: Structures (Design) – A National Standard of Canada" Canadian Standards Association 2004, Rexdale, Canada, 214 pp.

CSI (2010). SAP2000 – Integrated software for structural analysis and design. Computers and Structures, Berkeley, California.

Doepker, B. (2008). "Evaluation of Practical Methods for the Evaluation of Concrete Walls", MA.Sc. Thesis, University of Washington, Seattle.

Englekirk, R. E. (2007). "Rational Seismic Design Procedures for Shear Wall Braced Buildings", online publication.

FEMA 356 (2000). Prestandard and Commentary for the Seismic Rehabilitation of Buildings, FEMA 356 Report, prepared by the American Society of Civil Engineers for the Federal Emergency Management Agency, Washington, D. C.

Fronteddu, L. F. (1992). “Response of reinforced concrete to reverse cyclic loading”, MA.Sc thesis, The University of British Columbia, Vancouver, Canada.

Gerin, M., and Adebar, P. (2004). “Accounting for Shear in Seismic Analysis of Concrete Structures”, Proceedings of 13th World Conference on Earthquake Engineering, Vancouver, Canada.

Gerin, M., and Adebar, P. (2009). “Simple Rational Model for Reinforced Concrete Subjected to Seismic Shear”, Journal of Structural Engineering, 135(7): 753-761.

Hancock, J., Bommer, J. J., and Stafford, P. J. (2008). “Numbers of scaled and matched accelerograms required for inelastic dynamic analyses”, Earthquake Engineering & Structural Dynamics, 37(14), 1585-1607.

Heo, Y. A., Kunnath, S. K., and Abrahamson, N. (2011). “Amplitude-scaled versus spectrum-matched ground motions for seismic performance assessment”, Journal of Structural Engineering, 137(3), 278-288.

Huang, Y. N., Whittaker, A. S., Luco, N., and Hamburger, R. O. (2011). “Scaling earthquake ground motions for performance-based assessment of buildings”, Journal of Structural Engineering, 137(3), 311-321.

Ibrahim, A. M. M. (2000). “Linear and nonlinear flexural stiffness models for concrete walls in high-rise buildings”, Ph.D. Thesis, The University of British Columbia, Vancouver, Canada.

Ibrahim, A. M. M., and Adebar, P. (2004). “Effective Flexural Stiffness for Linear Seismic Analysis of Concrete Walls”, Canadian Journal of Civil Engineering, 31(4): 597-607.

Jayaram, N., Lin, T., and Baker, J. W. (2011). “A computationally efficient ground motion selection algorithm for matching a target response spectrum mean and variance”, Earthquake Spectra, 27(3), 797-815.

Katsanos, E. I., Sextos, A. G., and Manolis, G. D. (2010). “Selection of earthquake ground motion records: A state-of-the-art review from a structural engineering prospective”, Soil Dynamics & Earthquake Engineering, 30(3), 157-169.

Keintzel, E. (1990). “Seismic design shear forces in reinforced concrete cantilever shear wall structures”, European Journal of Earthquake Engineering, 3, 7-16.

Kent, D. C., and Park, R. (1971). “Flexural members with confined concrete”, Journal of the Structural Division, 97(ST7), 1969-1990.

Khaled, A., Tremblay, R., and Massicotte, B. (2011). “Combination rule for the prediction of the seismic demand on columns of regular bridges under bilateral earthquake components”, Canadian Journal of Civil Engineering, 38(6): 698-709.

Korchinski, A. D. (2007). "Investigation of Effective Stiffness of High-rise Concrete Shear Walls", MA.Sc. Thesis, The University of British Columbia, Vancouver, Canada.

Krolicki, J., Maffei, J., and Calvi, G. M. (2011). "Shear strength of reinforced concrete walls subjected to cyclic loading", Journal of Earthquake Engineering, 15(S1): 30-71.

Kurama, Y. C. and Farrow, K. T. (2003). "Ground Motion Scaling Methods for Different Site Conditions and Structure Characterstics", Earthquake Engineering & Structural Dynamics, 32(15): 2425-2450.

Lestuzzi, P. (2002). "Effective Stiffness of RC Walls in Dynamic Tests", Proceedings of 12th European Conference on Earthquake Engineering, London, UK.

Luco, N., and Bazzurro, P. (2007). "Does amplitude scaling of ground motion records result in biased nonlinear structural drift responses?", Earthquake Engineering & Structural Dynamics., 36(13), 1813-1835.

Martinelli, P., and Filippou, F. C. (2009). "Simulation of the shaking table test of a seven-story shear wall building", Earthquake Engineering and Structural Dynamics, 38(5), 587-607.

Menegotto, M., and Pinto, P. E. (1973). "Method of analysis for cyclically loaded reinforced concrete plane frames including changes in geometry and non-elastic behavior of elements under combined normal force and bending", Proceedings of IABSE Symposium on Resistance and Ultimate Deformability of Structures Acted on by Well Defined Repeated Loads, Lisbon, pp. 15-22.

Moehle, J., Bozorgnia, Y., and Yang, T. Y. (2007). "The Tall Building Initiative", SEAOC convention proceedings: 315-324.

Naeim, F., and Lew, M., (1995). "On the use of design spectrum compatible time histories", Earthquake Spectra, 11(1), 111-127.

National Research Council Canada. (2005). National Building Code of Canada. Canadian Commission on Building and Fire Codes, Institute for Research in Construction, Ottawa, Ontario.

Naumoski, N. D. (2001). Program SYNTH Generation of Artificial Accelerograms Compatible with a Target Spectrum, Computer Program and Supporting Documentation, Carleton University, Ottawa.

Nielsen, G. M., Almufti, I., Mahin, S. A., and Willford, M. R. (2010). "Performance of Rocking Core Walls in Tall Buildings under Severe Seismic Motions", Proceedings of the 9th U.S. National and 10th Canadian Conference on Earthquake Engineering, Toronto, Canada.

OpenSees (2008). Open System for Earthquake Engineering Simulation (OpenSees), Computer Program and Supporting Documentation, Pacific Engineering Research Centre, University of California, Berkeley [14 May 2008].

OpenSHA. (2009). Open Seismic Hazard Analysis, http://www.opensha.org [9 August 2012].

Orakcal, K., and Wallace, J. W. (2006). "Flexural Modeling of Renforced Concrete Walls - Experimental Verification", ACI Structural Journal, 130(2), 196-206.

Palermo, D., and Vecchio, F. J. (2004). "Compression field modeling of reinforced concrete subjected to reversed loading: verification", ACI Structural Journal, 101(2): 155-164.

Panagiotou, M., Restrepo, J. I., and Conte, J. P. (2007). "Shake table test of a 7-story full scale reinforced concrete structural wall building slice phase I: rectangular wall section", Report No. SSRP-07-07, University of California, San Diego.

Panagiotou, M. (2008). "Seismic Design, Testing, and Analysis of Reinforced Concrete Wall Buildings", Ph.D. Thesis, University of California, San Diego.

Panneton, M., Leger, P., and Tremblay, R. (2006). "Inelastic Analysis of a Reinforced Concrete Shear Wall Building according to the National Building Code of Canada", Canadian Journal of Civil Engineering, 33(7): 854-871.

Paulay, T., and Priestley, M. J. N. (1992). "Seismic Design of Reinforced Concrete and Masonry Buildings," John Wiley and Sons, New York, N. Y.

Paulay, T. (2001). "Seismic response of structural walls: recent developments", Canadian Journal of Civil Engineering, 28(6): 922-937.

PEER GMSM, Haselton, C. B., editor. (2009). "Evaluation of ground motion selection and modification methods: predicting median interstory drift response of buildings", Pacific Engineering Research Centre, University of California, Berkeley.

PEER Tall Building Initiative (2010). "Guidelines for performance-based seismic design of tall buildings", Pacific Engineering Research Centre, University of California, Berkeley.

PEER (2010). "PEER NGA database flatfile", Pacific Engineering Research Centre, University of California, Berkeley.

Pennucci, D., Sullivan, T.J., and Calvi, G.M. (2010). "Evaluation of higher mode effects in tall building response", 14th European Conference on Earthquake Engineering, Ohrid, Macedonia.

Priestley, M. J. N. (2003). "Does Capacity Design Do the Job? An Examination of Higher Mode Effects in Cantilever Walls", Symposium to celebrate the lifetime contributions of professors emeriti Tom Paulay and Bob Park.

Priestley, M.J.N, and Amaris, A. (2003). "Dynamic amplification of seismic moments and shear forces in cantilever walls", fib symposium, Concrete Structures in Seismic Regions, Athens, Greece.

Priestley, M. J. N., Calvi, G. M., and Kowalsky, M. J. (2007). "Displacement Based Seismic Design of Structures", IUSS Press, Pavia, Italy.

Risk Engineering Inc, (2010). "EZ-Frisk™ (version 7.01).

Rajaee Rad, B., and Adebar, P. (2009). “Seismic Design of High-Rise Concrete Walls: Reverse Shear due to Diaphragms below Flexural Hinge”, Journal of Structural Engineering, 135(8): 916-924.

Rutenberg, A., and Nsieri, E. (2006). “The Seismic Shear Demand in Ductile Cantilever Wall Systems and the EC8 Provisions”, Bulletin of Earthquake Engineering, 4(1):1-21.

Schotanus, M., and Maffei, J. (2007). “Appropriate stiffness and modeling assumptions for high-rise concrete wall buildings”, Seminar and workshop discussing the results of the 7-story building slice dynamic test.

SEAONC. (2007). SEAONC Recommended Administrative Bulletin for San Francisco, Structural Engineers Association of Northern California, San Francisco.

Shome, N., and Cornell, C. A. (1998). “Normalized and scaling accelerograms for nonlinear structural analysis”, Proceedings of 6th National Conference on Earthquake Engineering, Seattle, WA.

Somerville, P. (1997). “Development of ground motion time histories for phase 2 of the FEMA/SAC steel project”, Report SAC/BD-97/4, SAC Joint Venture, Sacramento, California.

Sullivan, T. J., Priestley, M. J. N., and Calvi, G. M. (2008). “Estimating the higher-mode response of ductile structure”, Journal of Earthquake Engineering, 12(3): 456-472.

Taucer, F. F., Spacone, E., and Filippou, F. C. (1991). “A fiber beam-column element for seismic response analysis of reinforced concrete structures”, Report No. UCB/EERC-91/17, Earthquake Engineering Research Center, University of California, Berkeley.

Thomsen, J. H., and Wallace, J. W. (2004). “Experimental verification of displacement-based design procedures for slender reinforced concrete structural walls”, Journal of Structural Engineering, 130(4): 618-630.

Wallace, J. W. (2007). “Modelling Issues for Tall Reinforced Concrete Core Wall Buildings”, The Structural Design of Tall and Special Buildings, 16(5): 615-632.

Watson-Lamprey, J., and Abrahamson, N. A. (2006). "Selection of ground motion time series and limits on scaling", Soil Dynamics and Earthquake Engineering, 26(5), 477-482.

White, T. W. (2004). “Seismic Demands in High-rise Concrete Walls”, Ph.D. Thesis, The University of British Columbia, Vancouver, Canada.

Wood, R. L., and Hutchinson, T. C. (2010). “Effects of ground motion scaling on nonlinear higher mode building response”, Proceedings of the 9th U.S. National and 10th Canadian Conference on Earthquake Engineering, Toronto, Canada.

Wong, J. C. M. (2010). “Practical analysis and investigation of the shake table test of a seven-story concrete shear wall structure using ETABS”, CIVL 598 Directed Studies Report, Department of Civil Engineering, The University of British Columbia, Vancouver, Canada.

Appendix A:

Cross Sectional Layout of the Example Core Walls

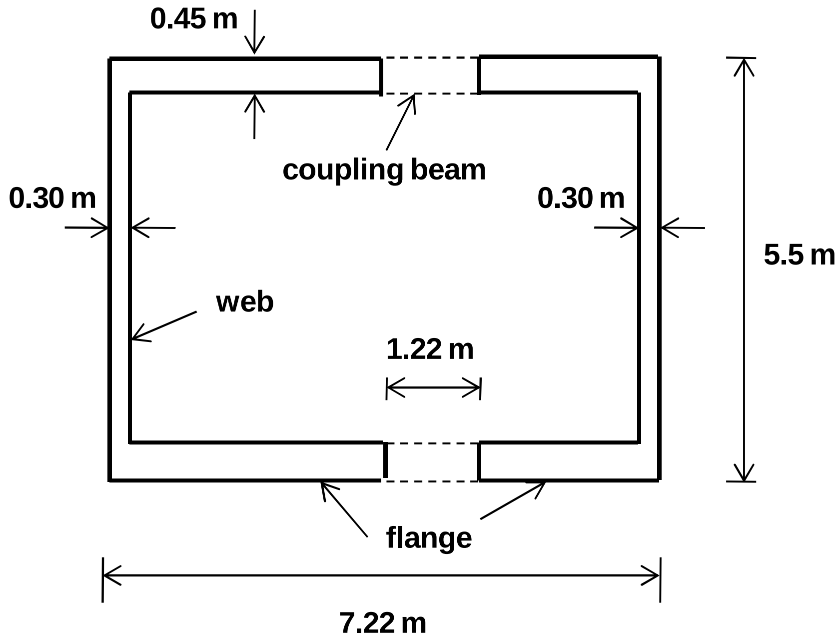

Figure A.1 Outline of the core walls in 10 story buildings.

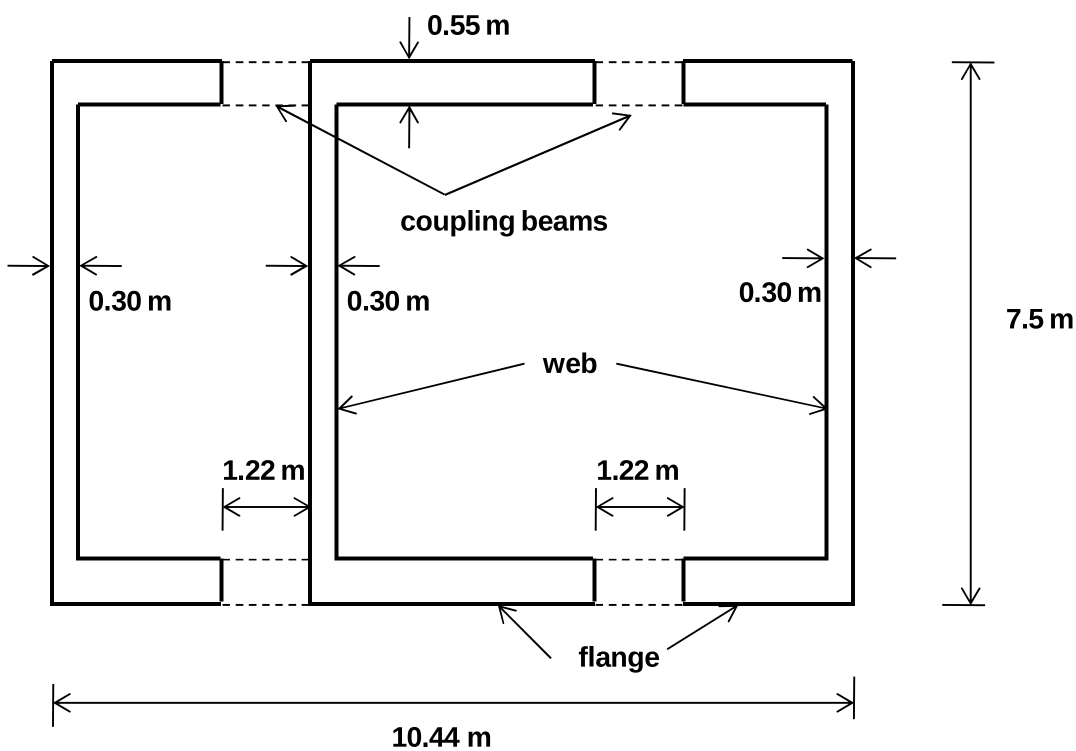

Figure A.2 Outline of the core walls in 20 story building.

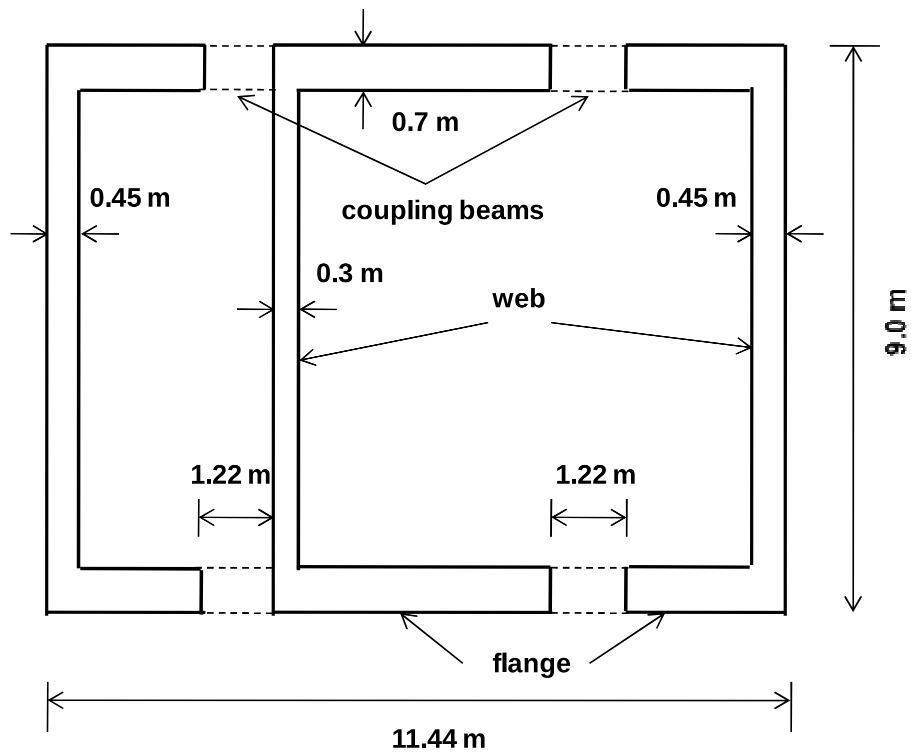

Figure A.3 Outline of the core walls in 30 story buildings.

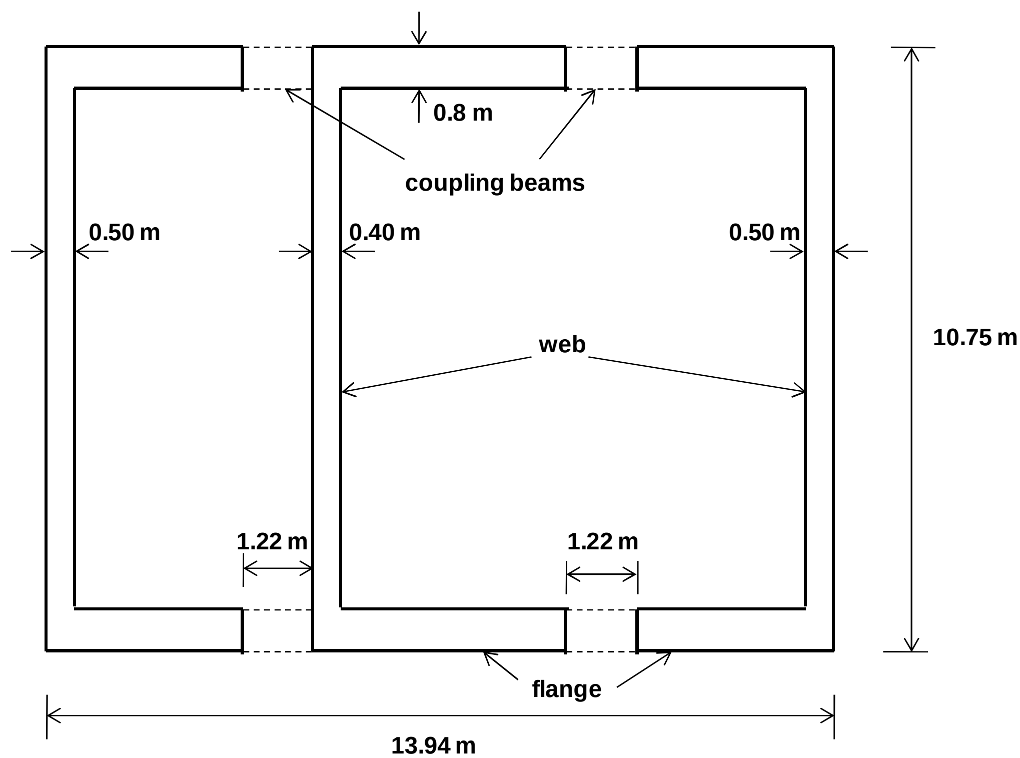

Figure A.4 Outline of the core walls in 40 story buildings.

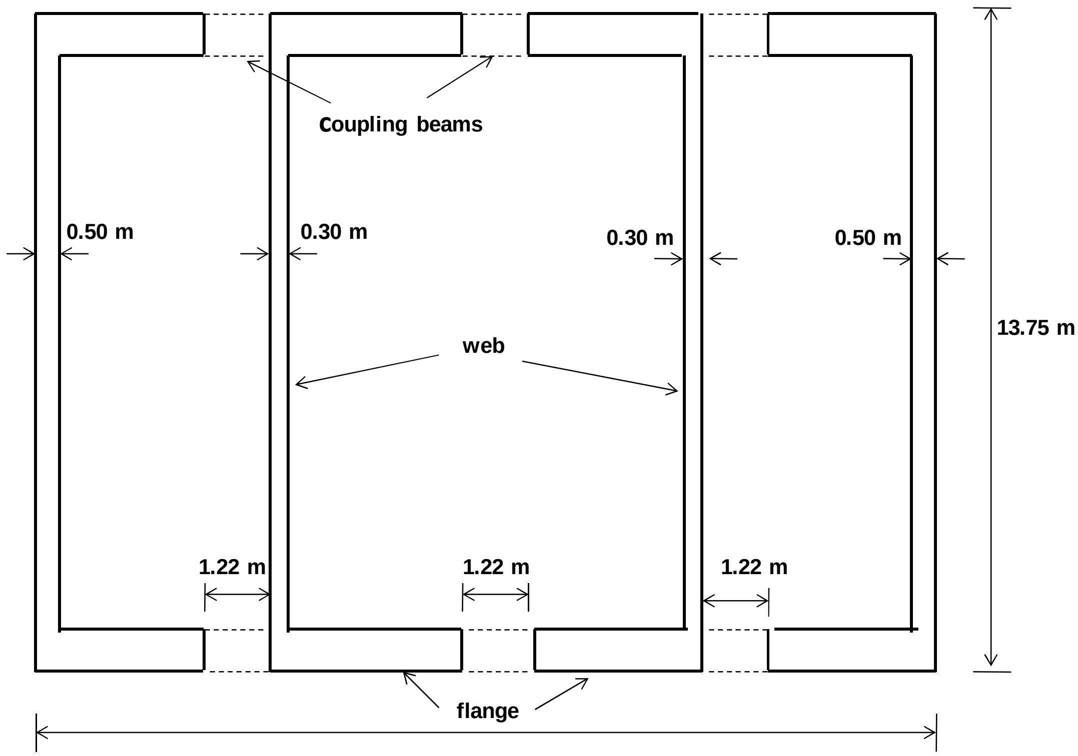

Figure A.5 Outline of the core walls in 50 story buildings.

Appendix B:

Tabular Data for Example Core Walls

Table B.1 Longitudinal reinforcement percentage in the flange (ρ_f) and nominal bending moment capacity (M_n) for 10 story walls.

		ρ_f (%)				M_n (kNm)			
h (m)	P/f'$_c$A$_g$	R_g=1.7	R_g=2.6	R_g=4.2	R_g=5.2	R_g=1.7	R_g=2.6	R_g=4.2	R_g=5.2
0	0.059	4.00	2.50	1.20	0.45	262599	182992	112533	72037
4.5	0.050	4.00	2.50	1.20	0.45	257499	177648	106979	66335
7.3	0.045	4.00	2.50	1.20	0.45	254274	174269	103467	62766
10.1	0.039	3.29	2.09	1.05	0.45	213320	148654	91671	59183
12.9	0.033	2.58	1.68	0.90	0.45	171863	122869	79876	55588
15.7	0.028	1.87	1.27	0.75	0.45	129783	96791	67956	51982
18.5	0.022	1.16	0.86	0.60	0.45	87139	70480	55975	48363
21.3	0.017	0.45	0.45	0.45	0.45	43997	44003	43997	44734
24.1	0.011	0.45	0.45	0.45	0.45	40330	40330	40330	41094
26.9	0.006	0.45	0.45	0.45	0.45	36718	36718	36718	37445
29.7	0.000	0.45	0.45	0.45	0.45	33026	33026	33026	33026

ρ_f = 0.45% is minimum longitudinal reinforcement in the flanges, longitudinal reinforcement in the web, ρ_w = 0.25% over the height for all walls, total flange cross sectional area = 5.4 m^2.

Table B.2 Longitudinal reinforcement percentage in the flange (ρ_f) and nominal bending moment capacity (M_n) for 20 story wall.

h (m)	P/f'$_c$A$_g$	ρ_f (%)	M_n (kNm)
0	0.087	0.60	255915
4.5	0.080	0.60	243861
7.3	0.076	0.60	236334
10.1	0.072	0.60	228786
12.9	0.068	0.60	221217
15.7	0.063	0.60	213628
18.5	0.059	0.60	206018
21.3	0.055	0.60	198387
24.1	0.051	0.60	190735
26.9	0.046	0.60	183063
29.7	0.042	0.60	175370
32.5	0.038	0.60	167656
35.3	0.034	0.60	159922
38.1	0.030	0.60	152167
40.9	0.025	0.60	144391
43.7	0.021	0.60	136594
46.5	0.017	0.60	128777
49.3	0.013	0.60	120938
52.1	0.008	0.60	113080
54.9	0.004	0.60	105200
57.7	0.000	0.60	97300

ρ_f = 0.60% is minimum longitudinal reinforcement in the flanges, ρ_w = 0.25% over the height for all walls, total flange cross sectional area = 8.8 m^2.

Table B.3 Longitudinal reinforcement percentage in the flange (ρ_f) and nominal bending moment capacity (M_n) for 30 story walls.

			ρ_f (%)				M_n (kNm)			
h (m)	P/f'_cA_g [1]	P/f'_cA_g [2]	R_g=1.4	R_g=2.4	R_g=3.1	R_g=4.3	R_g=1.4	R_g=2.4	R_g=3.1	R_g=4.3
0	0.101	0.061	3.50	1.20	0.50	0.50	1138624	669081	523832	375018
4.5	0.096	0.057	3.50	1.20	0.50	0.50	1120863	650381	504846	363399
7.3	0.092	0.055	3.50	1.20	0.50	0.50	1109766	638700	492987	356155
10.1	0.089	0.053	3.50	1.20	0.50	0.50	1098640	626989	481099	348902
12.9	0.086	0.051	3.50	1.20	0.50	0.50	1087485	615250	469182	341638
15.7	0.083	0.049	3.50	1.20	0.50	0.50	1076302	603483	457237	334364
18.5	0.079	0.047	3.34	1.15	0.50	0.50	1032968	581263	445262	327080
21.3	0.076	0.045	3.18	1.10	0.50	0.50	989470	558984	433258	319785
24.1	0.073	0.043	3.03	1.05	0.50	0.50	945807	536645	421226	312481
26.9	0.069	0.041	2.87	1.00	0.50	0.50	901979	514246	409165	305166
29.7	0.066	0.039	2.71	0.95	0.50	0.50	857987	491787	397075	297841
32.5	0.063	0.037	2.55	0.90	0.50	0.50	813829	469268	384955	290506
35.3	0.059	0.035	2.39	0.85	0.50	0.50	769507	446690	372807	283161
38.1	0.056	0.033	2.24	0.80	0.50	0.50	725020	424051	360630	275805
40.9	0.053	0.031	2.08	0.75	0.50	0.50	680369	401353	348425	268440
43.7	0.050	0.029	1.92	0.70	0.50	0.50	635552	378594	336190	261064
46.5	0.046	0.027	1.76	0.65	0.50	0.50	590571	355776	323926	253677
49.3	0.043	0.025	1.61	0.60	0.50	0.50	545425	332898	311634	246281
52.1	0.040	0.024	1.45	0.55	0.50	0.50	500114	309960	299312	238875
54.9	0.036	0.022	1.29	0.50	0.50	0.50	454638	286962	286962	231458
57.7	0.033	0.020	1.13	0.50	0.50	0.50	408998	274583	274583	224031
60.5	0.030	0.018	0.97	0.50	0.50	0.50	363192	262175	262175	216594
63.3	0.026	0.016	0.82	0.50	0.50	0.50	317222	249738	249738	209146
66.1	0.023	0.014	0.66	0.50	0.50	0.50	271088	237272	237272	201689
68.9	0.020	0.012	0.50	0.50	0.50	0.50	224788	224777	224777	194221
71.7	0.017	0.010	0.50	0.50	0.50	0.50	212253	212253	212253	186743
74.5	0.013	0.008	0.50	0.50	0.50	0.50	199700	199700	199700	179255
77.3	0.010	0.006	0.50	0.50	0.50	0.50	187119	187119	187119	171757
80.1	0.007	0.004	0.50	0.50	0.50	0.50	174508	174508	174508	164248
82.9	0.003	0.002	0.50	0.50	0.50	0.50	161869	161869	161869	156730
85.7	0.000	0.000	0.50	0.50	0.50	0.50	149201	149201	149201	149201

[1]axial compression force for R_g = 1.4, 2.4, and 3.1, [2]axial compression force for R_g = 4.3, ρ_f = 0.50 is minimum longitudinal reinforcement in the flanges, longitudinal reinforcement in the web, ρ_w = 0.25% over the height for all walls, total flange cross sectional area = 12.6 m^2.

Table B.4 Longitudinal reinforcement percentage in the flange (ρ_f) and nominal bending moment capacity (M_n) for 40 story walls.

			ρ_f (%)		M_n (kNm)	
h (m)	P/f'_cA_g [1]	P/f'_cA_g [2]	R_g=2.6	R_g=4.4	R_g=2.6	R_g=4.4
0	0.114	0.062	0.52	0.52	1080128	635365
4.5	0.109	0.060	0.52	0.52	1049021	623757
7.3	0.107	0.059	0.52	0.52	1029616	616528
10.1	0.104	0.058	0.52	0.52	1010172	609294
12.9	0.101	0.056	0.52	0.52	990690	602055
15.7	0.098	0.055	0.52	0.52	971169	594812
18.5	0.095	0.054	0.52	0.52	951610	587563
21.3	0.093	0.053	0.52	0.52	932013	580309
24.1	0.090	0.051	0.52	0.52	912377	573051
26.9	0.087	0.050	0.52	0.52	892703	565787
29.7	0.084	0.049	0.52	0.52	872990	558519
32.5	0.081	0.048	0.52	0.52	853239	551246
35.3	0.079	0.047	0.52	0.52	833450	543968
38.1	0.076	0.045	0.52	0.52	813622	536685
40.9	0.073	0.044	0.52	0.52	793756	529397
43.7	0.070	0.043	0.52	0.52	773851	522104
46.5	0.067	0.042	0.52	0.52	753909	514806
49.3	0.065	0.040	0.52	0.52	733927	507503
52.1	0.062	0.039	0.52	0.52	713908	500196
54.9	0.059	0.038	0.52	0.52	693849	492883
57.7	0.056	0.037	0.52	0.52	673753	485566
60.5	0.053	0.036	0.52	0.52	653618	478244
63.3	0.051	0.034	0.52	0.52	633445	470916
66.1	0.048	0.033	0.52	0.52	613233	463584
68.9	0.045	0.032	0.52	0.52	592983	456247
71.7	0.042	0.031	0.52	0.52	572695	448905
74.5	0.039	0.029	0.52	0.52	552368	441558
77.3	0.036	0.028	0.52	0.52	532003	434207
80.1	0.034	0.027	0.52	0.52	511599	426850
82.9	0.031	0.026	0.52	0.52	491157	419488
85.7	0.028	0.025	0.52	0.52	470677	412122
88.5	0.025	0.023	0.52	0.52	450158	404750
91.3	0.022	0.022	0.52	0.52	429601	397374
94.1	0.020	0.021	0.52	0.52	409005	389993
96.9	0.017	0.020	0.52	0.52	388371	382607
99.7	0.014	0.018	0.52	0.52	367699	375216
102.5	0.011	0.017	0.52	0.52	346988	367820
105.3	0.008	0.016	0.52	0.52	326239	360419
108.1	0.006	0.015	0.52	0.52	305452	353013
110.9	0.003	0.013	0.52	0.52	284626	345603
113.7	0.000	0.012	0.52	0.52	263761	338187

[1]axial compression stress ratio for R_g = 2.6, [2]axial compression stress ratio for R_g = 4.4, ρ_f = 0.52% is minimum longitudinal reinforcement in the flanges, ρ_w = 0.25% over the height for all walls, total flange cross sectional area = 18.4 m^2.

Table B.5 Longitudinal reinforcement percentage in the flange (ρ_f) and nominal bending moment capacity (M_n) for 50 story walls.

			ρ_f (%)				M_n (kNm)			
h (m)	P/f'_cA_g [1]	P/f'_cA_g [2]	R_g=1.4	R_g=2.1	R_g=2.4	R_g=4.1	R_g=1.4	R_g=2.1	R_g=2.4	R_g=4.1
0	0.127	0.062	3.50	1.00	0.48	0.48	3924905	2481567	2178190	1297803
4.5	0.123	0.060	3.50	1.00	0.48	0.48	3873583	2428376	2124611	1270573
7.3	0.120	0.059	3.50	1.00	0.48	0.48	3841579	2395210	2091203	1253613
10.1	0.118	0.058	3.50	1.00	0.48	0.48	3809521	2361990	2057741	1236640
12.9	0.115	0.056	3.50	1.00	0.48	0.48	3777410	2328717	2024226	1219655
15.7	0.113	0.055	3.50	1.00	0.48	0.48	3745245	2295389	1990657	1202657
18.5	0.110	0.054	3.50	1.00	0.48	0.48	3713026	2262008	1957034	1185646
21.3	0.108	0.053	3.50	1.00	0.48	0.48	3680754	2228573	1923358	1168622
24.1	0.105	0.052	3.41	0.95	0.48	0.48	3594022	2165762	1889628	1151585
26.9	0.103	0.050	3.31	0.90	0.48	0.48	3507113	2102839	1855844	1134536
29.7	0.100	0.049	3.22	0.85	0.48	0.48	3420026	2039807	1822006	1117473
32.5	0.098	0.048	3.12	0.80	0.48	0.48	3332762	1976664	1788115	1100398
35.3	0.095	0.047	3.03	0.75	0.48	0.48	3245321	1913411	1754170	1083311
38.1	0.093	0.045	2.93	0.70	0.48	0.48	3157703	1850048	1720172	1066210
40.9	0.090	0.044	2.84	0.65	0.48	0.48	3069907	1786575	1686120	1049097
43.7	0.088	0.043	2.75	0.60	0.48	0.48	2981934	1722991	1652014	1031970
46.5	0.085	0.042	2.65	0.55	0.48	0.48	2893783	1659297	1617854	1014831
49.3	0.083	0.040	2.56	0.48	0.48	0.48	2805456	1583641	1583641	997680
52.1	0.080	0.039	2.46	0.48	0.48	0.48	2716951	1549374	1549374	980515
54.9	0.078	0.038	2.37	0.48	0.48	0.48	2628269	1515054	1515054	963338
57.7	0.075	0.037	2.27	0.48	0.48	0.48	2539409	1480680	1480680	946148
60.5	0.073	0.036	2.18	0.48	0.48	0.48	2450372	1446252	1446252	928945
63.3	0.070	0.034	2.08	0.48	0.48	0.48	2361158	1411770	1411770	911729
66.1	0.068	0.033	1.99	0.48	0.48	0.48	2271767	1377235	1377235	894500
68.9	0.065	0.032	1.90	0.48	0.48	0.48	2182198	1342646	1342646	877259
71.7	0.063	0.031	1.80	0.48	0.48	0.48	2092452	1308003	1308003	860005
74.5	0.060	0.029	1.71	0.48	0.48	0.48	2002528	1273307	1273307	842738
77.3	0.058	0.028	1.61	0.48	0.48	0.48	1912428	1238557	1238557	825459
80.1	0.055	0.027	1.52	0.48	0.48	0.48	1822150	1203754	1203754	808166
82.9	0.053	0.026	1.42	0.48	0.48	0.48	1731695	1168896	1168896	790861
85.7	0.050	0.025	1.33	0.48	0.48	0.48	1641062	1133985	1133985	773543
88.5	0.048	0.023	1.24	0.48	0.48	0.48	1550252	1099021	1099021	756212
91.3	0.045	0.022	1.14	0.48	0.48	0.48	1459265	1064003	1064003	738868
94.1	0.043	0.021	1.05	0.48	0.48	0.48	1368101	1028931	1028931	721512
96.9	0.040	0.020	0.95	0.48	0.48	0.48	1276759	993805	993805	704143
99.7	0.038	0.018	0.86	0.48	0.48	0.48	1185240	958626	958626	686761
102.5	0.035	0.017	0.76	0.48	0.48	0.48	1093544	923393	923393	669366
105.3	0.033	0.016	0.67	0.48	0.48	0.48	1001670	888106	888106	651958
108.1	0.030	0.015	0.57	0.48	0.48	0.48	909619	852766	852766	634538
110.9	0.028	0.014	0.48	0.48	0.48	0.48	817391	817372	817372	617105
113.7	0.025	0.012	0.48	0.48	0.48	0.48	781924	781924	781924	599659

			ρ_f (%)				M_n (kNm)			
h (m)	P/f'_cA_g[1]	P/f'_cA_g[2]	R_g=1.4	R_g=2.1	R_g=2.4	R_g=4.1	R_g = 1.4	R_g = 2.1	R_g = 2.4	R_g = 4.1
116.5	0.023	0.011	0.48	0.48	0.48	0.48	746423	746423	746423	582200
119.3	0.020	0.010	0.48	0.48	0.48	0.48	710868	710868	710868	564728
122.1	0.018	0.009	0.48	0.48	0.48	0.48	675259	675259	675259	547244
124.9	0.015	0.007	0.48	0.48	0.48	0.48	639597	639597	639597	529747
127.7	0.013	0.006	0.48	0.48	0.48	0.48	603881	603881	603881	512237
130.5	0.010	0.005	0.48	0.48	0.48	0.48	568111	568111	568111	494714
133.3	0.008	0.004	0.48	0.48	0.48	0.48	532287	532287	532287	477179
136.1	0.005	0.003	0.48	0.48	0.48	0.48	496410	496410	496410	459630
138.9	0.003	0.001	0.48	0.48	0.48	0.48	460480	460480	460480	442069
141.7	0.000	0.000	0.48	0.48	0.48	0.48	424495	424495	424495	424495

[1]axial compression stress ratio for R_g = 1.4, 2.1, and 2.4, [2]axial compression stress ratio for R_g = 4.1, ρ_f = 0.48% is minimum longitudinal reinforcement in the flanges, ρ_w = 0.25% over the height for all walls, total flange cross sectional area = 22.95 m^2.

Table B.6 Cracked flexural stiffness (EI_{cr}) for 10 story walls.

	EI_{cr} (KNm^2)*10^8			
h (m)	R_g=1.7	R_g=2.6	R_g=4.2	R_g=5.2
0	4.30	2.68	1.28	0.33
4.5	4.30	2.68	1.28	0.33
7.3	4.30	2.68	1.28	0.33
10.1	3.66	2.27	1.09	0.33
12.9	2.98	1.82	0.94	0.33
15.7	2.26	1.34	0.73	0.33
18.5	1.50	0.87	0.52	0.33
21.3	0.60	0.33	0.33	0.33
24.1	0.60	0.33	0.33	0.33
26.9	0.60	0.33	0.33	0.33
29.7	0.60	0.33	0.33	0.33

Table B.7 Cracked flexural stiffness (EI_{cr}) for 30 story walls.

	EI_{cr} (kNm^2)*10^9			
h (m)	R_g=1.4	R_g=2.4	R_g=3.1	R_g=4.3
0	2.59	1.05	0.52	0.52
4.5	2.59	1.05	0.52	0.52
7.3	2.59	1.05	0.52	0.52
10.1	2.59	1.05	0.52	0.52
12.9	2.59	1.05	0.52	0.52
15.7	2.59	1.05	0.52	0.52
18.5	2.48	1.01	0.52	0.52
21.3	2.39	0.98	0.52	0.52
24.1	2.29	0.94	0.52	0.52
26.9	2.19	0.90	0.52	0.52
29.7	2.09	0.87	0.52	0.52
32.5	1.98	0.83	0.52	0.52
35.3	1.88	0.79	0.52	0.52
38.1	1.78	0.75	0.52	0.52
40.9	1.67	0.71	0.52	0.52
43.7	1.56	0.67	0.52	0.52
46.5	1.46	0.63	0.52	0.52
49.3	1.34	0.60	0.52	0.52
52.1	1.23	0.55	0.52	0.52
54.9	1.11	0.52	0.52	0.52
57.7	1.00	0.52	0.52	0.52
60.5	0.88	0.52	0.52	0.52
63.3	0.76	0.52	0.52	0.52
66.1	0.64	0.52	0.52	0.52
68.9	0.52	0.52	0.52	0.52
71.7	0.52	0.52	0.52	0.52
74.5	0.52	0.52	0.52	0.52
77.3	0.52	0.52	0.52	0.52
80.1	0.52	0.52	0.52	0.52
82.9	0.52	0.52	0.52	0.52
85.7	0.52	0.52	0.52	0.52

Table B.8 Cracked flexural stiffness (EI_{cr}) for 50 story walls.

	EI_{cr} (kNm^2)*10^{10}			
h (m)	R_g=1.4	R_g=2.1	R_g=2.4	R_g=4.1
0	1.15	0.40	0.23	0.23
4.5	1.15	0.40	0.23	0.23
7.3	1.15	0.40	0.23	0.23
10.1	1.15	0.40	0.23	0.23
12.9	1.15	0.40	0.23	0.23
15.7	1.15	0.40	0.23	0.23
18.5	1.15	0.40	0.23	0.23
21.3	1.15	0.40	0.23	0.23
24.1	1.14	0.39	0.23	0.23
26.9	1.10	0.37	0.23	0.23
29.7	1.07	0.34	0.23	0.23
32.5	1.06	0.34	0.23	0.23
35.3	1.03	0.32	0.23	0.23
38.1	0.99	0.28	0.23	0.23
40.9	0.96	0.29	0.23	0.23
43.7	0.94	0.27	0.23	0.23
46.5	0.91	0.25	0.23	0.23
49.3	0.89	0.23	0.23	0.23
52.1	0.85	0.23	0.23	0.23
54.9	0.75	0.23	0.23	0.23
57.7	0.79	0.23	0.23	0.23
60.5	0.78	0.23	0.23	0.23
63.3	0.74	0.23	0.23	0.23
66.1	0.72	0.23	0.23	0.23
68.9	0.69	0.23	0.23	0.23
71.7	0.66	0.23	0.23	0.23
74.5	0.62	0.23	0.23	0.23
77.3	0.59	0.23	0.23	0.23
80.1	0.56	0.23	0.23	0.23
82.9	0.54	0.23	0.23	0.23
85.7	0.51	0.23	0.23	0.23
88.5	0.48	0.23	0.23	0.23
91.3	0.45	0.23	0.23	0.23
94.1	0.42	0.23	0.23	0.23
96.9	0.37	0.23	0.23	0.23
99.7	0.36	0.23	0.23	0.23
102.5	0.31	0.23	0.23	0.23
105.3	0.27	0.23	0.23	0.23
108.1	0.26	0.23	0.23	0.23
110.9	0.23	0.23	0.23	0.23
113.7	0.23	0.23	0.23	0.23
116.5	0.23	0.23	0.23	0.23

	EI_{cr} (kNm^2)*10^{10}			
h (m)	R_g=1.4	R_g=2.1	R_g=2.4	R_g=4.1
119.3	0.23	0.23	0.23	0.23
122.1	0.23	0.23	0.23	0.23
124.9	0.23	0.23	0.23	0.23
127.7	0.23	0.23	0.23	0.23
130.5	0.23	0.23	0.23	0.23
133.3	0.23	0.23	0.23	0.23
136.1	0.23	0.23	0.23	0.23
138.9	0.23	0.23	0.23	0.23
141.7	0.23	0.23	0.23	0.23

Table B.9 Bending moment at crack opening (M_{co}) and bending moment at crack closing (M_{cc}) for 10 story walls.

	M_{co} (kNm)	M_{cc} (kNm)			
h (m)	R_g=1.7 to 5.2	R_g=1.7	R_g=2.6	R_g=4.2	R_g=5.2
0	51238	-182806	-95059	-34965	-11852
4.5	47414	-186630	-98883	-38789	-18082
7.3	45008	-189036	-101289	-41195	-20488
10.1	42601	-158622	-84744	-36668	-25257
12.9	40238	-128165	-68155	-32097	-27663
15.7	37832	-97751	-51610	-27570	-30027
18.5	35426	-67337	-35064	-23042	-32433
21.3	33063	-36880	-18476	-18471	-34796
24.1	30657	-39285	-20877	-20877	-11852
26.9	28293	-41648	-23240	-23240	-18082
29.7	25887	-44054	-25646	-25646	-20488

Table B.10 Bending moment at crack opening (M_{co}) and bending moment at crack closing (M_{cc}) for 20 story wall.

h (m)	M_{co} (kNm)	M_{cc} (kNm)
0	168107	28030
4.5	160118	20042
7.3	155148	15071
10.1	150177	10100
12.9	145206	5130
15.7	140235	159
18.5	135265	-4812
21.3	130294	-9782
24.1	125323	-14753
26.9	120353	-19724
29.7	115382	-24695
32.5	110411	-29665
35.3	105440	-34636
38.1	100470	-39607
40.9	95499	-44578
43.7	90528	-49548
46.5	85557	-54519
49.3	80587	-59490
52.1	75616	-64460
54.9	70645	-69431
57.7	65675	-74402

Note: cracked flexural stiffness $EI_{cr} = 0.28*10^9$ kNm^2 is constant over the height.

Table B.11 Bending moment at crack opening (M_{co}) and bending moment at crack closing (M_{cc}) for 30 story walls.

	M_{co} (kNm)		M_{cc} (kNm)			
h (m)	R_q=1.4 to 3.1	R_q=4.3	R_q=1.4	R_q=2.4	R_q=3.1	R_q=4.3
0	355938	260666	-391629	3925	124311	29039
4.5	343622	253346	-403945	-8391	111995	21718
7.3	335954	248790	-411613	-16059	104327	17163
10.1	328286	244235	-419281	-23727	96659	12608
12.9	320618	239680	-426949	-31395	88991	8053
15.7	312950	235125	-434617	-39064	81322	3498
18.5	305281	230570	-415131	-38133	73654	-1058
21.3	297613	226014	-395645	-37202	65986	-5613
24.1	289945	221459	-376159	-36271	58318	-10168
26.9	282277	216904	-356673	-35340	50650	-14723
29.7	274609	212349	-337187	-34410	42981	-19278
32.5	266940	207794	-317701	-33479	35313	-23834
35.3	259272	203238	-298215	-32548	27645	-28389
38.1	251604	198683	-278729	-31617	19977	-32944
40.9	243936	194128	-259243	-30686	12309	-37499
43.7	236268	189573	-239757	-29755	4641	-42054
46.5	228599	185018	-220271	-28825	-3028	-46610
49.3	220931	180462	-200785	-27894	-10696	-51165
52.1	213263	175907	-181299	-26963	-18364	-55720
54.9	205595	171352	-161813	-26032	-26032	-60275
57.7	197927	166797	-142326	-33700	-33700	-64830
60.5	190258	162242	-122840	-41369	-41369	-69386
63.3	182590	157686	-103354	-49037	-49037	-73941
66.1	174922	153131	-83868	-56705	-56705	-78496
68.9	167254	148576	-64382	-64373	-64373	-83051
71.7	159586	144021	-72041	-72041	-72041	-87606
74.5	151918	139466	-79710	-79710	-79710	-92162
77.3	144249	134910	-87378	-87378	-87378	-96717
80.1	136581	130355	-95046	-95046	-95046	-101272
82.9	128913	125800	-102714	-102714	-102714	-105827
85.7	121245	121245	-110382	-110382	-110382	-110382

Table B.12 Bending moment at crack opening (M_{co}) and bending moment at crack closing (M_{cc}) for 40 story wall.

h (m)	M_{co} (kNm)	M_{cc} (kNm)
0	456891	6542
4.5	449520	-830
7.3	444933	-5416
10.1	440347	-10003
12.9	435760	-14590
15.7	431173	-19176
18.5	426587	-23763
21.3	422000	-28350
24.1	417413	-32936
26.9	412827	-37523
29.7	408240	-42109
32.5	403654	-46696
35.3	399067	-51283
38.1	394480	-55869
40.9	389894	-60456
43.7	385307	-65042
46.5	380720	-69629
49.3	376134	-74216
52.1	371547	-78802
54.9	366961	-83389
57.7	362374	-87976
60.5	357787	-92562
63.3	353201	-97149
66.1	348614	-101735
68.9	344028	-106322
71.7	339441	-110909
74.5	334854	-115495
77.3	330268	-120082
80.1	325681	-124669
82.9	321094	-129255
85.7	316508	-133842
88.5	311921	-138428
91.3	307335	-143015
94.1	302748	-147602
96.9	298161	-152188
99.7	293575	-156775
102.5	288988	-161362
105.3	284401	-165948
108.1	279815	-170535
110.9	275228	-175121
113.7	270642	-179708

Note: cracked flexural stiffness EI_{cr} = 1.26*10^9 kNm^2.

Table B.13 Bending moment at crack opening (M_{co}) and bending moment at crack closing (M_{cc}) for 50 story walls.

	M_{co} (kNm)		M_{cc} (kNm)			
h(m)	R_g=1.4 to 2.4	R_g=4.1	R_g=1.4	R_g=2.1	R_g=2.4	R_g=4.1
0	1502333	940047	-674723	535531	787264	224978
4.5	1467444	923015	-709612	500642	752375	207945
7.3	1445736	912417	-731321	478933	730666	197347
10.1	1424027	901819	-753030	457224	708957	186749
12.9	1402318	891221	-774739	435515	687248	176151
15.7	1380609	880623	-796447	413807	665539	165553
18.5	1358900	870025	-818156	392098	643831	154955
21.3	1337192	859427	-839865	370389	622122	144357
24.1	1315483	848829	-815887	372885	600413	133759
26.9	1293774	838231	-791909	375382	578704	123161
29.7	1272065	827633	-767932	377878	556995	112563
32.5	1250356	817035	-743954	380374	535287	101965
35.3	1228648	806437	-719976	382870	513578	91367
38.1	1206939	795839	-695998	385367	491869	80769
40.9	1185230	785241	-672020	387863	470160	70171
43.7	1163521	774643	-648043	390359	448451	59573
46.5	1141812	764045	-624065	392856	426743	48975
49.3	1120104	753447	-600087	405034	405034	38377
52.1	1098395	742849	-576109	383325	383325	27779
54.9	1076686	732251	-552131	361616	361616	17181
57.7	1054977	721653	-528154	339907	339907	6583
60.5	1033268	711055	-504176	318199	318199	-4015
63.3	1011560	700457	-480198	296490	296490	-14613
66.1	989851	689859	-456220	274781	274781	-25211
68.9	968142	679261	-432242	253072	253072	-35809
71.7	946433	668663	-408265	231363	231363	-46407
74.5	924724	658065	-384287	209655	209655	-57005
77.3	903016	647467	-360309	187946	187946	-67603
80.1	881307	636869	-336331	166237	166237	-78201
82.9	859598	626271	-312353	144528	144528	-88799
85.7	837889	615673	-288375	122819	122819	-99397
88.5	816180	605075	-264398	101111	101111	-109995
91.3	794472	594477	-240420	79402	79402	-120593
94.1	772763	583879	-216442	57693	57693	-131191
96.9	751054	573281	-192464	35984	35984	-141789
99.7	729345	562683	-168486	14275	14275	-152387
102.5	707636	552085	-144509	-7433	-7433	-162985
105.3	685928	541487	-120531	-29142	-29142	-173583
108.1	664219	530889	-96553	-50851	-50851	-184181
110.9	642510	520291	-72575	-72560	-72560	-194779
113.7	620801	509693	-94269	-94269	-94269	-205377
116.5	599092	499095	-115977	-115977	-115977	-215975
119.3	577384	488497	-137686	-137686	-137686	-226573
122.1	555675	477899	-159395	-159395	-159395	-237171
124.8	533966	467301	-181104	-181104	-181104	-247769
127.7	512257	456703	-202813	-202813	-202813	-258367
130.5	490548	446105	-224521	-224521	-224521	-268965
133.3	468840	435507	-246230	-246230	-246230	-279563
136.1	447131	424909	-267939	-267939	-267939	-290161

	M_{co} (kNm)		M_{cc} (kNm)			
h (m)	R_q=1.4 to 2.4	R_q=4.1	R_q=1.4	R_q=2.1	R_q=2.4	R_q=4.1
138.9	425422	414311	-289648	-289648	-289648	-300759
141.7	403713	403713	-311357	-311357	-311357	-311357

Appendix C:

Hysteretic Force - Displacement Relationship Used for Single-Degree-of-Freedom Oscillators

Figure C.1 shows a schematic of the hysteretic force - displacement relationship used in time history analysis of the single-degree-of-freedom (SDOF) oscillators in chapter 3. According to this model, the backbone of the hysteretic model (denoted as path A) consist of a linear segment until shear force reaches V_{co}, followed by a nonlinear curve until it reached the shear force at the flexural capacity of the wall V_n. Note that V_{co} corresponds to shear force at crack opening and is a function of the lower-bound bending moment (Adebar and Ibrahim 2002) and lateral load distribution acting on the wall. The slope of the linear segment of path A, k_i, is the initial stiffness of the wall and depends on the wall height and gross flexural stiffness EI_g. Korchinski (2007) defined a fourth - order polynomial to model the nonlinear segment of the backbone curve. The solution of the polynomial requires five pieces of information to determine five constants of the polynomial. Four constants can be determined by inserting the position of start and endpoints of the curve as well as the slope of the curve at these points. The fifth constant can be obtained by defining an additional point that the curve must pass through between the start and endpoints of the curve. The displacement at flexural capacity, Δ_{yUB}, is calculated by integrating the curvatures determined from the bending moment diagram using the upper-bound bending moment - curvature relationship (Adebar and Ibrahim 2002) over the height of the wall. For displacements greater than Δ_{yUB}, the envelope is defined by a linear segment with a slope equal to 2% of the initial stiffness k_i to model strain hardening of the reinforcement.

The hysteretic path consists of a series of linear paths originating from V_{co} to a point on the envelope corresponding to maximum previous displacement (denoted as path C). The slope of the loading paths tend to decrease as displacement increases; however, in the cases that Δ_{yLB} is exceeded, all subsequent loading paths follow the lower-bound reloading path regardless of maximum previous displacement (denoted as path E). Lower-bound yield displacement, Δ_{yLB}, is calculated by integrating curvatures determined from lower-bound trilinear bending moment - curvature relationship (Adebar and Ibrahim 2002) over the height of the wall.

Unloading paths return linearly from maximum displacement to shear force at crack closing, V_{cc} (denoted as path B). This parameter is a function of bending moment at which cracks will close due to the presence of axial load. For simplicity, it is assumed that the unloading point is located at the linear segment of path A, i.e. zero residual displacement when pushing back the wall to the origin for positive values of V_{cc}. In cases that V_{cc} is negative, the hysteretic model exhibits residual displacement (denoted as path D). Note that V_{cc} is negative for walls with low amount of axial compression force and high percentage of longitudinal reinforcement.

For mid-cycle reloading, the reloading path follows the initial slope k_i from the point where it leaves the unloading path (denoted as path F). The reloading path intersects and follows a linear path from V_{co} to maximum previous displacement. In the cases that maximum previous displacement exceeds Δ_{yLB}, mid-cycle reloading follows the initial stiffness k_i until it joins the lower-bound reloading path.

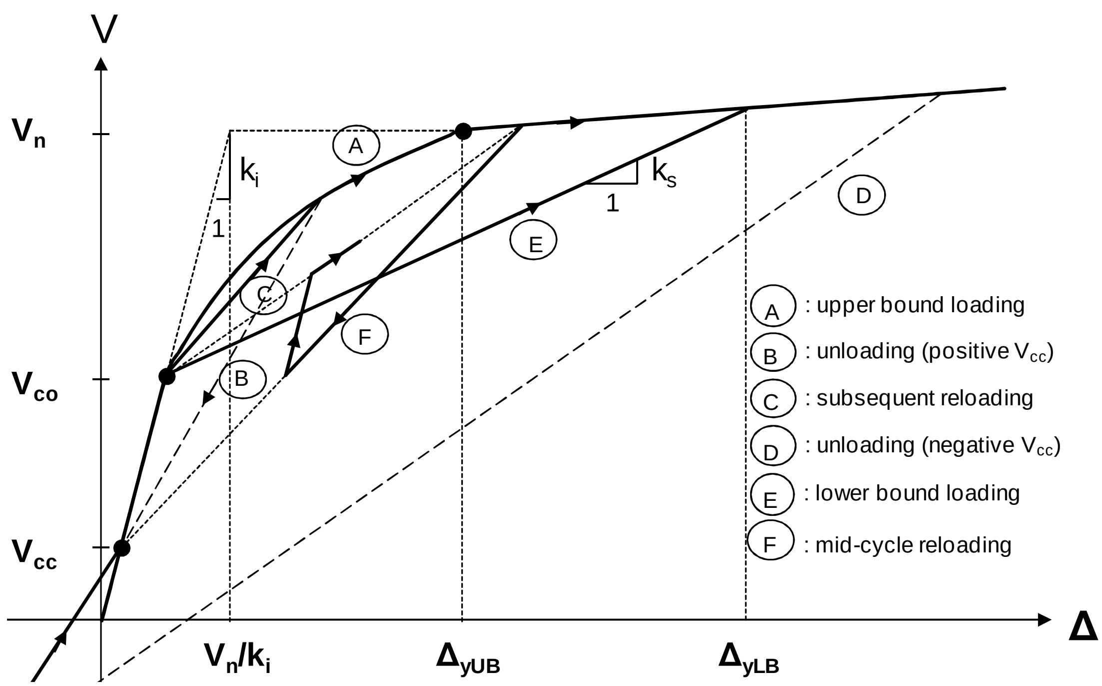

Figure C.1 Hysteretic force - displacement relationship used in SDOF oscillators.

Appendix D:

Mean Spectra of Ground Motions Used in Chapter 3

B.1 Mean Spectra for Ground Motions Scaled to the UHS between $0.2T_1$ and $1.5T_1$

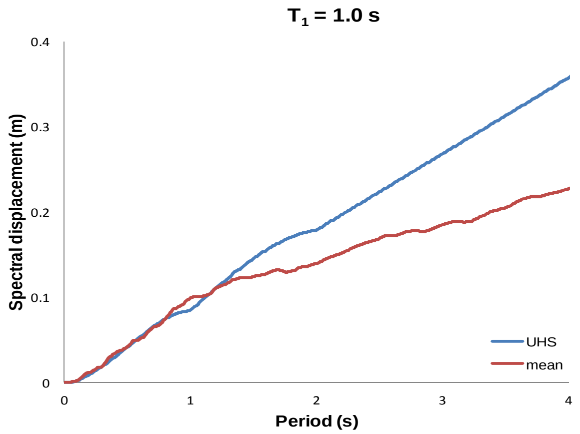

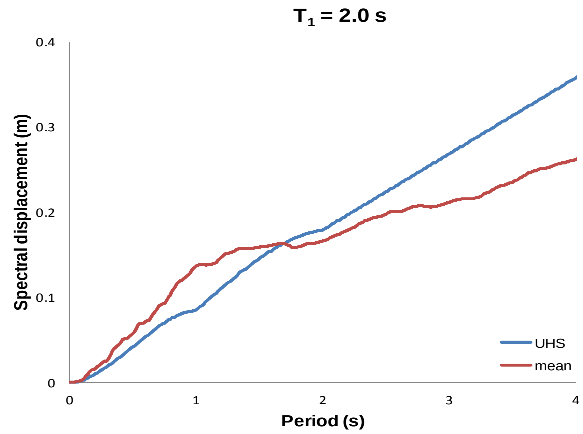

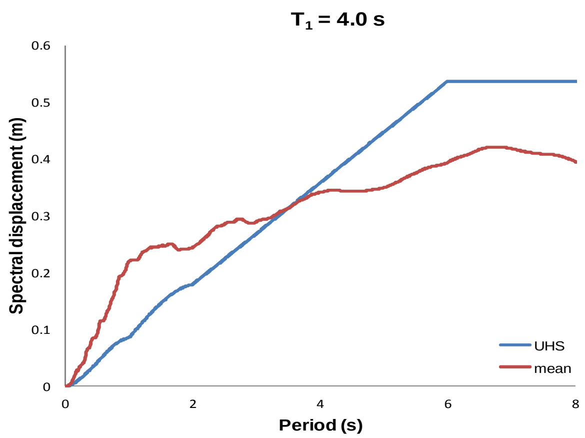

B.2 Mean Spectrum for Spectrum Matched Ground Motions

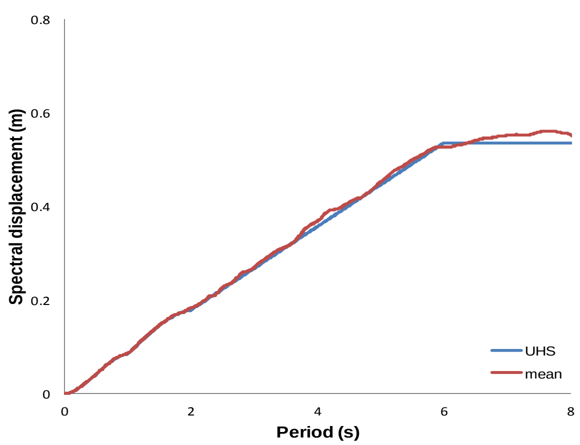

B.3 Mean Spectra for Ground Motions Scaled to the UHS at the fundamental period T_1

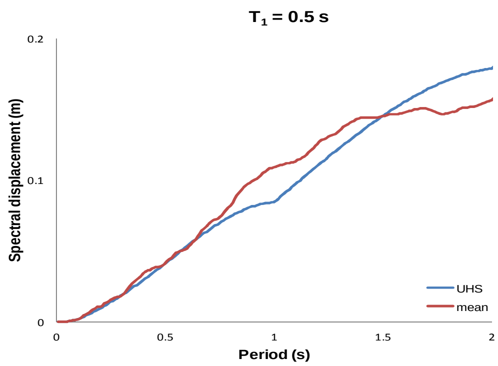

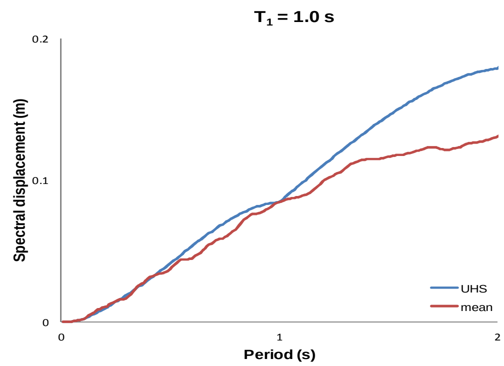

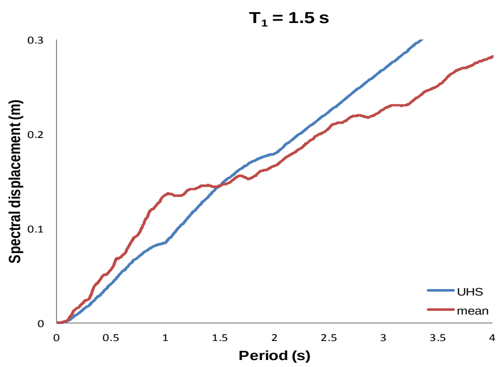

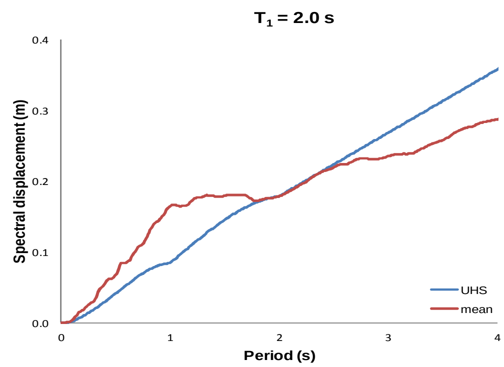

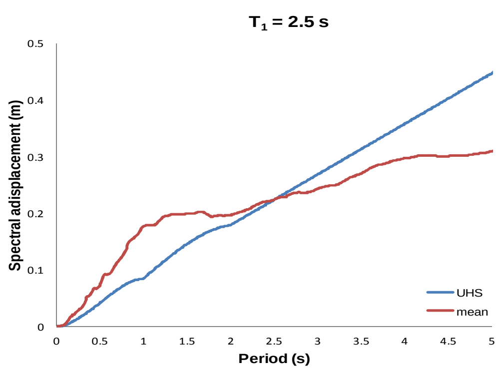

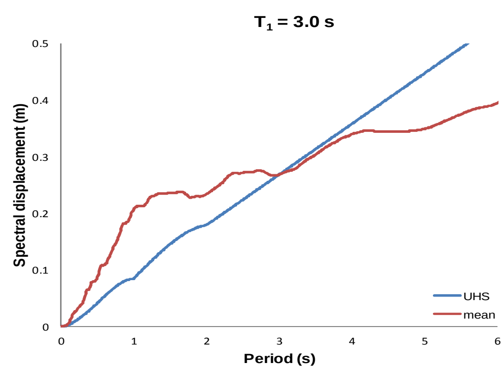

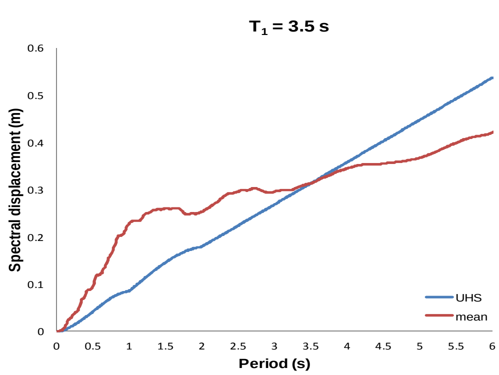

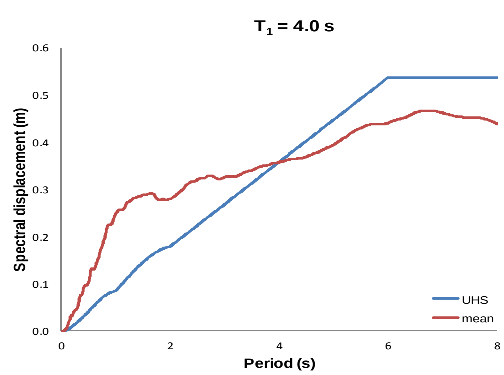

B.4 Mean Spectra for Ground Motions Scaled to the UHS between T_1 and $1.5T_1$

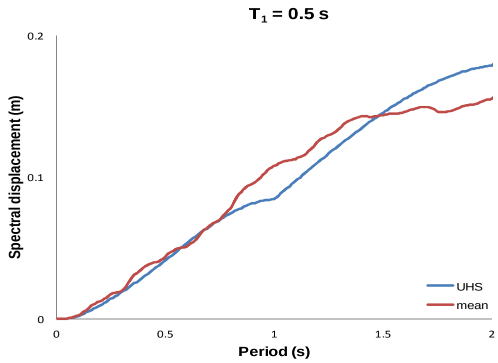

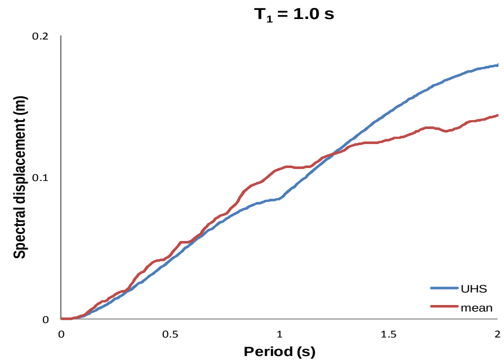

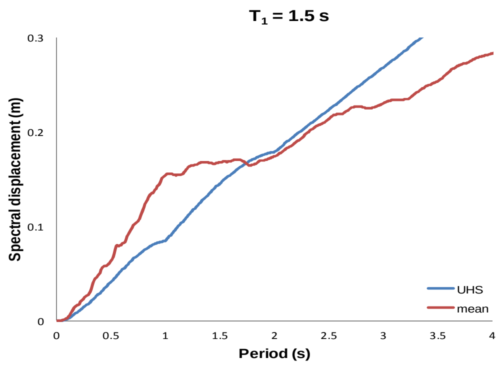

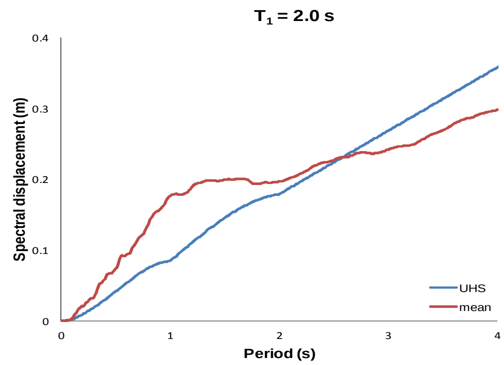

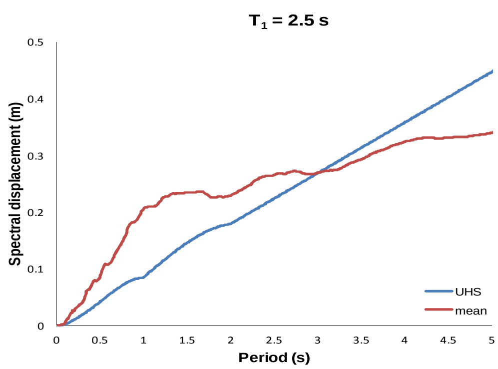

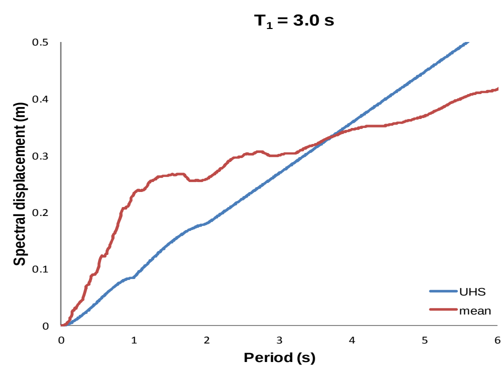

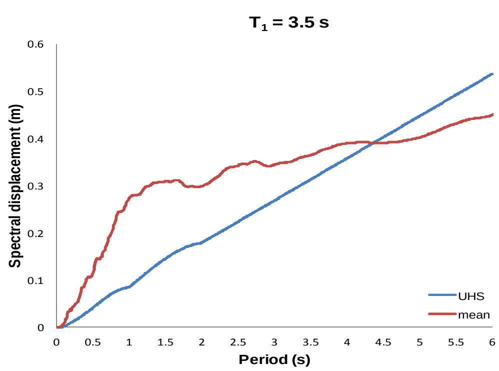

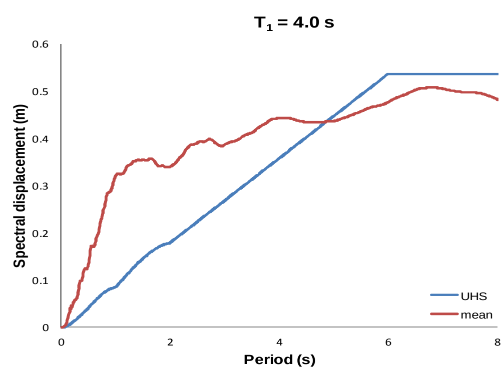

Appendix E:

Effective Stiffness of the 13 Walls Using SDOF Approach Corresponding to Different Ground Motion Scaling Methods

E.1 Effective Stiffness Corresponding to Spectrum Matched Ground Motions

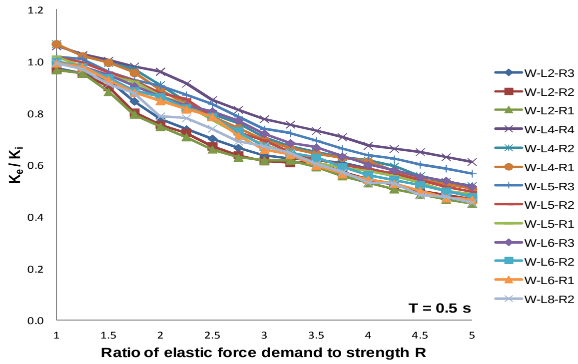

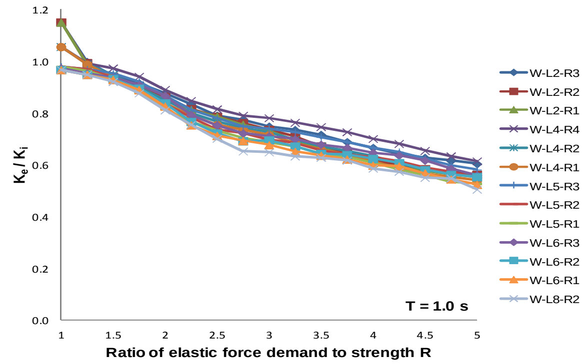

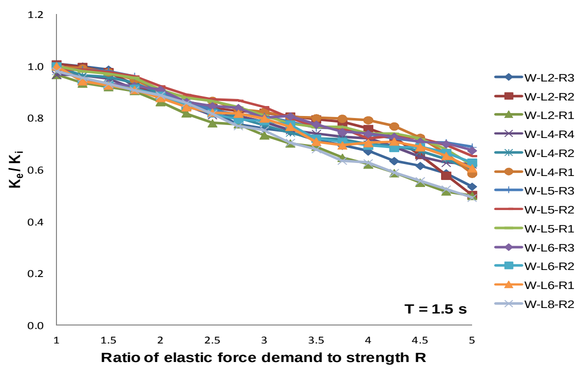

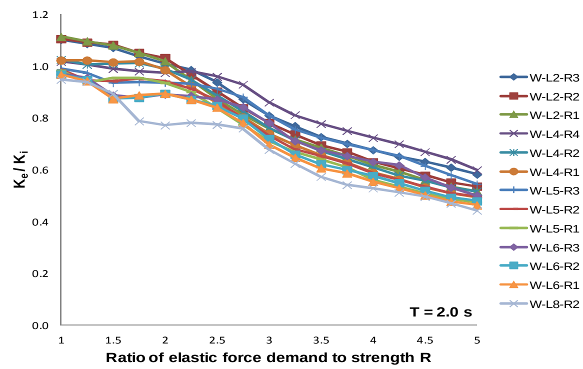

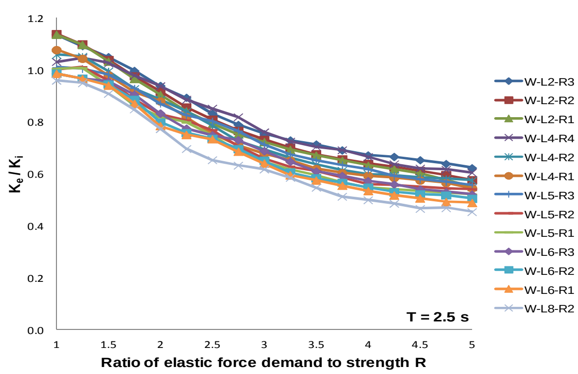

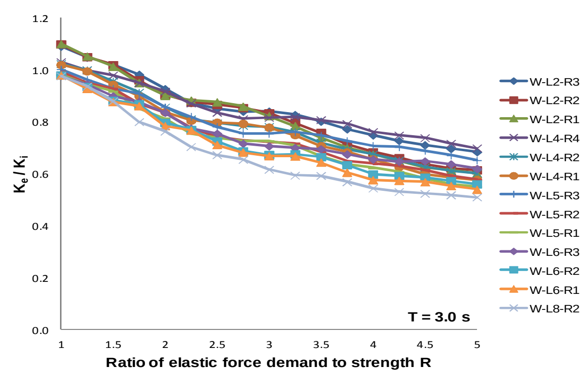

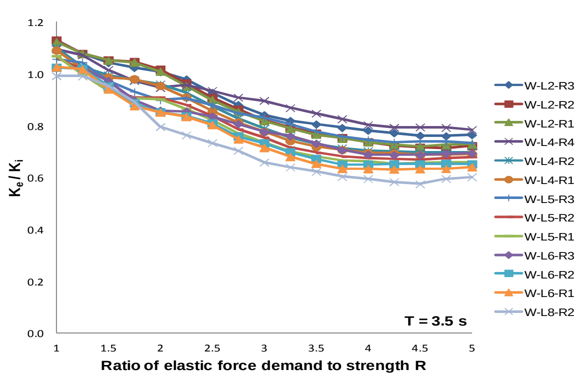

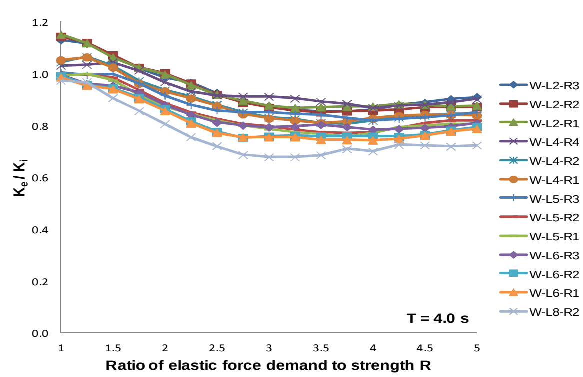

E.2 Effective Stiffness Corresponding to Ground Motions Scaled to the UHS at T_1

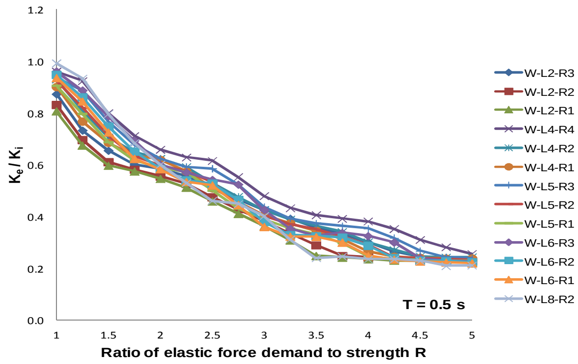

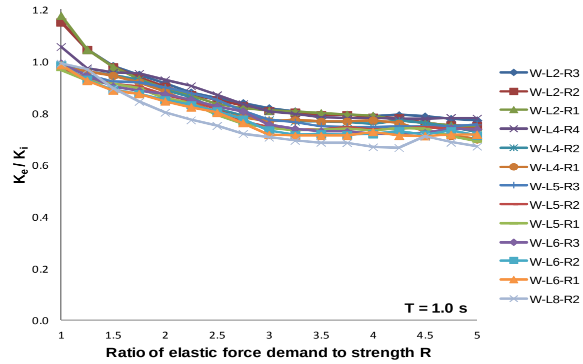

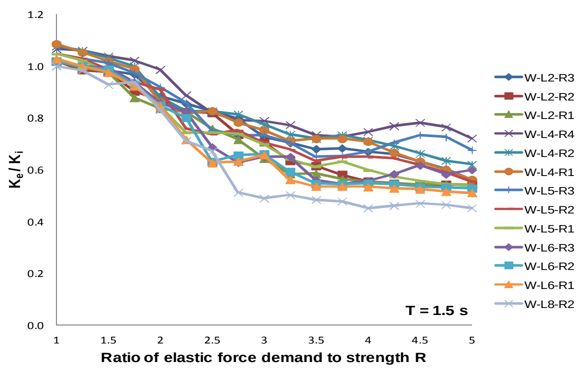

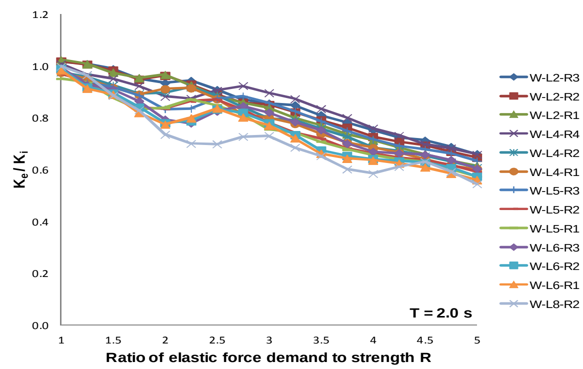

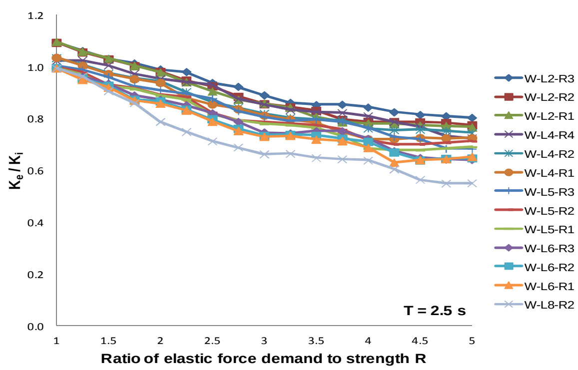

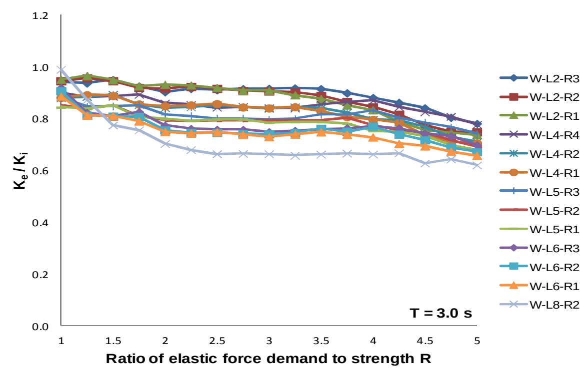

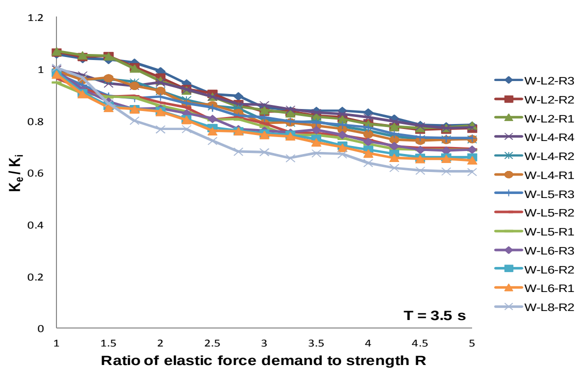

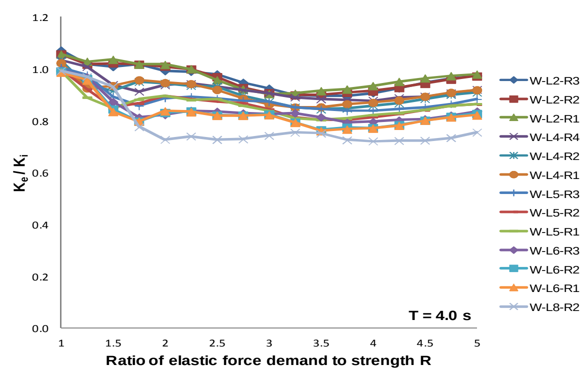

E.3 Effective Stiffness Corresponding to Ground Motions Scaled to the UHS between T_1 and $1.5T_1$